ADAS-EU R(12)PU04

ADAS-EU
ADAS for fusion in Europe

Grant: 224607

Luis Fernández-Menchero, Stuart Henderson and Hugh Summers

PUBL4: Neutral Beam Emission: The Motional Stark Effect

01 Nov 2012

Workpackages : 26-6-4
Category : DRAFT – CONFIDENTIAL

PUBL4: Neutral Beam Emission: The Motional Stark Effect

Luis Fernández-Menchero, Stuart Henderson and Hugh Summers

Department of Physics, University of Strathclyde, Glasgow, UK

Abstract: *The report focuses mainly on two areas of the Motional Stark Effect (MSE) with respect to neutral beam atoms entering in a tokamak — field ionisation and asymmetric cross sections. Detail is also given to the labelling of quantum states when dealing with the MSE. In addition, the integration of these effects into the Atomic Data Analysis Structure (ADAS) code, ADAS305 , is described. It is seen that the field ionisation effects on highly excited states can form an asymmetric distribution of electrons. This asymmetry is then conserved as the electrons cascade down to lower states. Therefore, due to these indirect cascade effects, it is seen that the field ionisation could be a theoretical cause for an observed asymmetry in the* D_α *emission lines of the Stark multiplet. The current method for calculating the cross sections presumes that the electrons are sitting in isotropic, isolated atom states. These states are not true when the beam atoms are travelling at a speed across the magnetic field lines of the plasma. It is seen that the electron distribution is pulled to its k quantum number and stretched to its m magnetic number. A new means of calculating these asymmetric cross sections are detailed.*

Contents

Preface

This article is the one of a series of technical notes which are being prepared as useful extracts during the longer term construction of the next edition of the ADAS user manual. As such it reflects a change in style, planned for the new manual. It will be more book-like, examining and explaining in detail the physics basis behind the commitment to certain approaches in ADAS and how these work out in practice. The new manual will remain technically detailed with extended appendices. However, it is hoped this will be ameliorated by much more emphasis on worked examples. That is to say the actual manoeuvres, adopted by experienced ADAS users in getting the atomic modelling into application scenarios will be mapped, rather as an expert system. It has become clear that, for some, ADAS operates in a somewhat rarefied atmosphere in which too much is assumed. It is this which I wish to improve upon.

Chapter 1

Introduction

The world energy problem is highly debated subject (Nuclear Power: Keeping the Options Open, 2003), with various solutions put forward as a solution. This report is concerned with aspects of the magnetic confinement approach to fusion as a long-term solution. In this approach, deuterium and tritium isotopes of hydrogen, in the form of an ionised plasma, are confined by a magnetic field for sufficiently long times and at sufficiently high density and temperature such that thermonuclear reactions can take place. These reactions release 15 MeV per reaction through the kinetic energy of the neutron and alpha particle products. Once the process has achieved 'ignition', the reactions are self-sustaining through the containment of the alpha particle product whose thermalised energy sustains the plasma. The broad situation has been described in the introduction to the fourth year project of Henderson [1] and a full overview of the fusion process can be found in Mc Cracken and Stott [2].

There are various different magnetic confinement fusion systems with different confining field geometries and different methods for creating the fields, such as stellarators and tokamaks. The most successful to date is the tokamak design which comprises a toroidal configuration. This is the principal method being followed by the international community and details of the physical basis, systems and performance capabilities of the tokamak system can be found in Wesson [3]. The largest current tokamak is the EFDA-JET Facility at Culham Laboratory near Oxford. Constructed and operated by the European Union, it remains the lead system in the world. It had its first plasma in 1983 and then went onto achieve the world's first controlled release of fusion power in 1991 and then later in 1997 produced the world's highest release of fusion power — 16 megawatts of fusion from a total input power of 24 megawatts. The JET machine is currently undergoing a large upgrade (EP2 — extended performance level 2) due for completion in April 2011, so that it can help and influence the design and scientific planning of the next stage in tokamak development for fusion — ITER. This International Tokamak Experimental Reactor is a twelve billion Euro project, being constructed at Cadarache in the South of France by a consortium of countries led by the European Union, USA, Japan, Russian Federation, India, China and South Korea. A schematic of ITER can be seen in figure 1.1

In order for the plasma to reach the temperatures required to allow the fusion of two elements, the tokamak uses a number of methods for heating, including ohmic heating (from the large toroidal current of the tokamak design), radio waves heating for the ions at the cyclotron resonance frequency (ICRH), microwave heating for the electrons at its cyclotron resonance frequency too (ECRH), and Neutral Beam Injection (NBI). It is the diagnostic capabilities of the neutral beam injection method with which this report is concerned here. The principle is straightforward. An energetic neutral atom, which because of its neutrality can pass through the plasma confining field, is injected into the plasma. After it reaches a certain distance, generally within the core of the plasma region, the neutral atoms ionise and thereafter disperse their kinetic energy among the plasma ions; thus heating the plasma. At JET, the primary function of the neutral beams is for heating purposes, and therefore the injected species is deuterium atoms and ultimately will be a mixture of deuterium and tritium at ITER. For JET, injected atom energies must be greater than of the order of 50 keV/amu to penetrate sufficiently into the core of the plasma (depending on the density and size of the plasma). In addition, sustained power greater than of the order of 20 MW is required. The requirements for ITER are much more demanding. At a recent science meeting at EFDA-JET the capabilities being put in place during the JET EP2 and the requirements for ITER were summarised by Ciric [4] and Mc Adams [5].

The next section will summarise these meetings. The diagnostic beam being designed for ITER will lead us into section 1.2 where the importance of beam emission spectroscopy with respect to monitoring key diagnostic parameters

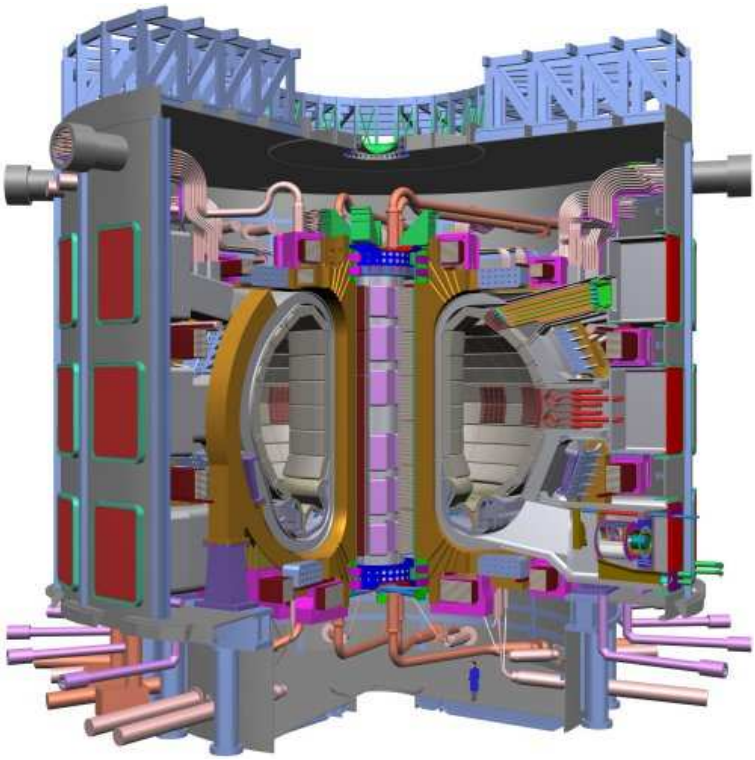

Figure 1.1: A schematic drawing of ITER.

of the plasma is explained. Section 1.3 will highlight the key issue of diagnosis with which this report will be looking at more specifically — the motional Stark effect. The last section of this chapter will detail how the emission spectra of the beam can be used to identify the key parameters.

1.1 Neutral Beam Characteristics

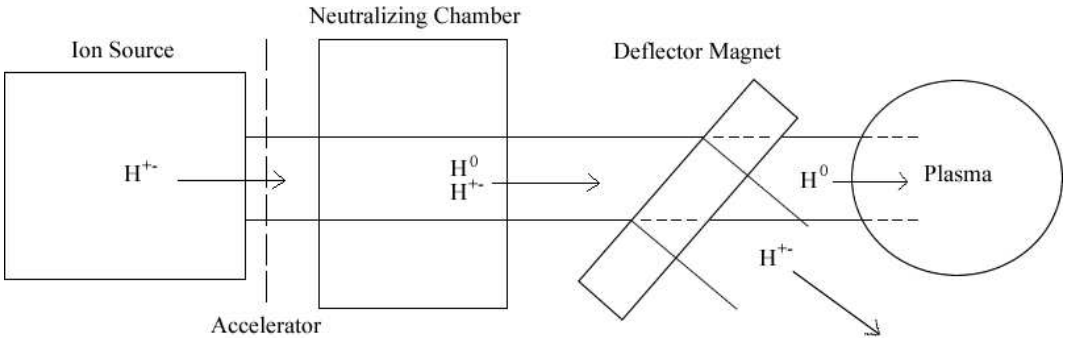

Figure 1.2: Neutral Beam principle for positive and negative ion sources. Here, H is used to denote the deuterium and tritium atoms typically used in JET and ITER.

For magnetic confinement fusion, there are two types of neutral beam which accelerate either positive or negative hydrogen isotope ions. When the energies of the beam are required to be greater than 60 keV/amu, the neutralization of positive ions becomes inefficient and negative ion sources are preferred. In the case of ITER, where the neutral heating beam energies are required to be of the order 1 MeV, the negative ion sources will be put into action. However, for JET and other current machines, positive ions sources are used for heating. The first stage of the neutral beam is a discharge (low temperature plasma). The discharge will contain species e, H, H^+, H_2^+, H_3^+ and H^-. The abundance of each species is optimised through temperature and density to favour the configuration being used. In particular for

positive ion acceleration, the presence of the species H^+, H_2^+, H_3^+ is of greatest concern, while for negative acceleration it is the H^- concentration, formed by vibrational excitation of H_2 followed by the dissociative attachment reaction

$$\begin{aligned} e^- + H_2(v^*) &\rightarrow H_2(v'^*) + e^- \\ e^- + H_2(v^*) &\rightarrow H_2^- \rightarrow H^- + H^+, \end{aligned} \tag{1.1}$$

which must be optimised. Cesium is used to aid this process as the minimum energy required to release its electrons is very low so these electrons can then bind to the H to form H^-. If there is a negative voltage applied across the discharge, the positive ions will be accelerated into a neutralising chamber and there will be a backstream of electrons. Conversely, a positive voltage will accelerate the negative species in the direction of the neutralising chamber and create a backstream of positive ions. The backstream of electrons are relatively easy to decelerate however the positive ions may cause a large amount of sputtering through collision with the source. There are therefore a number of different design features associated with the negative and positive ion sources.

The neutralization stage then establishes the key neutral beam populations which matter for plasma heating and diagnostic studies. Positive species then undergo Charge eXchange Recombination (CXR) reactions with a molecular hydrogen gas cloud which neutralise the ion. The neutralising reactions can be written as

$$\begin{aligned} H^+(E) + H &\rightarrow H(E) + X \\ H_2^+(E) + H &\rightarrow H(E/2) + X \\ H_3^+(E) + H &\rightarrow H(E/3) + X, \end{aligned} \tag{1.2}$$

where E is the energy of the accelerated positive ions and X is defined as any other charged or slow reactants. Therefore, there are now three energy fractions of H which enter the plasma. Negative ion neutralization is by stripping reactions such as

$$H^-(E) + H_2 \rightarrow H(E) + D_2 + e, \tag{1.3}$$

and only a single energy component is present in the final neutral beam. However, only a certain fraction of the ionic species will be neutralised through these processes. An electromagnet must be put in place to deflect these residual fast ions to a cooled ion dump that can withstand heavy ion bombardment. It is also important to ensure the purity of the neutral beam by stopping any slow moving particles from the neutralising gas cloud from diffusing into the plasma. This is achieved through using powerful vacuum pumping technology. A basic schematic for the neutral beam is outlined in figure 1.2. Some further details of the JET and ITER neutral injection systems are given below.

1.1.1 JET Positive Ion Neutral Injection

The JET Neutral Beam Injection (NBI) System uses Positive Ion Neutral Injectors (PINIs). There are two Neutral Injection Boxes (NIBs) which are both equipped with up to eight PINIs (Duesing *et al.* [6]). Within the NIB the PINIs are arranged in two vertical banks of four, with each set of four then split into two pairs sharing the same deflecting magnet. An outline of this arrangement can be seen in figure 1.3a). The maximum energy of these PINIs is sufficient enough to penetrate into the core of JET ($R \approx 3$ m). The EP1 system configuration of neutral beams in JET was brought to an end in 2009. This enhancement program brought significant success in its last two years, providing routine and reliable high power operation. It achieved the highest average injected power of 12.1 MW and longest NBI pulse length of 7.2 s as well as other world records. The new EP2 system is being designed to produce a number of upgrades to the old system. The deuterium NB power is to be increased to 34 MW, the beam pulse length at full power to be increased to 20 s and the reliability and availability of the NBs have to be improved. This should be achieved through a number of different methods. To summarise, the ion source will be changed from a so called supercusp system (Duesing *et al.* [6]) to a chequerboard system. A supercusp system uses magnetic filters which enhance the number of monoatomic ions, leading to a high fraction of full energy neutrals. The new chequerboard magnetic configuration will produce a higher fraction of molecular ions, which leads to a higher fractional energy and thus higher power. This can be seen in figure 1.4, where it is seen that the new EP2 system will produce more of the fractional energy components which leads to a higher total power being injected into the plasma. This is a critical issue for the development of beam emission diagnostic analysis. In addition, it will produce a uniform ion source plasma leading to a lower beam divergence. Lastly, the high voltage power supplies serving the eight PINIs will be replaced with four new 130 kV / 130 A High Voltage Power Supply modules.

During the summer months of 2009, two of these EP2 PINIs were installed in positions 1 and 3 of Octant 8 NIB. They managed to produce a record injected power for a single JET PINI of 2.08 MW. The EP2 PINIs will also be tried

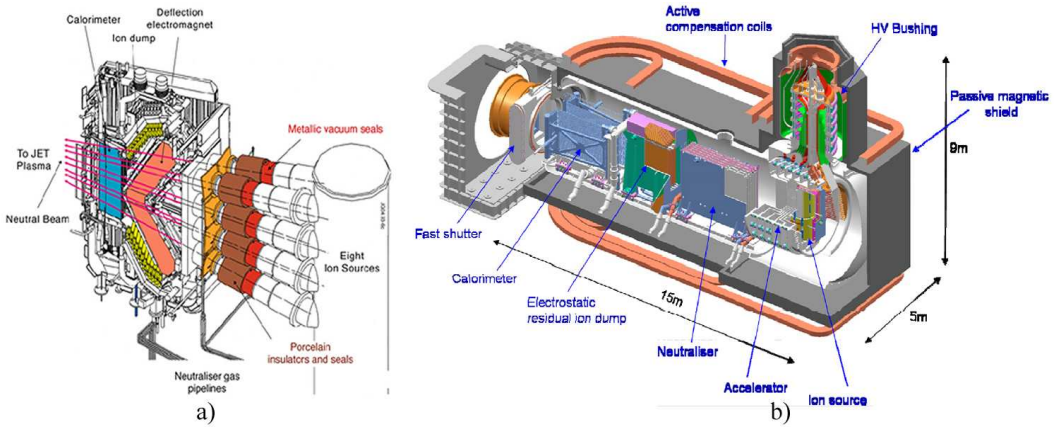

Figure 1.3: a) An illustration of a JET Neutral Injection Box and b) a schematic of ITER neutral beam.

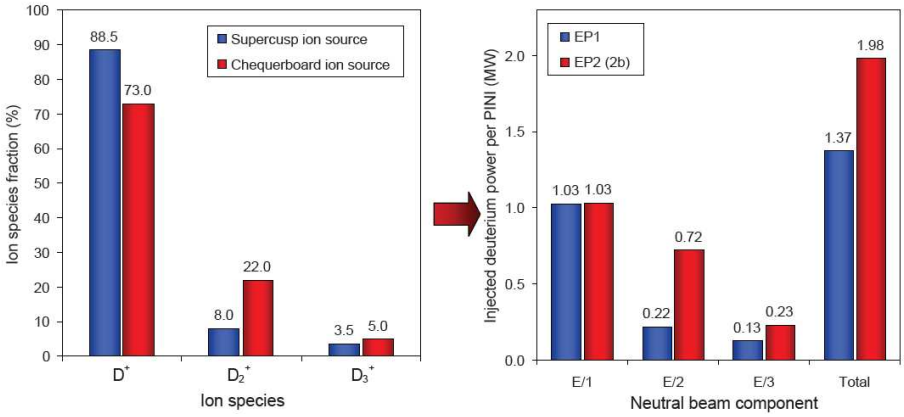

Figure 1.4: Two graphs showing the effect of changing the ion source on the positive ion neutral injectors used at JET from the supercusp to the chequerboard system. Image Credit: Ciric [4].

with tritium and helium atoms. The inclusion of these new NB configurations along with the new ITER-Like Wall [7] will contribute significantly to the success of the future JET campaigns in support of ITER.

1.1.2 ITER Negative Ion Neutral Injection

ITER will require neutral beams with a greater energy and thus penetration (ITER $R \approx 6$ m) due to its larger radius and higher density. Therefore, the NBI System in ITER will use a negative ion source as illustrated in figure 1.3b). It can be seen from figure 1.5 that the energies of the beam must be of the order 1 MeV for efficient heating of the ITER plasma. Due to the large diagnostic capabilities of the neutral beams, ITER will have two types of beam in operation: one beam will be solely for heating and will inject neutral deuterium, these beam energies must be greater than 1000 keV; the other beam will be purely for diagnostic use and will inject neutral hydrogen, for it the energies being used will be of the order 100 keV. Therefore, as ITER will be relying heavily on the accuracy and reliability of beam spectroscopy to monitor key plasma parameters, it is important that attention is turned to diagnosis of the beam emission.

1.2 Beam Emission and Spectroscopy

When the beam enters the plasma, the neutral atoms have collisions with the ions and electrons in the plasma and interact with magnetic and electric fields present in the plasma. These interactions with the field and plasma species

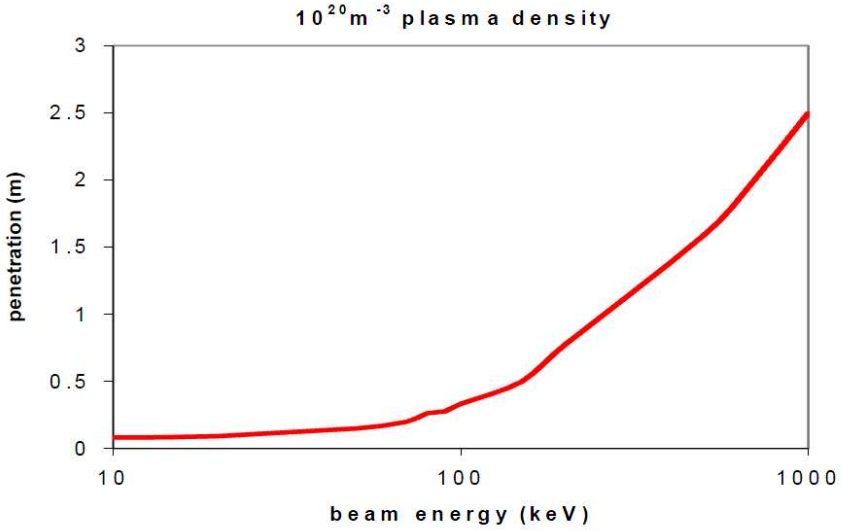

Figure 1.5: A graph showing the penetration distance of a neutral beam for various energies. Image Credit: Mc Adams (2010) [5].

cause the neutral atoms to become excited and ionised. As the excited beam atoms relax back down to their ground state, they emit radiation. This composite of processes leads to three principal effects — CXR spectroscopy, Beam eMission Spectroscopy (BMS) and Beam Stopping (BS). CXR is how the beam causes the plasma ions to radiate, BMS is the emission of the beam atoms themselves and BS is the effective loss rate of atoms from the beam caused by ionisation or charge exchange with plasma ions.

As the beam leaves the NBI and enters the plasma, it firstly passes through the narrow Scrape Off Layer (SOL). This layer is formed through the small amount of residual plasma separating the edge of the plasma (often referred to as the separatrix) and the tokamak vessel. It is a low density region at relatively low temperatures. As this layer is very narrow, the beam atoms pass straight through with little effect on the population structure of the neutral atoms. Emission from the beam in this region is negligible compared with emission of thermal neutral deuterium always present in the outer regions of the plasma near the vessel wall (Mc Neil, 1989 [8]). As the beam enters the confined core plasma, the density of the electrons increases by a factor of three or four and temperature of the electron and plasma ions rise dramatically to large values ($\simeq$ 3000 keV in the JET tokamak). Now, there is almost no thermal deuterium as it has been ionised and recycled by the plasma. The principal emission driven by the beam is firstly that from full ionised plasma impurity ions following charge exchange reactions between the fully ionised plasma species (both hydrogen nuclei and impurities) and the neutral beam atoms.

Understanding this spectrum is of great diagnostic benefit and is projected to be used as a direct measure of fusion 'ash' in the new generation tokamak, ITER. Von Hellermann *et al.* [9] provide accurate data which can be used to model this CX emission. Secondly there is the emission from the beam atoms themselves. Particularly the Balmer series emission in the visible spectral region is evident and characteristically displaced from the natural wavelengths due to Doppler effect (of the fast moving beam atoms with respect to the spectrometer line-of-sight). Generally, the D_α lines are compared with computer simulated spectra which relies on key parameters within the plasma. The CX and BM spectra can be used to find the ion temperature (Kallne *et al.* [10], plasma rotation, impurity concentrations (Boileau *et al.* [11]), internal magnetic and electric fields (Mandl *et al.* [12]) and if the polarisation of the emission is studied one may also determine the magnetic field pitch angle and therefore produce a current density profile [13]. The graph shown in figure 1.6 shows a visible spectrum in the vicinity of H_α. It shows the very broad CXR emission approximately centered on the natural wavelength. This is broad due to the Doppler Effect because of the fact the plasma species are at very high temperatures. The three complex Doppler shifted components are the beam emission and are due to the three fractional energy components of the neutral beam (from the positive ion source). The narrow lines at the natural position are emission of thermal (not beam) hydrogen and deuterium at the edge of the plasma in the vicinity of the scrape-off-layer. They are sharper as they are at lower temperatures than the core plasma species. All these emission are determined theoretically by modelling the collisional, radiative and recombination processes

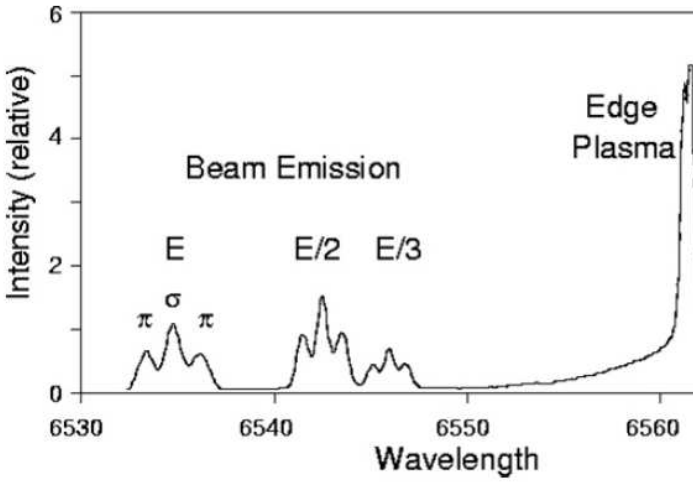

Figure 1.6: A graph showing the visible spectrum, near the D_α line, observed during a neutral beam pulse into a magnetically confined plasma. The three Doppler shifted components are the beam emission due to the three fractional energy components of the neutral beam. The thermal hydrogen and deuterium at the edge of the plasma cause the two spiked features at longer wavelengths. The broad feature in the vicinity of these narrow spikes is due to the CXR emission of the plasma species. Image credit: Von Hellermann *et al.* [9]

between the neutral beam atoms and the plasma ions and electrons.

The distance at which the neutral beam atoms become fully ionised is determined by a value known as the 'stopping coefficient'. The beam attenuation length is of great importance. If the beam travels too far it may cause significant damage to the opposite plasma wall and if it does not travel far enough into the core, the heating will be very inefficient. The fourth year report of Henderson [1], discussed in detail the various atomic processes used in calculating this stopping coefficient. In particular, it paid close attention to the population structure of each principal and orbital angular moment quantum shell of the beam atoms in a statistical sense from the balance of atomic processes.

The aim of this report, is to further the studies and discussions of the previous report into the field of BMS combined with a more careful approach to the effects of the magnetic and induced Lorentz field on the emission spectrum. When the beam atoms are travelling through the plasma at a speed, v, they are subject to a large Lorentz electric field perpendicular to the direction of propagation and the magnetic field, this disturbs the atomic level structure of the beam hydrogen atoms causing splitting up of the H_α emission into Stark components as seen in figure 1.6 and modifies the population structure as discussed below.

1.3 Motional Stark Effect

As described earlier, the hydrogen beam atom in a fusion plasma experiences a magnetic field $\vec{B}$ of intensity $\sim 3\,\mathrm{T}$ and because of its velocity $\vec{v}$ across the magnetic field a large Lorentz electric field $\vec{v}\times\vec{B}$ of $\sim 100\,\mathrm{kV/cm}$. In this typical set up, the magnetic field is negligible compared to the Lorentz electric field. Therefore, the neutral beam atoms are perturbed according to the first order disturbance (linear in electric field) of the energy eigenstates, this is known as the Motional Stark Effect. If the speed of the neutral beam atoms was reduced to zero, then there would only be the magnetic field acting on the atoms, this would again cause a first order disturbance (linear in magnetic field) on the energy eigenstates which is known as the Paschen-Back Effect. With a non-hydrogenic atom, the Stark effect would normally be quadratic and the magnetic field disturbance still linear but much weaker, called the Zeeman effect. These differences occur because of the energy level separations of the isolated, field-free, atoms, isolated hydrogen atom levels have an accidental degeneracy of the l-shells of the same n-shell which is not present in non-hydrogenic atoms and ions.

In a detailed study of the following sections, it will become evident that the effects of the electric and magnetic field disturbances must be examined for different magnitudes of field. This will include ranges where the field disturbances can be treated purely as perturbation on the isolated atom states and where the field disturbances are the dominant process in the determination of energy eigenstates. The induced Lorentz field is always perpendicular to the magnetic field. For a pure magnetic field disturbance the angular momentum about the field direction is a constant of motion with the m quantum number assigned. For the pure Lorentz field case, the angular momentum about the field direction is again a constant of the motion with the m quantum number assigned, but this is perpendicular to the magnetic field. Therefore, when the electric and magnetic fields are comparable, there is not an angular momentum component which is a constant of the motion and so there is no well defined m quantum number. When solving for the pure electric field case, the Schrödinger equation can be solved in parabolic coordinates with a new constant of motion (the Runge-Lenz vector) which leads to a new quantum number, defined as k. However, now the usual orbital quantum number l arising from the squared angular momentum operator is no longer a constant of motion. Therefore, there is a lot of confusion as to what labelling convention to use on the atomic states as the fields are explored. Usual quantum numbers are no longer exact and their breakdown must be examined carefully. The computer codes, used in the following sections give correct solutions, but the interpretation in terms of usual quantum numbers, polarisation etc. is not immediate or necessarily possible.

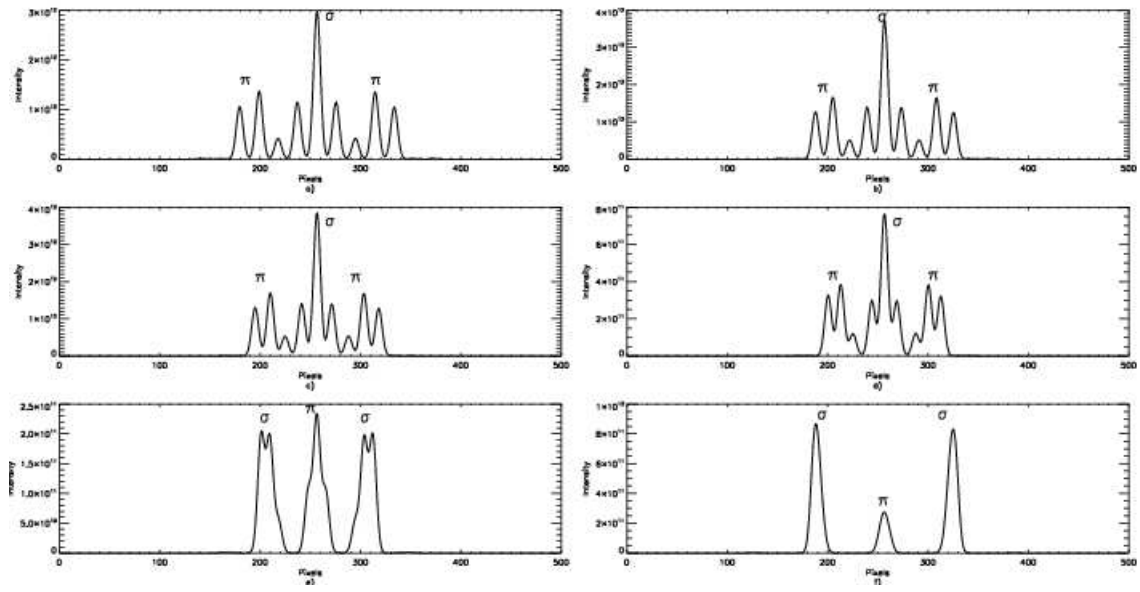

Figure 1.7: A magnetic field of 1.4 T and beam energy of 0.24 MeV/amu is present in a) then as we move through to f) the effects of changing the beam energy down to 100 eV/amu and increasing the magnetic field to 40 T in six steps are shown. The π and σ indicate the two types of polarisation. Although these magnetic and electric fields are not so relevant to a fusion reactor, they have been chosen to exaggerate the evolution of moving from one field to another. Graphs were obtained from the ADAS routine, ADAS305.

These effects of exploring the different field perturbations are illustrated in figure 1.7. The evolution of the H_α multiplet can be seen as the beam speed is decreased. One can immediately see the characteristic fifteen (although only nine of which are visible) allowed transitions associated with the Stark effect initially begin to transform into the characteristic three main transition lines of the Paschen-Back effect. However, an important feature of this evolution is the polarisation, indicated by π and σ. It is clear that as you move from one regime to another, the two polarisations interchange. Although this may not produce any problems in a computer calculation, it can cause confusion when comparing experimental data to the simulated emission spectra.

When dealing with the field values at JET, there is a further independent non-orthogonal electric field which must also be considered. First order perturbation theory in the non-relativistic isolated atom Hamiltonian may be used to calculate both the Stark term (with the external field) and the Zeeman or Paschen-Back term.

1.4 Diagnostics

Spectroscopy on JET is key to interpreting what is happening inside the plasma. To do this, extensive studies must be made into energy levels, oscillator strengths and electron-ion, ion-ion and ion-atom cross sections. The two spectral scenarios that occur along the beam path can be used for diagnostic purposes, CXRS allows the light impurities in the plasma to be studied where they would generally be fully ionised. The width and displacement of the charge exchange induced spectral lines give the ion temperature and plasma rotation (Boileau *et al.* , [11]). However, to accurately interpret these spectral lines, one must exclude the 'cold effects' of the plasma (that is emission from the cold edge of the plasma not driven by the beams) and the bremsstrahlung background radiation. The cold effects are illustrated by the narrow features of small thermal Doppler temperature, such as of HeII, BeII, HI and DI in the absence of beams and superimposed on the spectral intervals used to analyst the charge exchange emission. In addition, the shape of the spectral line is governed by the variation of CX cross section with energy.

At the beam emission stage, the H_α features become dominant. Again the cold components within the plasma must be considered when dealing with beam emission. The Stark components of the beam emission are resolved into their π and σ polarisations. As the beam atoms are travelling at such high speeds, the dominant excitation reaction is through positive ion impact. The diagnostic potential of the beam emission is huge and Mandl *et al.* (1993) [12] provide a detailed review of each procedure. To summarise, the combined Doppler shifts of the emission can provide detail as to the radial and vertical position of the observation. If the observation volume is directly perpendicular to the observation viewing point, then there should be no Doppler shift present. If the volume is before this point along the observation line, then there will be a blue shift and likewise if it is after then there will be a red shift. This is advantageous to know because it gives a good indication as to what part of the plasma is being diagnosed. The strength of the Lorentz field acting on the beam can be calculated by working out the spacing between each of the Stark components — the stronger the field, the larger the distance between each of the components. As the Lorentz field is always perpendicular to the magnetic field, if the direction of the magnetic field changes this will also induce a change to the direction of the Lorentz field. This is measured by studying the polarisation patterns of the emission light. Being able to deduce the direction of the magnetic field is essential as this allows measurement of the pitch angle. In addition, Z_{eff} may be derived from the ratio of the Stark to CX feature. However this interpretation requires accurate fundamental cross section knowledge [14].

The main focus of modern fusion plasma diagnosis has focused on polarisation measurements of particular components of the H_α Stark multiplet for magnetic field characteristics. It is rather difficult to initiate this approach on ITER and so fresh attention has been directed at full population and emission modelling of the sort carried out in the ADAS subroutine, ADAS305. Experimental teams in Madison, Wisconsin and at General Atomics, San Diego are collaborating with EFDA-JET on exploring the use of ADAS305 predictive capabilities in their spectral analysis. Therefore, as these codes are in active use, it is important to explore the accuracy to which these generated emission lines match that of the experimental emission lines. For example, in experiment, it is evident that there is a persistent observation of a slight asymmetry between the blue and red shifted Stark components of the H_α Stark multiplet [15]. The ADAS305 does not give any indication of this asymmetry. It is possible that this asymmetry can arise from geometrical observation effects and line-of-sight superpositions for the multiple beams being fired into the tokamak at JET. However, there are also possible theoretical reasons lying above perturbation theory.

The aim of this report is to examine refinement of the theoretical picture at the heart of ADAS305, with a view to its upgrading. Therefore, the two new features of this report are field ionisation and asymmetric cross sections, field

ionisation has the potential to cause an asymmetry within the population structure at high principal n-shells and has not been included at this stage in ADAS305. This effect could then be passed on down to the lower shells which could cause a distortion to the visible beam emission lines. In addition, the asymmetric Stark-state electron probability distribution around the atom affects the model. The current method of dealing with cross sections is by use of the impact parameter approach, this approach focuses on an isolated, isotropic atom case, however, the beam is no longer isotropic when it enters the plasma, the colliding plasma ion is now approaching the target distorted hydrogen atom from a cone of directions, so one can no assume the simple isotropic case. The next chapter will detail the atomic physics of the motional Stark effect which will provide the foundation for the rest of the report. In chapter 3, the methods used to find the field ionisation rates will be reviewed, the chapter will then focus on implementing one of the methods discussed. H ow the field ionisation effects the population structure will then be the topic of chapter 5. In the chapter 4 it will be detailed the method of the complex coordinate integration to solve the Stark effect in neutral hydrogen atom beyond perturbation theory, and get exact results for the position of the resonances, the widths and the wave functions. From that point, the focus will turn to these so called asymmetric cross sections, chapter 6 will first review the methods of solving the cross sections for the isolated atom case, and then it will turn to focus on the asymmetric atom case. A summary of these findings will then be put forward in chapter 7.

Chapter 2

Field Perturbation

The basic components of a tokamak magnetic confinement system are the toroidal and poloidal field coils. The toroidal field coils surround the tokamak vessel, forcing the charged plasma species to orbit around the torus. There are two poloidal field coils which produce a field around the plasma cross section. This set up can be seen from figure 2.1. The

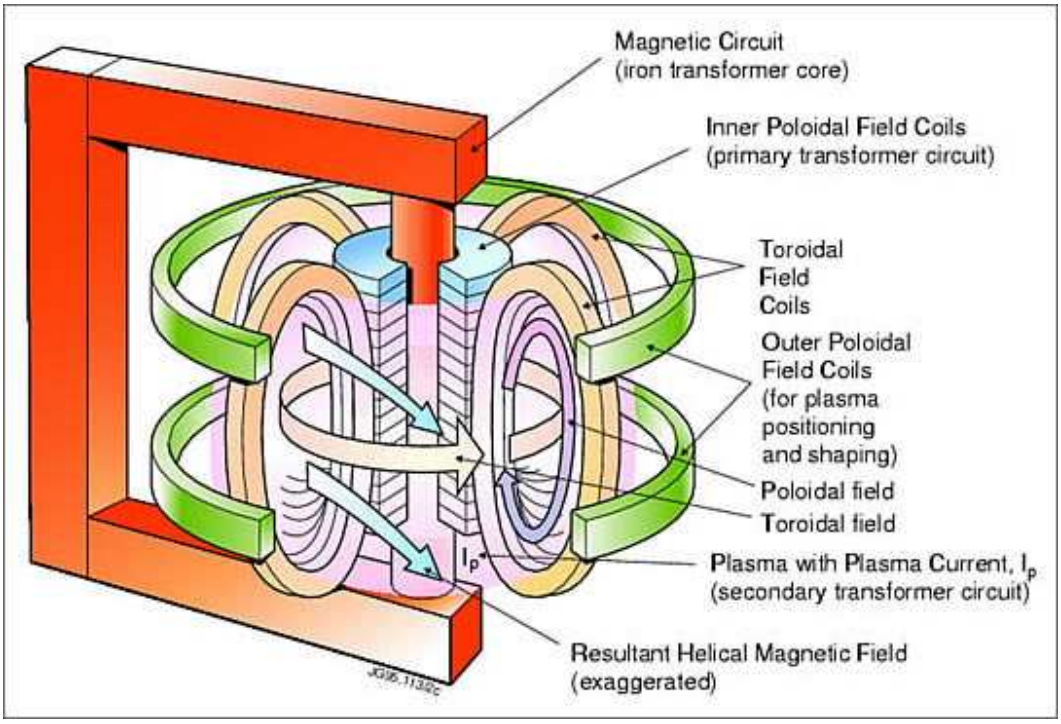

Figure 2.1: The principle magnetic circuits of JET's tokamak.

toroidal fields at JET are typically of the order $B \sim 3\,\mathrm{T}$. When the neutral beam crosses this field, there is a generated Lorentz field,

$$\vec{F}_{\mathrm{Lor}} = \vec{v} \times \vec{B}, \tag{2.1}$$

where $\vec{v}$ is the speed of the atom, this field is generally of the order $\sim 10^5\,\mathrm{V/cm}$. To this field, one has to add the electric one present in the tokamak $\vec{F}$, for example, this which produces the toroidal current. The various field values can be seen in figure 2.2 for two different magnetic field values.

The non-relativistic, field-free Hamiltonian for the hydrogen atom is

$$H_0 = \frac{p^2}{2\mu_e} - \frac{e^2}{4\pi\epsilon_0 r}, \tag{2.2}$$

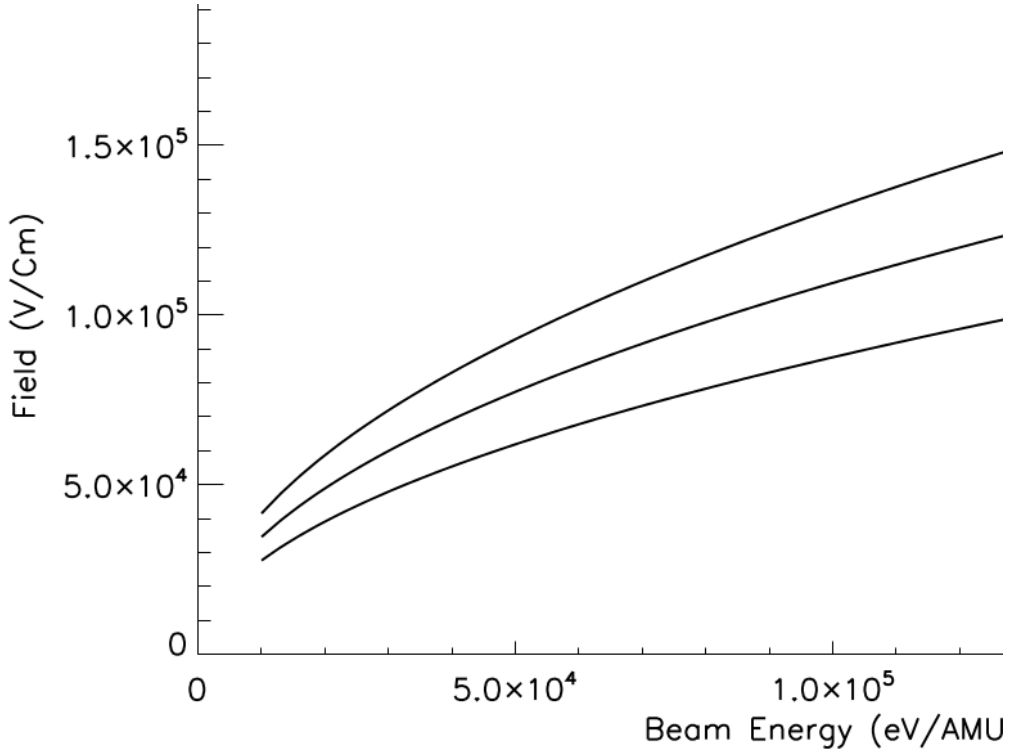

Figure 2.2: A graph showing the field values typically generated at JET. The x-axis shows the energy of the neutral beam and the three different lines correspond to three different magnetic fields, 2 T, 2.5 T and 3 T. The field values are given in the commonly used units of V/cm.

where $\vec{p}$ is the momentum operator, e the electron charge, r the relative radial coordinate with origin in the nucleus and $\mu_{\rm e}$ is the reduced mass of the electron given by,

$$\mu_{\rm e} = \frac{m_{\rm e} m_p}{m_{\rm e} + m_p}\,, \tag{2.3}$$

m_p may represent a proton or deuteron and $m_{\rm e}$ is the electron mass.

The eigenstates of this Hamiltonian are commonly expressed as $|nlm_l m_s\rangle$ where n is the principal quantum number associated with the energy eigenvalue. l the orbital angular momentum quantum number and m_l the orbital magnetic quantum number are associated with the commuting observables L^2 and L_z of the angular momentum operator $\vec{L}$, m_s the spin magnetic quantum number (the spin angular momentum quantum number s takes only the value $1/2$ in hydrogen atom) is associated with the observable S_z of the spin angular momentum $\vec{S}$. H, L^2 and L_z, S^2 and S_z, form a complete set of commuting observables (CSCO) which naturally arise in the spherical polar coordinate picture. They have wave functions $\psi_{nlm_l m_s}(r,\theta,\phi,\sigma)$ and energy eigenvalues

$$E_{nlm_l m_s} = \frac{I_H}{n^2}\,, \tag{2.4}$$

where I_H the Rydberg energy unit for hydrogen. With no external fields and neglecting the fine structure, the energy depends only in the n main quantum number.

The analytic expression of the orbital part of the normalised wave functions for the bounded states is

$$\psi_{nlm_l}(r,\theta,\phi) = \sqrt{\left(\frac{2}{n}\right)^3 \frac{(n-l-1)!}{2n\,(n+l)!}}\, {\rm e}^{-\frac{r}{n}} \left(\frac{2r}{n}\right)^l {\rm L}^{2l+1}_{n-l-1}\left(\frac{2r}{n}\right) {\rm Y}_{lm}(\theta,\phi) \tag{2.5}$$

where ${\rm L}^{2l+1}_{n-l-1}$ is the Laguerre associated polynomial of grad $n-l-1$ and ${\rm Y}_{lm}$ is the spherical harmonic (see [16]).

A basis of states $|nlm_l s m_s\rangle$ is used by ADAS305 for easy evaluation of the magnetic and electric perturbations. The Breit-Pauli relativistic corrections given by Bethe and Salpeter [17], which include the one-body relativistic operators

(mass variation, spin-orbit and Darwin terms) and the two-body relativistic terms (spin-other-orbit, spin-spin, spin-orbit, Darwin, contact spin-spin and orbit-orbit), are evaluated by ADAS305. These relativistic corrections to the above for hydrogen are quite small, however current BMS observations can distinguish. As the Breit-Pauli terms include the spin-orbit interaction, this means that m_l and m_s are no longer good quantum numbers. Now, $\vec{j} = \vec{l} + \vec{s}$ commutes with the Hamiltonian. Therefore j and m_j, the quantum numbers associated with J^2 and J_z replace m_l and m_s and the relevant basis states are $|nls\,jm\rangle$. The spin-orbit interaction splits terms of different j into separate levels. For ADAS305, it is convenient to evaluate the Breit-Pauli terms in the $|nl\,jm\rangle$ representation and transform back to the $|nlm_lm_s\rangle$ representation matrices before including the field perturbations. This step was implemented in ADAS305 by Summers and Ghanghara (private communication).

Inclusion of external fields is correctly done within the Dirac Hamiltonian for hydrogen with the substitution $\vec{p} \rightarrow \vec{p} + \frac{e\vec{A}}{c}$, where $\vec{A} \equiv (\vec{A}, i\phi)$ is the field potential four-vector and $\vec{p}$ the momentum four-vector. As shown by Bethe and Salpeter [17], the diamagnetic part involving A^2 is negligible except for very strong fields, so only the part which is linear in the field potential matter here. This can be resolved into separate magnetic and electric perturbations expressible in terms of the magnetic and electric dipole moments of the hydrogen atom, which is the approach used in ADAS305.

The perturbed Hamiltonian is $H = H_0 + H_{md} + H_{ed}$. The magnetic part is

$$H_{md} = -\vec{\mu} \cdot \vec{B} \tag{2.6}$$

where

$$\vec{\mu} = -\frac{\mu_B}{\hbar}(\vec{L} + g_e\vec{S}) \tag{2.7}$$

μ_B is the Bohr magneton and g_e the gyromagnetic constant of the electron, which values

$$g_e = 2 + \frac{\alpha}{\pi} + \ldots = 2.0023\,, \tag{2.8}$$

α is the fine structure constant

$$\alpha = \frac{e}{4\pi\epsilon_0\hbar c} \approx \frac{1}{137}\,. \tag{2.9}$$

This takes account of the spin contribution to the magnetic moment, including its anomalous moment which comes from relativistic theory. The electric part is

$$H_{ed} = -\vec{d} \cdot \vec{F} \tag{2.10}$$

where F is the total electric field, counting the pure electric and the Lorentz ones, and

$$\vec{d} = -e\vec{r}. \tag{2.11}$$

There is a similar electric dipole contribution to the perturbed Hamiltonian if there is any additional shear electric field in the plasma.

2.1 Paschen-Back effect

For hydrogen in tokamaks, with magnetic fields $B \sim 3\,\mathrm{T}$, the magnetic dipole perturbation greatly exceeds the spin-orbit separation of fine structure levels, so the Rydberg states $|nlm_lm_s\rangle$ should be used as appropriate basis set, neglecting the spin-orbit contribution. With the z-axis of quantisation along the magnetic field direction, the H_{md} matrix is diagonal in this basis and the Paschen-Back energy levels are obtained immediately as

$$E^{(1)}_{nlm_lm_s} = \frac{\mu_B}{\hbar} B\,(m_l + g_e m_s) \tag{2.12}$$

As the basis set functions are eigenfunctions of the z projection of the orbital and spin angular momenta, the Paschen-Back operator does not couple different functions of the basis set, so the wave function at first order perturbation theory is zero, only the energies are perturbed at first order.

If the atom is under an intense electric field and a magnetic one simultaneously we lose the spherical symmetry, so we can not choose the magnetic field pointing in the z direction without losing generality, as in the case of only

magnetic field. In this case it is convenient to choose the z direction as the electric field vector, and the magnetic field vector is contained in the zx plane, so it is decomposed in a parallel and perpendicular component to the electric field $\vec{F}$:

$$\begin{aligned} \vec{F} &= F\,\hat{z} \\ \vec{B} &= B_{\parallel}\,\hat{z} + B_{\perp}\,\hat{x}\,. \end{aligned} \tag{2.13}$$

Then the equation 2.7 must be written as:

$$H_{PB} = \frac{\mu_B}{\hbar}\left[B_{\parallel}\,(L_z + g_e S_z) + B_{\perp}\,(L_x + g_e S_x)\right]. \tag{2.14}$$

The parallel term is 2.12, and to calculate the perpendicular one, we write the angular momentum L_x as a combination of the raising and lowering operators [18]

$$\begin{aligned} j_+ &= j_x + i j_y \\ j_- &= j_x - i j_y\,, \end{aligned} \tag{2.15}$$

which fulfil

$$\begin{aligned} j_z\,|\,j\,m\rangle &= \hbar\,j\,|\,j\,m\rangle \\ j_+\,|\,j\,m\rangle &= \hbar\,\sqrt{j(j+1) - m(m+1)}\,|\,j\,m+1\rangle \\ j_-\,|\,j\,m\rangle &= \hbar\,\sqrt{j(j+1) - m(m-1)}\,|\,j\,m-1\rangle\,, \end{aligned} \tag{2.16}$$

which leads to the matrix elements of the Hamiltonian:

$$\begin{aligned} \frac{\mu_B}{\hbar}\,B_{\perp}\left\langle n\,l\,m_l\,s\,m_s\,|\,L_x + g_e S_x\,|\,n'\,l'\,m'_l\,s\,m'_s\right\rangle = \frac{\mu_B}{2\hbar}\,B_{\perp}\Big[& \sqrt{l'(l'+1) - m'_l(m'_l+1)}\,\delta_{nn'}\,\delta_{ll'}\,\delta_{m_l m'_l+1}\,\delta_{m_s m'_s} \\ & + \sqrt{l'(l'+1) - m'_l(m'_l-1)}\,\delta_{nn'}\,\delta_{ll'}\,\delta_{m_l m'_l-1}\,\delta_{m_s m'_s} \\ & + g_e\,\sqrt{3/4 - m'_s(m'_s+1)}\,\delta_{nn'}\,\delta_{ll'}\,\delta_{m_l m'_l}\,\delta_{m_s m'_s+1} \\ & + g_e\,\sqrt{3/4 - m'_s(m'_s-1)}\,\delta_{nn'}\,\delta_{ll'}\,\delta_{m_l m'_l}\,\delta_{m_s m'_s-1}\Big]\,. \end{aligned} \tag{2.17}$$

For a magnetic field which does not point in the z direction, there are couplings between the states of different m_l and m_s.

ADAS305 correctly obtains these values if the Lorentz field is switched-off apart from a weak disturbance and splitting (since it includes the Breit-Pauli relativistic corrections).

The transition lines for the Paschen-Back effect, from the hydrogen $3d\,^2D \rightarrow 2p\,^2P$ shell, can be seen in figure 2.3. There are nine transitions in this case, split into three degenerate energy levels, $\Delta M = 0, \pm 1$. These three characteristic emission lines are shown in figure 2.4.

2.2 Fine structure

If the external fields are weak or null, the fine structure is the dominant perturbation. In general, the order of this perturbation is

$$\frac{E^{(1)}}{E^{(0)}} = \alpha^2 \sim 10^{-4} \tag{2.18}$$

where α is the fine structure constant 2.9.

The fine structure Hamiltonian comes from the series expansion of the Dirac equation and it has three terms: relativistic, spin-orbit coupling and Darwin, which can be written as [19]:

$$H_{fe} = -\frac{p^4}{8\mu^3 c^2} + \frac{1}{2}\,\frac{Ze^2}{4\pi\epsilon_0}\,\frac{1}{r^3}\,\vec{L}\cdot\vec{S} + \frac{\hbar^2}{8\mu^2 c^2}\,\frac{Ze^2}{4\pi\epsilon_0}\,4\pi\delta^{(3)}(\vec{r})\,. \tag{2.19}$$

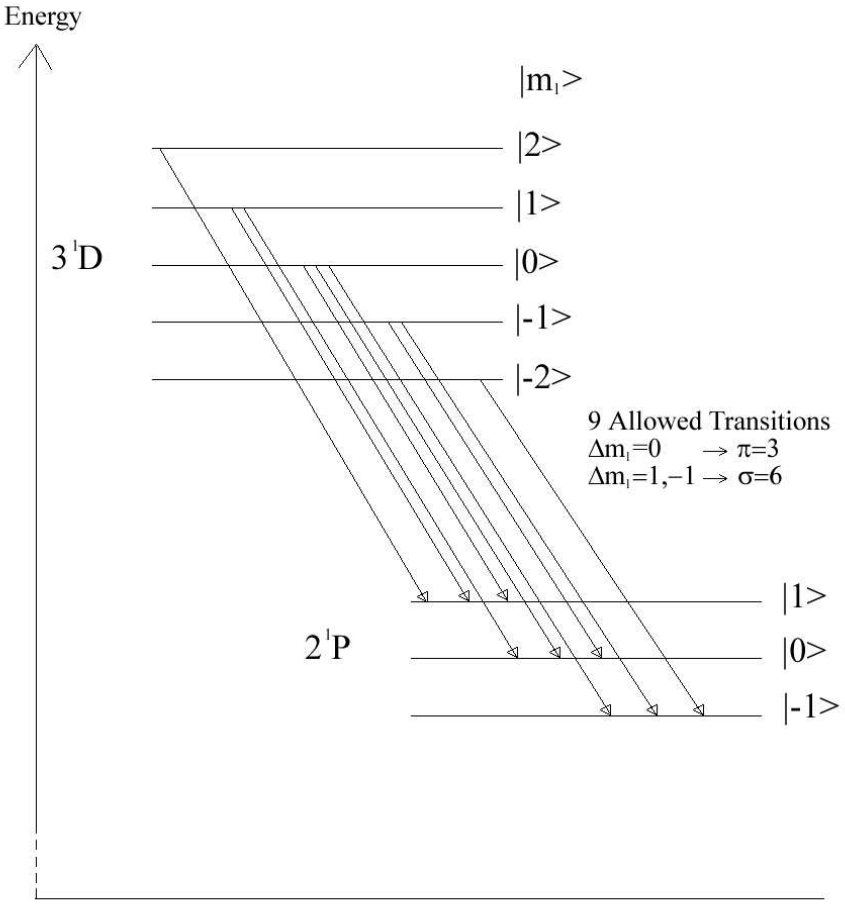

Figure 2.3: A diagram showing the allowed transitions from the hydrogen levels, $3d\,^2D \rightarrow 2p\,^2P$. The diagram labels the levels in terms of their m_l quantum number. Allowed transitions are transitions where $\Delta m_l = \pm 1, 0$. There are three $\Delta m_l = 0$, or π transitions and six $\Delta m_l = \pm 1$, or σ transitions.

The fine structure Hamiltonian is diagonal in the basis set $|nljm_j\rangle$, one have to introduce the total angular momentum quantum number j, resulting of coupling the orbital and spin angular momenta $\vec{J} = \vec{L} + \vec{S}$. Then the coupled states $|nljm_j\rangle$ can be written in terms of the uncoupled ones $|nlm_lm_s\rangle$ through the Clebsch-Gordan coefficients:

$$|\,n\,l\,j\,m_j\rangle \;=\; \sum_{m_l m_s} \langle l\,m_l\,1/2\,m_s\,|\,j\,m_j\rangle\,|\,n\,l\,m_l\,m_s\rangle \tag{2.20}$$

where $\langle j_1 m_1 j_2 m_2 | JM\rangle$ are the Clebsch-Gordan coefficients, whose expression, values and properties can be found in any basic quantum mechanics book. The energies are obtained as [19]

$$E^{(1)}_{nljm_j} \;=\; (Z\alpha)^4\,\frac{\mu c^2}{2n^3}\left(\frac{1}{j\,+\,1/2}\;-\;\frac{3}{4n}\right). \tag{2.21}$$

In basis set $|nlm_lm_s\rangle$ the fine structure Hamiltonian becomes non-diagonal, and its matrix elements value, applying 2.20

$$\langle n\,l\,m_l\,m_s\,|\,H_{fe}\,|\,n'\,l'\,m'_l\,m'_s\rangle \;=\; (Z\alpha)^4\,\frac{\mu c^2}{2n^3}\sum_{jm_j}\langle l\,m_l\,1/2\,m_s\,|\,j\,m_j\rangle^*\,\langle l'\,m'_l\,1/2\,m'_s\,|\,j\,m_j\rangle\left(\frac{1}{j\,+\,1/2}\;-\;\frac{3}{4n}\right)\delta_{nn'}\,. \tag{2.22}$$

2.22 shows that the perturbation Hamiltonian becomes block-diagonal in the main quantum number n, which determines the zero-order energy, which is degenerate in l, m_l and m_s, and at perturbation theory the zero-order degenerate

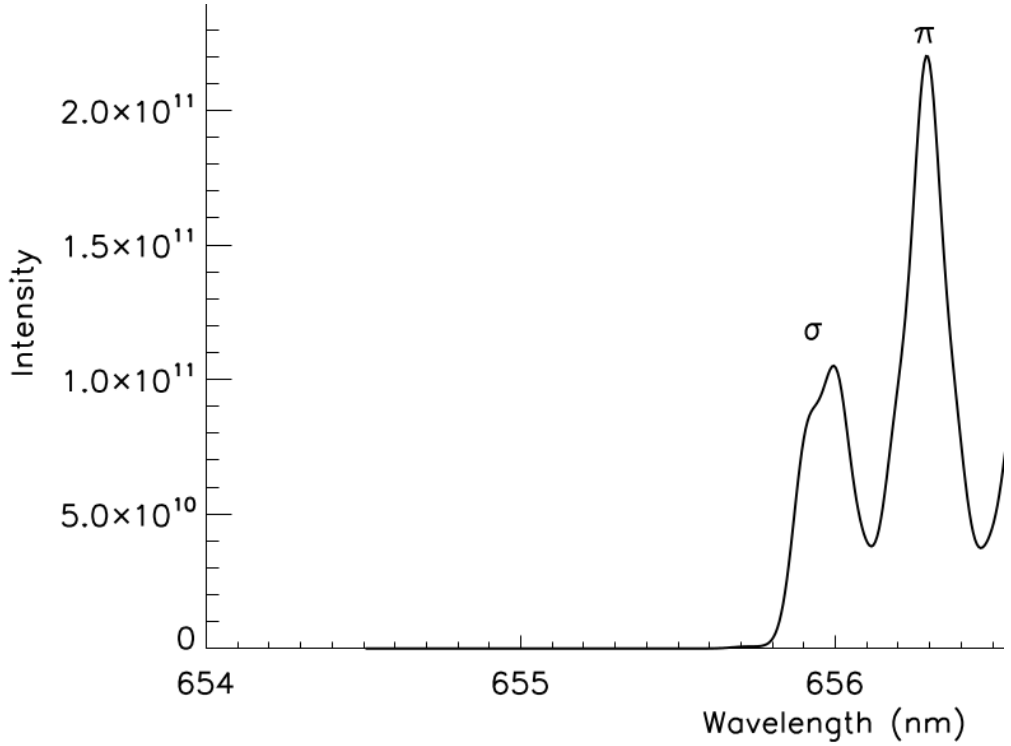

Figure 2.4: The pseudo-Paschen-Back lines are simulated in ADAS305 by turning the energy of the beam down to 5 keV/amu and setting the toroidal field, $B = 3.5\,\mathrm{T}$. This emission still therefore contains a small perturbation from the Lorentz electric field.

states are not coupled at first order, only at second and following ones, so in this case the first-order perturbation wave function is also zero, the first-order eigenfunctions are obtained just by the unitary transformation 2.20.

2.3 Zeeman effect

For completeness, the case when the magnetic dipole perturbation is much less than the spin-orbit, separation of fine structure levels is also considered, although this is not relevant to hydrogen in tokamak plasma. The modified basis states $|nljm_j\rangle$ are appropriate and the expectation of H_{md} is evaluated for these states to give

$$E^{(1)}_{nljm_j} \;=\; \frac{I_H}{n^2} \;+\; E^{(fe)}_{nj} \;+\; \mu_B g_j B m_j \tag{2.23}$$

with $E^{(fe)}_{nlj}$ the fine-structure correction for the energy level and g_j the generalised Zeeman gyromagnetic constant

$$g_j \;=\; 1 + \frac{j(j+1) \;+\; s(s+1) \;-\; l(l+1)}{2j(j+1)}\,. \tag{2.24}$$

Again ADAS305 can reproduce this case.

2.4 Linear Stark Effect

We suppose now that the Lorentz electric field, $\vec{F}_{\mathrm{Lor}}$, is acting in the z-direction, this will produce a force on the hydrogen atom's electron cloud in the opposite way of z-direction. Eigenstates of the field perturbed Hamiltonian will have electron probability distributions distorted along the z-direction, with lower energy states in the antiparallel

direction and higher energy states in the parallel direction. The effect of this perturbation was discovered by Stark [20], and was therefore known as the Stark effect. The Stark effect is considerably more complex than the Zeeman effect and was the first application of the perturbation theory in quantum mechanics. An in-depth overview of the theory can be found in Condon and Shortley [21], Bethe and Salpeter [17] and Gallagher [22]. Anyway later works proved that perturbation theory has several inconsistencies when it is applied to Stark effect, we are going to show in this section the results which it leads. In chapter 4 we shall show the technique of complex coordinate integration, which leads to exact results for the Stark effect problem.

For the $|nlm_lm_s\rangle$ basis of ADAS305, and assuming the axis of quantisation is in the Lorentz electric field direction, then the m_l and m_s (and so also $m = m_l+m_s$) are good quantum numbers, the n and l however are not. For electric fields of the order $\sim$ 100 kV/cm and for states $n \leq 4$, the energy level disturbance is small compared with the separation between n-shells. So ADAS305 evaluates the perturbation H_{ed} between all states of the same n but not between states of different n, this allows l-shell mixing but not n-shell mixing. The H_{ed} is parity breaking and this coupled with the effective degeneracy of the l substates allows the linear Stark effect in hydrogen. Up until the studies of this report, ADAS305 operated as above, with resolved n-shells up to $n = 4$. For the present investigation, ADAS305 has been extended to deal with n-shells up to $\sim$ 12, for such shells, the field disturbance approaches and exceeds the unperturbed separation between n-shells. It might be considered appropriate therefore to evaluate the H_{ed} matrix also between different n-shells. In practice this is not correct since there is another quantum number (k) associated with Stark oriented states whose selection rules allow crossing of levels of different n. So n-shell mixing is not of concern until above another limit - that of field ionisation. This is a new complexity, not included in ADAS305 and requires a different viewpoint. For that reason, treatment of the hydrogen atom in parabolic coordinates is reviewed below.

There is a second point. Diagonalising H_{ed} gives first order Stark field perturbed energy levels, but does not identify these states, other than by index number in the computer code. In principle, the m_l and m_s quantum numbers remains good, but are only identifiable explicitly if initially $|nlm_lm_s\rangle$ states are set up in the field direction. For the mixed electric and magnetic field case, this is not necessarily so and, as already pointed out, m_l and m_s would also breakdown. There are two possible routes, namely to use the transformation matrix diagonalising H_{ed} to transform the L_z and S_z matrices and the matrix of the operator associated with k (the Runge-Lenz vector). This would give the purity of states in any situation. Another route is to follow the locus of a state from a known situation (pure Stark or pure Paschen-back) as the further perturbative fields are switched on. At this stage neither strategy has been implemented in ADAS305, as the main concern is situations close to the Stark limit. However, for the latter case, in section 2.7, a procedure for state identification is presented. Without state identification, the whole physical situation can be examined within the computer code, including radiation emission, polarisation etc. It is only at the connection with experiment that identifications may be helpful. Finally, what experience shows is that the effort of labelling the states, taking in account n-mixing or going to second or third order perturbation theory is not valuable in comparison with using an exact method as complex coordinate integration, so we have changed our strategy for ADAS305 and next improvements will include exact Stark wave functions obtained in terms of complex coordinate integration as is explained in chapter 4.

To summarise, for the present objectives, the Stark effect can be thought of as two separate areas — one area that deals with the atomic energies and intensities of the distorted electrons and another area which deals with the field's ability to remove an electron entirely from the nucleus. The first part is the area of concern in this section and the second part will be dealt with in chapter 3.

As shown by Schrödinger [23] and Epstein [24], explicit solution of the electric field perturbed hydrogen atom is also possible in using parabolic coordinates. These coordinates can be defined through Cartesian and spherical coordinates by

$$\begin{aligned} \xi &= r + z = r(1 + \cos\theta) \\ \eta &= r - z = r(1 - \cos\theta) \\ \phi &= \tan^{-1}\frac{y}{x}, \end{aligned} \tag{2.25}$$

or alternatively

$$\begin{aligned} x &= \sqrt{\xi\eta}\,\cos\phi \\ y &= \sqrt{\xi\eta}\,\sin\phi \\ z &= \frac{\xi-\eta}{2} \\ r &= \frac{\xi+\eta}{2}\,. \end{aligned} \tag{2.26}$$

The coordinate surfaces are paraboloids of revolutions for ξ and η and meridian planes for ϕ. This is shown through a 3D graphical picture in figure 2.5. It is seen that those with $\xi = A$ extend to $z = -\infty$ and those with $\eta = A$ extend to $z = \infty$ where A is a positive constant.

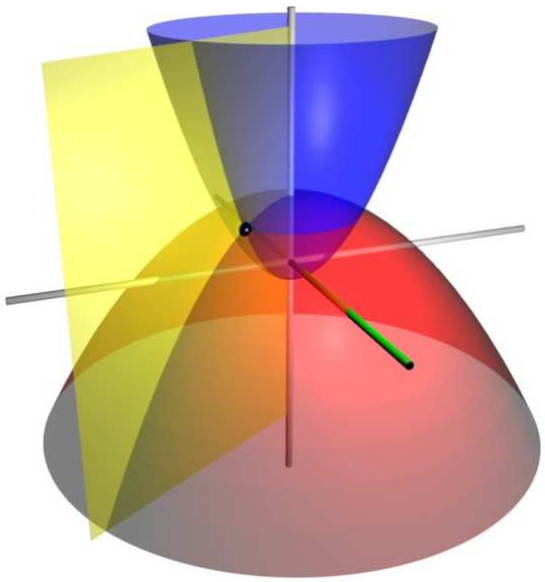

Figure 2.5: Coordinate surfaces of the 3D parabolic coordinates. The red paraboloid corresponds to $\xi = 2$ and the blue paraboloid corresponds to $\eta = 1$ and the yellow half plane corresponds to $\phi = 60^0$. The three surfaces intersect at point P, shown as a small black sphere.

Using these coordinates, the Schrödinger equation for an electron orbiting a singly charged ion with an external field F pointing in the z-direction, is given by

$$\left[-\frac{\nabla^2}{2} - \frac{2}{\xi+\eta} + F\,\frac{\xi-\eta}{2}\right]\psi = E\,\psi\,, \tag{2.27}$$

where

$$\nabla^2 = \frac{4}{\xi+\eta}\,\frac{\partial}{\partial\xi}\left(\xi\,\frac{\partial}{\partial\xi}\right) + \frac{4}{\xi+\eta}\,\frac{\partial}{\partial\eta}\left(\eta\,\frac{\partial}{\partial\eta}\right) + \frac{1}{\xi\eta}\,\frac{\partial^2}{\partial\phi^2}, \tag{2.28}$$

and E is the energy. Now, the wave function can be separated in terms of the two parabolic variables, ξ and η:

$$\psi = \frac{1}{\sqrt{2\pi}}\,u(\xi)\,v(\eta)\,\mathrm{e}^{im\phi}\,, \tag{2.29}$$

which allow equations for the separated functions u and v to be written as

$$\begin{aligned} \frac{\mathrm{d}}{\mathrm{d}\xi}\left(\xi\,\frac{\mathrm{d}u}{\mathrm{d}\xi}\right) + \left(E\,\frac{\xi}{2} + Z_1 - \frac{m^2}{4\xi} - F\,\frac{\xi^2}{4}\right)u &= 0 \\ \frac{\mathrm{d}}{\mathrm{d}\eta}\left(\eta\,\frac{\mathrm{d}v}{\mathrm{d}\eta}\right) + \left(E\,\frac{\eta}{2} + Z_2 - \frac{m^2}{4\eta} + F\,\frac{\eta^2}{4}\right)v &= 0\,. \end{aligned} \tag{2.30}$$

This firstly shows the wave functions are degenerate for $\pm m$. The separation constants, Z_1 and Z_2 are known as the generalised charges , and can be though as which bind the electron in the ξ and η coordinates, they are coupled by

$$Z_1 + Z_2 = 1\,. \tag{2.31}$$

If the the equations are solved for bounded states ($E < 0$) in the zero field case, where the effect of field is calculated through perturbation theory, then the zero-order functions, u and v can be solved in terms of Laguerre polynomials. This gives

$$\begin{aligned} u_{n_1 n_2 m}(\xi) &= N_u \sqrt{\epsilon}\, \mathrm{e}^{-\frac{1}{2}\epsilon\xi} (\epsilon\xi)^{\frac{|m|}{2}} \mathrm{L}^{|m|}_{n_1}(\epsilon\xi) \\ v_{n_1 n_2 m}(\eta) &= N_v \sqrt{\epsilon}\, \mathrm{e}^{-\frac{1}{2}\epsilon\eta} (\epsilon\eta)^{\frac{|m|}{2}} \mathrm{L}^{|m|}_{n_2}(\epsilon\eta)\,, \end{aligned} \tag{2.32}$$

where $E = -\frac{1}{2}\epsilon^2$ and

$$\begin{aligned} n_1 &= 0, 1, 2, \ldots \\ n_2 &= 0, 1, 2, \ldots\,, \end{aligned} \tag{2.33}$$

the two new quantum numbers obtained from the relations in equation 2.32, they are related with the nodes of the Laguerre polynomials and to the original quantum numbers, n and m, through

$$n = n_1 + n_2 + |m| + 1\,. \tag{2.34}$$

Often, these two new quantum numbers are defined as one quantum number k,

$$k = n_1 - n_2\,. \tag{2.35}$$

k is related to the Runge-Lenz vector, which is defined as [25]

$$\vec{K} = m Z \mathrm{e}^2 \hat{r} - \frac{1}{2}\left(\vec{p} \times \vec{L} - \vec{L} \times \vec{p}\right). \tag{2.36}$$

Classically, the Runge-Lenz vectors points in the direction along the major axis of the ellipse which describes the trajectory of the classical particle in the Coulomb potential, and its length is equal to the eccentricity of the orbit. The z component of the Runge Lenz vector is expressed in parabolic coordinates as

$$K_z = \frac{\xi - \eta}{\xi + \eta} - \frac{2\eta}{\xi + \eta}\frac{\partial}{\partial\xi}\left(\xi\frac{\partial}{\partial\xi}\right) + \frac{2\xi}{\xi + \eta}\frac{\partial}{\partial\eta}\left(\eta\frac{\partial}{\partial\eta}\right) + \frac{\xi - \eta}{2\xi\eta}\frac{\partial^2}{\partial\phi^2}\,, \tag{2.37}$$

which commutes with the Hamiltonian and the z component of the angular momentum.

In these terms the generalised charges 2.31 result

$$\begin{aligned} Z_{1 n_1 n_2 m} &= \frac{2n_1 + |m| + 1}{2(n_1 + n_2 + |m| + 1)} \\ Z_{2 n_1 n_2 m} &= \frac{2n_2 + |m| + 1}{2(n_1 + n_2 + |m| + 1)}\,, \end{aligned} \tag{2.38}$$

and the energy

$$\epsilon_{n_1 n_2 m} = \frac{1}{n_1 + n_2 + |m| + 1} = \frac{1}{n} \tag{2.39}$$

The normalisation constants N_u, N_v result:

$$\begin{aligned} N_u &= \frac{\sqrt[4]{2}}{\sqrt{(n_1 + n_2 + |m| + 1)}} \sqrt{\frac{n_1!}{(n_1 + |m|)!}} \\ N_v &= \frac{\sqrt[4]{2}}{\sqrt{(n_1 + n_2 + |m| + 1)}} \sqrt{\frac{n_2!}{(n_2 + |m|)!}}\,, \end{aligned} \tag{2.40}$$

which leads to the expression of the total zero-order wave function as follows:

$$\Psi_{n_1 n_2 m}(\xi,\eta,\varphi) \;=\; \frac{1}{n\sqrt{\pi}}\,\sqrt{\frac{n_1!}{(n_1+|m|)!}}\,\sqrt{\frac{n_2!}{(n_2+|m|)!}}\,e^{im\varphi}\,e^{-\frac{1}{2}\epsilon(\xi+\eta)}\,\epsilon^{|m|+1}(\xi\eta)^{\frac{|m|}{2}}\,L_{n_1}^{|m|}(\epsilon\xi)\,L_{n_2}^{|m|}(\epsilon\eta) \tag{2.41}$$

This solution makes also diagonal the z component of the Runge-Lenz vector, being its eigenvalues

$$K_z\,|\,n\,k\,m\,\rangle \;=\; \frac{k}{n}\,|\,n\,k\,m\,\rangle \tag{2.42}$$

Now, to solve the calculation of the perturbation of the atom due to an electric field in the z-direction, the matrix of $\langle z\rangle$ with regard to the states of the same n is required. This is done through using known properties of Laguerre polynomials [16]. The diagonal elements, to first order perturbation with field strength F, have the value

$$\langle n\,k\,m\,|\,z\,|\,n\,k\,m\rangle \;=\; \frac{3}{2}\,n\,k\,. \tag{2.43}$$

Therefore, the first order alteration to the energy level, E, in atomic units is given by

$$E \;=\; -\frac{1}{2n^2} \;+\; \frac{3}{2}\,F\,n\,k\,. \tag{2.44}$$

Although there is no explicit dependence on m, there is an indirect dependence through the dependence of n and k on m. It can also be seen that states that lie on the $+z$-axis will have higher energies than those which lie on the $-z$-axis. By setting n_1 and n_2 to $n-1$ and 0, the highest and lowest energies are obtained respectively. The separation between these points is given by,

$$\Delta E \;=\; 3\,F\,n\,(n-1)\,. \tag{2.45}$$

Therefore, the larger the diameter of the electrons classical orbit the greater the potential difference between opposite points in that orbit.

Although higher order terms are negligible in equation 2.44 in low lying n-states in a JET plasma, they become more significant at higher n-states. The correction to this energy was calculated by Ishida and Hiyama [26]. Their result is

$$\begin{aligned} E \;=\; & -\frac{1}{2n^2} \;+\; \frac{3}{2}\,F\,n\,k \;- \\ & \frac{1}{16}\,F^2\,n^4\left(17\,n^2 \;-\; 3\,k^2 \;-\; 9\,m^2 \;+\; 19\right) \;+ \\ & \frac{3}{32}\,F^3\,n^7\,k\left(23\,n^2 \;-\; k^2 \;+\; 11\,m^2 \;+\; 39\right). \end{aligned} \tag{2.46}$$

Now, there is also a direct dependence on m given in the second order shift. In addition, the second order shift is always to lower energies and remains unaltered on interchange of k and $-k$. So the atom configuration effects the first and third order shift, not the second.

The expression of the wave functions at higher order perturbation theory is very tedious and requires a great effort to obtain, so as it was mentioned above, an alternative method becomes valuable to get the energies and wave functions.

These energy levels given by equation 2.47 can be plotted as a function of field. There are two situations that can occur: an adiabatic reaction and a diabatic one, if the coupling between the states is strong, one can think of the reaction to be of diabatic nature and the crossing will occur, this is shown in figure 2.6. However, if the coupling is weak, then it can be thought of as adiabatic and the energy levels will get to the point of crossing then veer off in the opposite direction as shown in figure 2.7. Therefore one must consider the field at which these reactions are occurring and the nucleus of the species to determine the coupling. It is seen from figure 2.6 that for a hydrogen nucleus in JET conditions, the mixing begins to occur for $n > 6$ before the point at which the level classically ionises.

If the diabatic reactions are considered, one must carefully consider how the wave functions are treated at the point of mixing. The reason why the levels cross despite having the same m is because the parabolic coordinates also diagonalise the Runge-Lenz vector, where there are different eigenvalues in the two crossing states. The Runge-Lenz

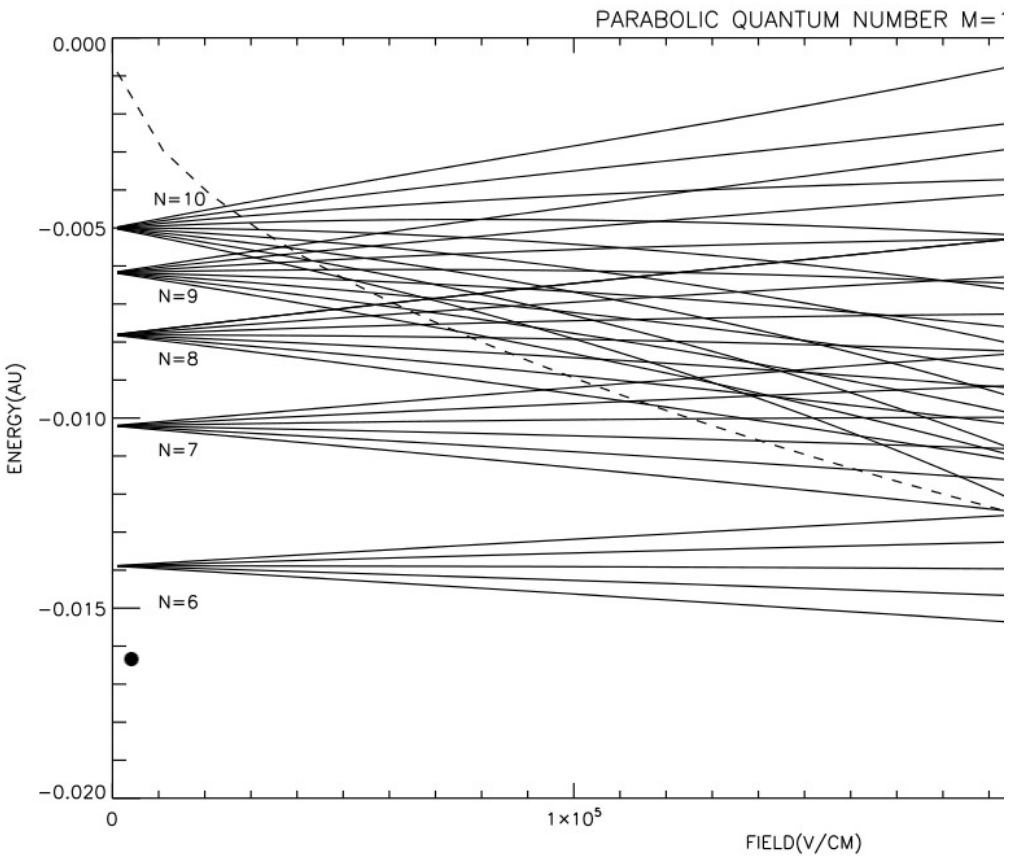

Figure 2.6: A graph showing the mixing of Stark energy levels for hydrogen at various field intensities with $m = 0$. The dashed line shows the classical ionisation limit.

vector is used classically to describe the shape and orientation of the orbit of one body around another. At zero field the Runge-Lenz vector and angular momentum are conserved and Park (1960) [28] showed that using this fact one could relate the parabolic and spherical states through a Clebsch-Gordan coefficient. This transformation coefficient is given in terms of Wigner-3J symbols as

$$\langle n\,k\,m\,|\,n\,l\,m\rangle \;=\; (-1)^{\frac{1-n+k+m}{2}+l}\,\sqrt{2l+1}\begin{pmatrix} \frac{n-1}{2} & \frac{n-1}{2} & l \\ \frac{m+k}{2} & \frac{m-k}{2} & -m \end{pmatrix}, \tag{2.47}$$

where

$$|\,n\,k\,m\rangle \;=\; \sum_{l=0}^{n-1} |\,n\,l\,m\rangle\,\langle n\,l\,m\,|\,n\,k\,m\rangle\,. \tag{2.48}$$

These two equations allow the two coordinate states to be transformed from one to another at zero field.

This configuration of solving with respect to z-axis is an important point to note, and one which this report shall come back to in section 6.7. The transitions associated with the H_α line can be seen in figure 2.8. The allowed transitions are the usual $\Delta m = 0, \pm 1$. Although there are no specific selection rules with respect to the parabolic quantum numbers, transitions which involve a change in sign in k are mostly weak, that is the reason why generally only nine main transition lines are seen for the H_α transition instead of fifteen. The intensities for the first four Balmer transition lines can be seen in figure 2.9.

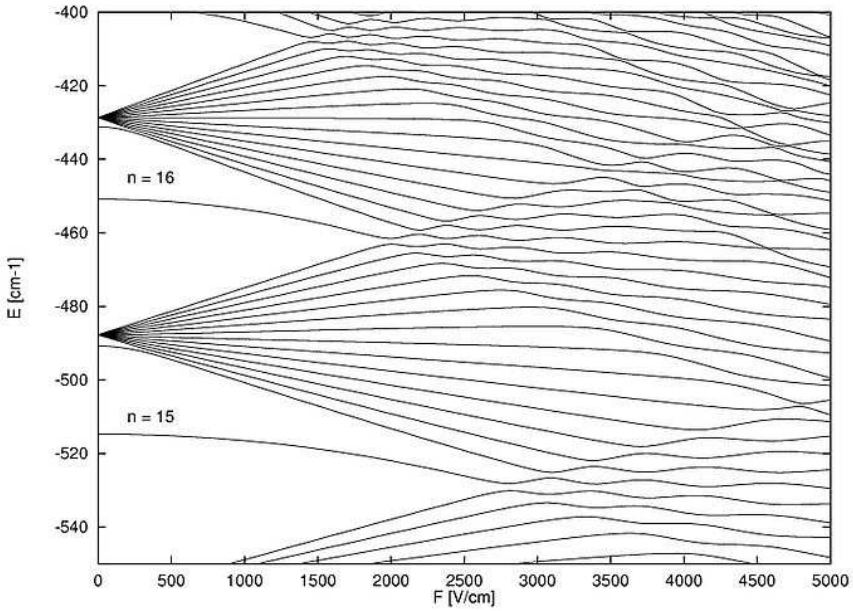

Figure 2.7: A graph showing the mixing of Stark energy levels for lithium at various fields with $m = 0$. Image credit: Courtney *et al.* [27].

2.5 Matrix elements of Stark perturbations

At first order perturbation theory, we can treat the Stark Hamiltonian as a perturbation over the Rydberg states $|nlm_l sm_s\rangle$ as usual

$$\left\langle n\, l\, m_l\, s\, m_s \,|\, Fz \,|\, n'\, l'\, m_l'\, s\, m_s' \right\rangle . \tag{2.49}$$

Writing $z = r\cos\theta = \sqrt{\frac{4\pi}{3}} r Y_{10}(\theta, \phi)$, and applying the Wigner-Eckart theorem [29], we can separate the integral in a radial and angular part:

$$\begin{aligned} \left\langle n\, l\, m_l\, s\, m_s \,|\, Fz \,|\, n'\, l'\, m_l'\, s\, m_s' \right\rangle &= F\, \langle n\, l \| r \| n'\, l' \rangle\, \sqrt{(2l+1)(2l'+1)}\, (-1)^{m_l} \begin{pmatrix} l & 1 & l' \\ 0 & 0 & 0 \end{pmatrix} \begin{pmatrix} l & 1 & l' \\ -m_l & 0 & m_l' \end{pmatrix} \\ &= F\, \langle n\, l \| r \| n'\, l' \rangle\, (-1)^{l-l'-1} \sqrt{\frac{2l+1}{2l'+1}}\, \langle l\, 0\, 1\, 0 \,|\, l'\, 0 \rangle\, \langle l\, m_l\, 1\, 0 \,|\, l'\, m_l' \rangle \end{aligned} \tag{2.50}$$

where the reduced matrix element $\langle nl \| r \| n'l' \rangle$ is the integral

$$\langle nl \| r \| n'l' \rangle = \sqrt{\left(\frac{4}{nn'}\right)^3 \frac{(n-l-1)!}{2n(n+l)!} \frac{(n'-l'-1)!}{2n'(n'+l')!}} \int_0^\infty \mathrm{d}r\, \mathrm{e}^{-\frac{n+n'}{nn'}r} \frac{2^{l+l'}}{n^l\, n'^{l'}}\, r^{l+l'+1}\, \mathrm{L}_{n-l-1}^{2l+1}\left(\frac{2r}{n}\right) \mathrm{L}_{n'-l'-1}^{2l'+1}\left(\frac{2r}{n'}\right) . \tag{2.51}$$

This operation is mainly which makes ADAS305 to get the Stark perturbation terms.

2.6 Polarisation

Now that splitting of spectral lines has been established for each perturbation term, it is important to consider the polarisations of the $\Delta m_l = 0$ and $\Delta m_l = 1$ transitions. The radiation can either be linearly or circularly polarised with respect to the field axis. Generally, the linear ($\Delta m_l = 0$) and perpendicular ($\Delta m_l = 1$) components of the radiation are

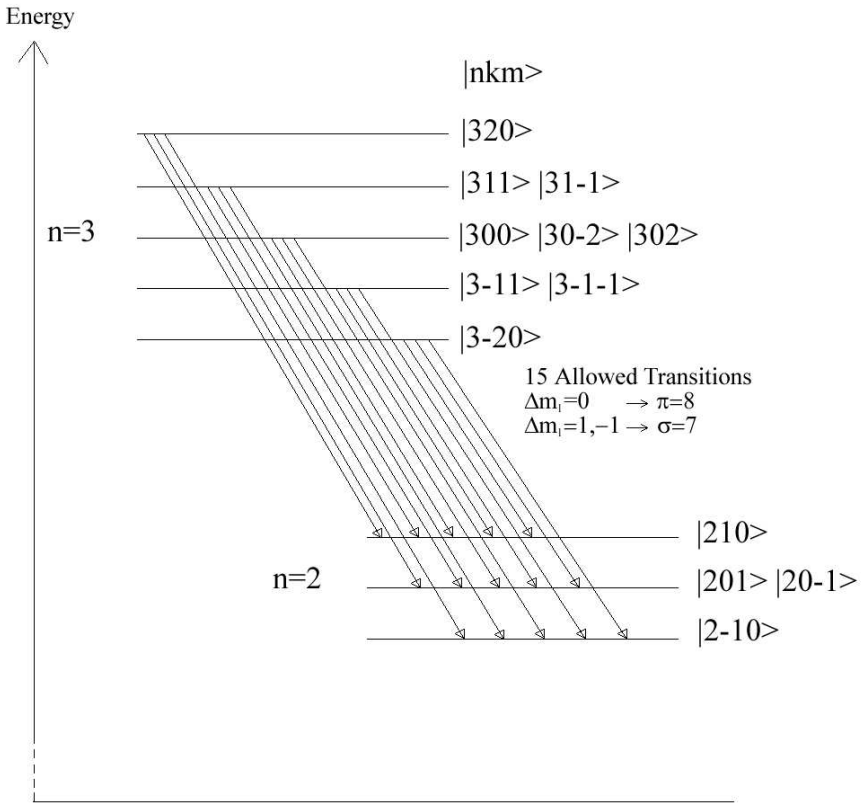

Figure 2.8: A diagram showing the 15 allowed Stark transitions of the Balmer alpha line.

labelled π and σ respectively, ADAS305 has the ability to quench or amplify either type of radiation. In experiment this is done by using polarises set up to deal with each type of radiation, the observed asymmetry of the motional Stark multiplet is mainly in the π radiation, therefore, it is useful to have the ability of quenching either the π or σ radiation as it allows analysis of one certain set of transitions. Condon and Shortley [21] provide an overview of the dipole radiation field, a general summary can be written by considering the average Poynting vector given by

$$S_{av} = \frac{c}{4\pi}\left(\vec{F}\times\vec{B}^{*} + \vec{F}^{*}\times\vec{B}\right) \tag{2.52}$$

where $\vec{F}$ and $\vec{B}$ are the electric and magnetic field vectors. The Poynting vector (Poynting, 1884 [30]) is directed along the energy flux of the electromagnetic field.

Firstly the π radiation is considered, for this analysis it is assumed that the dipole moment is directed along the z-axis, in a fusion plasma, this assumption is correct if the magnetic field is labelled the x-axis and the beam is travelling along the y-axis, the dipole is oscillating in the xy plane therefore the radiation is linearly polarised with the electric vector in the plane determined by r_0 and the dipole moment. The intensity, at an angle θ with the z-axis, is therefore

$$S_{av} = \frac{ck^4}{8\pi r^2} V(r)^2 \sin^2\theta\,\vec{r}_0\,. \tag{2.53}$$

Now, for the σ radiation, the dipole is now oscillating in the xz plane. The vector is now circularly polarised and the intensity is given by

$$S_{av} = \frac{ck^4}{8\pi r^2}\frac{1}{2} V(r)^2 (1 + \cos^2\theta)\,\vec{r}_0\,. \tag{2.54}$$

Keeping the plasma orientation as stated above, this means that if the viewing angle of the beam emission was set to look along the xy plane ($\theta = 90^0$), then one would receive half the amount of σ radiation and the full amount of π radiation. If the viewing angle is rotated to $\theta = 0$, one would only receive the full amount σ radiation and no π radiation. This change in intensity can be seen in figure 2.10.

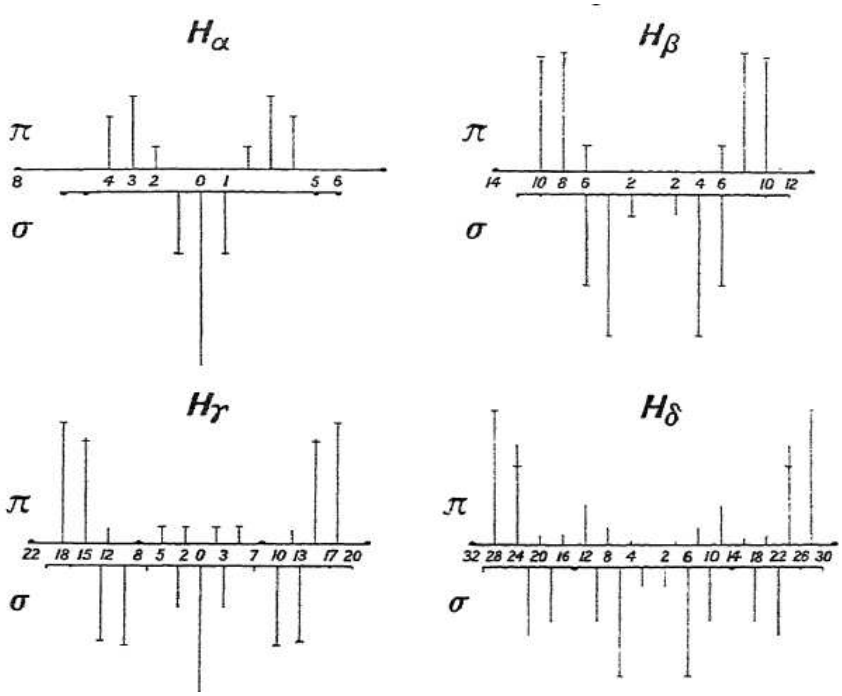

Figure 2.9: Graphs showing the relative intensities and polarisations of the first four lines of the Balmer series. Image credit: Condon & Shortley [21]

2.7 Motional Stark Effect

The previous six sections have developed a strategy for describing the perturbations for the separate electric and magnetic field cases. However, it becomes slightly more complex when dealing with the motional Stark effect of the neutral beam. Now, there is a Lorentz electric field and a magnetic field which must be treated together. It was briefly mentioned in section 2.4 how this idea of two different fields may have the potential to cause a misinterpretation of experimental measurements. The polarisation labels, π and σ must be treated with their respective dipole moment axis. In addition, the quantum numbers used to describe the transitions must always commute with the Hamiltonian.

A solution to this problem is to try and find a way of 'grading' the set of quantum numbers. More specifically, in the purely Lorentz case, the Runge-Lenz vector is multiplied by the transformation matrix and a diagonal matrix will be generated. All off-diagonals elements should be zero while the diagonal elements should be equal to the k quantum numbers. As the magnetic field is increased, these off-diagonal elements will begin to stray from zero. The amount by which they stray coupled by a visual analysis of the emission lines can be used as a guide to which labelling system to use.

So, although there is a certain grade to the quantum number, there is no real definition to this grade, i.e. what grade tells us when the Lorentz term is comparable to the Paschen-Back term. To get around this problem, one would also look to diagonalise the L_z and S_z matrices to obtain the m_l and m_s quantum numbers along the diagonal of the respective generated matrices. Again, in a pure Paschen-Back case, the off-diagonals in these matrices should be zero. So, if the code is set up initially with the Paschen-Back term being negligible compared to the Lorentz term, then off-diagonal terms from the generated matrices of L_z and S_z should roughly be at their maximum deviation away from zero. The order of the maximum deviation is set as a normalisation value for each off-diagonal term in the k, m_l and m_s matrix. Now, with each grade normalised, it is more clear when the two field terms are equal to each other and when one can say which field effect is in dominance. ADAS305 does not yet transform the angular and other matrices, however this step is not complex and is hoped to be carried out in the near future.

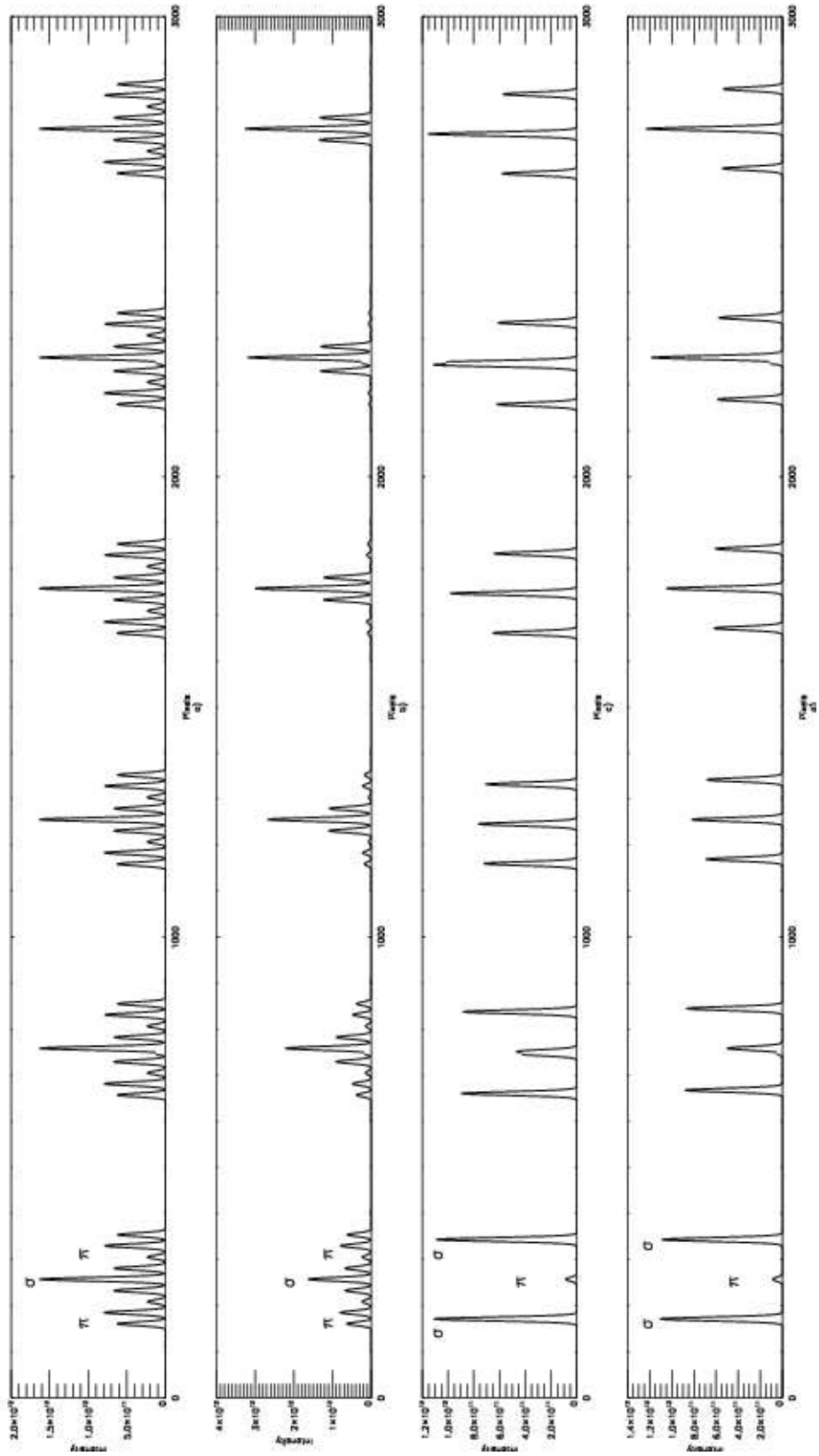

Figure 2.10: For the Stark effect, the evolution of the observational line moving from the x-axis to the z-axis, (staying perpendicular to the Lorentz field along the y-axis) is shown in a). In b) we see the evolution of the observational line moving from the x-axis to the y-axis (moving from perpendicular to parallel with the Lorentz field). For the Paschen-Back effect, the evolution of the observational line moving from the x-axis to the z-axis (moving from parallel to perpendicular with the magnetic field along the x-axis) is shown in c). In d) we see the evolution of the observational line from the x-axis to the y-axis (moving from parallel to perpendicular with the magnetic field). Graphs were obtained from the ADAS code ADAS305.

Chapter 3

Field ionisation

The atomic levels of an atom in the presence of a field become narrow bands of a continuum which get wider as the field increases. Therefore, in order to fully describe the Stark effect, the center of the band, E_0, and the band width, Γ, should be determined, the band width can be thought of as a complex eigenvalue, i.e. $E = E_0 + i\Gamma$, the imaginary part of this complex eigenvalue contribute with a decaying factor in the phase evolution of the time-dependent Schrödinger equation, so it is interpreted as the probability that will field will altogether remove the electron from the nucleus. The method of finding the center of the band or resonance E_0 through perturbation theory was described in section 2.4. This chapter will be concerned with a semiempirical theory of calculating Γ and how it may be a possible theoretical solution to the slight persistent asymmetry experimentally observed within the Stark H_{alpha} multiplet. This chapter will also provide a broad overview of the different methods put forward to try and solve this complex energy eigenvalue problem to give an indication as to the benefits and downfalls of each method.

The imaginary part of the energy can be also calculated through perturbation theory at order higher than second, including in the perturbation matrix the states of the continuum of the field-free hydrogen atom. Once again the effort necessary to do that is larger than making an exact calculation through complex coordinate integration and the quality of the results is poor, so it is not valuable and in this chapter we will focus in the semiempirical methods much faster.

The possibility of removing an electron entirely from the atom through applying an external field was first discussed by Oppenheimer (1928) [31], Oppenheimer deduced an expression for the ionisation probability for the ground state, no long after, Rausch von Traubenberg (1929) [32] [33] produced experimental results which verified the field ionisation concept. It was found that the higher energy Stark shifted states were harder to ionise than the lower energy Stark shifted ones, this poses a complex problem involving asymmetries within the Stark multiplet. It is advantageous to find out at what atomic configuration this asymmetry becomes dominant at various field values, this will allow determination of whether the ionisation rate is greater than other processes occurring in the atom in plasma, such as radiative decay and collisional processes. More specifically, it will be looked at with respect to the processes occurring in BMS calculated by ADAS305, if it is a dominant process then one would expect this to filter through into Stark shifted spectral lines. Throughout the years, there have been many different methods proposed to calculate the reasoning and theory behind this. In section 3.2, the different methods in calculating the field ionisation rates will be discussed and compared in detail. The final sections will then move to focus on the method chosen for this report and how it can be integrated into ADAS305.

3.1 Classical ionisation limit

The combined Coulomb-Stark potential acting on the atom is given in atomic units by

$$V = -\frac{1}{r} + \vec{F}_{\mathrm{Lor}}\,\vec{r}. \tag{3.1}$$

Therefore, if the electron is lying along the z-axis, the potential is of the form shown in figure 3.1 for positive and negative z. This shows that the motion in the positive z direction is bounded for all energies as $V(z) \rightarrow F_{\mathrm{Lor}}z$ for

$z \rightarrow \infty$. However the motion is unbounded in the negative z direction as $V(z) \rightarrow -F_{\text{Lor}}|z|$ for $z \rightarrow -\infty$. It is seen that once the electron has reached potential, $V = -2\sqrt{F_{\text{Lor}}}$ it becomes classically ionised, this corresponds to $z = -\sqrt{F_{\text{Lor}}}$. It should be noted though that this result is only valid for $m = 0$ where $r = |z|$, when $m \neq 0$ then $r = \sqrt{x^2 + y^2 + z^2}$.

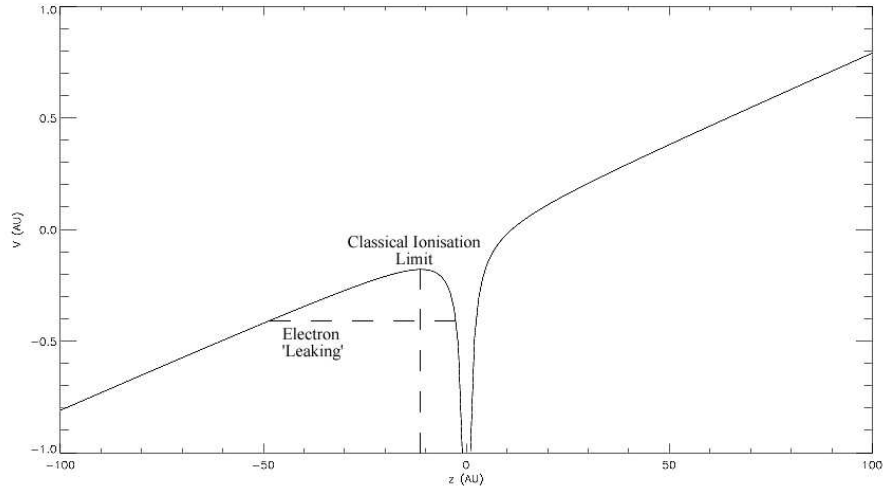

Figure 3.1: The combined Coulomb-Stark potential of an atom sitting along the z-axis in an electric field $F_{\text{Lor}} = 0.008$ a.u.

This classical picture is not adequate to describe the field ionisation. It does not account for the fact that the higher energy, 'blue' Stark states are harder to ionise than the lower energy, 'red' Stark states, Bethe and Salpeter [17] stipulated a rule, based on equation 3.1, where energetically lower substates of the same n are less stable, in other words, states present on the $-z$ side of the atom are more easily ionised than states on the $+z$ side. If the parabolic states described in section 2.4 are again considered, then this corresponds to states with high n_2 and low n_1 (or k negative). Evidence for this was found for this by Lanczos (1930) [34], who showed that 'blue' components of the H_γ line remained sharper and stronger as higher fields were applied. This is a rather surprising result as one would expect the states of higher energy to have a more penetrable barrier to go through, however, the red components, although they rise from a lower state of energy, are on the energetically unstable side of the atom. There exists a point where the 'leaking' of electrons can occur, as shown in figure 3.1, at this point the electron is ionised, although, this rule is not absolute. Results from Bailey *et al.* [35] proved that this rule could be broken at high values of n. In other words, the ionisation curves for high n_2 begin to cross curves of lower n_2. Therefore, to understand this further, it is necessary to study this quantum tunnelling of the potential barrier in more detail.

3.2 Potential barrier penetration

To understand the barrier penetration one needs to consider the two expressions written in equation 2.30 from chapter 2. They can be re-written in the form

$$\frac{\mathrm{d}^2\chi_i}{\mathrm{d}\sigma_i^2} + \frac{\chi_i}{2}\left[W - V(\sigma_i)\right] = 0\,, \tag{3.2}$$

where $i = 1, 2$, W is the energy, χ_1 and χ_2 are the wave functions u and v respectively and the σ_1 and σ_2 are the parabolic coordinates ξ and η respectively which are given by

$$V(\xi) = 2\left(-\frac{Z_1}{\xi} + \frac{m^2 - 1}{4\xi^2} + \frac{F_{\text{Lor}}\,\xi}{4}\right), \tag{3.3}$$

and

$$V(\eta) = 2\left(-\frac{Z_2}{\eta} + \frac{m^2 - 1}{4\eta^2} - \frac{F_{\text{Lor}}\,\eta}{4}\right). \tag{3.4}$$

These two potentials show the same characteristics as the classical potential given in equation 3.1, with $V(\xi)$ representing the $+z$-axis and $V(\eta)$ representing the $-z$-axis. The effective potential in equation 3.4 has a maximum and tends

to $-\infty$ when η tends to infinity, therefore the eigenvalues of the potential have a quasi-discrete spectrum and can be considered to be complex. The imaginary part is connected with the tunnelling through the potential barrier.

There have been many different ways of treating this problem. Firstly, Lanczos (1930) [34] studied the problem using the Wentzel-Kramers-Brillouin (WKB) approximation in the one-dimensional Schrödinger case. In the WKB approximation, the wave function is recast as an exponential function, semi-classically expanded, and then either the amplitude or the phase is taken to be slowly changing (Karnakov and Krainov, 2012 [36]), in other words, for this example the WKB approximation presumes that $\frac{\partial^2 \chi_i}{\partial \sigma_i^2} = 0$, however, the WKB approximation breaks down where the potential reaches the classical turning point, therefore Lanczos calculated results only for the levels which were well below the peak of the effective potential barrier. Rice and Good (1962) [37] later reviewed the problem and treated it with the full three-dimensional picture in the WKB approximation, this enabled them to calculate the half-widths (Γ) near the potential barrier. Bailey *et al.* [35] produced a review of the two methods described by Lanczos and Rice and Good, they found that Rice and Good neglected the $(m^2 - 1)$ term which Lanczos did include in his results, this term proved to be of significance in the ordering of thresholds for large m-values, in addition, Rice and Good used an iterative formula for the energy levels whereas Lanczos used the perturbation method to third order in his evaluation, these two different means of calculating the energy levels at high field conditions caused the highest discrepancy, which was however less than experimental uncertainties. At lower fields the two methods gave very good agreement with each other.

This WKB method provided very reliable results, however as this method is based on a tunnelling process it cannot describe the ionisation rates above the potential barrier, so an exact method of solution was then the ultimate goal. Alexander [38] carried out calculations for the ionisation rate from the ground state of hydrogen using the Breit-Wigner parametrisation formula, these results were then backed up by Hehenberger *et al.* (1974) [39] by using the method of exploiting the poles of Weyl's m-function in the complex plane. However, a method which could have been seen as benchmark at the time, was then produced by Damburg and Kolosov [40], they provided an exact numerical solution for both the energy levels and their width, they took explicit advantage of the exact separability of the Schrödinger equation in parabolic coordinates and used recurrence relations to find the solutions, the only limiting factor in their method was the fact that it must be repeated for each state and each intensity of the field. Luc-Koenig and Bachelier (1980) [41] tried to then find a quicker exact solution using the Breit-Wigner parametrisation formula, however this still proved to be a long way around the problem. Later, Farrely and Reinhardt (1983) [42] found a discrepancy in the exact calculations by Damburg and Kolosov, they used a semiclassical complex rotation, $r \rightarrow re^{i\theta}$.

There have been more recent attempts to build an exact solution to this problem (Tian, 2002 [43]), but due to the time restrictions of this report, analytical expressions were sought after instead which can be used to quickly work out the ionisation rates at each regime, this is also an important issue for this theory to be efficiently added into ADAS305. It is a big ask for the ADAS305 to include a thorough calculation, as those describe above, for each individual level along with the complex calculations it is already performing and still be used in an efficient manner, these analytical expressions could be done by using certain assumptions, applicable to the regime in question, which simplify the problem.

If the first regime is taken to be states lying well below the potential barrier, Damburg and Kolosov [44] provide a semi-empirical formula to calculate these states, the expression they give was formulated through applying an asymptotic expansion in Γ, this gives reasonable agreement with their previous exact numerical results. Two more papers then followed to expand on the work of Rice and Good by finding the ionisation rates near the potential barrier (Drukarev [45]; Kadomtsev and Smirnov [46]), the formulae obtained by Kadomtsev and Smirnov however turned out to be erroneous (Drukarev [47]) and the calculations from Drukarev [45] didn't give good agreement with the exact results of Damburg and Kolosov [40]. Therefore, to try and find a reliable solution to this regime, Kolosov (1983) came up with a method using the Breit-Wigner parametrisation formula, this method provided good agreement with the exact numerical calculations. The last regime approximation, states lying well above the potential barrier, was then completed by Kolosov [48], however, this method still required a rather complex solution as it adopted the asymptotic expression of the amplitude of the incoming wave at infinity and the Wronskian of the Schrödinger equation solutions to calculate the ionisation rate. No further method of this regime has so far been found, so this report will work on the basis of applying the second regime equation the third. The next three sections will describe the exact method of calculating the ionisation rates in each regime and will go on to give a summary of the results found using these equations.

3.3 Below Potential Barrier

The well known asymptotic expansion of E_0 in a power series of $F_{\rm Lor}$ is derived through means of perturbation theory, Damburg and Kolosov [44] describe a procedure for finding the asymptotic expansion of $F_{\rm Lor}$ for Γ, again this theory starts by considering the two parabolic solutions to the Schrödinger equation as described in equation 2.30. When using the perturbation theory, both of these potentials are treated as one-dimensional Schrödinger equations having bound states, however, this is only actually true for the solution to the wave function, u. This potential always has bound states therefore n_1 is always a good quantum number, however, it is only true to say that the solution to v has bound states well below the potential i.e. n_2 is only a good quantum number below the barrier. To get around this problem, Damburg and Kolosov suggest a slightly modified solution of equation 2.30. By changing the variable η to ρ:

$$\rho \;=\; (-2E)^{\frac{1}{2}}\,\eta \tag{3.5}$$

and introducing the new parameters

$$R \;=\; \frac{(-2E)^{\frac{3}{2}}}{F_{\rm Lor}} \tag{3.6}$$

and

$$\lambda \;=\; Z_2\,(-E)^{-\frac{1}{2}}\,. \tag{3.7}$$

The solution then becomes

$$\frac{{\rm d}^2U}{{\rm d}\rho^2} \;+\; \left(\frac{1\;-\;m^2}{4\rho} \;+\; \frac{\lambda}{\rho} \;-\; \frac{1}{4} \;+\; \frac{\rho}{4R}\right) U \;=\; 0\,. \tag{3.8}$$

The method then goes on to solve this equation in two regions; the first region $0 \le \rho < \rho_1$, where $\rho_1 \ll R$ and the second region $\rho_0 < \rho < \infty$ where $\rho_0 < \rho_1$. Once these solutions are obtained, they are linked together in a matching region $\rho_0 < \rho < \rho_1$, where both of them are valid. The asymptotic expression they derive for Γ is given by

$$\Gamma \;=\; \frac{(4R)^{2n_2+m+1}}{n^3 n_2!(n_2+m)!}\,\exp[y]\,, \tag{3.9}$$

with

$$y \;=\; -\frac{2}{3}\,R \;-\; \frac{1}{4}\,n^3\,F_{\rm Lor}\left(34\,n_2^2 \;+\; 34\,n_2\,m \;+\; 46\,n_2 \;+\; 7\,m^2 \;+\; 23\,m \;+\; \frac{53}{3}\right). \tag{3.10}$$

This formula is only valid for field strengths

$$F_{\rm Lor} \ll \left[8\,n^3\,(2\,n_2 \;+\; m \;+\; 1)\right]^{-1} \tag{3.11}$$

which can be also be written as $R \ll 16\lambda$.

Due to the nature of this equation, it is necessary to build up a test module in Fortran before it is implemented into the already complex ADAS305, the code written in Fortran was named *fldizn*. To calculate the energy level the third order perturbation method, described by the equation 2.47, was used. In order to calculate the field ionisation, firstly a system for labelling states must be determined, this requires three main loops for each principal n-shell — magnetic number m and parabolic quantum numbers n_1 and n_2. For each configuration the code tests the numbers against equation 2.34, if they are valid then the states are stored in a vector for each number and the code progresses. This method assumes a degeneracy in spin, which will not be sufficient when dealing with magnetic processes in ADAS305.

Due to the exponential term, the equation has the ability to overload the computer with large factors which in reality should cancel out each other, the exponential becomes very large at high fields, n-shell or n_2, in addition, at high values of n_2, the factorial and the exponent of the R term also becomes very large. Because of that is more practical to deal with the logarithm of Γ and calculate it as

$$\log\Gamma \;=\; (2n_2 + m + 1)\,\log(4R) \;-\; 3\,\log n \;-\; \log(n_2!) \;-\; \log\left((n_2+m)!\right) \;+\; y\,. \tag{3.12}$$

This expression does not overflow the machine.

3.4 Near Potential Barrier

Now, using the same notation as that given in section 3.3, Kolosov (1983) [49] considered the regime $R \approx 16\lambda$ ($F_{\rm Lor} \approx [8n^3(2n_2+m+1)]^{-1}$). For the analysis, it is assumed that there is no incoming wave at infinity, it then follows the same principle as described in the previous section, the final solution involves a rather complex iterative solution to find the energy level which is then used to find the ionisation rate. The iterative method they suggest is outlined as follows: firstly, there are three variables which should be iterated together: λ_1, ϵ and R. The λ_1 value is given by

$$\lambda_1 \;=\; n_1 \;+\; \frac{1}{2}\,(m+1) \;+\; \frac{1}{4R}\,(6n_1^2 + 6n_1 m + 6n_1 + m^2 + 3m + 2)\,, \tag{3.13}$$

and ϵ by

$$\epsilon \;=\; \frac{\sqrt{2}\,\frac{R}{3} \;-\; \pi\,(2n_2+m+1) \;+\; \arg\Gamma\left(\frac{1}{2} \;+\; i\epsilon\right)}{\log 4\;\sqrt{2}\,R}, \tag{3.14}$$

where $\arg\Gamma$ denotes the argument of the complex number (angle with the real positive axis) of the Euler Γ function, and its expressions are given in full in Kolosov (1983) [49]. The method for evaluating R involves an iterative process using an equation provided for the energy level,

$$E \;=\; -\frac{1}{2}\left(\lambda_1 \;+\; \frac{1}{16}\,R \;-\; \frac{\epsilon}{\sqrt{2}}\right)^{-2}. \tag{3.15}$$

If this value is substituted into equation 3.6, then R is calculated through the Newton-Rabson algorithm:

$$R_{n+1} \;=\; \frac{1}{2}\left(R_n \;+\; \left(\lambda_1 \;+\; \frac{1}{16}\,R_n \;-\; \frac{\epsilon}{\sqrt{2}}\right)^{-3}\;\frac{1}{F_{\rm Lor}}\right), \tag{3.16}$$

where the initial guess R_0 is given by

$$R_0 \;=\; \frac{3\pi}{\sqrt{2}}\,(2n_2+m+1)\,. \tag{3.17}$$

The method starts by calculating λ_1 using R_0, this value of λ_1 along with R_0 is then substituted into equation 3.17, for the first iteration ϵ is set to zero. Once R_1 has been found, the starting value of ϵ is found through solving equations 3.6 and 3.15, then the new value of R is substituted back into $lambda_1$ and then on calculating R_2, the new values of λ_1 and ϵ are used. This method is repeated until the energy rounds off to its final value, after this energy is found, the level width is found through using the following expression,

$$\Gamma \;=\; \frac{F_{\rm Lor}\;\log[1+\exp(-2\pi\epsilon)]}{2\;\sqrt{-E}\,\left[\left(\frac{1}{4} \;+\; \frac{\lambda_1}{R}\right)\left(\log 4\;\sqrt{2}\,R \;-\; {\rm Re}\psi\left(\frac{1}{2}+i\epsilon\right)\right) \;-\; 1\right]}, \tag{3.18}$$

where ${\rm Re}\psi\left(\frac{1}{2}+i\epsilon\right)$ means the real part of the complex number and the analytical expression of the function ψ is shown again in Kolosov (1983) [49].

It was found that this method managed to reproduce the tabled ionisation rates given in Kolosov (1983) [49], however for other field values at various n-shell within this regime, the method provided rather temperamental results for the ionisation rate as described in the next section. This is due to the fact that a small change in energy level produced a massive change in ionisation rate, an easier way of implementing this method was through using known values of energy level using the perturbation theory. Now, an iterative process is not needed, as the equations can be solved directly by substituting in the energy level, this makes the method more robust to different electron configurations and field values, although due to the fact that this regime is now dealing with stronger fields than in the previous section, one must be cautious as to where the perturbation method of calculating the energy level breaks down.

3.5 Implementing Code

With the methods for calculating the ionisation rates now discussed, there are three main questions which need to be addressed: i) at what configuration the codes break down, ii) at what quantum shells and field values do the ionisation

rates become important, and iii) how will the independent code need to be altered to fit into the main population code, ADAS305. To answer the first question, the typical field values of JET will be neglected, and the code will be used in a more exploratory manner, a plot of results from the independent code *fldizn.for* can be seen in figure 3.2, there are a number of points which can be seen through these plots. Firstly, it can be seen that the two methods have reasonable agreement in ionisation rates approaching the potential barrier, however, after this point, the ionisation rates calculated using the method described in section 3.3 (method one from now on) tend to 'overshoot' the rates calculated using the theory in section 3.4 (method two from now on), however, the point at which the dotted curve begins to turn back on itself could be considered the point at which both the energy equations and method two equations break down. It is difficult to compare this point as there have been very limited results given in the regime just above the potential barrier (after the point of classical ionisation). The paper which dealt with this regime (Kolosov, 1987 [48]) produced values for fields much larger than of interest to this report ($F_{\mathrm{Lor}} > 2 \times 10^{13}$ V/cm). From a classical point of view, this seems quite contradictory that the field ionisation rates should begin decrease after this point as the field.

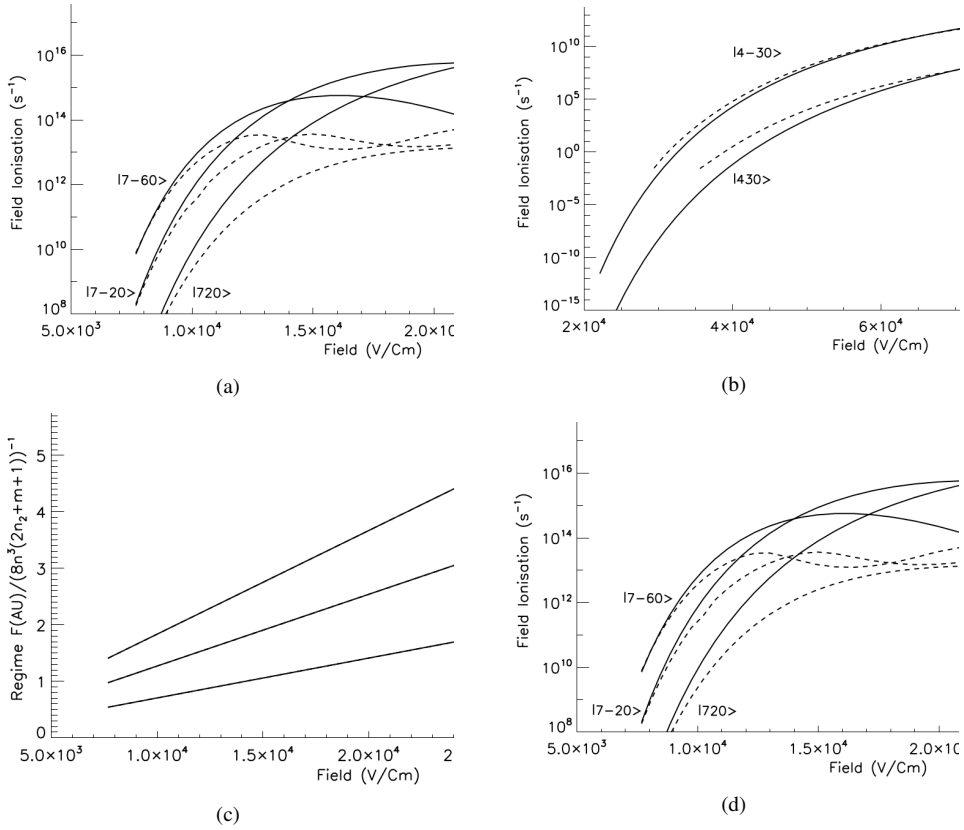

Figure 3.2: This figure provides an analysis of two principal n-shells: $n = 4$ and $n = 7$. In graphs a) and c) the ionisation rates are plotted against field. The solid lines represent the rates calculated using the method described in section 3.3 and the dotted lines represent the rates calculated using the method described in section 3.4. The plots in b) and d) show the regimes in which the two graphs in a) and c) are being projected through. The electron configurations are shown in the format $|n\,k\,m\rangle$.

To provide some clarity on how well these results can be trusted, table 3.1 compares tabulated results from Damburg and Kolosov [44] and Kolosov (1983) [49] with the computed results from the independent code *fldizn*. It is seen that as the field increases the results tend away from the tabulated values of Damburg and Kolosov, this could be due to the method of calculating the energy level, in the case of the results calculated by Kolosov (1983) [49], this method was found to show a very large change of ionisation rate with energy level, this made this adopted method quite volatile as a very small discrepancy between the energy value calculated against the energy value used by Kolosov saw a very large difference as shown by the $|5\ -4\,0\rangle$ ionisation probability, however this method did provide reasonable accuracy for the majority of results. For the purposes of this report, the errors of these values are of an acceptable range, this is due to the fact that this report is being used to show a general picture of the effects of field ionisation, the degree of accuracy will become valid when this general picture is accepted and implemented into a full diagnostic of the beam emission spectra. In addition, it will be seen that when this method is implemented into

$\|n\,k\,m\rangle$	Field (AU)	Damburg and Kolosov [44]	Calculated
$\|5\,3\,1\rangle$	1.4×10^{-04}	1.55×10^{-11}	1.66×10^{-11}
	1.6×10^{-04}	1.07×10^{-09}	1.18×10^{-09}
	1.8×10^{-04}	2.67×10^{-08}	3.04×10^{-08}
$\|2\,-1\,0\rangle$	2.5×10^{-03}	8.55×10^{-11}	1.03×10^{-10}
	3.0×10^{-03}	1.03×10^{-08}	1.40×10^{-08}
	3.5×10^{-03}	2.62×10^{-07}	4.23×10^{-07}
$\|10\,9\,0\rangle$	1.4×10^{-05}	1.07×10^{-12}	2.32×10^{-12}
	1.6×10^{-05}	2.75×10^{-10}	4.29×10^{-10}
	1.8×10^{-05}	1.19×10^{-08}	2.17×10^{-08}
		Kolosov (1983) [49]	Calculated
$\|5\,-4\,0\rangle$	1.0×10^{-04}	1.92×10^{-06}	1.03×10^{-11}
$\|10\,-9\,0\rangle$	1.0×10^{-05}	2.54×10^{-08}	3.88×10^{-08}
	1.1×10^{-05}	7.46×10^{-07}	1.23×10^{-07}
$\|13\,-2\,2\rangle$	4.3×10^{-06}	9.38×10^{-09}	8.40×10^{-09}
$\|5\,-4\,0\rangle$	2.9×10^{-06}	1.10×10^{-08}	1.94×10^{-08}

Table 3.1: Tabulated results of Damburg and Kolosov [44] and Kolosov (1983) [49] compared against the approach adopted in this report for method one and method two.

ADAS305, it can use the already calculated energy levels to aid the calculations providing more robust results.

Now the independent testing has been studied, the focus will be turned to implementing these rates into the population model, ADAS305. The first problem to tackle, is the assignment of parabolic states to the energy values calculated in ADAS305, detail is first needed to describe how the code creates the array of energy values, the code solves for the eigenvalues by directly solving the matrix of wave functions with respect to the z-axis, this produces an array of dimension $2n^2$. The energy levels are produced from highest to lowest, or from $-k \rightarrow +k$, with each k quantum number there is a degenerate magnetic number and in addition the code now takes into the spin of the electron. The integrated field ionisation code must produce three arrays of the same dimension for n_1, n_2 and m corresponding to the energy array.

One can go about solving this from a top down approach. Firstly a loop around k is started, the next loop to start is that around spin, in this case this will name both spin systems with the same parabolic quantum numbers, Within this spin loop lies a loop around n_1 and n_2, it is important to note that this loop starts at $n_1 = n_2 = n - 1$ and works back until $n_1 = n_2 = 0$. Going through these parabolic numbers, the code calculates a value of m from the condition, $|m| = n - n_1 - n_2 - 1$, if the value of m calculated is less than n then the code stores the set of n_1, n_2 and m, then on the next array point places n_1, n_2 and $-m$, this method produces an array which provides an accurate assignment system to any principal n-shell. A demonstration of the code used to assign these quantum numbers, namely $getpn.for$, is shown in figure 3.3, the graph on the left is a plot of the energy values produced in ADAS305 in order of the array position, on the right, the calculated parabolic numbers have been used to work out the energy in the code $fldizn$. It does not matter that the energy values are different, it is the trend that is of importance in this case.

With the numbering scheme in place, focus can be turned back to the ionisation rates. To test the code had been implemented successfully, a plot of ionisation rates and energy values were compared to the same plot produced by the independent code. The results can be seen in figure 3.4.

There is quite a dramatic difference between the two ionisation rates calculated for the different codes, in the independent code, the ionisation rates are rapidly decreasing due to the high field condition, however, in the ADAS305 code, the ionisation are still giving 'reasonable' rates. The plots show very different values of energy between the two codes, at this point some attention should be drawn to the method by which ADAS305 calculates the energy levels.

The independent code, as discussed, calculates energy levels using a perturbation method, therefore, the zero-field Hamiltonian is diagonalised with respect to the z-axis, and then the perturbations are added to the eigenvalues. The ADAS305 code on the other hand, diagonalises the perturbed Hamiltonian with respect to the z-axis, it does this by using the LA-PACK code, $ZHPEV$, the Z implies that it solves for the double precision complex Hamiltonian, therefore, one can conclude that by implementing the code into ADAS305, it has improved the robustness of the code through it is more accurate means of determining the energy level.

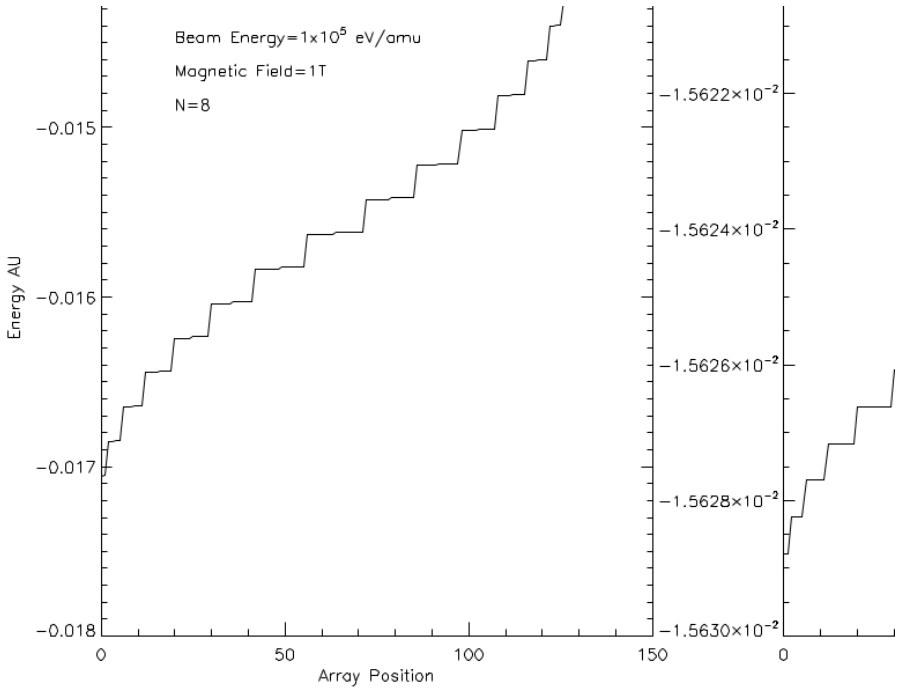

Figure 3.3: Two graphs to compare the parabolic quantum numbering scheme used in the subroutine *getpn*. The graph on the left shows the energies produced by ADAS305 plotted as a function of index. The graph on the right shows the energies produced by *fldizn* using the parabolic quantum numbers assigned to each array position. This was done for $n = 8$.

However, there still remains the problem of the high field scenario, it is seen from figure 3.5 that the levels still have a levelling off point where the high field kicks in. The results are still not accurate for this high field regime, however, the rates behave slightly less erratic, chapter 5 will describe how the field ionisation effects the population structure of the atom, this will ultimately go on to show if there are distortions or asymmetries to the beam emission Stark multiplet due to the field ionisation.

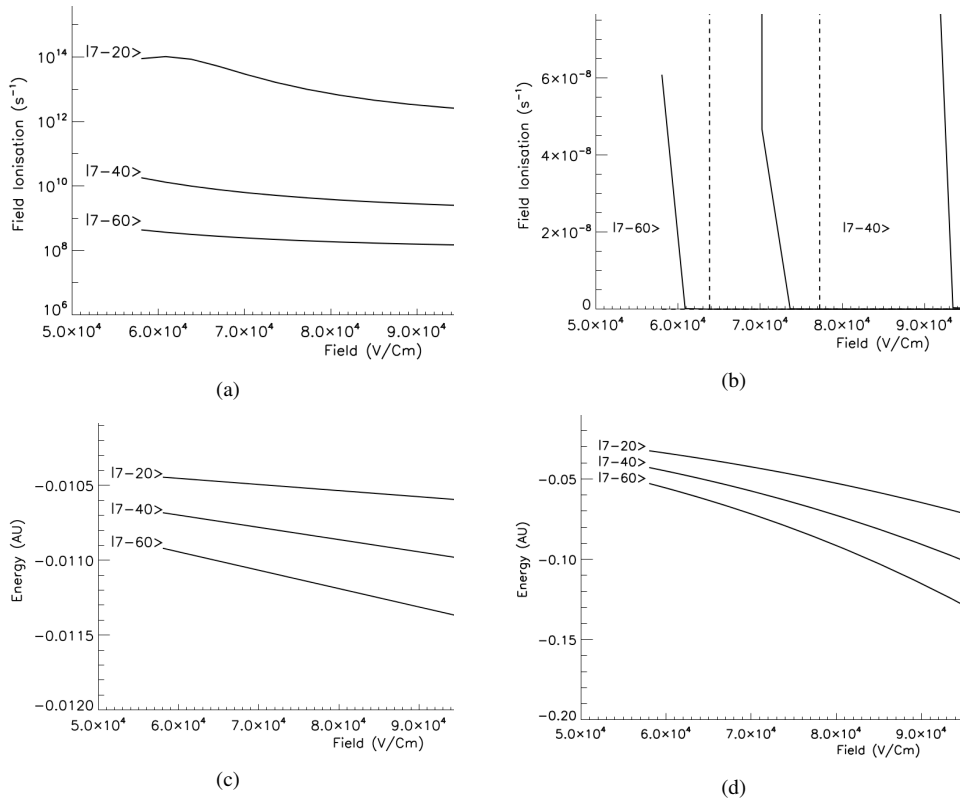

Figure 3.4: A comparison between ADAS305 and fldizn is drawn. In a) and b) the ionisation rates for various $|nkm\rangle$ states are produced by ADAS305 and fldizn respectively. The energy levels for the two codes respectively are then shown in c) and d).

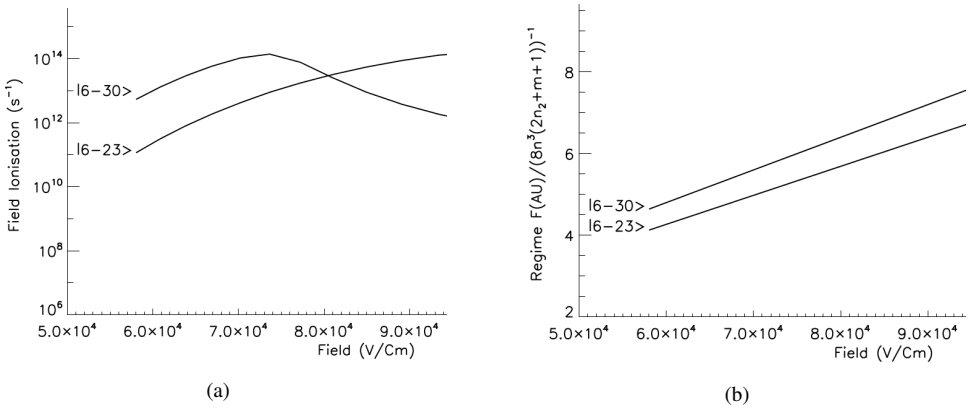

Figure 3.5: Two graphs showing the behaviour of the ionisation rates in different regimes. In a) the ionisation rates for given $|n\,k\,m\rangle$ states are plotted and in b) the regime is given for the same field and $|n\,k\,m\rangle$ states.

Chapter 4

Exact Stark effect, the complex coordinate method

4.1 Inconsistencies of perturbation theory for Stark effect

In last two chapters we showed the application of the perturbation theory to a neutral hydrogen atom under a constant electric field. Nevertheless we did not checked whether the system in treatment fulfils the hypothesis of perturbation theory:

$$H = H_0 + V \tag{4.1}$$

$$H_0 \, \phi_k^{(0)} = \epsilon_k^{(0)} \, \phi_k^{(0)} , \tag{4.2}$$

with the perturbation V that must fulfil

$$\langle \phi_k \, | \, V \, | \, \phi_k \rangle \ll \epsilon_k^{(0)} \tag{4.3}$$

and

$$\langle \phi_k \, | \, V \, | \, \phi_l \rangle \ll \epsilon_k^{(0)} - \epsilon_l^{(0)} \tag{4.4}$$

for all k and l.

In figure 3.1 is shown the combined potential Coulomb and constant electric field. The perturbation is a linear term in z, and it is the dominating one asymptotically in comparison with the Coulomb one, which goes like $\frac{1}{r}$, it does not matter how small is the field. A potential which does not tend to zero asymptotically is not a perturbation, so it can not be treated in terms of perturbation theory.

In the other hand, the spectrum of the hydrogen atom under a constant electric field has also a topology absolutely different to the field-free one. The Stark atom has no bounded states, but resonances, and any real number is an eigenvalue of the Stark Hamiltonian, so we have a continuum spectrum which is the hole real line. Inside this continuum spectrum, one can find resonances, which tend to the hydrogen bounded states eigenvalues when the field intensity tends to zero. These resonances have a continuum component, so they have a certain time of live, even the ground state, and their wave functions are not square integrable.

Taking in account that, perturbation theory has critical inconsistencies when it is applied to the problem of a hydrogen atom under a constant electric field which makes its results non trustful. If we want to get proper results for energies, state widths and wave functions through perturbation theory we need to go to high order, second or third, and include states of the continuum in the perturbative series, the only way to get an imaginary part for the eigenvalues, such work requires an effort as big as using a consistent *ab initio* method, what is going to be shown in this chapter.

However the results here obtained are not going to be included in ADAS305 during present campaign, they are a good comparison with the ones obtained by semiempirical methods explained in chapters 2 and 3 and the scientific quality of the work is very high.

4.2 The complex coordinate rotation

The method is explained in detail in [50] and [51], the radial coordinate r is rotated in complex plane an angle ϑ

$$r' \;=\; r\,\mathrm{e}^{i\vartheta}\,, \tag{4.5}$$

so the Hamiltonian is transformed as follows:

$$H(\vartheta) \;=\; -\frac{\mathrm{e}^{-2i\vartheta}}{2}\,\nabla^2 \;-\; \frac{\mathrm{e}^{-i\vartheta}}{r} \;+\; \mathrm{e}^{i\vartheta}\,F\,r\,\cos\theta\,. \tag{4.6}$$

The rotated Hamiltonian 4.6 has lost the hermiticity, so its eigenvalues are now complex. The new complex type of the coordinate transform the oscillatory behaviour of the resonances in an exponential decay, making them square integrable. In general there are three types of transformation of the eigenvalues:

- Bounded states remain unchanged.
- Continuum branches are rotated an angle 2ϑ with the real axis, with origin in the threshold energy.
- Resonances are exposed in the complex plane once the rotation angle ϑ is greater then the argument of the complex root of the resonance.

Let the complex energy of the resonance be:

$$E \;=\; E_r \;-\; i\,\frac{\Gamma}{2} \;=\; |E|\,\mathrm{e}^{i\beta}\,, \tag{4.7}$$

where E_r is the position of the resonance and Γ the width. If the rotation angle ϑ is greater than the argument of the resonance β, the resonance becomes visible in the complex plane in a position independent of the rotation angle from this threshold.

We write the Hamiltonian 4.6 in parabolic coordinates:

$$H(\vartheta) \;=\; -\frac{2\,\mathrm{e}^{-2i\vartheta}}{\xi+\eta}\,\frac{\partial}{\partial\xi}\left(\xi\,\frac{\partial}{\partial\xi}\right) \;-\; \frac{2\,\mathrm{e}^{-2i\vartheta}}{\xi+\eta}\,\frac{\partial}{\partial\eta}\left(\eta\,\frac{\partial}{\partial\eta}\right) \;-\; \frac{\mathrm{e}^{-2i\vartheta}}{2\xi\eta}\,\frac{\partial^2}{\partial\varphi^2} \;-\; \frac{2\,\mathrm{e}^{-i\vartheta}}{\xi+\eta} \;+\; \frac{\mathrm{e}^{i\vartheta}}{2}\,F\,(\xi\,-\,\eta)\,, \tag{4.8}$$

and the wave function as an expansion in a basis set separating the variables

$$\Psi(\xi,\eta,\varphi) \;=\; \frac{1}{\sqrt{2\pi}}\,\mathrm{e}^{im\varphi}\,\sum_{k=1}^{N}\sum_{l=1}^{N} c_{klm}\,g_k(\xi)\,g_l(\eta)\,, \tag{4.9}$$

where $\{g_k(x)\}_{k=1}^{N}$ are basis set functions.

Then we can obtain the matrix elements of the Hamiltonian in terms of the proposed basis set as follows:

$$\begin{aligned}
H_{klk'l'm}(\vartheta) \;&=\; \langle g_k\,g_l\,|\,H(\vartheta)\,|\,g_{k'}\,g_{l'}\,\rangle \\
&=\; \int_0^\infty \mathrm{d}\xi \int_0^\infty \mathrm{d}\eta\,\frac{1}{4}\,(\xi\,+\,\eta)\,g_k^*(\xi)\,g_l^*(\eta)\,H(\vartheta)\,g_k(\xi)\,g_l(\eta) \\
&=\; \int_0^\infty \mathrm{d}\xi \int_0^\infty \mathrm{d}\eta\,g_k^*(\xi)\,g_l^*(\eta)\left[-\frac{\mathrm{e}^{-2i\vartheta}}{2}\,\frac{\partial}{\partial\xi}\left(\xi\,\frac{\partial}{\partial\xi}\right) \;-\; \frac{\mathrm{e}^{-2i\vartheta}}{2}\,\frac{\partial}{\partial\eta}\left(\eta\,\frac{\partial}{\partial\eta}\right) \;+\; \frac{\mathrm{e}^{-2i\vartheta}\,m^2}{8}\left(\frac{1}{\xi}\,+\,\frac{1}{\eta}\right)\right. \\
&\quad \left. -\,\frac{\mathrm{e}^{-i\vartheta}}{2} \;+\; \frac{\mathrm{e}^{i\vartheta}}{8}\,F\,(\xi^2\,-\,\eta^2)\right]\,g_k(\xi)\,g_l(\eta)\,,
\end{aligned} \tag{4.10}$$

and the overlaps:

$$\begin{aligned}
S_{klk'l'm} \;&=\; \langle g_k\,g_l\,|\,g_{k'}\,g_{l'}\,\rangle \\
&=\; \int_0^\infty \mathrm{d}\xi \int_0^\infty \mathrm{d}\eta\,\frac{1}{4}\,(\xi\,+\,\eta)\,g_k^*(\xi)\,g_l^*(\eta)\,g_{k'}(\xi)\,g_{l'}(\eta)\,,
\end{aligned} \tag{4.11}$$

where the variable φ has been already integrated. In equation 4.10, the term in m^2 becomes singular in $\xi, \eta = 0$ if the basis functions have not an appropriate behaviour, and it can lead to numerical instabilities, this can be fixed making the transformation

$$g_k(x) \;=\; x^{\frac{|m|}{2}}\, f_k(x)\,, \tag{4.12}$$

so the Hamiltonian matrix results in terms of f:

$$\begin{aligned} H_{klk'l'm}(\vartheta) \;=\; & \int_0^\infty \mathrm{d}\xi \int_0^\infty \mathrm{d}\eta\, \xi^{|m|}\, \eta^{|m|}\, f_k^*(\xi)\, f_l^*(\eta) \left[-\frac{\mathrm{e}^{-2i\vartheta}}{2} \left(\xi\, \frac{\mathrm{d}^2 f_{k'}(\xi)}{\mathrm{d}\xi^2}\, f_{l'}(\eta) \;+\; \eta\, f_{k'}(\xi)\, \frac{\mathrm{d}^2 f_{l'}(\eta)}{\mathrm{d}\eta^2} \right.\right. \\ & \left. + (|m| \;+\; 1)\, \frac{\mathrm{d} f_{k'}(\xi)}{\mathrm{d}\xi}\, f_{l'}(\eta) \;+\; (|m| \;+\; 1)\, f_{k'}(\xi)\, \frac{\mathrm{d} f_{l'}(\eta)}{\mathrm{d}\eta} \right) \\ & \left. + \left(-\frac{\mathrm{e}^{-i\vartheta}}{2} \;+\; \frac{\mathrm{e}^{i\vartheta}}{8}\, F\, (\xi^2 \;-\; \eta^2) \right) f_{k'}(\xi)\, f_{l'}(\eta) \right] \end{aligned} \tag{4.13}$$

and the overlaps:

$$S_{klk'l'm} \;=\; \int_0^\infty \mathrm{d}\xi \int_0^\infty \mathrm{d}\eta\, \frac{1}{4}\, (\xi \;+\; \eta)\, \xi^{|m|}\, \eta^{|m|}\, f_k^*(\xi)\, f_l^*(\eta)\, f_{k'}(\xi)\, f_{l'}(\eta)\,, \tag{4.14}$$

remaining all the terms now regular.

Operating the expression for Hamiltonian and overlap matrixes 4.13 and 4.14 they are simplified splitting the double integrals as follows:

$$H_{klk'l'm}(\vartheta) \;=\; -\,\frac{\mathrm{e}^{-2i\vartheta}}{2}\, (\mathcal{T}_{kk'}\, \mathcal{I}_{ll'} \;+\; \mathcal{I}_{kk'}\, \mathcal{T}_{ll'}) \;-\; \frac{\mathrm{e}^{-i\vartheta}}{2}\, \mathcal{I}_{kk'}\, \mathcal{I}_{ll'} \;+\; \frac{\mathrm{e}^{i\vartheta}}{8}\, F\, (\mathcal{F}_{kk'}\, \mathcal{I}_{ll'} \;-\; \mathcal{I}_{kk'}\, \mathcal{F}_{ll'}) \tag{4.15}$$

and

$$S_{klk'l'm} \;=\; \frac{1}{4}\, (\mathcal{S}_{kk'}\, \mathcal{I}_{ll'} \;+\; \mathcal{I}_{kk'}\, \mathcal{S}_{ll'}) \tag{4.16}$$

where we have defined the matrix of the single integrals

$$\begin{aligned} \mathcal{T}_{kk'} \;&=\; \int_0^\infty \mathrm{d}x\, x^{|m|}\, f_k^*(x) \left[x\, \frac{\mathrm{d}^2}{\mathrm{d}x^2} \;+\; (|m| \;+\; 1)\, \frac{\mathrm{d}}{\mathrm{d}x} \right] f_{k'}(x) \\ \mathcal{I}_{kk'} \;&=\; \int_0^\infty \mathrm{d}x\, x^{|m|}\, f_k^*(x)\, f_{k'}(x) \\ \mathcal{F}_{kk'} \;&=\; \int_0^\infty \mathrm{d}x\, x^{|m|+2}\, f_k^*(x)\, f_{k'}(x) \\ \mathcal{S}_{kk'} \;&=\; \int_0^\infty \mathrm{d}x\, x^{|m|+1}\, f_k^*(x)\, f_{k'}(x)\,. \end{aligned} \tag{4.17}$$

Then we can determine the coefficients of the expansion solving the secular equation

$$(\mathbf{H} \;-\; \mathbf{E}\,\mathbf{S})\,\mathbf{C} \;=\; 0 \tag{4.18}$$

4.3 The choose of a basis set

In [52] it is used a basis set of Laguerre-mesh functions $\{f_i\}_{i=1}^N$, defined as follows [53]:

$$f_i(x) \;=\; (-1)^i\, \sqrt{x_i}\, \frac{\mathrm{L}_N(x)\, \mathrm{e}^{-\frac{x}{2}}}{x \;-\; x_i}\,, \tag{4.19}$$

where $\mathrm{L}_N(x)$ is the Laguerre polynomial of grad N, and x_i is its i-th zero. The efficiency and stability of this basis set for hydrogen atom problems was analysed by Vinke and collaborators 1993 in [54].

In Baye and Heenen 1986 [53] it is made the algebra with rigorous proving of the properties of a Lagrange-mesh basis set. The functions must fulfil two properties:

$$f_i(x_j) \;=\; \lambda_i^{-\frac{1}{2}}\, \delta_{ij}\,, \tag{4.20}$$

and

$$\int_a^b \mathrm{d}x\, f_i(x)\, f_j(x) \;=\; \delta_{ij}\,. \tag{4.21}$$

Then the integral of any function can be with a good accuracy approximated by the Gauss quadrature formula

$$\int_a^b \mathrm{d}x\, g(x) \;\approx\; \sum_{i=1}^{N} \lambda_i\, g(x_i)\,. \tag{4.22}$$

This method allows us to calculate the integrals involved in the variational method by a very fast way with quite good accuracy.

The quotient $\frac{\mathrm{L}_N(x)}{x-x_i}$ has an avoidable singularity in $x = x_i$, and it is a polynomial of grad $N-1$ in the hole complex plane except this singularity. Even when the basis functions are changed just in the point of this avoidable singularity all of them become analytical, this singularity can lead to computational problems in its neighbourhood, which can slow considerably the calculations and even crush them. To avoid this singularity we expand the Laguerre polynomials in its Taylor series centered in it as follows:

$$\mathrm{L}_N(x) \;=\; \sum_{j=0}^{N} \frac{1}{j!}\, \frac{\mathrm{d}^j \mathrm{L}_N(x)}{\mathrm{d}x^j}\bigg|_{x=x_i} (x - x_i)^j\,. \tag{4.23}$$

As x_i is by definition a zero of the Laguerre polynomial, the zero order term of 4.23 cancels, we also use the derivative property of the Laguerre polynomials

$$\frac{\mathrm{d}^j}{\mathrm{d}x^j}\mathrm{L}_N^{\alpha}(x) \;=\; (-1)^j\, \mathrm{L}_{N-j}^{\alpha+j}(x)\,. \tag{4.24}$$

We define the Laguerre-mesh polynomials Λ_{Ni} as

$$\Lambda_{Ni}(x) \;=\; (-1)^i\, \sqrt{x_i}\, \frac{\mathrm{L}_N(x)}{x - x_i}\,, \tag{4.25}$$

and introducing 4.23 and 4.24 in 4.25 we get a closed expression for $\Lambda_{Ni}(x)$ as follows:

$$\Lambda_{Ni}(x) \;=\; (-1)^i\, \sqrt{x_i} \sum_{j=0}^{N-1} \frac{(-1)^{j+1}}{(j+1)!}\, \mathrm{L}_{N-j-1}^{j+1}(x_i)\, (x - x_i)^j\,. \tag{4.26}$$

Comparing with the property 4.20 we obtain the value of the weights λ_i as

$$\lambda_i \;=\; \frac{\mathrm{e}^{x_i}}{x_i\, (\mathrm{L}_{N-1}^{1}(x_i))^2}\,, \tag{4.27}$$

and the property 4.21 can be proved through the properties of the Laguerre generalised polynomials, in the interval $(a, b) \equiv (0, +\infty)$ of the real line.

For calculations, it is useful to know the expressions of the first and second derivatives of $\Lambda_{Ni}(x)$ too, which can be easily calculated from expansion 4.26:

$$\begin{aligned} \Lambda'_{Ni}(x) \;&=\; (-1)^{i+1}\, \sqrt{x_i} \left[\frac{\mathrm{L}_{N-1}^{1}(x)}{x - x_i} \;+\; \frac{\mathrm{L}_N(x)}{(x - x_i)^2} \right] \\ &=\; (-1)^i\, \sqrt{x_i} \sum_{j=0}^{N-2} \frac{(-1)^j\, (j+1)}{(j+2)!}\, \mathrm{L}_{N-j-2}^{j+2}(x_i)\, (x - x_i)^j\,, \end{aligned} \tag{4.28}$$

$$\begin{aligned} \Lambda''_{Ni}(x) \;&=\; (-1)^i\, \sqrt{x_i} \left[\frac{\mathrm{L}_{N-2}^{2}(x)}{x - x_i} \;+\; 2\, \frac{\mathrm{L}_{N-1}^{1}(x)}{(x - x_i)^2} \;+\; 2\, \frac{\mathrm{L}_N(x)}{(x - x_i)^3} \right] \\ &=\; (-1)^i\, \sqrt{x_i} \sum_{j=0}^{N-3} \frac{(-1)^{j+1}\, (j+1)\, (j+2)}{(j+3)!}\, \mathrm{L}_{N-j-3}^{j+3}(x_i)\, (x - x_i)^j\,, \end{aligned} \tag{4.29}$$

so the kinetic term of 4.17 is expressed as

$$\mathcal{T}_{kk'} = \int_0^\infty \mathrm{d}x\, x^{|m|}\, \mathrm{e}^{-x}\, \Lambda_{Nk}(x) \left[x\, \Lambda''_{Nk'}(x) + (|m| + 1 - x)\, \Lambda'_{Nk'}(x) + \left(\frac{1}{4} x - \frac{1}{2}|m| - \frac{1}{2} \right) \Lambda_{Nk'}(x) \right], \tag{4.30}$$

and the others

$$\begin{aligned} \mathcal{I}_{kk'} &= \int_0^\infty \mathrm{d}x\, x^{|m|}\, \mathrm{e}^{-x}\, \Lambda_{Nk}(x)\, \Lambda_{Nk'}(x) \\ \mathcal{F}_{kk'} &= \int_0^\infty \mathrm{d}x\, x^{|m|+2}\, \mathrm{e}^{-x}\, \Lambda_{Nk}(x)\, \Lambda_{Nk'}(x) \\ \mathcal{S}_{kk'} &= \int_0^\infty \mathrm{d}x\, x^{|m|+1}\, \mathrm{e}^{-x}\, \Lambda_{Nk}(x)\, \Lambda_{Nk'}(x) \end{aligned} \tag{4.31}$$

To calculate the matrix elements it is necessary to get the roots of the Laguerre polynomials as accurate as possible, to do that we took advantage of the property of the roots of the Laguerre polynomials, that all of them are real, positive and of multiplicity one. We made a search on the positive real line starting at zero and increasing the step in 10^{-3} units, when we found two points x_1 and x_2 such as $\mathrm{L}(x_1)\mathrm{L}(x_2) < 0$ then we have a root in between, then we applied a bisection method with precision 10^{-12} and obtained the root. To evaluate the Laguerre polynomial we used the recursive formula

$$\begin{aligned} \mathrm{L}_0(x) &= 1 \\ \mathrm{L}_1(x) &= 1 - x \\ N\,\mathrm{L}_N(x) &= (2N - 1 - x)\,\mathrm{L}_{N-1}(x) - (N - 1)\,\mathrm{L}_{N-2}(x)\,. \end{aligned} \tag{4.32}$$

The calculated roots of the Laguerre polynomials are shown in appendix B.

Now we will check the stability of the calculation respect the accuracy of the roots of the Laguerre polynomials, for that goal we make an error analysis of expression 4.25 of Laguerre-mesh polynomials

$$\delta\Lambda_{Ni} = \left(\sqrt{x_i}\, \frac{|\mathrm{L}_N|}{(x - x_i)^2} + \frac{1}{2\sqrt{x_i}} \left| \frac{\mathrm{L}_N}{x - x_i} \right| \right) \delta x_i\,, \tag{4.33}$$

and the expression 4.26 of its Taylor expansion

$$\delta\Lambda_{Ni} = \left(\sqrt{x_i} \sum_{j=0}^{N-2} \frac{(j+1)}{(j+2)!}\, |\mathrm{L}^{j+2}_{N-j-2}(x_i)|\, |x - x_i|^j + \frac{1}{2\sqrt{x_i}} \sum_{j=0}^{N-1} \frac{1}{(j+1)!}\, |\mathrm{L}^{j+1}_{N-j-1}(x_i)|\, |x - x_i|^j \right) \delta x_i\,. \tag{4.34}$$

The error in direct expression 4.25 is proportional to the relation $\frac{1}{(x-x_i)^2}$, so it is large in the neighbourhood of the singularity, and even diverge on it. On the other hand, the error of the Taylor expansion 4.26 is proportional to a power of $(x - x_i)$, it tends to constant in the neighbourhood of the singularity and it blows up as x spreads of it. So we have two complementary regions and to optimise the calculation we choose for the evaluation of the Laguerre-mesh polynomials the direct expression 4.25 in the region far of the singularity $x < x_{i-1}$; $x > x_{i+1}$, and the Taylor expansion 4.26 in its neighbourhood $x_{i-1} \le x \le x_{i+1}$, for the extremes we take as $x_0 = 0$ and $x_{N+1} = 2x_N - x_{N-1}$. For the expressions of the derivatives the argument is equivalent.

4.4 Implementation

The implementation of the complex coordinate rotation method to get the states of the Stark hydrogen atom is spread in two steps: the calculation of the integrals 4.30 and 4.31 and the diagonalisation of the Hamiltonian matrix 4.15.

In the first step we calculate the ground $N \times N$ matrices of the integrals $\mathcal{T}_{kk'}$, $\mathcal{I}_{kk'}$, $\mathcal{F}_{kk'}$ and $\mathcal{S}_{kk'}$ for each value of the magnetic quantum number m, and they are now usable for any value of the field intensity F and the complex rotation angle ϑ, so this step takes a few computation time in comparison with the diagonalisation. In that sense it is valuable to increase the quality of the calculation of the integrals even at a cost of increasing the computation time, so

we did not use the Gauss quadrature formula, but a complete numerical integration for each element, using a variable step Simpson formula. This is made by the routine *starkinteg*, it calculates the four ground matrices and stores them in a binary file, prepared to be read by the next routine.

In a second step we build the Hamiltonian and overlap matrices and solve the secular equation to get the eigenvalues and eigenfunctions. This is made by the routine *starkccr*.

Firstly the matrixes $H_{klk'l'}$ and $S_{klk'l'}$ of dimension $N^2 \times N^2$ are built making the tensorial products 4.15 and 4.16 respectively, for a fixed value of the field intensity F and the rotation angle ϑ. Afterwards it is solved the diagonalisation using the computing library Linear Algebra PACKage (LAPACK), we chose the subroutine for solving a secular equation of a general non-Hermitian double precision complex matrix *zggev*.

We solved the eigenvalue problem varying the electric field intensity F from zero to 0.01 a.u. = 5.142×10^9 V/m and for each one the complex rotation angle ϑ between zero and 40^0.

4.5 Results

We used a basis set of Laguerre-mesh polynomials with $N = 30$, which corresponds to 900 basis functions, thereby obtained acceptably accurate results for all the resonances with principal quantum number $n \leq 5$ and for the values of the magnetic quantum number $m = 0 - 4$. We varied the field intensity from zero to 0.01 a.u., which corresponds to $5.142 \cdot 10^9$ V/m. The resonances above $n \geq 6$ are strongly mixed with the continuum. To isolate these ones, the basis set should be increased.

4.5.1 Energies and state widths for the Stark Hydrogen Atom

Applying the complex coordinate method one has to change the value of the complex rotation angle ϑ in order to distinguish the resonances of the continuum states sea. In figures 4.1 and 4.2 it is showed respectively the real and imaginary part of the obtained roots versus the complex rotation angle, then the behaviour of the roots is appreciated. Most states change their value with the angle, they can be recognised as continuum states, but there are some of them which remain constant since a value of the angle, in terms of the complex coordinate rotation theorem, these states are identified as the resonances. The constant values, when the lines become flat, are related to the energy (real part) and width (imaginary part) of the resonance. Also for these constant values, the wave function of the resonance becomes invariant but phase and square integrable.

Identifying the resonances as in Fig **??** for several values of F and m we get the diagram of energies and widths. In Fig 4.3 we show the identified energies for the shells $n = 2 - 5$ of the hydrogen atom under a constant electric field versus the field intensity. The behaviour for the upper shells $n = 3 - 5$ deviate from the linearity predicted by perturbation theory. In Fig 4.4 the widths for the same shells are shown. The value of the widths increases quite rapidly with the field, so the states become more unstable and the autoionization term should be taken in account in collision radiative models.

4.5.2 Wave functions

The great advantage of complex coordinate rotation method is that we can obtain the wave functions exactly in terms of the precision of our chosen basis set. With the variational method, the wave functions of the identified states are obtained as a linear combination of the basis functions.

In figures 4.5 – 4.14 the wave functions for several states of the Stark Hydrogen Atom are shown for a value of the electric field intensity of 0.0020 a.u. as a colour map versus the two parabolic coordinates ξ and η. We can obtain

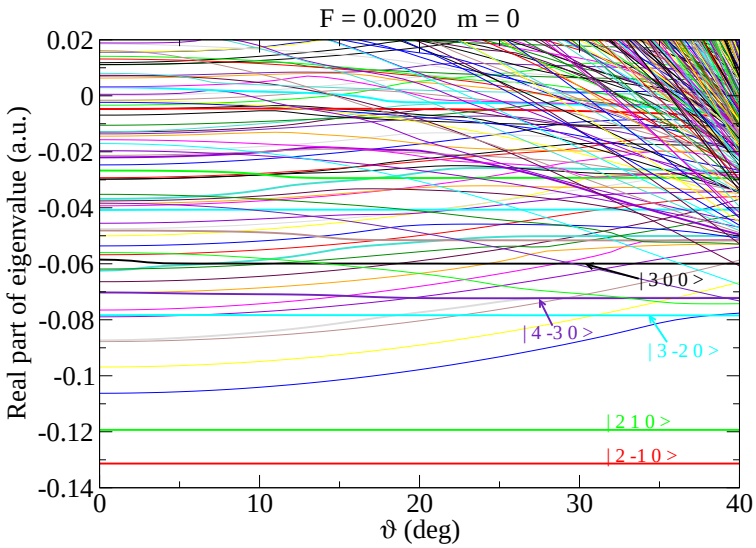

Figure 4.1: Real part of the calculated eigenvalues for the Hydrogen atom under a constant electric field versus the complex coordinate rotation angle.

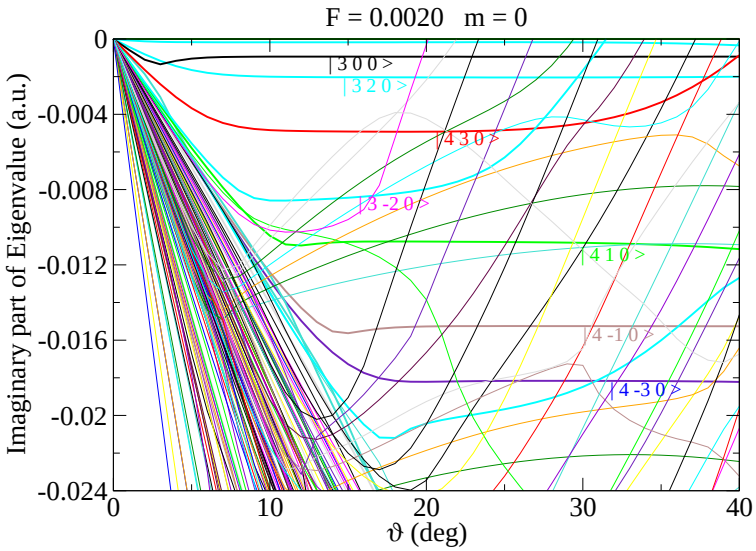

Figure 4.2: Imaginary part of the calculated eigenvalues for the Hydrogen atom under a constant electric field versus the complex coordinate rotation angle.

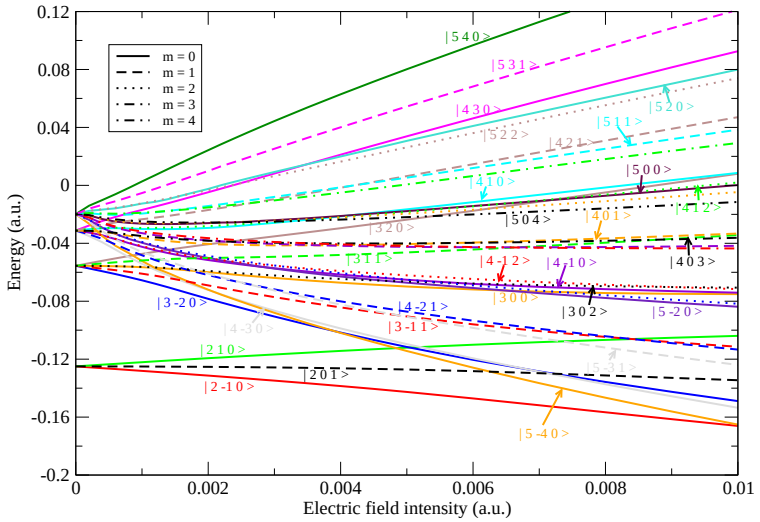

Figure 4.3: Energies of the first resonances of the Hydrogen atom under a constant electric field versus the intensity of such field.

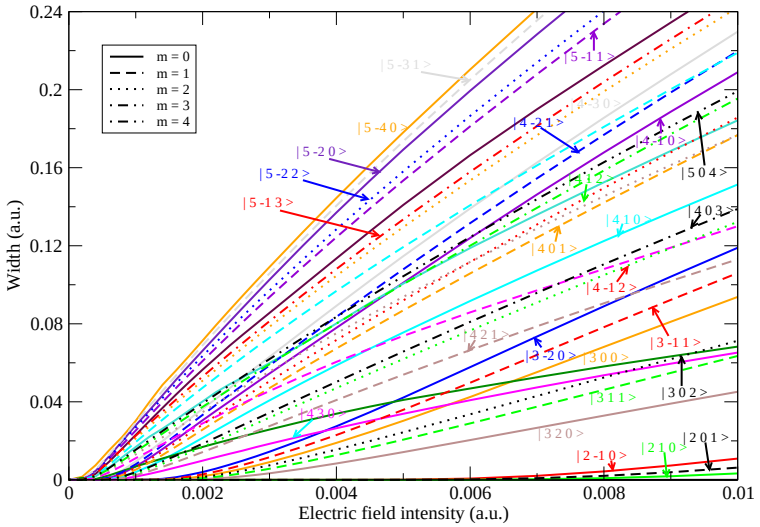

Figure 4.4: State widths of the first resonances of the Hydrogen atom under a constant electric field versus the intensity of such field.

partially integrated wave functions through the integration of them in one of the parabolic variables

$$\begin{aligned} \psi_\xi(\xi) &= \int_0^\infty \mathrm{d}\eta\, \psi(\xi,\eta) \\ \psi_\eta(\eta) &= \int_0^\infty \mathrm{d}\xi\, \psi(\xi,\eta)\,, \end{aligned} \tag{4.35}$$

If we compare the result with the zero field case 2.32, then we can relation the approximated quantum numbers $\tilde{n}_1$, $\tilde{n}_2$ with the minimum of the module of the partially integrated wave functions, which will tend to a node in the limit when the field intensity tends to zero. These wave functions contain the whole information about the system.

A surprising result is that for a constant value of n, the energies increase as k increases, but the widths decrease, so in the same shell states with a higher energy and closer to the ionization limit live longer before ionizing. That can be explained from examination of the wave functions.

Comparing the wave functions for the states $|\,\tilde{n}\,\tilde{k}\,m\rangle$ and $|\,\tilde{n}\;-\tilde{k}\,m\rangle$ we observe that for negative $\tilde{k}$ the partially integrated $|\psi_\eta|^2$ function encloses a larger area beneath it than the other one $|\psi_\xi|^2$. In addition almost the whole probability lies close to $\xi = 0$, so in the case of $\tilde{k} < 0$ the wave function lies on the η axis and $\xi \approx 0$, which corresponds to the negative z semiaxis. In our case $F > 0$, the potential barrier is placed on the negative z axis side with a monotonic increase in the positive z direction. So the main part of the probability lies above the potential barrier for $\tilde{k} < 0$ such that the probability to tunnel through it will be higher. Therefore the widths increase. Just the opposite holds for $\tilde{k} > 0$. In this case the highest probability concentration is in the region $\eta \approx 0$, $\xi > 0$, which corresponds to the positive z semiaxis. Thus with the potential monotonic slope, the main probability for finding the electron is where the potential barrier is wide and the probability to tunnel is much lower. To understand the behaviour of the state widths, it is clear that one has to look not only the energies, but also at the wave functions of the states.

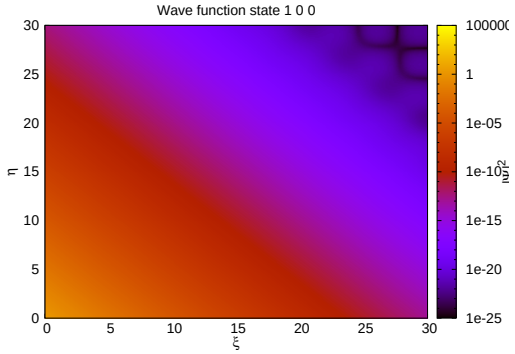

(a) $|\psi_{100}|^2(\xi,\eta)$

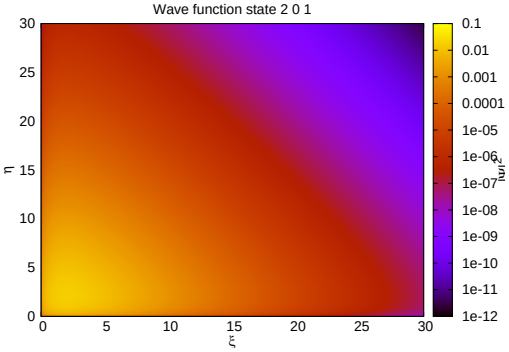

(d) $|\psi_{201}|^2(\xi,\eta)$

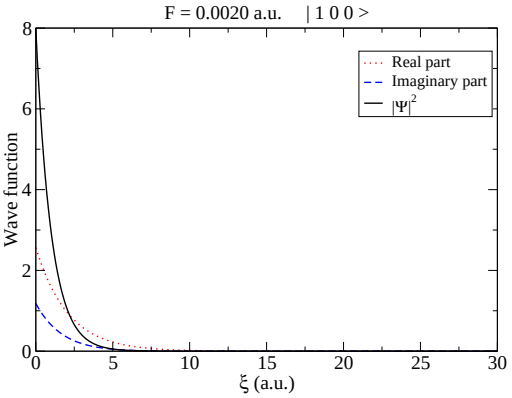

(b) $\psi_{\xi 100}(\xi)$

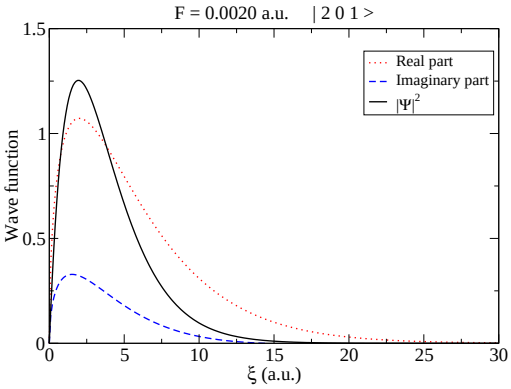

(e) $\psi_{\xi 201}(\xi)$

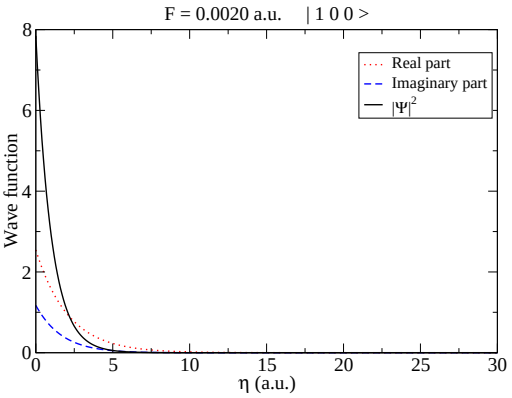

(c) $\psi_{\eta 100}(\eta)$

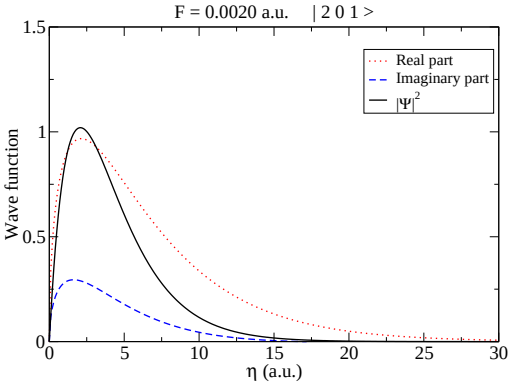

(f) $\psi_{\eta 201}(\eta)$

Figure 4.5: Wave function of the Stark states $|\,1\,0\,0\,\rangle$ and $|\,2\,0\,1\,\rangle$ for a field intensity of $F = 0.0020$ a.u..

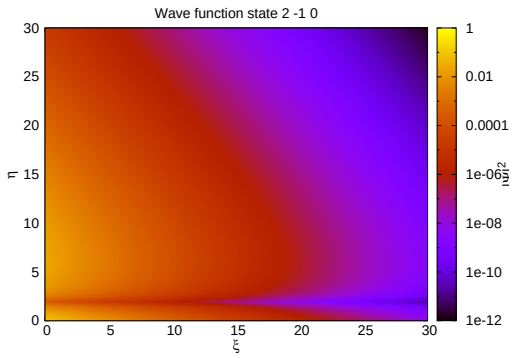

(a) $|\psi_{2-10}|^2(\xi,\eta)$

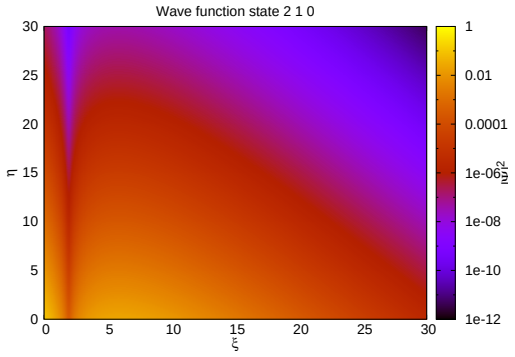

(d) $|\psi_{210}|^2(\xi,\eta)$

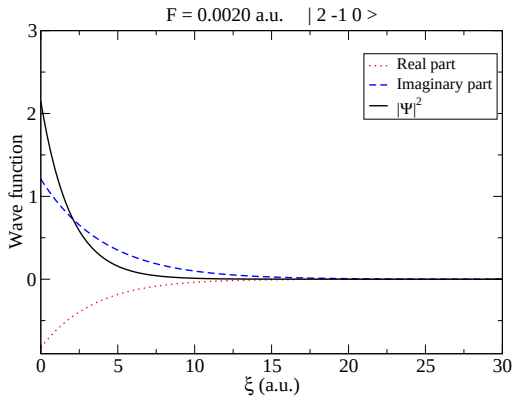

(b) $\psi_{\xi 2-10}(\xi)$

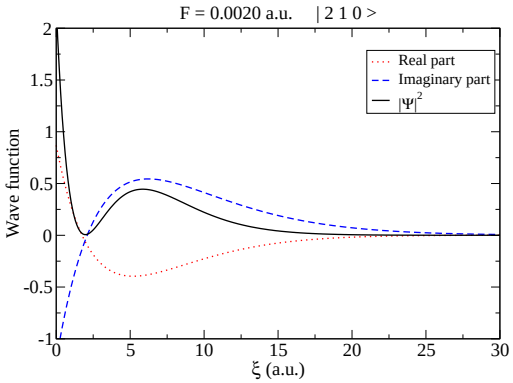

(e) $\psi_{\xi 210}(\xi)$

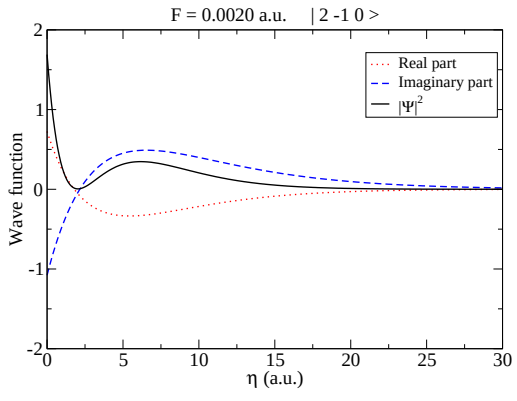

(c) $\psi_{\eta 2-10}(\eta)$

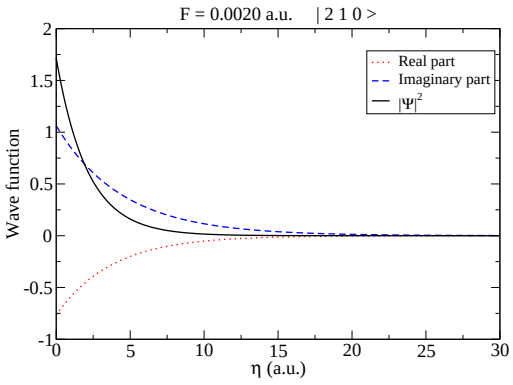

(f) $\psi_{\eta 210}(\eta)$

Figure 4.6: Wave function of the Stark states $|\,2\ -1\,0\,\rangle$ and $|\,2\,1\,0\,\rangle$ for a field intensity of $F = 0.0020$ a.u..

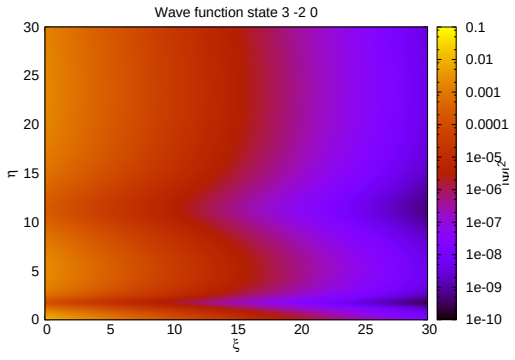

(a) $|\psi_{3-20}|^2(\xi,\eta)$

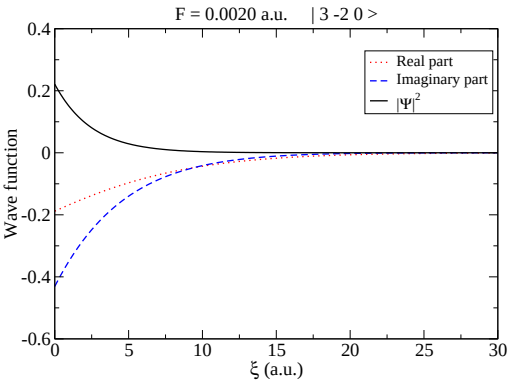

(b) $\psi_{\xi 3-20}(\xi)$

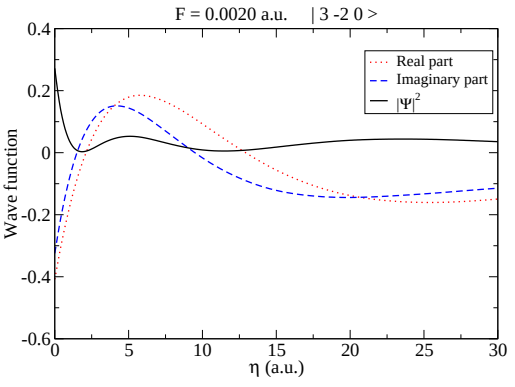

(c) $\psi_{\eta 3-20}(\eta)$

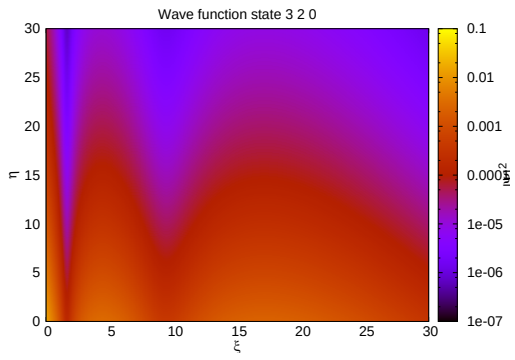

(d) $|\psi_{320}|^2(\xi,\eta)$

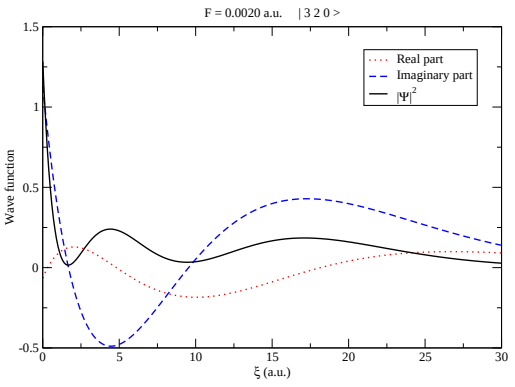

(e) $\psi_{\xi 320}(\xi)$

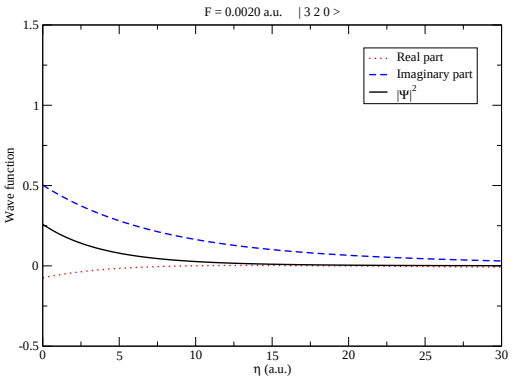

(f) $\psi_{\eta 320}(\eta)$

Figure 4.7: Wave function of the Stark states $|3\ -2\ 0\rangle$ and $|3\ 2\ 0\rangle$ for a field intensity of $F = 0.0020$ a.u..

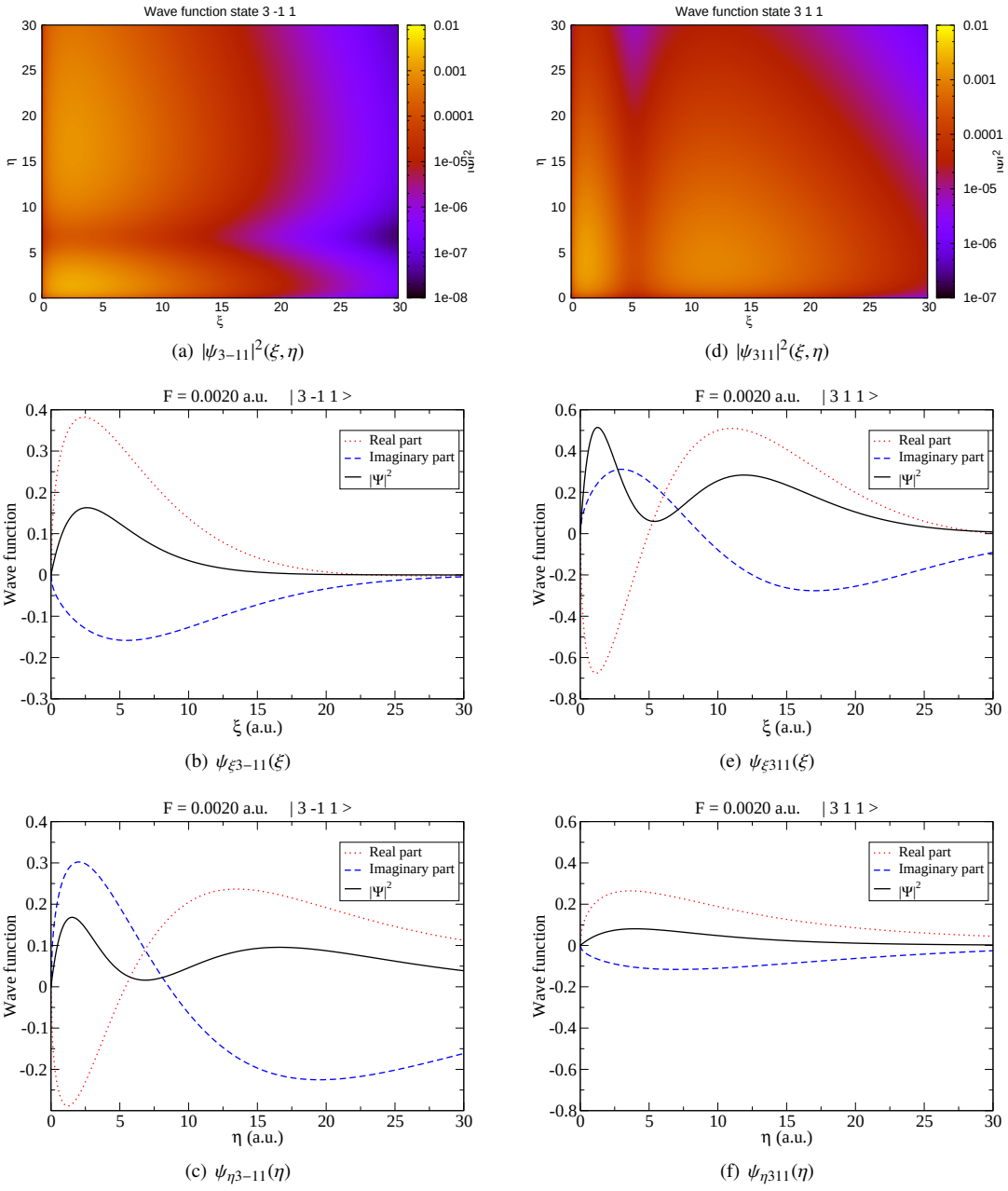

(a) $|\psi_{3-11}|^2(\xi,\eta)$ (d) $|\psi_{311}|^2(\xi,\eta)$

(b) $\psi_{\xi 3-11}(\xi)$ (e) $\psi_{\xi 311}(\xi)$

(c) $\psi_{\eta 3-11}(\eta)$ (f) $\psi_{\eta 311}(\eta)$

Figure 4.8: Wave function of the Stark states $|\,3\ -1\ 1\,\rangle$ and $|\,3\ 1\ 1\,\rangle$ for a field intensity of $F = 0.0020$ a.u..

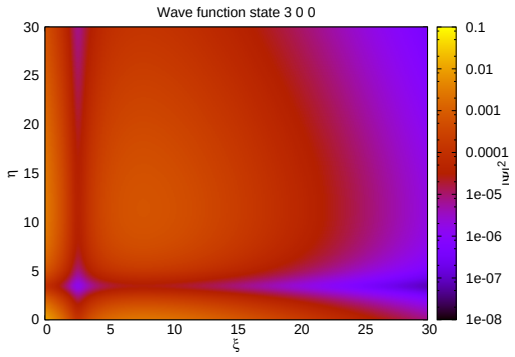

(a) $|\psi_{300}|^2(\xi,\eta)$

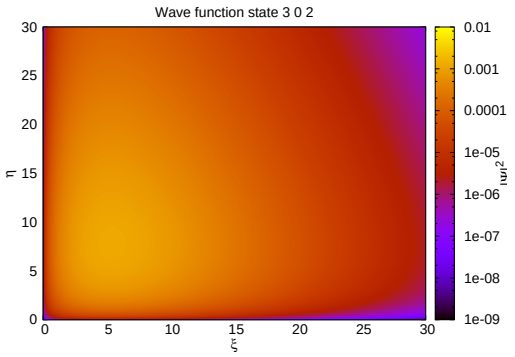

(d) $|\psi_{302}|^2(\xi,\eta)$

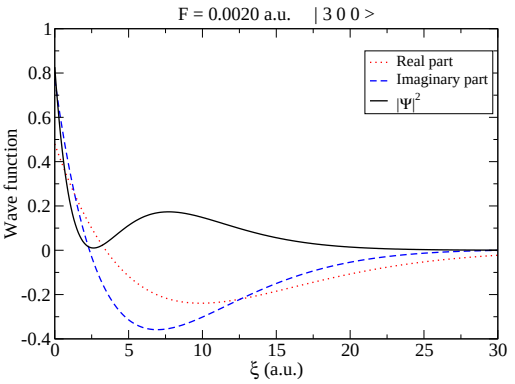

(b) $\psi_{\xi 300}(\xi)$

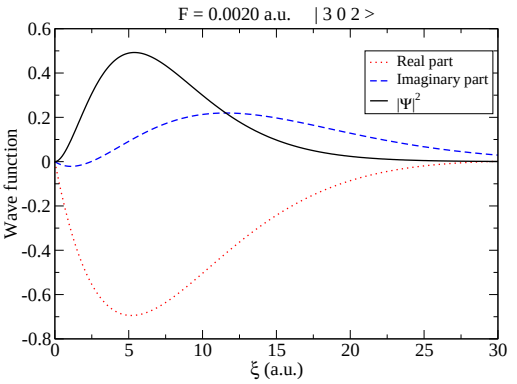

(e) $\psi_{\xi 302}(\xi)$

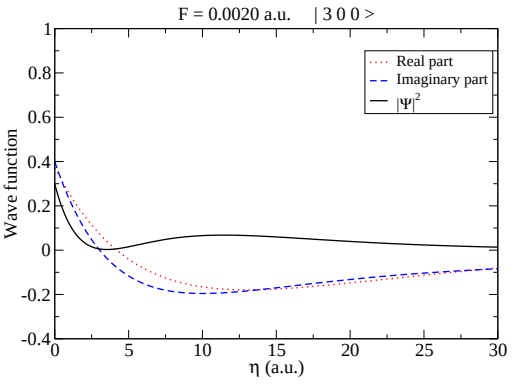

(c) $\psi_{\eta 300}(\eta)$

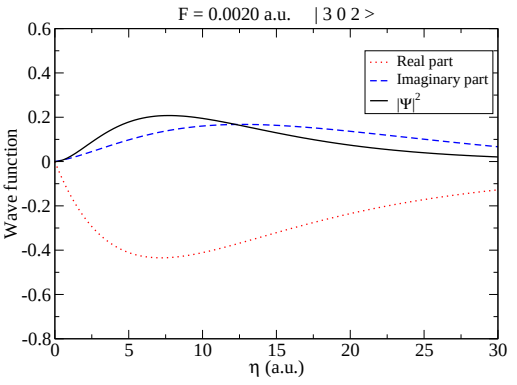

(f) $\psi_{\eta 302}(\eta)$

Figure 4.9: Wave function of the Stark states $|\,3\,0\,0\,\rangle$ and $|\,3\,0\,2\,\rangle$ for a field intensity of $F = 0.0020$ a.u..

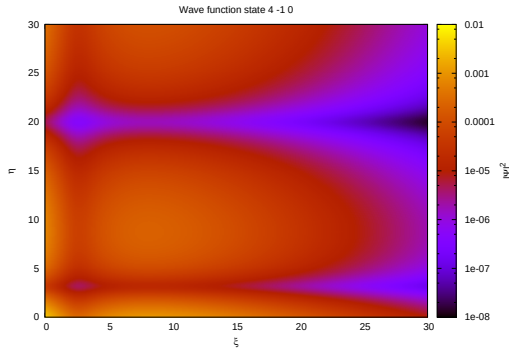

(a) $|\psi_{4-10}|^2(\xi,\eta)$

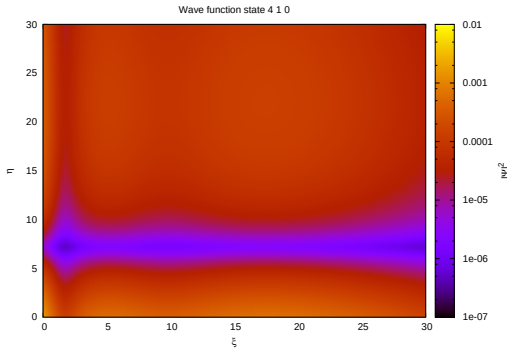

(d) $|\psi_{410}|^2(\xi,\eta)$

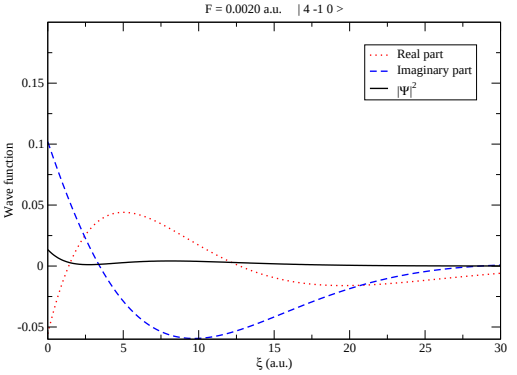

(b) $\psi_{\xi 4-10}(\xi)$

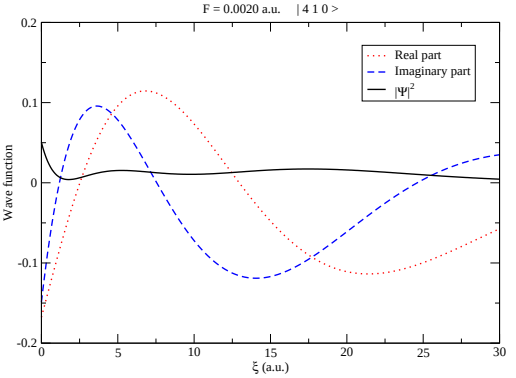

(e) $\psi_{\xi 410}(\xi)$

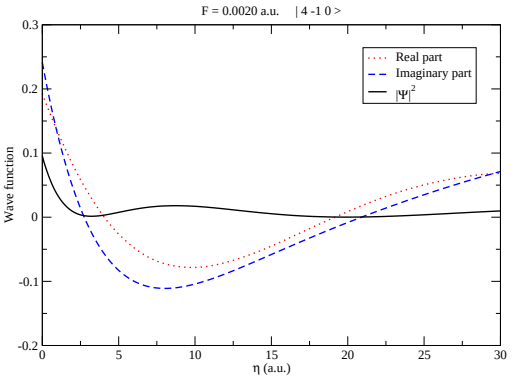

(c) $\psi_{\eta 4-10}(\eta)$

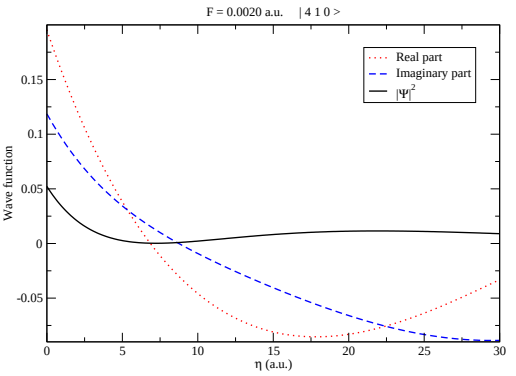

(f) $\psi_{\eta 410}(\eta)$

Figure 4.10: Wave function of the Stark states $|4\ -1\ 0\rangle$ and $|4\ 1\ 0\rangle$ for a field intensity of $F = 0.0020$ a.u..

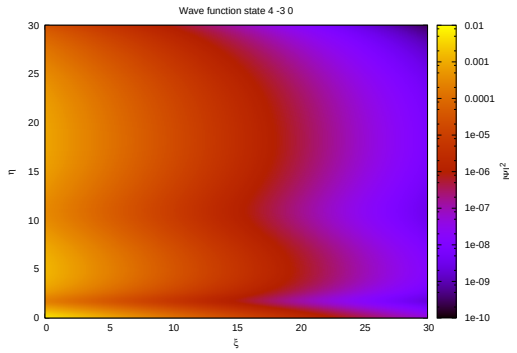

(a) $|\psi_{4-30}|^2(\xi,\eta)$

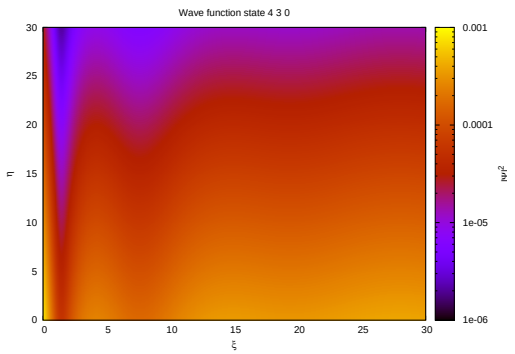

(d) $|\psi_{430}|^2(\xi,\eta)$

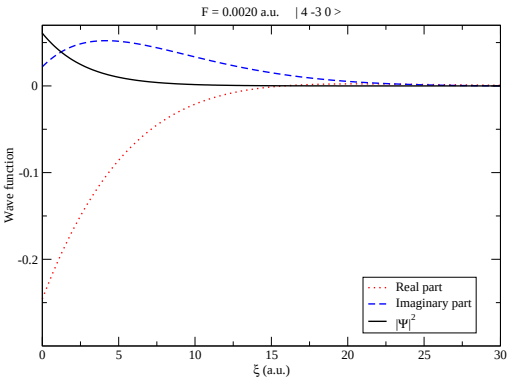

(b) $\psi_{\xi 4-30}(\xi)$

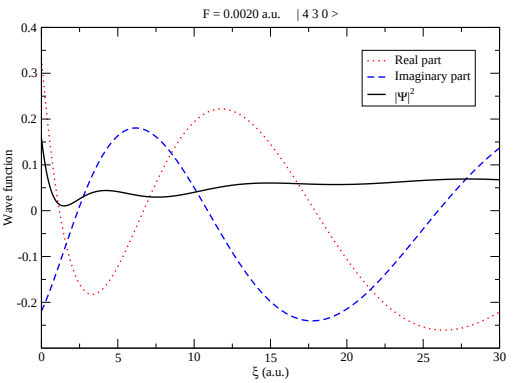

(e) $\psi_{\xi 430}(\xi)$

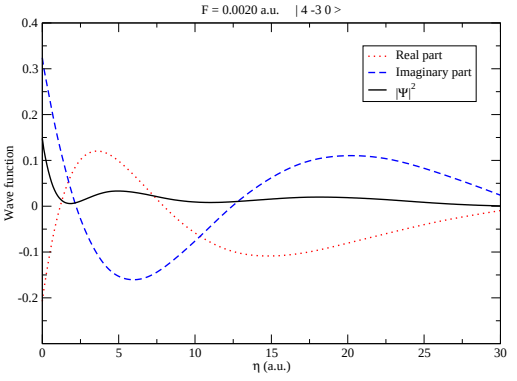

(c) $\psi_{\eta 4-30}(\eta)$

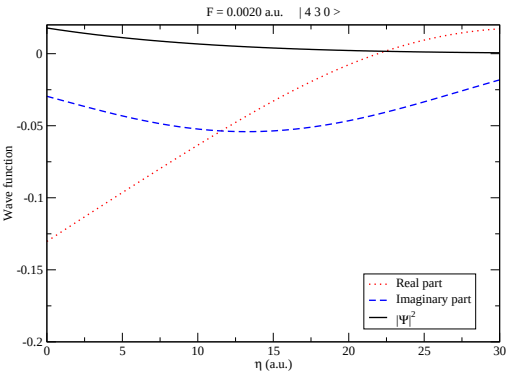

(f) $\psi_{\eta 430}(\eta)$

Figure 4.11: Wave function of the Stark states $|4\ -3\,0\rangle$ and $|4\,3\,0\rangle$ for a field intensity of $F = 0.0020$ a.u..

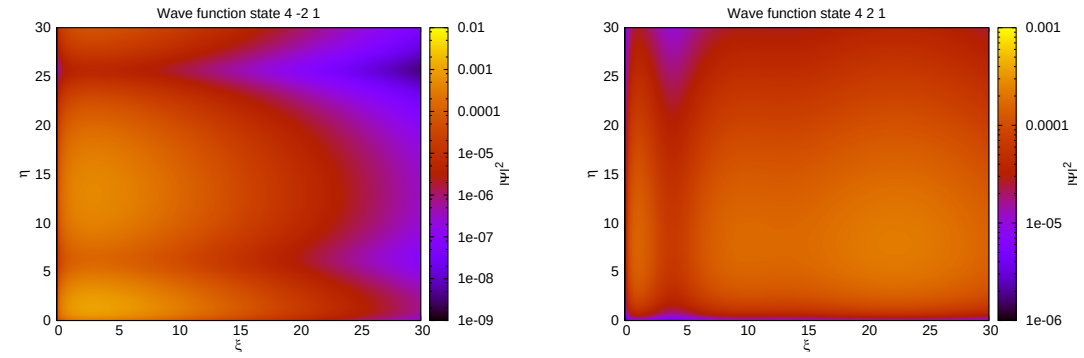

(a) $|\psi_{4-21}|^2(\xi,\eta)$

(d) $|\psi_{421}|^2(\xi,\eta)$

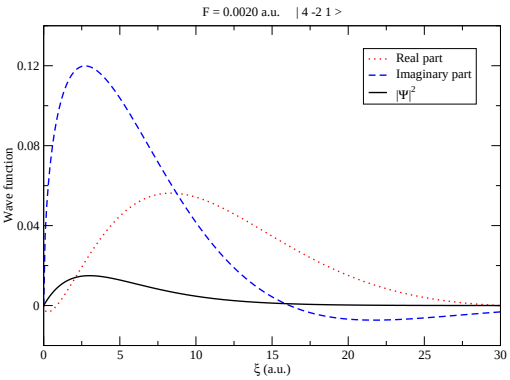

(b) $\psi_{\xi 4-21}(\xi)$

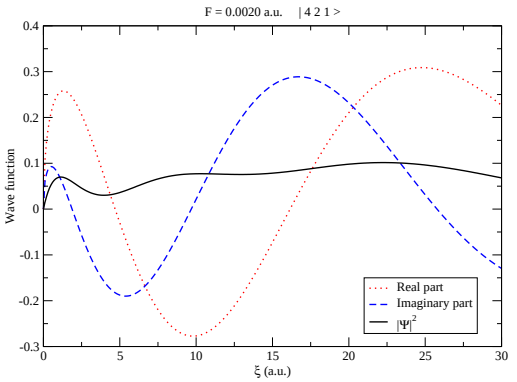

(e) $\psi_{\xi 421}(\xi)$

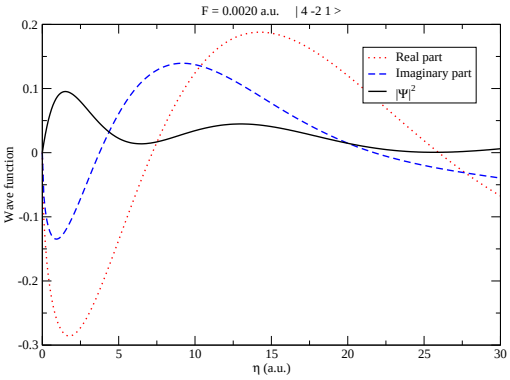

(c) $\psi_{\eta 4-21}(\eta)$

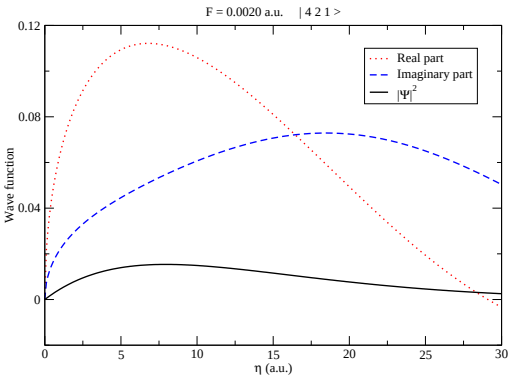

(f) $\psi_{\eta 421}(\eta)$

Figure 4.12: Wave function of the Stark states $|4\ -2\ 1\rangle$ and $|4\ 2\ 1\rangle$ for a field intensity of $F = 0.0020$ a.u..

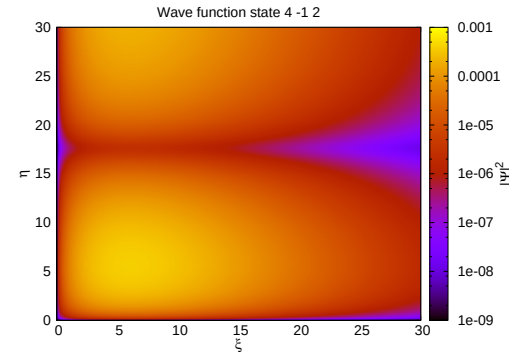

(a) $|\psi_{4-12}|^2(\xi,\eta)$

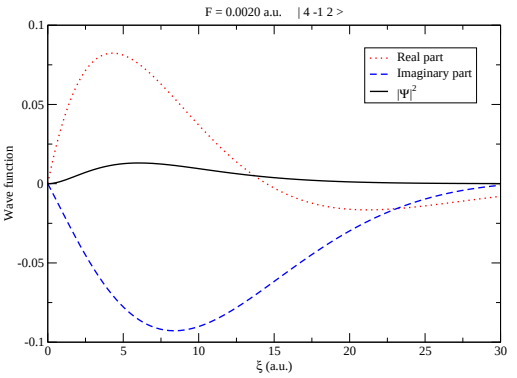

(b) $\psi_{\xi 4-12}(\xi)$

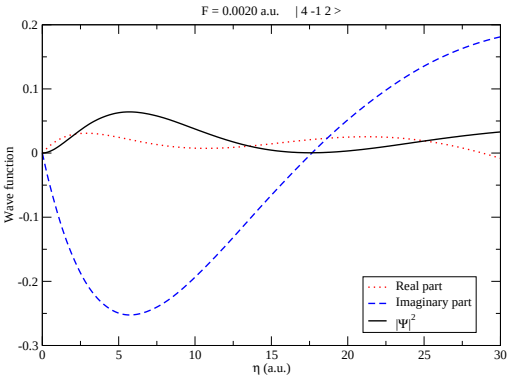

(c) $\psi_{\eta 4-12}(\eta)$

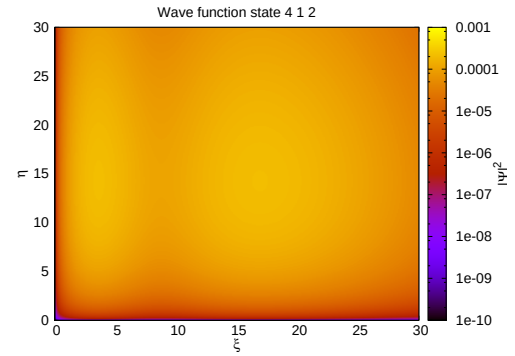

(d) $|\psi_{412}|^2(\xi,\eta)$

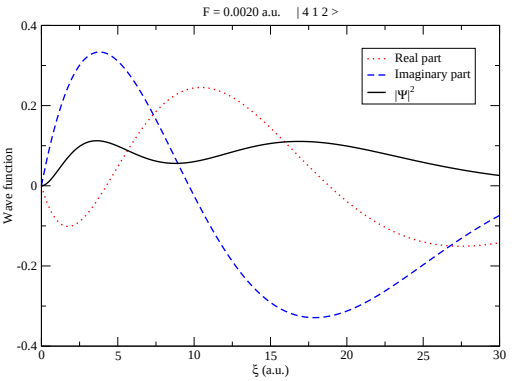

(e) $\psi_{\xi 412}(\xi)$

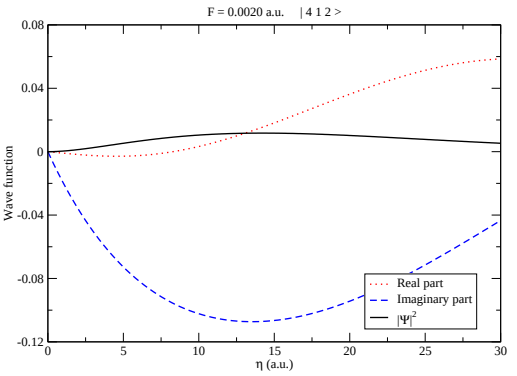

(f) $\psi_{\eta 412}(\eta)$

Figure 4.13: Wave function of the Stark states $|4\ -1\ 2\rangle$ and $|4\ 1\ 2\rangle$ for a field intensity of $F = 0.0020$ a.u..

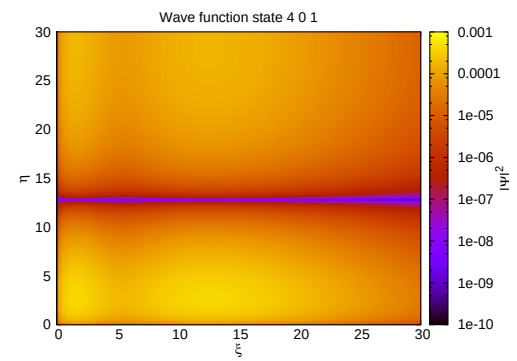

(a) $|\psi_{401}|^2(\xi,\eta)$

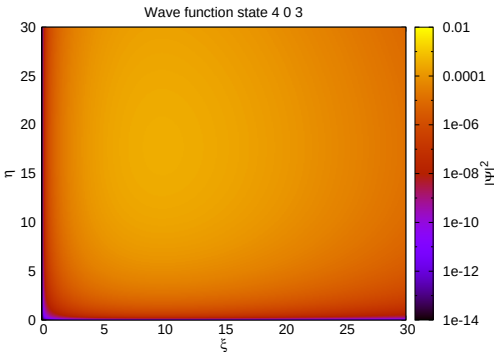

(d) $|\psi_{403}|^2(\xi,\eta)$

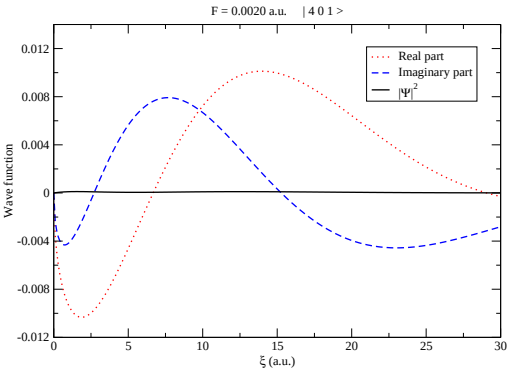

(b) $\psi_{\xi 401}(\xi)$

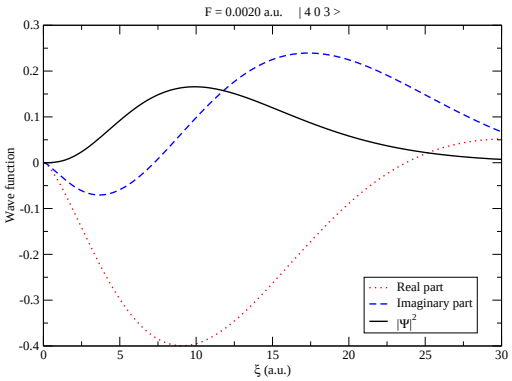

(e) $\psi_{\xi 403}(\xi)$

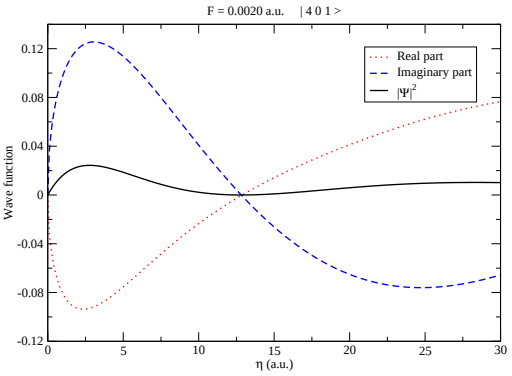

(c) $\psi_{\eta 401}(\eta)$

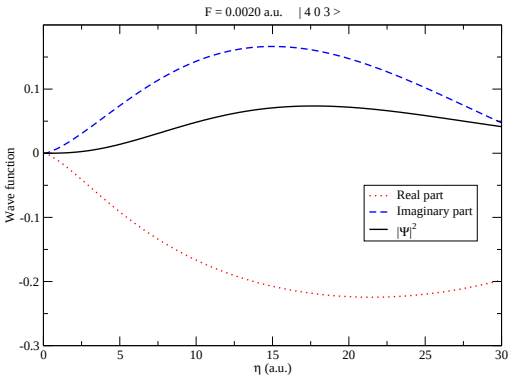

(f) $\psi_{\eta 403}(\eta)$

Figure 4.14: Wave function of the Stark states $|\,4\,0\,1\,\rangle$ and $|\,4\,0\,3\,\rangle$ for a field intensity of $F = 0.0020$ a.u..

4.6 Derived quantities

The wave functions contain all the information about the system, we can obtain any physical observable from them just making the bracket.

In the following sections we explain how to get these physical observables, which will be useful tools for practical applications, as plasma diagnostic.

4.6.1 Isotopic correction

For the calculation of the shown energies, widths and wave functions we used the Hamiltonian 4.8, where in the kinetic term appears the electron mass as the unit. If we want to calculate the exact Stark splitting of the hydrogen spectral lines we have to consider the isotopes, so we can determine for example the difference of the Stark structure of lines H_α, D_α or T_α.

We calculate the energy difference for the individual isotopes as

$$E_\mu \;=\; \frac{1}{\mu}\,E_1 \;+\; \left(1 \;-\; \frac{1}{\mu}\right)\left\langle \psi \;\middle|\; -\frac{\mathrm{e}^{-i\vartheta}}{r} \;+\; \mathrm{e}^{i\vartheta} F z \;\middle|\; \psi \right\rangle , \tag{4.36}$$

where E_μ are the obtained energies for reduced mass μ. Introducing in 4.36 the expression of the matrix elements we get

$$\left\langle \psi \;\middle|\; -\frac{\mathrm{e}^{-i\vartheta}}{r} \;+\; \mathrm{e}^{i\vartheta} F z \;\middle|\; \psi \right\rangle \;=\; \int_0^\infty \mathrm{d}\xi \int_0^\infty \mathrm{d}\eta\, \psi^* \left(-\frac{\mathrm{e}^{-i\vartheta}}{2} \;+\; \frac{\mathrm{e}^{i\vartheta}}{8} F\,(\xi^2 \;-\; \eta^2) \right) \psi\,, \tag{4.37}$$

and using the expansion of ψ in its basis set

$$\begin{aligned} \left\langle \psi \;\middle|\; -\frac{\mathrm{e}^{-i\vartheta}}{r} \;+\; \mathrm{e}^{i\vartheta} F z \;\middle|\; \psi \right\rangle \;=\; & \sum_{i_1, j_1 = 1}^{N} \sum_{i_2, j_2 = 1}^{N} c^*_{i_1 j_1 m}\, c_{i_2 j_2 m} \left[-\frac{\mathrm{e}^{-i\vartheta}}{2}\, \mathcal{I}_{i_1 i_2}\, \mathcal{I}_{j_1 j_2} \right. \\ & \left. +\; \frac{\mathrm{e}^{i\vartheta}}{8} F \left(\mathcal{F}_{i_1 i_2}\, \mathcal{I}_{j_1 j_2} \;-\; \mathcal{I}_{i_1 i_2}\, \mathcal{F}_{j_1 j_2} \right) \right] . \end{aligned} \tag{4.38}$$

In figures 4.15, 4.16 and 4.17 we show the isotopic corrections for the energies and widths of the defferent isotopes of hydrogen for the levels of $n \leq 3$. The transitions between these levels will form the Balmer α line. The correction is smaller as the mass of the nucleus increases.

Adding these corrections to the energy we can calculate the exact splitting of the Balmer H_α and D_α lines, which are important for the MSE spectroscopy. These splittings are shown in figures 4.18 and 4.19. It is divided into its three component groups: σ for $\Delta m = \pm 1$, $\Delta k = 0$; π^+ for $\Delta m = 0$, $\Delta k = +1$ and π^- for $\Delta m = 0$, $\Delta k = -1$. δ and ϕ transitions are very weak in comparison and they will not be seen in a real spectrum with a background.

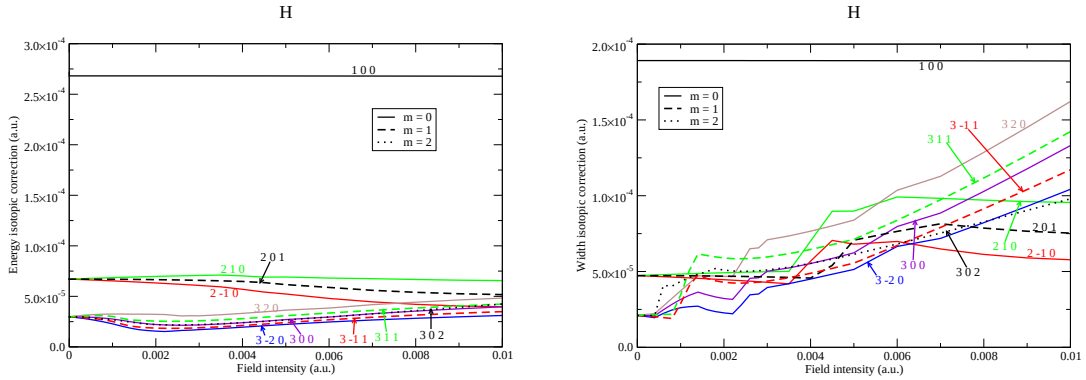

(a) Energy (b) Width

Figure 4.15: Isotopic corrections for the energies and widths of the levels $n \leq 3$ of hydrogen versus the field intensity

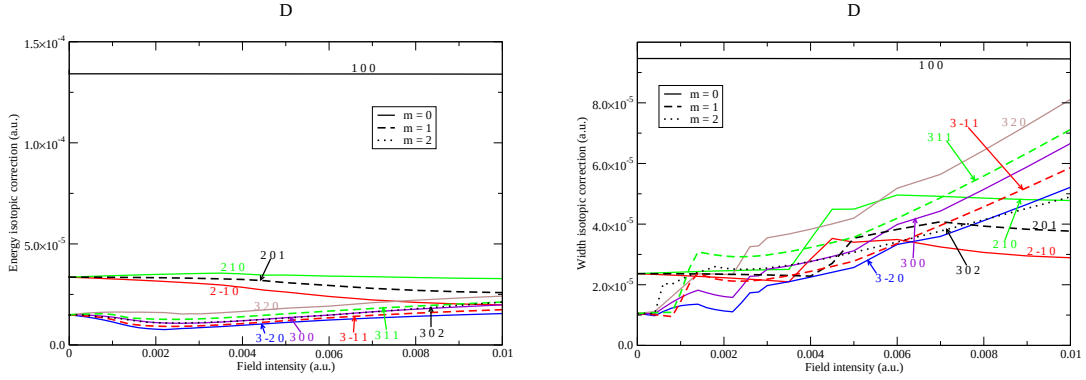

(a) Energy (b) Width

Figure 4.16: Isotopic corrections for the energies and widths of the levels $n \leq 3$ of deuterium versus the field intensity

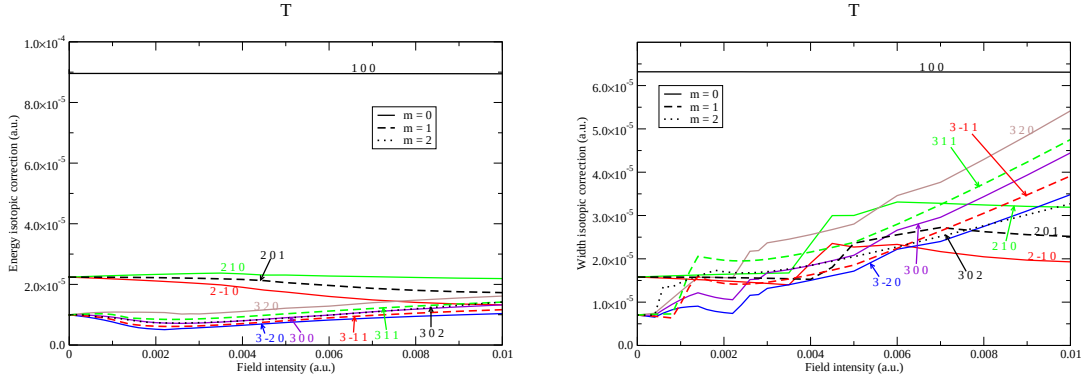

(a) Energy (b) Width

Figure 4.17: Isotopic corrections for the energies and widths of the levels $n \leq 3$ of tritium versus the field intensity

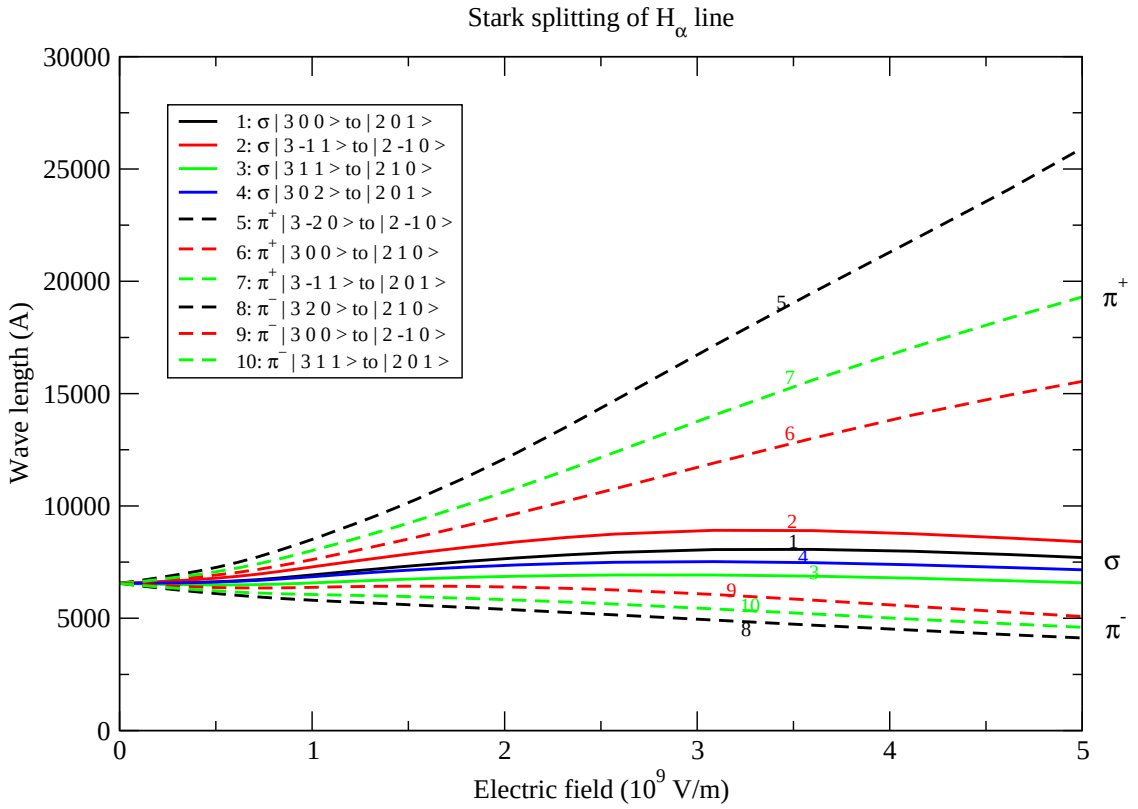

Figure 4.18: Stark splitting of the H_α line of hydrogen versus the electric field intensity.

4.6.2 Einstein transition coefficients

Once we get the wave functions we just have to bracket them with a physical observable to obtain its expected value. In order to calculate observables we must take in account that we rotated the coordinates in the complex plane to get the wave functions, so the physical positions and momentum must be written with the correct rotation:

$$\begin{aligned} x &\rightarrow x\,\mathrm{e}^{-i\vartheta} \\ \frac{\partial}{\partial x} &\rightarrow \frac{\partial}{\partial x}\,\mathrm{e}^{i\vartheta}, \end{aligned} \tag{4.39}$$

with $x = \xi, \eta$.

The first quantity we can calculate are the Einstein emission coefficients A and B, both are proportional to the modulus squared of the matrix element $|\langle\psi_1|\vec{r}|\psi_2\rangle|^2$. To calculate it we evaluate the matrix elements of each Cartesian component x, y and z as:

$$\begin{aligned} \left\langle \psi_1 \left| x\,\mathrm{e}^{-i\vartheta} \right| \psi_2 \right\rangle &= \frac{1}{2\pi}\,\mathrm{e}^{-i\vartheta} \int_0^{2\pi} \mathrm{d}\phi \int_0^{\infty} \mathrm{d}\xi \int_0^{\infty} \mathrm{d}\eta\, \frac{1}{4}\,(\xi + \eta)\,\psi_1^*(\xi,\eta)\,\mathrm{e}^{-im_1\phi}\,\sqrt{\xi\eta}\,\cos\phi\,\psi_2(\xi,\eta)\,\mathrm{e}^{im_2\phi} \\ &= \frac{1}{16\pi}\,\mathrm{e}^{-i\vartheta} \int_0^{2\pi} \mathrm{d}\phi \left(\mathrm{e}^{i(m_2-m_1+1)\phi} + \mathrm{e}^{i(m_2-m_1-1)\phi}\right) \int_0^{\infty} \mathrm{d}\xi \int_0^{\infty} \mathrm{d}\eta\,(\xi + \eta)\,\psi_1^*(\xi,\eta)\,\sqrt{\xi\eta}\,\psi_2(\xi,\eta) \\ &= \frac{1}{8}\,\mathrm{e}^{-i\vartheta}\,(\delta_{m_2 m_1 - 1} + \delta_{m_2 m_1 + 1}) \int_0^{\infty} \mathrm{d}\xi \int_0^{\infty} \mathrm{d}\eta\,\psi_1^*(\xi,\eta)\,(\xi + \eta)\,\sqrt{\xi\eta}\,\psi_2(\xi,\eta) \end{aligned} \tag{4.40}$$

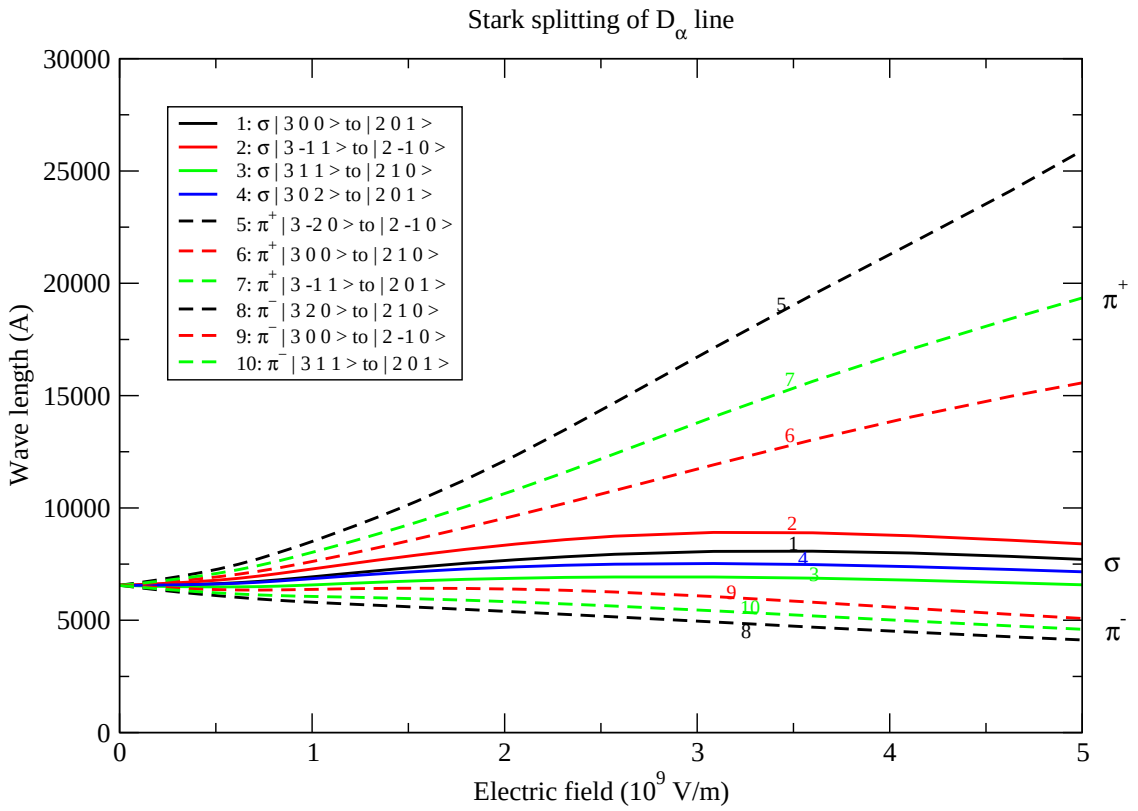

Figure 4.19: Stark splitting of the D_α line of deuterium versus the electric field intensity.

$$\begin{aligned}
\left\langle \psi_1 \left| y\, e^{-i\vartheta} \right| \psi_2 \right\rangle &= \frac{1}{2\pi} e^{-i\vartheta} \int_0^{2\pi} d\phi \int_0^\infty d\xi \int_0^\infty d\eta \, \frac{1}{4} (\xi + \eta)\, \psi_1^*(\xi,\eta)\, e^{-im_1\phi} \sqrt{\xi\eta}\, \sin\phi\, \psi_2(\xi,\eta)\, e^{im_2\phi} \\
&= \frac{1}{16\pi i} e^{-i\vartheta} \int_0^{2\pi} d\phi \left(e^{i(m_2-m_1+1)\phi} - e^{i(m_2-m_1-1)\phi} \right) \int_0^\infty d\xi \int_0^\infty d\eta\, (\xi + \eta)\, \psi_1^*(\xi,\eta)\, \sqrt{\xi\eta}\, \psi_2(\xi,\eta) \\
&= \frac{1}{8i} e^{-i\vartheta} \left(\delta_{m_2 m_1 - 1} - \delta_{m_2 m_1 + 1} \right) \int_0^\infty d\xi \int_0^\infty d\eta\, \psi_1^*(\xi,\eta)\, (\xi + \eta)\, \sqrt{\xi\eta}\, \psi_2(\xi,\eta) \qquad (4.41)
\end{aligned}$$

$$\begin{aligned}
\left\langle \psi_1 \left| z\, e^{-i\vartheta} \right| \psi_2 \right\rangle &= \frac{1}{2\pi} e^{-i\vartheta} \int_0^{2\pi} d\phi \int_0^\infty d\xi \int_0^\infty d\eta \, \frac{1}{4} (\xi + \eta)\, \psi_1^*(\xi,\eta)\, e^{-im_1\phi} \frac{1}{2} (\xi - \eta)\, \psi_2(\xi,\eta)\, e^{im_2\phi} \\
&= \frac{1}{16\pi} e^{-i\vartheta} \int_0^{2\pi} d\phi\, e^{i(m_2-m_1)\phi} \int_0^\infty d\xi \int_0^\infty d\eta\, (\xi + \eta)\, \psi_1^*(\xi,\eta)\, (\xi - \eta)\, \psi_2(\xi,\eta) \\
&= \frac{1}{8} e^{-i\vartheta}\, \delta_{m_1 m_2} \int_0^\infty d\xi \int_0^\infty d\eta\, \psi_1^*(\xi,\eta)\, (\xi^2 - \eta^2)\, \psi_2(\xi,\eta)\,. \qquad (4.42)
\end{aligned}$$

After splitting the angular part we obtain the first selection rule for electric dipole transition $\Delta m = 0, \pm 1$, which is exact for the Stark effect.

If we introduce in the parabolic parts of the wave function $\psi(\xi,\eta)$ the zero-field expressions 2.32 of the product of Laguerre polynomials, the operator $\xi\sqrt{\xi}$ which appears in the integrals for x and y can couple any pair of Laguerre polynomials, so we do not obtain any additional selection rule in the case $\Delta m = \pm 1$. Nevertheless in the integral for z, the operator ξ^2 only couples Laguerre polynomials with a difference of grad lower or equal to two [16], so we obtain a selection rule $\Delta n_1 = 0, \pm 1, \pm 2$, $\Delta n_2 = 0, \pm 1, \pm 2$, if $\Delta m = 0$, which corresponds to the radiation linearly polarised. As the wave functions for finite field are quite similar qualitatively to the ones for zero field, this selection rule should be fulfilled approximately for the approximate quantum numbers and $\tilde{n}_1$ and $\tilde{n}_2$.

To integrate the parabolic parts we use the wave functions expansions in the basis set 4.9:

$$\begin{aligned}
\psi_1(\xi,\eta) &= \sum_{i_1=1}^{N}\sum_{j_1=1}^{N} c_{1i_1j_1m_1}\,(\xi\eta)^{\frac{m_1}{2}}\,\mathrm{e}^{-\frac{\xi+\eta}{2}}\,\Lambda_{Ni_1}(\xi)\,\Lambda_{Nj_1}(\eta)\\
\psi_2(\xi,\eta) &= \sum_{i_2=1}^{N}\sum_{j_2=1}^{N} c_{2i_2j_2m_2}\,(\xi\eta)^{\frac{m_2}{2}}\,\mathrm{e}^{-\frac{\xi+\eta}{2}}\,\Lambda_{Ni_2}(\xi)\,\Lambda_{Nj_2}(\eta)
\end{aligned} \tag{4.43}$$

$$\begin{aligned}
\left\langle\psi_1\left|\,x\,\mathrm{e}^{-i\vartheta}\right|\psi_2\right\rangle &= \frac{1}{8}\,\mathrm{e}^{-i\vartheta}\,(\delta_{m_2m_1-1}+\delta_{m_2m_1+1})\sum_{i_1,j_1=1}^{N}\sum_{i_2,j_2=1}^{N} c^*_{1i_1j_1m_1}\,c_{2i_2j_2m_2}\\
&\quad\times\int_0^\infty \mathrm{d}\xi\int_0^\infty \mathrm{d}\eta\,(\xi+\eta)\,\sqrt{\xi\eta}\,(\xi\eta)^{\frac{|m_1|+|m_2|}{2}}\,\mathrm{e}^{-(\xi+\eta)}\,\Lambda^*_{Ni_1}(\xi)\,\Lambda^*_{Nj_1}(\eta)\,\Lambda_{Ni_2}(\xi)\,\Lambda_{Nj_2}(\eta)\\
&= \frac{1}{8}\,\mathrm{e}^{-i\vartheta}\,\delta_{m_2m_1-1}\sum_{i_1,j_1=1}^{N}\sum_{i_2,j_2=1}^{N} c^*_{1i_1j_1m_1}\,c_{2i_2j_2m_2}\,(\mathcal{S}_{i_1i_2m_2}\,\mathcal{I}_{j_1j_2m_2}+\mathcal{I}_{i_1i_2m_2}\,\mathcal{S}_{j_1j_2m_2})\\
&\quad+\frac{1}{8}\,\mathrm{e}^{-i\vartheta}\,\delta_{m_2m_1+1}\sum_{i_1,j_1=1}^{N}\sum_{i_2,j_2=1}^{N} c^*_{1i_1j_1m_1}\,c_{2i_2j_2m_2}\,(\mathcal{S}_{i_1i_2m_1}\,\mathcal{I}_{j_1j_2m_1}+\mathcal{I}_{i_1i_2m_1}\,\mathcal{S}_{j_1j_2m_1})
\end{aligned} \tag{4.44}$$

$$\begin{aligned}
\left\langle\psi_1\left|\,y\,\mathrm{e}^{-i\vartheta}\right|\psi_2\right\rangle &= \frac{1}{8i}\,\mathrm{e}^{-i\vartheta}\,(\delta_{m_2m_1-1}-\delta_{m_2m_1+1})\sum_{i_1,j_1=1}^{N}\sum_{i_2,j_2=1}^{N} c^*_{1i_1j_1m_1}\,c_{2i_2j_2m_2}\\
&\quad\times\int_0^\infty \mathrm{d}\xi\int_0^\infty \mathrm{d}\eta\,(\xi+\eta)\,\sqrt{\xi\eta}\,(\xi\eta)^{\frac{|m_1|+|m_2|}{2}}\,\mathrm{e}^{-(\xi+\eta)}\,\Lambda^*_{Ni_1}(\xi)\,\Lambda^*_{Nj_1}(\eta)\,\Lambda_{Ni_2}(\xi)\,\Lambda_{Nj_2}(\eta)\\
&= \frac{1}{8i}\,\mathrm{e}^{-i\vartheta}\,\delta_{m_2m_1-1}\sum_{i_1,j_1=1}^{N}\sum_{i_2,j_2=1}^{N} c^*_{1i_1j_1m_1}\,c_{2i_2j_2m_2}\,(\mathcal{S}_{i_1i_2m_2}\,\mathcal{I}_{j_1j_2m_2}+\mathcal{I}_{i_1i_2m_2}\,\mathcal{S}_{j_1j_2m_2})\\
&\quad-\frac{1}{8i}\,\mathrm{e}^{-i\vartheta}\,\delta_{m_2m_1+1}\sum_{i_1,j_1=1}^{N}\sum_{i_2,j_2=1}^{N} c^*_{1i_1j_1m_1}\,c_{2i_2j_2m_2}\,(\mathcal{S}_{i_1i_2m_1}\,\mathcal{I}_{j_1j_2m_1}+\mathcal{I}_{i_1i_2m_1}\,\mathcal{S}_{j_1j_2m_1})
\end{aligned} \tag{4.45}$$

$$\begin{aligned}
\left\langle\psi_1\left|\,z\,\mathrm{e}^{-i\vartheta}\right|\psi_2\right\rangle &= \frac{1}{8}\,\mathrm{e}^{-i\vartheta}\,\delta_{m_2m_1}\sum_{i_1,j_1=1}^{N}\sum_{i_2,j_2=1}^{N} c^*_{1i_1j_1m_1}\,c_{2i_2j_2m_2}\\
&\quad\times\int_0^\infty \mathrm{d}\xi\int_0^\infty \mathrm{d}\eta\,(\xi+\eta)\,(\xi-\eta)\,(\xi\eta)^{\frac{|m_1|+|m_2|}{2}}\,\mathrm{e}^{-(\xi+\eta)}\,\Lambda^*_{Ni_1}(\xi)\,\Lambda^*_{Nj_1}(\eta)\,\Lambda_{Ni_2}(\xi)\,\Lambda_{Nj_2}(\eta)\\
&= \frac{1}{8}\,\mathrm{e}^{-i\vartheta}\,\delta_{m_2m_1}\sum_{i_1,j_1=1}^{N}\sum_{i_2,j_2=1}^{N} c^*_{1i_1j_1m_1}\,c_{2i_2j_2m_2}\,(\mathcal{F}_{i_1i_2m_1}\,\mathcal{I}_{j_1j_2m_1}-\mathcal{I}_{i_1i_2m_1}\,\mathcal{F}_{j_1j_2m_1})\,.
\end{aligned} \tag{4.46}$$

So the dipole moment can be calculated in terms of the ground integrals 4.31 and the expansion coefficients. Once the modulus square of the matrix element is calculated the phase simplifies, so the Einstein coefficients remain independent of the complex rotation angle

$$\begin{aligned}
B_{21} &= \frac{4\pi^2}{3}\,\frac{e^2}{\hbar^2}\,\frac{g_2}{g_1}\,\left|\left\langle\psi_1\left|\,\vec{r}\,\right|\psi_2\right\rangle\right|^2\\
A_{21} &= \frac{(E_2-E_1)^3}{\hbar^2\pi^2c^3}\,B_{12}
\end{aligned} \tag{4.47}$$

Figure 4.20 shows the Einstein spontaneous emission coefficients for the transitions involved in the Balmer α line.

Combining figures 4.19 and 4.20, we show in figure 4.21 the modelled profile of the Balmer D_α and H_α lines for two field intensities of relevance to plasma physics. The illustrated profile corresponds to the corona regime, when only radiative decay is included and collisional redistribution is negligible. We have also not included the Doppler shift and broadening contributions, which will depend on plasma parameters not considered in present work, including the energy of the injected neutrals, the arrangement of the lines-of-sight and the electron temperature.

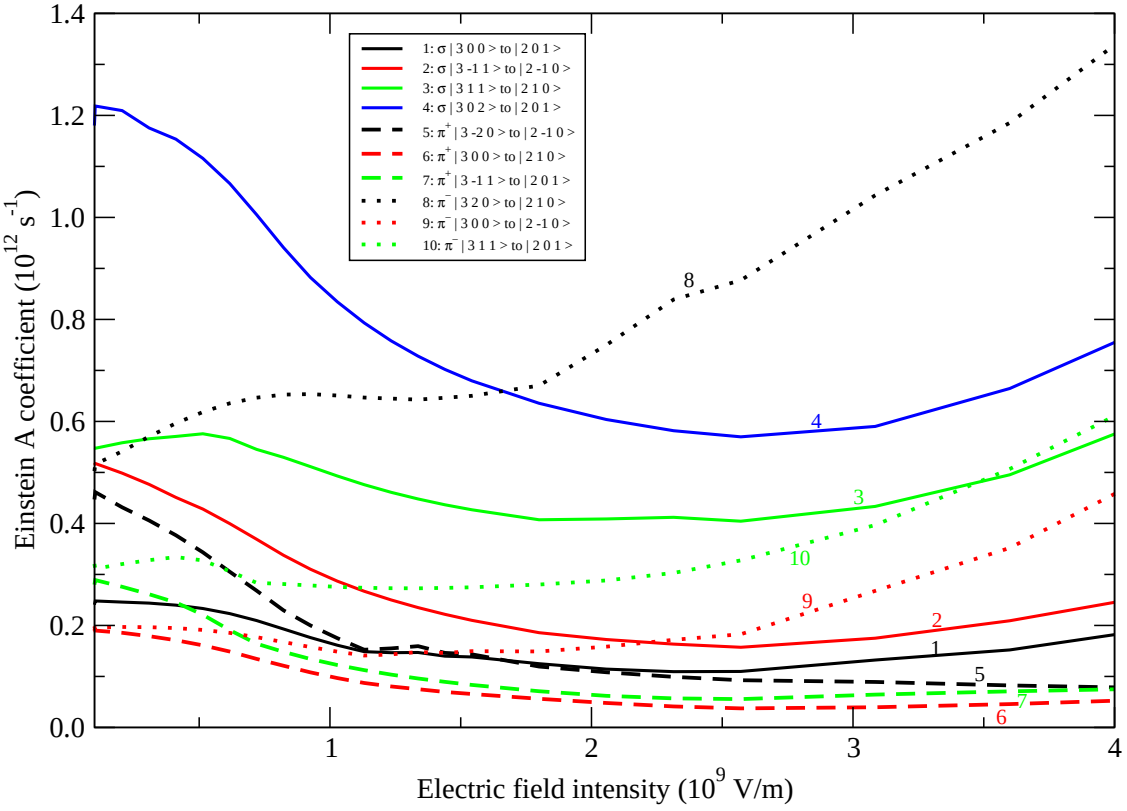

Figure 4.20: Einstein spontaneous emission coefficients of neutral hydrogen versus the electric field intensity.

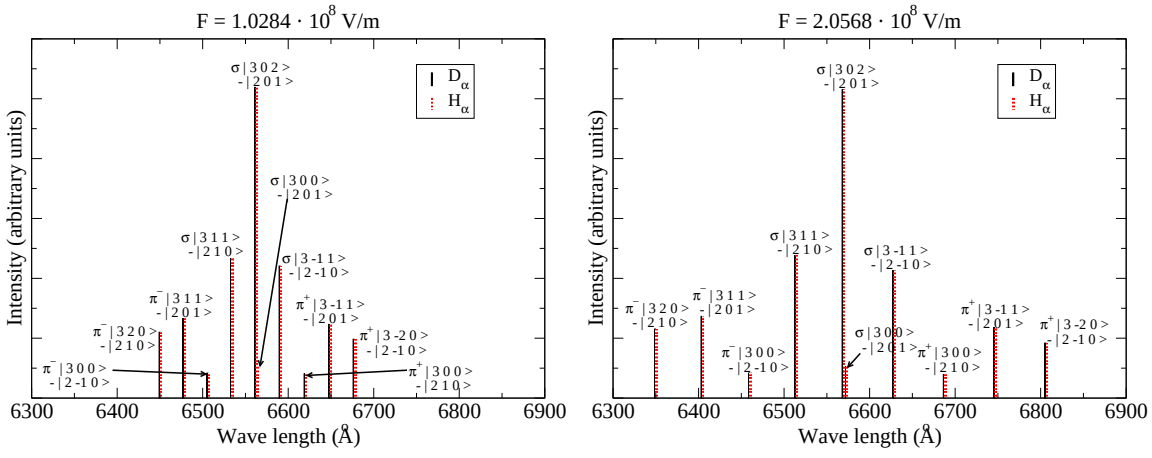

(a) $F = 1.0284 \cdot 10^8$ V/m (b) $F = 2.0568 \cdot 10^8$ V/m

Figure 4.21: Emission profile of the Balmer D_α and H_α lines for two different field intensities in corona equilibrium.

4.6.3 Runge-Lenz vector

$$\begin{aligned}\vec{K} &= \left(mZe^2 - x(p_y^2 + p_z^2) - p_x(yp_y + zp_z - i\hbar)\right)\hat{x} \\ &+ \left(mZe^2 - y(p_z^2 + p_x^2) - p_y(zp_z + xp_x - i\hbar)\right)\hat{y} \\ &+ \left(mZe^2 - z(p_x^2 + p_y^2) - p_z(xp_x + yp_y - i\hbar)\right)\hat{z} \end{aligned} \tag{4.48}$$

4.6.4 Orbital angular momentum

In a real situation in the neutral beam injectors of a fusion device, the electric field is produced by the fast motion of the neutrals in the intense magnetic field, which is known as the Loretz field

$$\vec{F} = \vec{v} \times \vec{B}, \tag{4.49}$$

with $\vec{v}$ the velocity of the neutrals and $\vec{B}$ the magnetic field. Then the electric and magnetic fields are present together and poynting in different directions. The magnetic field can be treated as a perturbation, as the field in a tokamak or stellerator is quite large, between 1 and 10 T, then the magnetic perturbation is higher than the fine structure, so we are in the Paschen-Bach regime, and we have to treat the orbital and spin angular momenta as uncoupled.

$$H_{PB} = \frac{\mu_B}{\hbar}\vec{B}\cdot(\vec{L} + g_e\vec{S}). \tag{4.50}$$

Any anomalous angular momentum coming from relativistic corrections can also be included.

As the electric and magnetic fields are not paralell, we can not choose the magnetic field poynting in the z direction as it is usually made when treating Paschen-Bach effect, and we must calculate all the spacial components of the orbital angular momentum. The transformation equations for the momenta from cartesian to parabolic coordinates are

$$\begin{aligned} p_x &= 2\frac{\sqrt{\xi\eta}}{\xi + \eta}\cos\phi\,(p_\xi + p_\eta) - \frac{1}{\sqrt{\xi\eta}}\sin\phi\,p_\phi \\ p_y &= 2\frac{\sqrt{\xi\eta}}{\xi + \eta}\sin\phi\,(p_\xi + p_\eta) + \frac{1}{\sqrt{\xi\eta}}\cos\phi\,p_\phi \\ p_z &= \frac{2}{\xi + \eta}(\xi p_\xi - \eta p_\eta). \end{aligned} \tag{4.51}$$

When the vectorial product is done, the coordinate is multiplied by a factor $e^{-i\vartheta}$ of the complex coordinate rotation angle, and the momentum by a $e^{i\vartheta}$, so both cancel each other and the angular momentum matrix elements remain independent of this complex rotation angle. Then the orbital angular momentum vector $\vec{L}$ can be splitted in its three cartesian components as follows:

$$\begin{aligned}\vec{L} &= (yp_z - zp_y)\hat{x} + (zp_x - xp_z)\hat{y} + (xp_y - yp_x)\hat{z} \\ &= -i\hbar\left[\sqrt{\xi\eta}\sin\phi\left(\frac{\partial}{\partial\xi} - \frac{\partial}{\partial\eta}\right) - \frac{1}{2}\frac{\xi - \eta}{\sqrt{\xi\eta}}\cos\phi\frac{\partial}{\partial\phi}\right]\hat{x} \\ &+ i\hbar\left[\sqrt{\xi\eta}\cos\phi\left(\frac{\partial}{\partial\xi} - \frac{\partial}{\partial\eta}\right) + \frac{1}{2}\frac{\xi - \eta}{\sqrt{\xi\eta}}\sin\phi\frac{\partial}{\partial\phi}\right]\hat{y} \\ &- i\hbar\frac{\partial}{\partial\phi}\hat{z}. \end{aligned} \tag{4.52}$$

In Stark effect the operator L^2 is no more conserved, so it is not useful to get its mean value, anyway it can be expressed in parabolic coordinates as

$$L^2 = (\xi + \eta)\left[-\eta\frac{\partial^2}{\partial\xi^2} - \xi\frac{\partial^2}{\partial\eta^2} - 2(\xi + \eta)\frac{\partial^2}{\partial\xi\partial\eta} - 3\left(\frac{\partial}{\partial\xi} + \frac{\partial}{\partial\eta}\right) + \frac{1}{4}\frac{\xi + \eta}{\xi\eta}\frac{\partial^2}{\partial\phi^2}\right]. \tag{4.53}$$

We calculate now the cartesian components of the orbital angular momentum

$$\begin{aligned}
\langle\psi_1\,|\,L_x\,|\,\psi_2\rangle &= -\frac{i\hbar}{2\pi}\int_0^{2\pi}\mathrm{d}\phi\int_0^{\infty}\mathrm{d}\xi\int_0^{\infty}\mathrm{d}\eta\,\frac{1}{4}\,(\xi+\eta)\,\psi_1^*(\xi,\eta)\,\mathrm{e}^{-im_1\phi}\\
&\quad\times\left[\sqrt{\xi\eta}\,\sin\phi\left(\frac{\partial}{\partial\xi}-\frac{\partial}{\partial\eta}\right)-\frac{1}{2}\,\frac{\xi-\eta}{\sqrt{\xi\eta}}\,\cos\phi\,\frac{\partial}{\partial\phi}\right]\psi_2(\xi,\eta)\,\mathrm{e}^{im_2\phi}\\
&= -\frac{\hbar}{8}\,(\delta_{m_1m_2+1}-\delta_{m_1m_2-1})\int_0^{\infty}\mathrm{d}\xi\int_0^{\infty}\mathrm{d}\eta\,\psi_1^*(\xi,\eta)\,(\xi+\eta)\,\sqrt{\xi\eta}\left(\frac{\partial}{\partial\xi}-\frac{\partial}{\partial\eta}\right)\psi_2(\xi,\eta)\\
&\quad-\frac{m_2\hbar}{16}\,(\delta_{m_1m_2-1}+\delta_{m_1m_2+1})\int_0^{\infty}\mathrm{d}\xi\int_0^{\infty}\mathrm{d}\eta\,\psi_1^*(\xi,\eta)\,\frac{\xi^2-\eta^2}{\sqrt{\xi\eta}}\,\psi_2(\xi,\eta)
\end{aligned}\tag{4.54}$$

$$\begin{aligned}
\left\langle\psi_1\,|\,L_y\,|\,\psi_2\right\rangle &= \frac{i\hbar}{2\pi}\int_0^{2\pi}\mathrm{d}\phi\int_0^{\infty}\mathrm{d}\xi\int_0^{\infty}\mathrm{d}\eta\,\frac{1}{4}\,(\xi+\eta)\,\psi_1^*(\xi,\eta)\,\mathrm{e}^{-im_1\phi}\\
&\quad\times\left[\sqrt{\xi\eta}\,\sin\phi\left(\frac{\partial}{\partial\xi}-\frac{\partial}{\partial\eta}\right)-\frac{1}{2}\,\frac{\xi-\eta}{\sqrt{\xi\eta}}\,\cos\phi\,\frac{\partial}{\partial\phi}\right]\psi_2(\xi,\eta)\,\mathrm{e}^{im_2\phi}\\
&= \frac{i\hbar}{8}\,(\delta_{m_1m_2+1}+\delta_{m_1m_2-1})\int_0^{\infty}\mathrm{d}\xi\int_0^{\infty}\mathrm{d}\eta\,\psi_1^*(\xi,\eta)\,(\xi+\eta)\,\sqrt{\xi\eta}\left(\frac{\partial}{\partial\xi}-\frac{\partial}{\partial\eta}\right)\psi_2(\xi,\eta)\\
&\quad+\frac{im_2\hbar}{16}\,(\delta_{m_1m_2+1}-\delta_{m_1m_2-1})\int_0^{\infty}\mathrm{d}\xi\int_0^{\infty}\mathrm{d}\eta\,\psi_1^*(\xi,\eta)\,\frac{\xi^2-\eta^2}{\sqrt{\xi\eta}}\,\psi_2(\xi,\eta)
\end{aligned}\tag{4.55}$$

$$\begin{aligned}
\langle\psi_1\,|\,L_z\,|\,\psi_2\rangle &= -\frac{i\hbar}{2\pi}\int_0^{2\pi}\mathrm{d}\phi\int_0^{\infty}\mathrm{d}\xi\int_0^{\infty}\mathrm{d}\eta\,\frac{1}{4}\,(\xi+\eta)\,\psi_1^*(\xi,\eta)\,\mathrm{e}^{-im_1\phi}\,\frac{\partial}{\partial\phi}\,\psi_2(\xi,\eta)\,\mathrm{e}^{im_2\phi}\\
&= \hbar m_2\,\delta_{m_1m_2}\,\delta_{12}\,.
\end{aligned}\tag{4.56}$$

The L_z component is already a conserved quantity, and the other components just couple states with $\Delta m = \pm 1$. To

determine the integrals we write the wave functions ψ_1 and ψ_2 as their expansions in the basis set as usually 4.43

$$
\begin{aligned}
\langle \psi_1 \,|\, L_x \,|\, \psi_2 \rangle \;=\; & -\frac{\hbar}{8}\,(\delta_{m_1 m_2+1} \,-\, \delta_{m_1 m_2-1}) \sum_{i_1 j_1=1}^{N} \sum_{i_2 j_2=1}^{N} c^{*}_{1 i_1 j_1 m_1}\, c_{2 i_2 j_2 m_2} \\
& \times \int_0^\infty \mathrm{d}\xi \int_0^\infty \mathrm{d}\eta\, \mathrm{e}^{-\frac{\xi+\eta}{2}}\, (\xi\eta)^{\frac{|m_1|}{2}}\, \Lambda^{*}_{N i_1}(\xi)\, \Lambda^{*}_{N j_1}(\eta)\, (\xi \,+\, \eta)\, \sqrt{\xi\eta} \left(\frac{\partial}{\partial \xi} \,-\, \frac{\partial}{\partial \eta} \right) \mathrm{e}^{-\frac{\xi+\eta}{2}}\, (\xi\eta)^{\frac{|m_2|}{2}}\, \Lambda_{N i_2}(\xi)\, \Lambda_{N j_2}(\eta) \\
& -\frac{m_2 \hbar}{16}\,(\delta_{m_1 m_2+1} \,+\, \delta_{m_1 m_2-1}) \sum_{i_1 j_1=1}^{N} \sum_{i_2 j_2=1}^{N} c^{*}_{1 i_1 j_1 m_1}\, c_{2 i_2 j_2 m_2} \\
& \times \int_0^\infty \mathrm{d}\xi \int_0^\infty \mathrm{d}\eta\, \mathrm{e}^{-\frac{\xi+\eta}{2}}\, (\xi\eta)^{\frac{|m_1|}{2}}\, \Lambda^{*}_{N i_1}(\xi)\, \Lambda^{*}_{N j_1}(\eta)\, \frac{\xi^2 \,-\, \eta^2}{\sqrt{\xi\eta}}\, \mathrm{e}^{-\frac{\xi+\eta}{2}}\, (\xi\eta)^{\frac{|m_2|}{2}}\, \Lambda_{N i_2}(\xi)\, \Lambda_{N j_2}(\eta) \\
= \; & -\frac{\hbar}{8}\,(\delta_{m_1 m_2+1} \,-\, \delta_{m_1 m_2-1}) \sum_{i_1 j_1=1}^{N} \sum_{i_2 j_2=1}^{N} c^{*}_{1 i_1 j_1 m_1}\, c_{2 i_2 j_2 m_2} \\
& \times \int_0^\infty \mathrm{d}\xi \int_0^\infty \mathrm{d}\eta\, \mathrm{e}^{-(\xi+\eta)}\, (\xi\eta)^{\frac{|m_1|+|m_2|}{2}}\, \Lambda^{*}_{N i_1}(\xi)\, \Lambda^{*}_{N j_1}(\eta)\, (\xi \,+\, \eta)\, \sqrt{\xi\eta} \\
& \times \left[\frac{m_2}{2} \left(\frac{1}{\xi} \,-\, \frac{1}{\eta} \right) \Lambda_{N i_2}(\xi)\, \Lambda_{N j_2}(\eta) \,+\, \Lambda'_{N i_2}(\xi)\, \Lambda_{N j_2}(\eta) \,-\, \Lambda_{N i_2}(\xi)\, \Lambda'_{N j_2}(\eta) \right] \\
& -\frac{m_2 \hbar}{16}\,(\delta_{m_1 m_2+1} \,+\, \delta_{m_1 m_2-1}) \sum_{i_1 j_1=1}^{N} \sum_{i_2 j_2=1}^{N} c^{*}_{1 i_1 j_1 m_1}\, c_{2 i_2 j_2 m_2} \\
& \times \int_0^\infty \mathrm{d}\xi \int_0^\infty \mathrm{d}\eta\, \mathrm{e}^{-(\xi+\eta)}\, (\xi\eta)^{\frac{|m_1|+|m_2|}{2}}\, \Lambda^{*}_{N i_1}(\xi)\, \Lambda^{*}_{N j_1}(\eta)\, \frac{\xi^2 \,-\, \eta^2}{\sqrt{\xi\eta}}\, \Lambda_{N i_2}(\xi)\, \Lambda_{N j_2}(\eta) \\
= \; & -\frac{\hbar}{8}\,\delta_{m_1 m_2+1} \sum_{i_1 j_1=1}^{N} \sum_{i_2 j_2=1}^{N} c^{*}_{1 i_1 j_1 m_1}\, c_{2 i_2 j_2 m_2} \left[-\frac{m_2}{2}\, \mathcal{B}_{i_1 i_2 m_2}\, \mathcal{I}_{j_1 j_2 m_2} \,+\, \frac{m_2}{2}\, \mathcal{I}_{i_1 i_2 m_2}\, \mathcal{B}_{j_1 j_2 m_2} \right. \\
& \qquad \left. +\, \mathcal{D}_{i_1 i_2 m_2}\, \mathcal{A}_{j_1 j_2 m_2} \,+\, \mathcal{C}_{i_1 i_2 m_2}\, \mathcal{B}_{j_1 j_2 m_2} \,-\, \mathcal{B}_{i_1 i_2 m_2}\, \mathcal{C}_{j_1 j_2 m_2} \,-\, \mathcal{A}_{i_1 i_2 m_2}\, \mathcal{D}_{j_1 j_2 m_2} \right] \\
& +\frac{\hbar}{8}\,\delta_{m_1 m_2-1} \sum_{i_1 j_1=1}^{N} \sum_{i_2 j_2=1}^{N} c^{*}_{1 i_1 j_1 m_1}\, c_{2 i_2 j_2 m_2} \left[-\frac{m_2}{2}\, \mathcal{B}_{i_1 i_2 m_1}\, \mathcal{I}_{j_1 j_2 m_1} \,+\, \frac{m_2}{2}\, \mathcal{I}_{i_1 i_2 m_1}\, \mathcal{B}_{j_1 j_2 m_1} \right. \\
& \qquad \left. +\, \mathcal{D}_{i_1 i_2 m_1}\, \mathcal{A}_{j_1 j_2 m_1} \,+\, \mathcal{C}_{i_1 i_2 m_1}\, \mathcal{B}_{j_1 j_2 m_1} \,-\, \mathcal{B}_{i_1 i_2 m_1}\, \mathcal{C}_{j_1 j_2 m_1} \,-\, \mathcal{A}_{i_1 i_2 m_1}\, \mathcal{D}_{j_1 j_2 m_1} \right] \\
& -\frac{m_2 \hbar}{16}\,\delta_{m_1 m_2+1} \sum_{i_1 j_1=1}^{N} \sum_{i_2 j_2=1}^{N} c^{*}_{1 i_1 j_1 m_1}\, c_{2 i_2 j_2 m_2} \left[\mathcal{B}_{i_1 i_2 m_2}\, \mathcal{I}_{j_1 j_2 m_2} \,-\, \mathcal{I}_{i_1 i_2 m_2}\, \mathcal{B}_{j_1 j_2 m_2} \right] \\
& -\frac{m_1 \hbar}{16}\,\delta_{m_1 m_2-1} \sum_{i_1 j_1=1}^{N} \sum_{i_2 j_2=1}^{N} c^{*}_{1 i_1 j_1 m_1}\, c_{2 i_2 j_2 m_2} \left[\mathcal{B}_{i_1 i_2 m_1}\, \mathcal{I}_{j_1 j_2 m_1} \,-\, \mathcal{I}_{i_1 i_2 m_1}\, \mathcal{B}_{j_1 j_2 m_1} \right], \qquad (4.57)
\end{aligned}
$$

$$
\begin{aligned}
\left\langle \psi_1 \left| L_y \right| \psi_2 \right\rangle &= \frac{i\hbar}{8} \left(\delta_{m_1 m_2+1} + \delta_{m_1 m_2-1}\right) \sum_{i_1 j_1=1}^{N} \sum_{i_2 j_2=1}^{N} c^*_{1 i_1 j_1 m_1} c_{2 i_2 j_2 m_2} \\
&\times \int_0^\infty \mathrm{d}\xi \int_0^\infty \mathrm{d}\eta\, \mathrm{e}^{-\frac{\xi+\eta}{2}} (\xi\eta)^{\frac{|m_1|}{2}} \Lambda^*_{N i_1}(\xi) \Lambda^*_{N j_1}(\eta) (\xi + \eta) \sqrt{\xi\eta} \left(\frac{\partial}{\partial\xi} - \frac{\partial}{\partial\eta}\right) \mathrm{e}^{-\frac{\xi+\eta}{2}} (\xi\eta)^{\frac{|m_2|}{2}} \Lambda_{N i_2}(\xi) \Lambda_{N j_2}(\eta) \\
&- \frac{i m_2 \hbar}{16} \left(\delta_{m_1 m_2+1} - \delta_{m_1 m_2-1}\right) \sum_{i_1 j_1=1}^{N} \sum_{i_2 j_2=1}^{N} c^*_{1 i_1 j_1 m_1} c_{2 i_2 j_2 m_2} \\
&\times \int_0^\infty \mathrm{d}\xi \int_0^\infty \mathrm{d}\eta\, \mathrm{e}^{-\frac{\xi+\eta}{2}} (\xi\eta)^{\frac{|m_1|}{2}} \Lambda^*_{N i_1}(\xi) \Lambda^*_{N j_1}(\eta) \frac{\xi^2 - \eta^2}{\sqrt{\xi\eta}} \mathrm{e}^{-\frac{\xi+\eta}{2}} (\xi\eta)^{\frac{|m_2|}{2}} \Lambda_{N i_2}(\xi) \Lambda_{N j_2}(\eta) \\
&= \frac{i\hbar}{8} \left(\delta_{m_1 m_2+1} + \delta_{m_1 m_2-1}\right) \sum_{i_1 j_1=1}^{N} \sum_{i_2 j_2=1}^{N} c^*_{1 i_1 j_1 m_1} c_{2 i_2 j_2 m_2} \\
&\times \int_0^\infty \mathrm{d}\xi \int_0^\infty \mathrm{d}\eta\, \mathrm{e}^{-(\xi+\eta)} (\xi\eta)^{\frac{|m_1|+|m_2|}{2}} \Lambda^*_{N i_1}(\xi) \Lambda^*_{N j_1}(\eta) (\xi + \eta) \sqrt{\xi\eta} \\
&\times \left[\frac{m_2}{2} \left(\frac{1}{\xi} - \frac{1}{\eta}\right) \Lambda_{N i_2}(\xi) \Lambda_{N j_2}(\eta) + \Lambda'_{N i_2}(\xi) \Lambda_{N j_2}(\eta) - \Lambda_{N i_2}(\xi) \Lambda'_{N j_2}(\eta)\right] \\
&+ \frac{i m_2 \hbar}{16} \left(\delta_{m_1 m_2+1} - \delta_{m_1 m_2-1}\right) \sum_{i_1 j_1=1}^{N} \sum_{i_2 j_2=1}^{N} c^*_{1 i_1 j_1 m_1} c_{2 i_2 j_2 m_2} \\
&\times \int_0^\infty \mathrm{d}\xi \int_0^\infty \mathrm{d}\eta\, \mathrm{e}^{-(\xi+\eta)} (\xi\eta)^{\frac{|m_1|+|m_2|}{2}} \Lambda^*_{N i_1}(\xi) \Lambda^*_{N j_1}(\eta) \frac{\xi^2 - \eta^2}{\sqrt{\xi\eta}} \Lambda_{N i_2}(\xi) \Lambda_{N j_2}(\eta) \\
&= \frac{i\hbar}{8} \delta_{m_1 m_2+1} \sum_{i_1 j_1=1}^{N} \sum_{i_2 j_2=1}^{N} c^*_{1 i_1 j_1 m_1} c_{2 i_2 j_2 m_2} \left[-\frac{m_2}{2} \mathcal{B}_{i_1 i_2 m_2} \mathcal{C}_{j_1 j_2 m_2} + \frac{m_2}{2} \mathcal{C}_{i_1 i_2 m_2} \mathcal{B}_{j_1 j_2 m_2}\right. \\
&\qquad \left. + \mathcal{E}_{i_1 i_2 m_2} \mathcal{I}_{j_1 j_2 m_2} + \mathcal{D}_{i_1 i_2 m_2} \mathcal{B}_{j_1 j_2 m_2} - \mathcal{B}_{i_1 i_2 m_2} \mathcal{D}_{j_1 j_2 m_2} - \mathcal{I}_{i_1 i_2 m_2} \mathcal{E}_{j_1 j_2 m_2}\right] \\
&+ \frac{i\hbar}{8} \delta_{m_1 m_2-1} \sum_{i_1 j_1=1}^{N} \sum_{i_2 j_2=1}^{N} c^*_{1 i_1 j_1 m_1} c_{2 i_2 j_2 m_2} \left[-\frac{m_2}{2} \mathcal{B}_{i_1 i_2 m_1} \mathcal{I}_{j_1 j_2 m_1} + \frac{m_2}{2} \mathcal{I}_{i_1 i_2 m_1} \mathcal{B}_{j_1 j_2 m_1}\right. \\
&\qquad \left. + \mathcal{D}_{i_1 i_2 m_1} \mathcal{A}_{j_1 j_2 m_1} + \mathcal{C}_{i_1 i_2 m_1} \mathcal{B}_{j_1 j_2 m_1} - \mathcal{B}_{i_1 i_2 m_1} \mathcal{C}_{j_1 j_2 m_1} - \mathcal{A}_{i_1 i_2 m_1} \mathcal{D}_{j_1 j_2 m_1}\right] \\
&\frac{i m_2 \hbar}{16} \delta_{m_1 m_2+1} \sum_{i_1 j_1=1}^{N} \sum_{i_2 j_2=1}^{N} c^*_{1 i_1 j_1 m_1} c_{2 i_2 j_2 m_2} \left[\mathcal{B}_{i_1 i_2 m_2} \mathcal{I}_{j_1 j_2 m_2} - \mathcal{I}_{i_1 i_2 m_2} \mathcal{B}_{j_1 j_2 m_2}\right] \\
&- \frac{i m_2 \hbar}{16} \delta_{m_1 m_2-1} \sum_{i_1 j_1=1}^{N} \sum_{i_2 j_2=1}^{N} c^*_{1 i_1 j_1 m_1} c_{2 i_2 j_2 m_2} \left[\mathcal{B}_{i_1 i_2 m_1} \mathcal{I}_{j_1 j_2 m_1} - \mathcal{I}_{i_1 i_2 m_1} \mathcal{B}_{j_1 j_2 m_1}\right], \qquad (4.58)
\end{aligned}
$$

where we have defined new ground matrixes

$$
\begin{aligned}
\mathcal{I}_{ijm} &= \int_0^\infty \mathrm{d}x\, \mathrm{e}^{-x} x^{|m|} \Lambda^*_{Ni}(x) \Lambda_{Nj}(x) \\
\mathcal{A}_{ijm} &= \int_0^\infty \mathrm{d}x\, \mathrm{e}^{-x} x^{|m|} x \Lambda^*_{Ni}(x) \Lambda_{Nj}(x) \\
\mathcal{B}_{ijm} &= \int_0^\infty \mathrm{d}x\, \mathrm{e}^{-x} x^{|m|} x^2 \Lambda^*_{Ni}(x) \Lambda_{Nj}(x) \\
\mathcal{C}_{ijm} &= \int_0^\infty \mathrm{d}x\, \mathrm{e}^{-x} x^{|m|} x \Lambda^*_{Ni}(x) \Lambda'_{Nj}(x) \\
\mathcal{D}_{ijm} &= \int_0^\infty \mathrm{d}x\, \mathrm{e}^{-x} x^{|m|} x^2 \Lambda^*_{Ni}(x) \Lambda'_{Nj}(x) . \qquad (4.59)
\end{aligned}
$$

With expressions 4.56, 4.57 and 4.58 we can calculate the orbital part for the magnetic perturbation, now we have to add the spin part. To calculate the components x and y of the spin operator we write them in terms of the raising

and lowering operators of the angular momentum j_+ and j_- as:

$$\begin{aligned} j_+ &= j_x + i j_y \\ j_- &= j_x - i j_y , \end{aligned} \tag{4.60}$$

which fulfil

$$\begin{aligned} j_z \,|\, j\, m\rangle &= \hbar\, j \,|\, j\, m\rangle \\ j_+ \,|\, j\, m\rangle &= \hbar\, \sqrt{j(j+1) - m(m+1)}\,|\, j\, m+1\rangle \\ j_- \,|\, j\, m\rangle &= \hbar\, \sqrt{j(j+1) - m(m-1)}\,|\, j\, m-1\rangle . \end{aligned} \tag{4.61}$$

That leads to a expresion for the spin opperator ($j = \frac{1}{2}$) as

$$\begin{aligned} \langle s\, m_{s1} \,|\, S_z \,|\, s\, m_{s2}\rangle &= \hbar\, \delta_{m_{s1} m_{s2}} \\ \langle s\, m_{s1} \,|\, S_x \,|\, s\, m_{s2}\rangle &= \frac{\hbar}{2} \left(\sqrt{3/4 - m_{s2}(m_{s2}+1)}\, \delta_{m_{s1} m_{s2}+1} + \sqrt{3/4 - m_{s2}(m_{s2}-1)}\, \delta_{m_{s1} m_{s2}-1} \right) \\ \left\langle s\, m_{s1} \left| S_y \right| s\, m_{s2} \right\rangle &= \frac{\hbar}{2i} \left(\sqrt{3/4 - m_{s2}(m_{s2}+1)}\, \delta_{m_{s1} m_{s2}+1} - \sqrt{3/4 - m_{s2}(m_{s2}-1)}\, \delta_{m_{s1} m_{s2}-1} \right) , \end{aligned} \tag{4.62}$$

so we can now get the total magnetic perturbation matrix as

$$H_B^{(1)} = \frac{\mu_B}{\hbar} \left\langle \psi_1\, m_{s1} \left| \vec{B} \cdot (\vec{L} + g_e \vec{S}) \right| \psi_2\, m_{s2} \right\rangle \tag{4.63}$$

4.6.5 Fine structure

The fine structure of the hydrogen atom is a contribution which could be of the same order than the magnetic perturbation in a tokamak. Including the fine structure correction in the first order perturbative hamiltonian will lead to more precise results to determine the exact splitting of the hydrogen lines.

The fine structure Hamiltonian is diagonal in the basis set $|\, n\, l\, j\, m_j\rangle$, so one option should be to write our calculated states $|\, \tilde{n}\, \tilde{k}\, m\, m_s\rangle$ as an expansion of them, and then get the matrix elements in terms of these expansion coefficients. Nevertheless this method is not practical because in Stark effect we have lost the quantum number l and the relation between $\tilde{k}$ and j is not a simple Clebsch Gordan factor. In addition write a Stark state with field non zero as this type of expansion, we have to include a complete basis set of states $|\, n\, l\, j\, m_j\rangle$, counting the continuum too, so this expansion will not be exact anyway.

As an alternative we calculate all the terms of the fine structure Hamiltonian individually

$$H_{fe} = -\frac{p^4}{8\mu^3 c^2} + \frac{1}{2} \frac{Ze^2}{4\pi\epsilon_0} \frac{1}{r^3} \vec{L} \cdot \vec{S} + \frac{\hbar^2}{8\mu^2 c^2} \frac{Ze^2}{4\pi\epsilon_0} 4\pi \delta^{(3)}(\vec{r}) . \tag{4.64}$$

Relativistic term

$$H_{rel} = -\frac{p^4}{8\mu^3 c^2} \tag{4.65}$$

Let's write the Stark Hamiltonian as

$$H = \frac{p^2}{2} + V , \tag{4.66}$$

where

$$V = -\frac{\mathrm{e}^{-i\vartheta}}{r} + \mathrm{e}^{i\vartheta} F z . \tag{4.67}$$

Then we get the expresion for p^2 as

$$p^2 = 2H - 2V , \tag{4.68}$$

and

$$p^4 \;=\; 4\,H^2 \;-\; 4\,H\,V \;-\; 4\,V\,H \;+\; 4\,V^2\,. \tag{4.69}$$

Then we can calculate the matrix element

$$\frac{\alpha^2}{8}\,\left\langle \psi_1 \,|\, p^4 \,|\, \psi_2 \right\rangle \;=\; \frac{\alpha^2}{2}\,\left[E_2\,\delta_{12} - \,(E_1 \,+\, E_2)\,\langle \psi_1 \,|\, V \,|\, \psi_2 \rangle \,+\, \left\langle \psi_1 \,|\, V^2 \,|\, \psi_2 \right\rangle\right]. \tag{4.70}$$

The element in V has been calculated in 4.38, its result is

$$\begin{aligned}\left\langle \psi_1 \,\middle|\, -\frac{\mathrm{e}^{-i\vartheta}}{r} \,+\, \mathrm{e}^{i\vartheta} F z \,\middle|\, \psi_2 \right\rangle \;&=\; \delta_{m_1 m_2} \sum_{i_1,j_1=1}^{N} \sum_{i_2,j_2=1}^{N} c^*_{1 i_1 j_1 m_1}\, c_{2 i_2 j_2 m_2} \left[-\frac{\mathrm{e}^{-i\vartheta}}{2}\, \mathcal{I}_{i_1 i_2 m_2}\, \mathcal{I}_{j_1 j_2 m_2} \right. \\ &\left. +\, \frac{\mathrm{e}^{i\vartheta}}{8}\, F\, \left(\mathcal{F}_{i_1 i_2 m_2}\, \mathcal{I}_{j_1 j_2 m_2} \,-\, \mathcal{I}_{i_1 i_2 m_2}\, \mathcal{F}_{j_1 j_2 m_2} \right) \right]. \end{aligned} \tag{4.71}$$

And the term in V^2 is

$$\begin{aligned} &\left\langle \psi_1 \,\middle|\, \mathrm{e}^{-2i\vartheta} \frac{4}{(\xi \,+\, \eta)^2} \,-\, 2\,F\,\frac{\xi - \eta}{\xi + \eta} \,+\, \mathrm{e}^{2i\vartheta}\,\frac{1}{4}\,F^2\,(\xi \,-\, \eta)^2 \,\middle|\, \psi_2 \right\rangle \\ =\;& \delta_{m_1 m_2} \int_0^\infty \mathrm{d}\xi \int_0^\infty \mathrm{d}\eta\, \frac{1}{4}\,(\xi \,+\, \eta)\, \psi_1^*(\xi,\eta) \left[\mathrm{e}^{-2i\vartheta} \frac{4}{(\xi \,+\, \eta)^2} \,-\, 2\,F\,\frac{\xi - \eta}{\xi + \eta} \,+\, \mathrm{e}^{2i\vartheta}\,\frac{1}{4}\,F^2\,(\xi \,-\, \eta)^2 \right] \psi_2(\xi,\eta) \\ =\;& \delta_{m_1 m_2} \int_0^\infty \mathrm{d}\xi \int_0^\infty \mathrm{d}\eta\, \psi_1^*(\xi,\eta) \left[\mathrm{e}^{-2i\vartheta} \frac{1}{\xi + \eta} \,-\, \frac{1}{2}\,F\,(\xi - \eta) \,+\, \mathrm{e}^{2i\vartheta}\,\frac{1}{16}\,F^2\,(\xi \,+\, \eta)\,(\xi \,-\, \eta)^2 \right] \psi_2(\xi,\eta) \end{aligned} \tag{4.72}$$

Spin orbit coupling

$$H_{so} \;=\; \frac{1}{2}\,\frac{Z e^2}{4\pi\epsilon_0}\,\frac{1}{r^3}\,\vec{L}\cdot\vec{S}\,. \tag{4.73}$$

We have to calculate the three spatial components of the vector $\frac{1}{r}\vec{L}$:

$$\begin{aligned} \frac{1}{r^3}\,L_x \;&=\; -\frac{8i\hbar}{(\xi \,+\, \eta)^3} \left[\sqrt{\xi\eta}\,\sin\phi \left(\frac{\partial}{\partial\xi} \,-\, \frac{\partial}{\partial\eta} \right) \,-\, \frac{1}{2}\,\frac{\xi - \eta}{\sqrt{\xi\eta}}\,\cos\phi\,\frac{\partial}{\partial\phi} \right] \\ \frac{1}{r^3}\,L_y \;&=\; \frac{8i\hbar}{(\xi \,+\, \eta)^3} \left[\sqrt{\xi\eta}\,\cos\phi \left(\frac{\partial}{\partial\xi} \,-\, \frac{\partial}{\partial\eta} \right) \,+\, \frac{1}{2}\,\frac{\xi - \eta}{\sqrt{\xi\eta}}\,\sin\phi\,\frac{\partial}{\partial\phi} \right] \\ \frac{1}{r^3}\,L_z \;&=\; -\frac{8i\hbar}{(\xi \,+\, \eta)^3}\,\frac{\partial}{\partial\phi}\,. \end{aligned} \tag{4.74}$$

And the components of $\vec{S}$ where calculated in 4.62.

Darwin term

$$H_D \;=\; \frac{\hbar^2}{8\mu^2 c^2}\,\frac{Z e^2}{4\pi\epsilon_0}\,4\pi\delta^{(3)}(\vec{r})\,. \tag{4.75}$$

In this case due to the δ we have just to evaluate the integrand of the matrix element in the origin $\xi = 0$, $\eta = 0$:

$$\begin{aligned} \frac{\pi\alpha^2}{2}\,\left\langle \psi_1 \,|\, \delta^{(3)}(\vec{r}) \,|\, \psi_2 \right\rangle \;&=\; \frac{\pi\alpha^2}{2}\,\delta_{m_1 m_2} \sum_{i_1,j_1=1}^{N} \sum_{i_2,j_2=1}^{N} c^*_{1 i_1 j_1 m_1}\, c_{2 i_2 j_2 m_2}\, (\xi\eta)^{m_2}\, \mathrm{e}^{-(\xi+\eta)}\, \Lambda^*_{N i_1}(\xi)\, \Lambda^*_{N j_1}(\eta)\, \Lambda_{N i_2}(\xi)\, \Lambda_{N j_2}(\eta) \\ &=\; \frac{\pi\alpha^2}{2}\,\delta_{m_1 m_2}\,\delta_{m_2 0} \sum_{i_1,j_1=1}^{N} \sum_{i_2,j_2=1}^{N} c^*_{1 i_1 j_1 m_1}\, c_{2 i_2 j_2 m_2}\, \Lambda^*_{N i_1}(0)\, \Lambda^*_{N j_1}(0)\, \Lambda_{N i_2}(0)\, \Lambda_{N j_2}(0)\,. \end{aligned} \tag{4.76}$$

This term is only non zero if $m_1 = m_2 = 0$.

Chapter 5

Population Modelling

The chapter 3 detailed how the field ionisation rates were calculated, and 4 with an *ab initio* method. However, no real concern was given to what effect these ionisation rates had on the overall emission multiplet calculated by ADAS305. It is expected that the ionisation rates will produce an asymmetry within the H_α multiplet due to the fact that the blue Stark shifted lines are harder to ionise than the red Stark shifted lines. To study this, the ionisation rates which come from the state widths must be added into the collisional radiative model built in ADAS305 and then compared against the other processes that are occurring at the same time. This chapter will build up the theory behind what is expected to happen with the population structure, due to the fact there is not an easy way of describing the ionisation rates past the classical ionisation limit, the report is not yet at the stage of providing a full analysis of results, however detail can be provided as to how to integrate the rates into ADAS305 and what the effects are when the two methods of calculating the ionisation results are put into action.

The population model is calculated through the use of the collisional-radiative matrix. This is described in full in Henderson (2009) [1]. To provide a summary, the time-dependent population equation can be written compactly as

$$C_{ij}\, N_j \;=\; N_e\, N_+\, r_i \;-\; \frac{\mathrm{d}N_i}{\mathrm{d}t}\,, \tag{5.1}$$

where C_{ij} is the Collisional-Radiative Matrix (CRM), r_i the recombination rates and i and j run over all levels of the atom. The CRM includes all the different processes that can excite, deexcite or ionise the atom, on the upper triangle, there are the processes which move the electron from a higher to lower excited state and the lower triangle includes the processes moving the electron from a lower to higher excited state. The diagonal is built up of the processes which remove the electron entirely from the atom, as it will be discussed, here is where the field ionisation rates must be added.

There are a number of points which must be looked at in order to study the field ionisation effect on the CRM, the ionisation rates must be compared to other processes effecting the beam atoms, this will provide information as to where the rates begin to become comparable. After this, it is possible to deduce whether any asymmetry will be due to direct ionisation of that specific level or whether it is due to the indirect ionisation of a higher energy level filtering through to the lower energy levels. When dealing with the latter case, the cascade matrix must be considered to see by what path the electrons decay.

5.1 Radiative Decay Rates

When a field is present, the radiative transitions are no longer from $n \to n'$, they are split into their respective substates and decay according to the appropriate selection rules either for electric or magnetic field perturbations. For each substate there will be a respective line strength, $S_{i\sigma j\rho}$, where $i > j$ corresponds to the respective principal n-shells and the Greek symbols correspond to the substates of i and j respectively.

One can relate the line strength to lifetime, or Einstein A coefficient, through the equation

$$A_{i\sigma\rightarrow j\rho} = \frac{1}{6}\frac{\alpha^4 c}{a_o}\left(\frac{E}{I_H}\right)^3 \frac{S_{i\sigma j\rho}}{e^2 a_0^2}, \tag{5.2}$$

where the constant $\frac{\alpha^4 c}{2a_0}$ values $8.032x10^9 s^{-1}$, a_0 is the Bohr radius and e is the elemental charge. The line strengths are calculated in ADAS305 and then related to the Einstein A coefficients through equation 5.2. The graph in figure 5.1 shows the typical radiative decay rates in JET conditions.

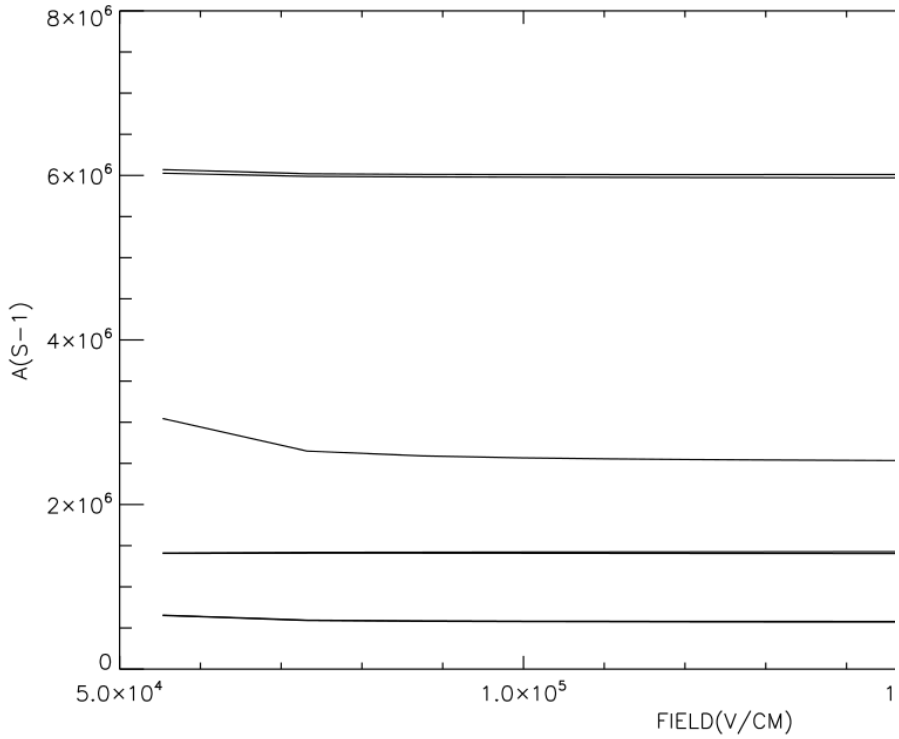

Figure 5.1: Einstein A coefficients for Stark states at various fields decaying to the ground state. Substates are labelled using the $|n\,k\,m\rangle$ convention.

The graph shows the radiative decay rates vary little with respect to the field that is applied to the atom. In addition, it reveals that as the electron moves further from the atom, the decay rates drop. Therefore, with respect to the field ionisation, as the electron moves into shells with n higher than four, the field ionisation begins to become dominant compared to the decay rates.

When viewing the Stark multiplet, it is clear that direct ionisation of the third principal n-shell will not produce any significant effects on the emission lines. In other words, before the electron has a chance to ionise, it will have decayed down to a lower state, however this assumes that the $n = 3$ electron shell is symmetric around the atom to begin with, if the higher states are included in the CRM, then this may not be the case, if there are asymmetries forming in the higher states, this could be conserved through the radiative decays of the electrons down into the lower states.

5.2 Cascade Effects

When an electron is in an excited state, it can decay down to a lower state through a number of ways, either directly or indirectly, the state in which it decays to is generally determined through the stated selection rules, however in terms of parabolic states, there are no real selection rules available, therefore it is advantageous to try and study where the electron is most probably going to end up through a decay. If it produces a random walk down through parabolic states, then any asymmetry formed through field ionisation effects will be lost from the higher states as the electrons will all mix together as they decay, However on the other hand, if some form of selection rule is present which favours

the electron decaying down the same 'side' of the atom, then any asymmetry will be conserved from the higher to lower excited electron states.

There is a way of modelling this behaviour in the form of what's commonly known as a cascade matrix. Due to the fact that the parabolic states are in question, this matrix will be dubbed the k-cascade matrix, with the k referring to the quantum number. States decaying down the negative k side corresponds to the $-z$-axis of the atom, Likewise the positive k side corresponds to the $+z$-axis of the atom. Equations to model this are formed by first letting $P_{i\sigma\to j\rho}$ equal the probability of a direct transition from $i\sigma$ to $j\rho$, given by

$$P_{i\sigma\to j\rho} = \frac{A_{i\sigma\to j\rho}}{A_{i\sigma}}, \tag{5.3}$$

where $A_{i\sigma}$ is the total spontaneous emission rate coefficient to all the different states from level $i\sigma$. Now, set $C_{i\sigma\to j\rho}$ as the probability that the population of $i\sigma$ is followed by a transition to $j\rho$ via all possible cascade paths, the general solution is

$$C_{i\sigma\to i\rho} = \sum_{p=i-1}^{j}\sum_{\eta=1}^{2p^2} P_{i\sigma\to p\eta}\, C_{p\eta\to j\rho}\,. \tag{5.4}$$

To model these cascades, the line strengths must therefore be computed for each n-shell. The ADAS305 code can be used to generate the line-strengths, it produces a matrix where the upper triangle corresponds to radiative decays, the diagonal gives out the ionisation probability for each state and the lower diagonal corresponds to collisional excitations. Therefore, the upper triangle is of interest here, it produces these values already in terms of the resolved Stark shifted line strengths, these can therefore be converted into Einstein-A coefficients using equation 5.2, these new upper triangle coefficients can then be used to form the general solution given in equation 5.4. However, the initial version of ADAS305 only resolves levels up to $n = 4$, Therefore this must be expanded to deal with n-shells up to level 8.

5.3 N-Shell Expansion

To show the indirect field effects of higher n-shells and produce cascade matrices for radiative decays down from $n = 8$, the initial version of ADAS305 was expanded to deal with resolved Stark states up to $n = 8$, beyond this energy level, the electrons can be considered to be ionised by collisions. For this expansion, the main problem is that of variable dimension size, as the resolution of the code is increased, so therefore must all the dimensions, the code does not provide documentation of how each variable dimension is built therefore work was carried out to produce equations which describe each dimension, these equations can be seen in appendix A.1. Once the dimensions were altered, the code was then altered to include resolved levels up to $n = 8$ with levels 9 and 10 being left unresolved, the code ran efficiently with this increase in resolution on a relatively low performance computer.

The expansion was firstly checked for accuracy by cross checking the summed line strengths calculated by the code with the accepted line strength values for each principal n-shell ($S_i = \sum_\sigma S_{i\sigma}$). A further check was carried out which viewed the Stark multiplet for the $n = 8 \to 7$ transition within hydrogen, the multiplet can be seen in figure 5.2, this multiplet is interesting as it shows the same features as the H_α transition, with the main σ radiation middle transition lines, followed by the two outer π radiation transition lines.

The method of producing the cascade matrix was then designed in subroutine $casmat.for$, an output file is generated which details the transition probabilities from the cascade matrix. For the higher n-shells, the states are defined by a temporary number system. The number beside each transition corresponds to the vector position which in turn can be converted into the parabolic quantum numbers through the theory described in chapter 3.5.

5.4 Results

With the subroutine casmat now included in the main code ADAS305, the cascade matrix can be computed. The results of this can be seen for the $|n\,k\,m\rangle$ transition from $|8\ -7\,0\rangle \to |3\ *\ *\rangle$ in figure 5.3, this graph reveals the most

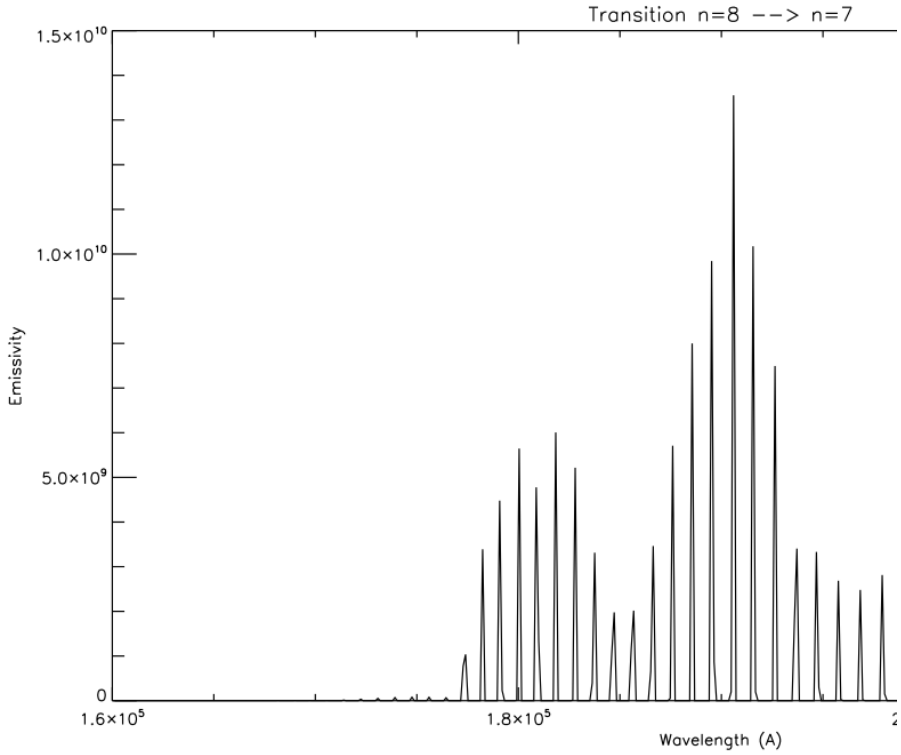

Figure 5.2: Graph showing the Stark multiplet for the $n = 8 \rightarrow 7$ transition at a beam energy of 100 keV/amu and magnetic field of 2 T.

probabilistic path of an electron as it decays, it appears that if the electron begins on the negative k side of the atom, or the red side, then as it decays it will tend to stay on this side of the atom, in addition it is very unlikely for a spin change to occur. The graph in figure 5.4 shows that the electron in energy state $|8\,7\,0\rangle$ is most likely to stay on the positive k side of the electron.

In order to check that the cascade matrix is giving meaningful results, it should show that the total probabilities of the various transitions from one state is equal to unity, in other words, in a system which is independent of time and isolated from any other system, an electron sitting in an excited state must decay down to its ground state, it cannot stay in the same excited one. It may be apparent then that the total probabilities in figures 5.3 and 5.4 do not add up to unity, this is due to the fact that it is missing the probabilities from the $n = 8 \rightarrow 1$ transitions, therefore these summed probabilities shown would require the addition of the probability of a direct transition down to the ground state in order for the check of unity to be valid.

Therefore, from the two graphs in figures 5.3 and 5.4, it is clear that the electrons do tend to stick their respective k states as they decay from higher to lower states, this means that one can expect any asymmetry formed in the higher states to be conserved as the electron falls to the lower states, however these ionisation rates must also be compared to the collisional cross sections, these cross sections will be discussed in more detail in chapter 6. If the cross sections for now are dampened, then it can be concluded that an asymmetry should be viewed for the H_α beam emission lines.

5.5 Implementing Code

Attention is now turned to the implementation of the field ionisation rates into the CRM. To do this, one must study the subroutine *hydemi.for*, located in the ADAS305 subroutine library, within this code, the collisionally induced transitions into other states are calculated. The non-ionising collisions are added to the off-diagonals and the ionising collisions are added to the diagonals, these rates are calculated in the subroutine *sigma*. The field ionisation rates can be added to these diagonal rates.

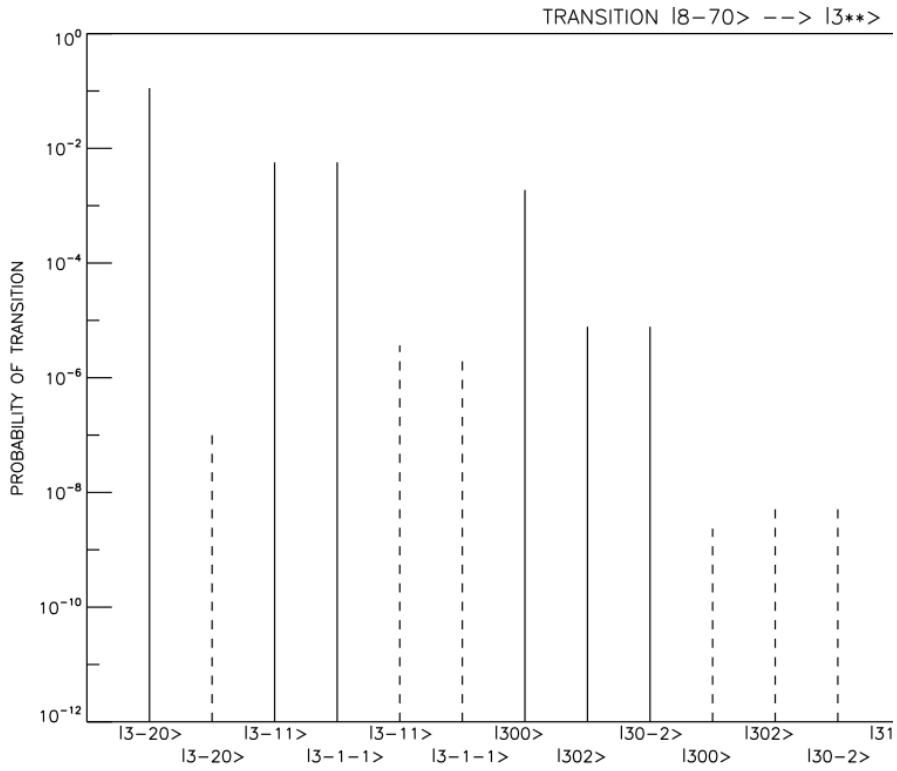

Figure 5.3: Cascade probabilities for the transition from $|n\,km\rangle$ state $|8\ -\ 7\,0\rangle\ \rightarrow\ |3\ *\ *\rangle$ for a beam energy of 1×10^5 eV/amu entering a field of 2 T. The dashed line represents transitions which undergo a spin change.

It is important to ensure the same units are being used in each rate, cross sections, as will be discussed in the next chapter, are measured in cm^2, the cross sections are then converted into the total reaction rate per unit volume,

$$R\ =\ n_1\,n_2\,\langle v\,Q\rangle \tag{5.5}$$

where n_i is the density of the species i, v the speed of the particles and Q the cross section. Therefore, the value of $\langle vQ\rangle$ gives the average over speeds, this is measured in m^3/s, the factor is then multiplied by the density in m^{-3}, and added to the off-diagonal of the collisional-radiative matrix. Now we get the collisional rate in s^{-1}, at this point the field ionisation rates can be added.

There are three competing processes in the off-diagonal section of the CR matrix: collisional ionisation, field ionisation and the total radiative decay probability, a comparison of these processes can be seen in table 5.1, this table shows how important it is to find a solution to the high field regime. It is evident that as the field increases, the ionisation rates are decreasing, the peak can thought of around $n = 6$, where the field ionisation rates are becoming comparable to the collisional processes, above and below this point the collisional rates are dominating. Therefore, at this state, one may not expect to see the hypothesised asymmetry, although an overall reduction to the intensity of the peaks should be evident, one can see this result in figure 5.5, it is clear that the intensity of the multiplet has decreased by an order of magnitude, further investigation of the high field regime is required to investigate the predicted asymmetry within the multiplet.

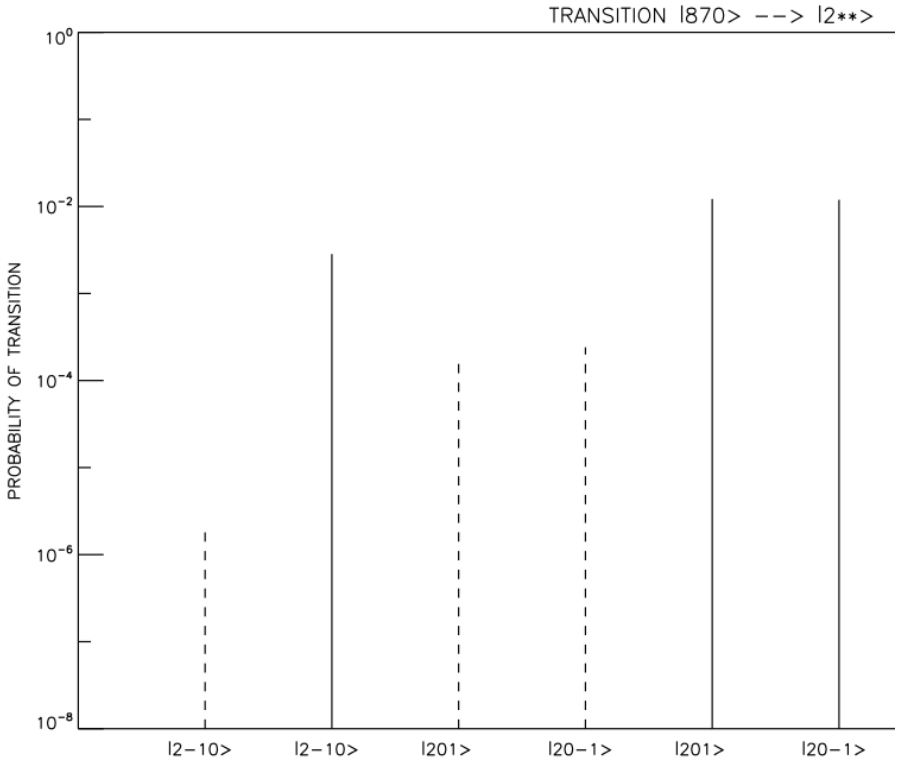

Figure 5.4: Cascade probabilities for the transition from $|n\,k\,m\rangle$ state $|8\,7\,0\rangle \rightarrow |2\,*\,*\rangle$ for a beam energy of 1×10^5 eV/amu entering a field of 2 T. The dashed line represents transitions which undergo a spin change.

$\|n\,k\,m\rangle$	Field ionisation	Collisional Ionisation	Total Radiative Decay
$\|5\ -4\,0\rangle$	1.373×10^{10}	1.682×10^{14}	2.207×10^{7}
$\|6\ -4\,1\rangle$	1.371×10^{12}	4.912×10^{14}	8.104×10^{6}
$\|6\ -3\,2\rangle$	1.221×10^{14}	6.047×10^{14}	4.071×10^{7}
$\|6\ -3\,0\rangle$	1.174×10^{14}	6.597×10^{14}	5.591×10^{6}
$\|7\ -4\,0\rangle$	5.878×10^{09}	1.056×10^{15}	3.459×10^{6}
$\|7\ -3\,1\rangle$	9.683×10^{10}	1.257×10^{15}	4.331×10^{6}
$\|8\ -7\,0\rangle$	2.934×10^{07}	7.153×10^{14}	4.426×10^{6}
$\|8\ -5\,2\rangle$	2.244×10^{08}	1.469×10^{15}	1.196×10^{6}

Table 5.1: Comparing transition rates in s^{-1} within the beam emission at field of 7.1×10^4 V cm^{-1}.

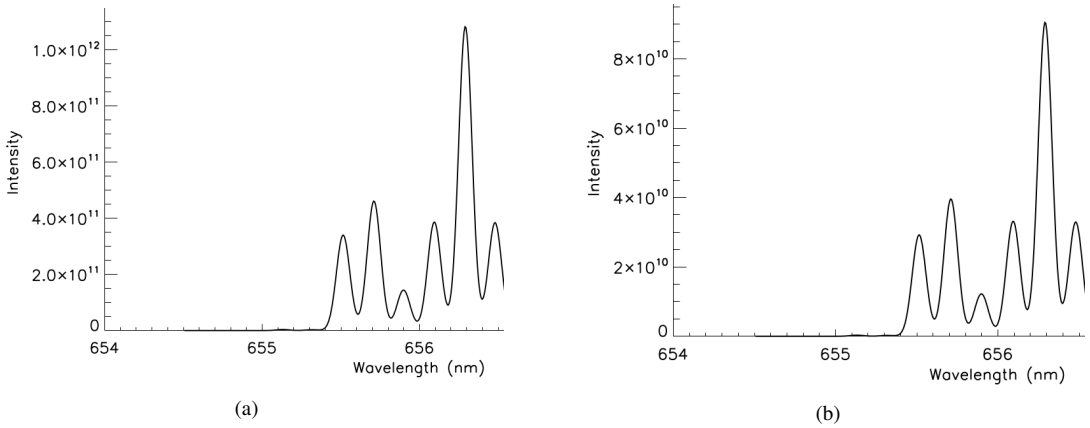

Figure 5.5: The beam emission of the H_α line at a field of 7.1×10^4 V cm^{-1} where a) the field ionisation rates are neglected and b) the field ionisation rates are added to the CR matrix.

Chapter 6

Asymmetric Cross Sections

In a plasma electrons ions and radiation are coexisting and time scale of collisions of neutral hydrogen atoms with electrons, protons and impurity ions are competitive with the radiative decays, so the transition or ionisation probability due to collisions should be included in the collision radiative model to have a good description of populations in each atomic state and emission. Current methods in ADAS305 and of Seaton (1962) [55] and Burgess and Summers (1976) [56] assume that the electrons are lying in their isolated atom states, in these states the electron cloud can be thought of as being symmetrical, this would therefore imply that the direction in which the beam atom hits the plasma species does not matter.

A hydrogen atom under constant simultaneous electric and magnetic fields is no longer spherically symmetrical and the orientation of the atom respect the colliding particle should be taken in account, so the problem gets closer to an ion–molecule collision than an ion–atom one, and the target should be described in terms of the approximated Stark quantum numbers $|\tilde{n}\,\tilde{k}\,\tilde{m}\rangle$.

At the impact energies of interests for our problem, the semiclassical straight-line impact parameter approximation is valid. This approximation considers the impacting particle which describes a classical straight line trajectory. This impact parameter method was used by Seaton (1962) [55].

6.1 Cross sections

For an incoming flux of particles Φ colliding against dispersion center in an initial state i and which will change it to a final state f, the differential cross section is defined as the particles deflected through an angle (θ, ϕ) for unit of time and solid angle:

$$\frac{\mathrm{d}\sigma_{if}}{\mathrm{d}\Omega} = \frac{\mathrm{Particlesdispersedindirection}\ (\theta,\phi)}{\mathrm{Incomingflux}}\,. \tag{6.1}$$

The cross section has units of surface.

Integrating the differential cross section, one obtains the total cross section:

$$\sigma_{if} = \int_{4\pi} \mathrm{d}\Omega\, \frac{\mathrm{d}\sigma_{if}}{\mathrm{d}\Omega}\,. \tag{6.2}$$

6.2 System of reference

In the following section we detail the criteria to establish the coordinate system to treat the collision of an ion or electron against a neutral hydrogen atom under constant electric and magnetic field so on. We denote with zxy the called laboratory system, where the collision takes place, in this system the origin is placed on the center of mass of the target, the z axis is chosen parallel to the initial momentum of the projectile, and the collision plane the zx plane,

which is the one containing the vectors of the initial and final momenta corresponding to the incoming and deflected projectile. In the impact parameter approximation the deflection is zero and the final velocity is equal to the initial one of the projectile, so the z axis is parallel to the classical velocity and the relative position vector between projectile and target is contained in the zx plane, in other words, the $\vec{b}$ vector representing the impact parameter is parallel to the x axis. The y axis remains in any case perpendicular to the collision plane.

We denote then with primes $z'x'y'$ the proper coordinate system internal for the target atom, this system is independent to any collision. In this sense following the criteria until now, we place the total electric field vector $\vec{F}$ (Lorentz and external) pointing to the z' direction, and the magnetic field vector $\vec{B}$ contained in the $z'x'$ axis. If there is no external field, or it is very low, like in an usual tokamak, then $\vec{F}$ and $\vec{B}$ are perpendicular and $\vec{B}$ will point in the x' direction.

Both reference systems have the same origin, so they are related through a 3D rotation, which is defined through the three Euler angles (Θ, Φ, Ψ). There are several ways to define the Euler angles [57], in this work we do it as follows:

1. Rotation angle Θ about the y axis. This angle will remain between the axis z and z'.
2. Rotation angle Φ about the z axis. This is the azimuthal angle, the one which makes the projection of the z' axis on the xy plane with the x axis.
3. Rotation angle Ψ about the new z' axis.

After multiplying the matrixes of the three rotations we get the the relation between the two reference systems as

$$\begin{pmatrix} z' \\ x' \\ y' \end{pmatrix} = \begin{pmatrix} \cos\Theta & \sin\Theta & 0 \\ -\sin\Theta\cos\Phi\cos\Psi & \cos\Theta\cos\Phi\cos\Psi & \sin\Phi\cos\Psi \\ +\sin\Theta\sin\Phi\sin\Psi & -\cos\Theta\sin\Phi\sin\Psi & +\cos\Phi\sin\Psi \\ \sin\Theta\sin\Phi\cos\Psi & -\cos\Theta\sin\Phi\cos\Psi & \cos\Phi\cos\Psi \\ +\sin\Theta\sin\Phi\sin\Psi & -\cos\Theta\cos\Phi\sin\Psi & -\sin\Phi\sin\Psi \end{pmatrix} \begin{pmatrix} z \\ x \\ y \end{pmatrix}. \tag{6.3}$$

If the target is cylindrically symmetrical, like in our case would be for magnetic field zero, then the rotation is independent of the third angle Ψ, which can be set to zero.

In the figure 6.1 it is displayed both coordinate systems in use, laboratory and molecular.

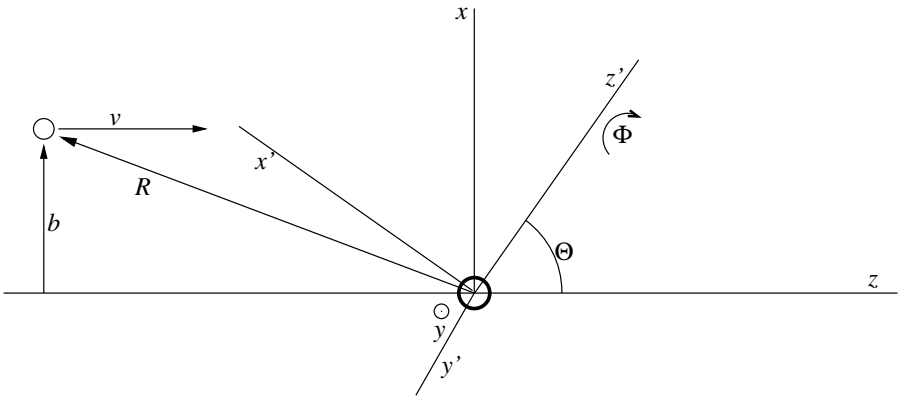

Figure 6.1: Coordinate system used for collision problems, laboratory and molecular.

6.3 Impact parameter method

This is a very common approximation used in atomic and molecular collision theory at energies between 10 eV and 10 keV for atomic mass unit when at least one of the systems in collision is electrically neutral. It supposes the

projectile moving in a straight-line classical trajectory, with a speed v and a closest approach distance, or impact parameter b, as it is graphically shown in figure 6.1. So the vector $\vec{R}$, which points from the center of mass of the target to the center of mass of the projectile, describes a classical trajectory

$$\vec{R} \;=\; \vec{b} \;+\; \vec{v}\,t\,. \tag{6.4}$$

With the chosen coordinate system, we suppose v pointing on the positive z axis and b on the x axis, t is the parameter of the trajectory and no the physical time, in the sense that the Schrödinger equation which describes the collision is a stationary one and not a time dependent one.

The Hamiltonian to describe the collision of an electron or a fully stripped ion against a neutral target (B) is

$$H(\vec{R},\vec{r}) \;=\; -\frac{1}{2\mu}\,\vec{\nabla}_{\vec{R}} \;+\; \frac{Z}{R} \;+\; H_{\mathrm{B}}(\vec{r})\,, \tag{6.5}$$

where $\vec{R}$ is the relative position vector between the target center of mass and the projectile, $\vec{r}$ the internal variables in the target system, μ is the reduced mass

$$\mu \;=\; \frac{M\,M_{\mathrm{B}}}{M+M_{\mathrm{B}}}\,, \tag{6.6}$$

M is the mass of the projectile, and M_{B} the mass of the target, and Z is the charge of the projectile in atomic units, which can value -1 in the case of an electron. The target B must fulfil the stationary Schrödinger equation when it is isolated

$$H_{\mathrm{B}}(\vec{r})\,\phi_\beta(\vec{r}) \;=\; \epsilon_\beta\,\phi_\beta(\vec{r})\,, \tag{6.7}$$

being β the states of the target isolated, in the case of a neutral hydrogen atom under constant electric and magnetic field, it will be the Stark states $\beta = |\tilde{n}\tilde{k}\tilde{m}\rangle$.

A detailed work about the semiclassical impact parameter method for describing ion-atom and ion-molecule collisions can be found in Seaton (1962) [55], Burgess and Summers (1976) [56] or Fernández-Menchero (2005) [58].

6.4 Transition probability

Firstly, a review of the method used previously by Seaton (1962) [55] is introduced. As the colliding particle moves towards the target, the motion is described by a classical orbit, $\vec{R}(t)$, the transition amplitude T_{if} from an initial state i to a final one f is treated using a perturbation theory which gives at first order

$$T_{if}(\vec{v},\vec{b}) \;=\; \frac{1}{w_i}\int_{-\infty}^{+\infty} \mathrm{d}t\,\mathrm{e}^{i\frac{\Delta\epsilon_{if}}{\hbar}t}\,V_{if}(t) \tag{6.8}$$

made the integral over a determined trajectory $(\vec{v},\vec{b})$, where w_i is the statistical weight of level i, so the degeneration, $\Delta\epsilon_{if} = \epsilon_f - \epsilon_i$ the energy difference between the final and initial state of the target and V_{ij} is the matrix element of interaction potential between states i and j, which for a one-electron atom is given by

$$V_{if} \;=\; \int \mathrm{d}^3\vec{r}\,\phi_i^*(\vec{r})\,\frac{Ze^2}{|\vec{R}(t)\;-\;\vec{r}|}\,\phi_i(\vec{r})\,, \tag{6.9}$$

where $\vec{r}$ represents the position vector of the electron respect the nucleus. For a multi-electron target, the expression is equivalent being $\vec{r}$ all the internal variables of the target.

The transition probability is then just the modulus square of the amplitude

$$P_{if}(\vec{v},\vec{b}) \;=\; |T_{if}(\vec{v},\vec{b})|^2\,. \tag{6.10}$$

And we get the total cross section for an impact energy E, related with the velocity as $E = \frac{1}{2}\mu v^2$ as the integral of the transition probability over all the classical impact parameters [55]:

$$\sigma_{if}(E) \;=\; \int \mathrm{d}^2\vec{b}\,P(E,\vec{b})\,. \tag{6.11}$$

If the target is isotropic, then the problem becomes cylindrically symmetrical and the transition probability just depends on the module of $\vec{b}$:

$$\sigma_{if}(E) \;=\; 2\pi \int_0^\infty \mathrm{d}b\, b\, P(E,b)\,. \tag{6.12}$$

To simplify the integral $\int_{-\infty}^{+\infty} \mathrm{e}^{ipt} V_{ij}\mathrm{d}t$ for a one-electron atom, the following steps are carried out:

$$V_{if} \;=\; Ze^2 \left\langle \Psi_i \left| \frac{1}{|\vec{r'} - \vec{r}|} \right| \Psi_j \right\rangle . \tag{6.13}$$

Assuming that the wave function has short range and the impact parameters relevant for the cross section are larger than it, $R \gg r$, then we can simplify the Coulomb potential $\frac{1}{|\vec{R}-\vec{r}|}$ as follows:

$$\begin{aligned}
\frac{1}{|\vec{R} - \vec{r}|} &= \frac{1}{\sqrt{R^2 - 2\vec{r}\cdot\vec{R} + r^2}} \\
&= \frac{1}{R\sqrt{1 - \frac{2\vec{r}\vec{R}+r^2}{R^2}}} \\
&= \frac{1}{R}\left[1 - \frac{1}{2}\left(\frac{2\vec{r}\cdot\vec{R} + r^2}{R^2}\right) + O\left(\left(\frac{2\vec{r}\cdot\vec{R} + r^2}{R^2}\right)^2\right)\right] \qquad (6.14)\\
&= \frac{1}{R} + \frac{\vec{r}\cdot\vec{R}}{R^3} + O\left(\left(\frac{r}{R}\right)^2\right), \qquad (6.15)
\end{aligned}$$

so

$$\left\langle \Psi_i \left| \frac{1}{|\vec{R} - \vec{r}|} \right| \Psi_j \right\rangle \;\approx\; \frac{1}{R} + \frac{1}{R^3}\,\vec{R}\cdot\langle\Psi_i\,|\,\vec{r}\,|\,\Psi_j\rangle\,, \tag{6.16}$$

the term on $\frac{1}{R}$ does not depend on the target electron variables $\vec{r}$ and does not affect the value of the matrix elements, so it can be neglected for the calculation of the transition probability. With this new expression for V_{if}, one obtains the new expression for the transition probability

$$P_{ij} \;=\; \frac{e^2}{\hbar^2 w_i}\left|\int_{-\infty}^{+\infty} \mathrm{d}t\, \mathrm{e}^{i\frac{\Delta\epsilon_{if}}{\hbar}t}\, \frac{1}{R^3(t)}\,\vec{R}\cdot\langle\Psi_i\,|\,\vec{r}\,|\,\Psi_j\rangle\right|^2 \;=\; \frac{e^4}{\hbar^2 3w_i}\,U_{if}\cdot\left|\int_{-\infty}^{+\infty}\mathrm{d}t\,\frac{\mathrm{e}^{ipt}\,\vec{R}(t)}{R^3(t)}\right|^2, \tag{6.17}$$

where $\frac{1}{3w_i}U_{if} = \frac{I_H}{\Delta\epsilon_{ij}}f_{i\to j}$, and $f_{i\to j}$ is the oscillator strength.

Now there are two scenarios: neutral target, so linear orbits, and charged target, then the orbits are hyperbolic, if the target is also spherically symmetrical, which is not the case of a Stark atom, then additional simplifications can be used.

6.5 Neutral and spherically symmetrical atoms

In this case we suppose no Coulomb global interaction between target and projectile, so the trajectory remains linear in the zx plane as

$$\begin{aligned} Z &= vt \\ X &= b\,, \end{aligned} \tag{6.18}$$

as it is shown in figure 6.1.

If equation 6.17 is again considered, only components z and x of the vector $\vec{I}_H$ have to be considered due to we are in a symmetrical case and we can focus just in a two-dimension problem. It can be solved by use of the modified Bessel functions, $k_0(x)$ and $k_1(x)$. For completeness, the steps involved in manipulating the integral are detailed, it is

first convenient to split the integral into its z and x parts, as the y part is equal to zero because the collision takes place in the zx plane, This gives

$$\begin{aligned} I_z &= \int_{-\infty}^{+\infty} \mathrm{d}t \, \frac{\mathrm{e}^{iKt} Z(t)}{R^3(t)} \\ I_x &= \int_{-\infty}^{+\infty} \mathrm{d}t \, \frac{\mathrm{e}^{iKt} X}{R^3(t)} \, . \end{aligned} \tag{6.19}$$

Operating:

$$\begin{aligned} I_z &= \int_{-\infty}^{+\infty} \mathrm{d}t \, \frac{\mathrm{e}^{iKt} vt}{(b^2 + (vt)^2)^{3/2}} \\ &= \frac{1}{bv} \int_{-\infty}^{+\infty} \mathrm{d}u \, \frac{u\mathrm{e}^{isu}}{(1+u^2)^{3/2}} \\ &= \frac{1}{bv} \left[is \int_{-\infty}^{+\infty} \mathrm{d}u \, \frac{\mathrm{e}^{isu}}{\sqrt{1+u^2}} \right] \\ &= \frac{1}{bv} \left[isK_0(s) \right] \, , \end{aligned} \tag{6.20}$$

and similarly for x,

$$\begin{aligned} I_x &= \int_{-\infty}^{+\infty} \mathrm{d}t \, \frac{\mathrm{e}^{iKt} b}{(b^2 + (vt)^2)^{3/2}} \\ &= \frac{1}{bv} \int_{-\infty}^{+\infty} \mathrm{d}u \, \frac{\mathrm{e}^{isu}}{(1+u^2)^{3/2}} \\ &= \frac{1}{bv} \left[-is \int_{-\infty}^{+\infty} \mathrm{d}u \, \frac{u\mathrm{e}^{isu}}{\sqrt{1+u^2}} \right] \\ &= \frac{1}{bv} \left[isK_1(s) \right] \, , \end{aligned} \tag{6.21}$$

where $u = \frac{vt}{b}$, $s = \frac{bK}{v}$ and $K_0(x)$ and $K_1(x)$ are the modified Bessel functions. This is a good place to stop following the method carried out by Seaton, this is because the analysis for the Stark case requires different mathematical steps to compensate for the asymmetric Stark states.

The modified Bessel functions, $K_0(x)$ and $K_1(x)$, can be solved by means of a polynomial approximation [16] for $0 < x \leq 2$:

$$\begin{aligned} K_0(x) &= -\log\left(\frac{x}{2}\right) I_0(x) \, - \, 0.57721566 \\ &\quad + 0.42278420 \left(\frac{x}{2}\right)^2 \, + \, 0.23069756 \left(\frac{x}{2}\right)^4 \\ &\quad + 0.03488590 \left(\frac{x}{2}\right)^6 \, + \, 0.00262698 \left(\frac{x}{2}\right)^8 \\ &\quad + 0.00010750 \left(\frac{x}{2}\right)^{10} \, + \, 0.00000740 \left(\frac{x}{2}\right)^{12} \, + \, \epsilon \end{aligned} \tag{6.22}$$

where the error $|\epsilon| < 10^{-8} x^{14}$ and

$$\begin{aligned} I_0(x) &= 1 \, + \, 3.5156229\, t^2 \, + \, 3.0899424\, t^4 \, + \, 1.2067492\, t^6 \\ &\quad + 0.2659732\, t^8 \, + \, 0.0360768\, t^{10} \, + \, 0.0045813\, t^{12} \, + \, \gamma \end{aligned} \tag{6.23}$$

with $t = \frac{x}{3.75}$ and the error $|\gamma| < 1.6 \times 10^{-7} t^{14}$. Similarly,

$$\begin{aligned} x\, K_1(x) &= x \log\left(\frac{x}{2}\right) I_1(x) \, + \, 1 \, + \, 0.15443144 \left(\frac{x}{2}\right)^2 \, - \, 0.67278579 \left(\frac{x}{2}\right)^4 \\ &\quad - 0.18156897 \left(\frac{x}{2}\right)^6 \, - \, 0.01919402 \left(\frac{x}{2}\right)^8 \\ &\quad - 0.00110404 \left(\frac{x}{2}\right)^{10} \, - \, 0.00004686 \left(\frac{x}{2}\right)^{12} \, + \, \nu \end{aligned} \tag{6.24}$$

where

$$\frac{I_1(x)}{x} = 0.5 + 0.87890594\,t^2 + 0.51498869\,t^4 + 0.15084934\,t^6 + 0.02658733\,t^8 + 0.00301532\,t^{10} + 0.00032411\,t^{12} + \nu \quad (6.25)$$

with $|\nu| < 7 \times 10^{-9} t^{14}$. For the purpose of this report, the limit of $0 < x \leq 2$ is valid. Abramowitz and Stegun [16] do provide equations for x within different limits using periodicity properties of K. A good way of testing these results is to compare the values produced using equations 6.22 and 6.24 with values given in tables from Seaton (1962) [55]. Although there are no specific values for $K_0(x)$ and $K_1(x)$, it is possible to produce an equation to match values given in tables from Seaton (1962) [55]. Therefore, if

$$\zeta(x) = x^2\,[K_0^2(x) + K_1^2(x)] \quad (6.26)$$

then it can be seen in figure 6.2 that equations 6.22 and 6.24 give good agreement to tabulated values given by Seaton.

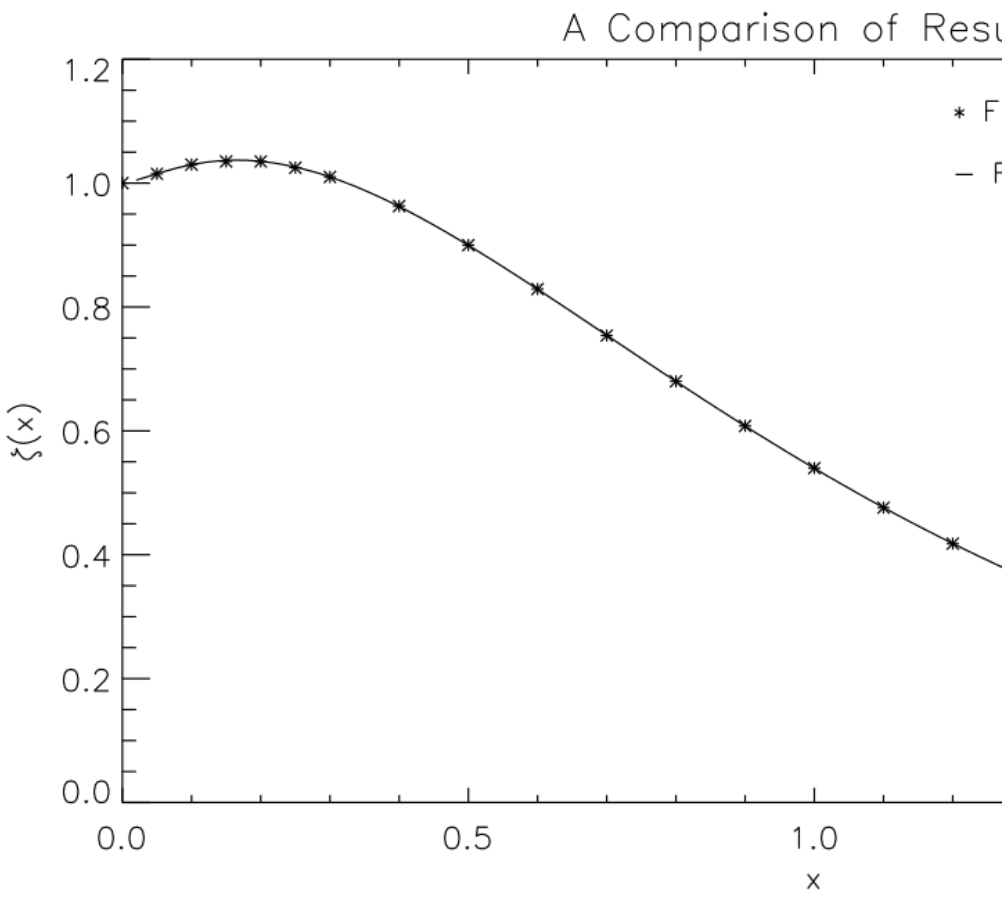

Figure 6.2: A comparison of results using equation 6.26 and from the table of values produced for the same equation in Seaton (1962) [55].

6.6 Charged Atoms

For the case of charged particle interaction, the orbit of the colliding particle is not a simple linear line, it follows hyperbolic pathways either towards or away from the target depending on whether the Coulomb force is attractive or repulsive. To follow the next steps, one should use the notation shown in figure 6.3.

Firstly, if electron–ion collisions are considered, μ is the reduced mass of the system, v is the colliding particles velocity and assuming the trajectory is in the zx plane, which we can describe in polar coordinates (R, θ) then the orbit

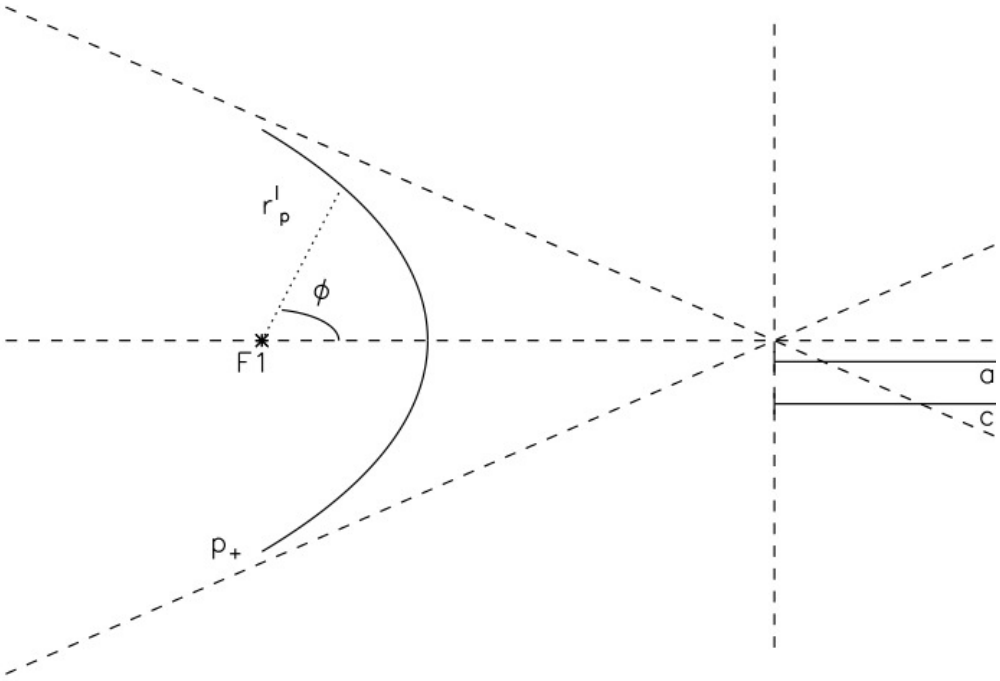

Figure 6.3: A figure showing the branching orbits for a positive and negative particle approaching a positive target.

is given by

$$R_e^{-1} = \frac{(1 - \epsilon\cos\theta)}{a(\epsilon^2 - 1)}, \tag{6.27}$$

where $a = \frac{Z_T Z_P e^2}{\mu v^2}$ is the hyperbole axis, $\epsilon = \sqrt{1 + \frac{\mu^2 v^4 R_i^2}{(Z_T Z_P)^2 e^4}}$ the eccentricity. The closest approach is when $\theta = \pi$, which yields $R_e^{-1} = \frac{1+\epsilon}{a(\epsilon-1)}$.

Now for ion–ion collisions, if μ is the reduced mass of the system, v is the colliding particles velocity and assuming the trajectory is in the zx plane the orbit is given by

$$R_p^{-1} = \frac{(1 + \epsilon\cos\theta)}{a(\epsilon^2 - 1)}. \tag{6.28}$$

The closest approach is when $\theta = 0$ which yields $R_p^{-1} = \frac{1+\epsilon}{a(\epsilon-1)}$ as in the ion–electron collision case. This value is not complete, it must be subtracted from the distance of the target to the focal point, f_1, which is equal to $2c$, therefore the closest approach is in fact $c + a$.

Burgess and Summers [56] provide a full detailed analysis on the steps involved in manipulating the integral into the form of the modified Bessel functions, $K_i(\xi\epsilon)$ and $K_i'(\xi\epsilon)$ where $\xi = pa/v$. It can be seen in figures 6.4 and 6.5 that these equations are also valid for the scenario detailed in the previous section, the figures show the orbits tending to their linear paths as the total charge is reduced, it should be noted that the procedure of solving the cross sections with this method will differ from that of Burgess and Summers due to the fact the Stark system is not isotropic. For the case of an isotropic atom, the interaction matrix may be factored out of the integration step, this step disregards any form of directionality, which must be kept in the Stark case.

To calculate the modified Bessel functions, $K_i(\xi\epsilon)$ and $K_i'(\xi\epsilon)$, the formulae given by Poquérusse and Alexiou

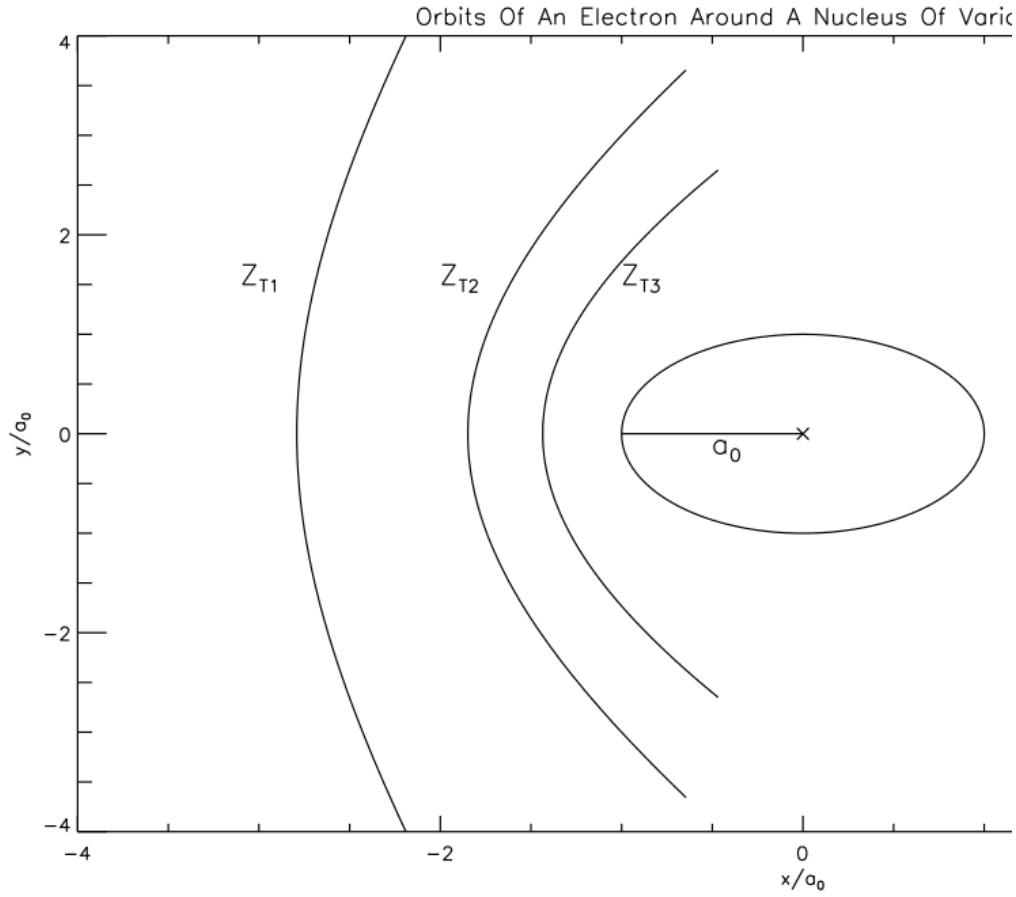

Figure 6.4: A trajectory model showing the paths of a negative colliding electron around a positive nucleus at position $x_0 = 0$, $y_0 = 0$ of various charge. Z_T represents $Z_e Z_i$ where $Z_e = 1$.

(1998) [59] are used, to summarise their results:

$$\begin{aligned} K_i(\xi\epsilon) &= e^{-\tau-\frac{\pi\xi}{2}} \frac{19h^4 + \log(1.06 + 1.07h^{-2})}{0.747 + 15.17h^5} \\ &\times\left[0.1275 + \frac{0.7 - 0.5\frac{\eta}{\epsilon}}{\epsilon^2} p^2 + 1.18\,p^3 + 0.47\,\frac{p^4}{\epsilon^2}\right. \\ &\left. + (1.97 + 1.6\,\epsilon^{-2})\,p^6 + p^9\right]^{-\frac{1}{18}} \end{aligned} \tag{6.29}$$

and

$$\begin{aligned} K_i'(\xi\epsilon) &= -e^{-\tau-\frac{\pi\xi}{2}} \frac{(0.282 - 0.1477\epsilon^{-2})h^{-3} + 0.335\epsilon^{-2} + 1.253h^3}{0.2905 - 0.1519\epsilon^{-2} - (0.1613 + 0.029\epsilon^{-2})\xi\epsilon^{-1} + h^5} \\ &\times\left[1.733 - 4\,\frac{\eta}{\epsilon}\,p^2 + \left(8.68 - 3.3\,\frac{\eta}{\epsilon}\right)p^3 + \left(7\,\frac{\eta}{\epsilon} + \frac{5}{\epsilon^2} - 7.43\right)p^4\right. \\ &\left. + \left(5.76 - 4\,\frac{\eta}{\epsilon}\right)p^6 + p^9\right]^{1/18} \end{aligned} \tag{6.30}$$

where

$$\begin{aligned} h &= (\xi\,\epsilon)^{1/3} \\ \eta &= \sqrt{\epsilon^2 - 1} \\ \tau &= \xi\,(\eta - \arctan(\eta)) \end{aligned} \tag{6.31}$$

and

$$p = \frac{\eta h}{\epsilon}\,. \tag{6.32}$$

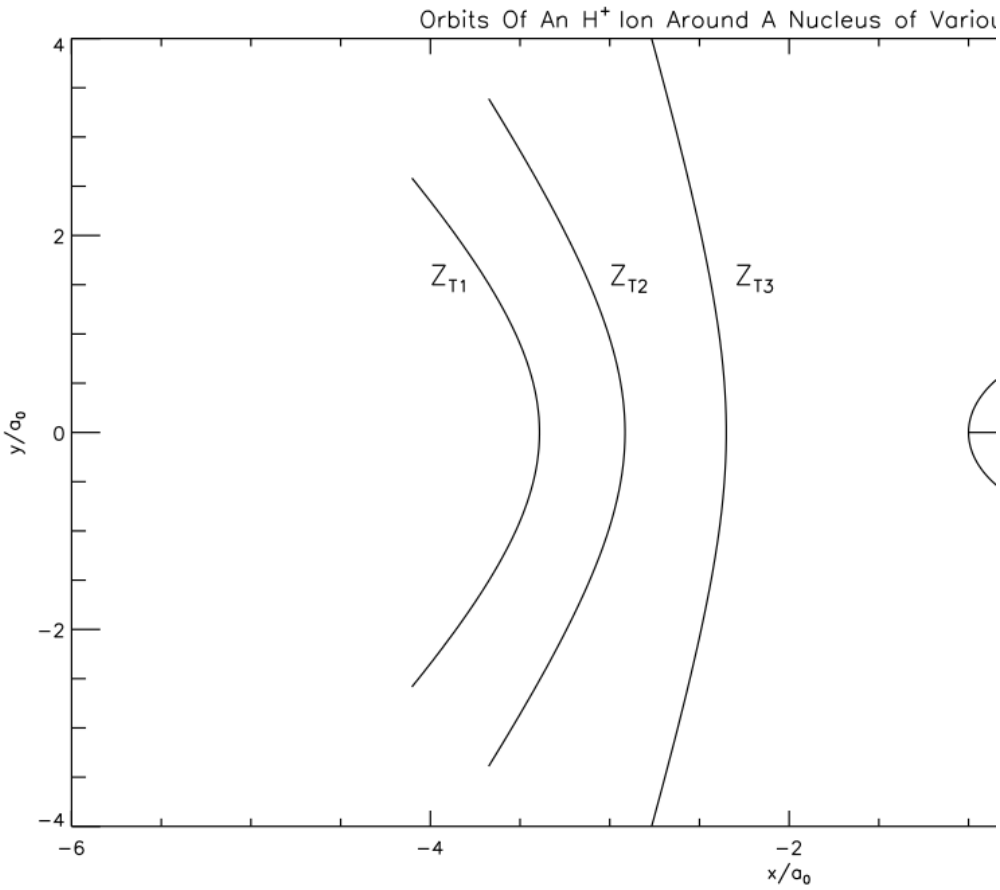

Figure 6.5: A trajectory model showing the paths of a colliding H^+ ion around a positive nucleus at position $x_0 = 0$, $y_0 = 0$ of various charge, Z_T. Z_T represents $Z_{iP}Z_{iT}$ where $Z_{iP} = 1$.

These formulae provide an accuracy of 0.1% or better over the entire (ξ, ϵ) half-plane. To provide a test for these equations, they may be compared against values given in tables from Burgess and Summers [56]. More specifically, the comparison will be against

$$X(\xi,\delta) \;=\; e^{\pi\xi}\,(\xi\epsilon)^2\left[K_i'^2(\xi\epsilon) \;+\; \frac{\epsilon^2-1}{\epsilon^2}\,K_i^2(\xi\epsilon)\right] \tag{6.33}$$

where $\delta = \xi\epsilon - \xi$. It is seen in figure 6.6 that the equations produce values which match the values given from Burgess and Summers.

6.7 Asymmetric Atoms

When the target is not spherically symmetrical the first difference with the symmetrical case is that the transition probability depends on the relative orientation of the target respect the colliding particle flux, so of the Euler angles in equation 6.3, so we get a directional transition amplitude $T(E,\vec{b};\Theta,\Phi,\Psi)$ and a directional cross section $\frac{d^3\sigma}{d\Theta d\Phi d\Psi}(E;\Theta,\Phi,\Psi)$. If we suppose a target randomly distributed we should measure an averaged cross section

$$\sigma_{if}(E) \;=\; \int_0^{\pi}\sin\Theta\,d\Theta\int_0^{2\pi}d\Phi\int_0^{2\pi}d\Psi\,\frac{d^3\sigma}{d\Theta\,d\Phi\,d\Psi}(E;\Theta,\Phi,\Psi)\,. \tag{6.34}$$

And if we expand expression 6.34 in terms of the transition probability we get

$$\sigma_{if}(E) \;=\; \int_0^{2\pi}d\phi\int_0^{\infty}b\,db\int_0^{\pi}\sin\Theta\,d\Theta\int_0^{2\pi}d\Phi\int_0^{2\pi}d\Psi\,P_{if}(E,b,\phi;\Theta,\Phi,\Psi)\,. \tag{6.35}$$

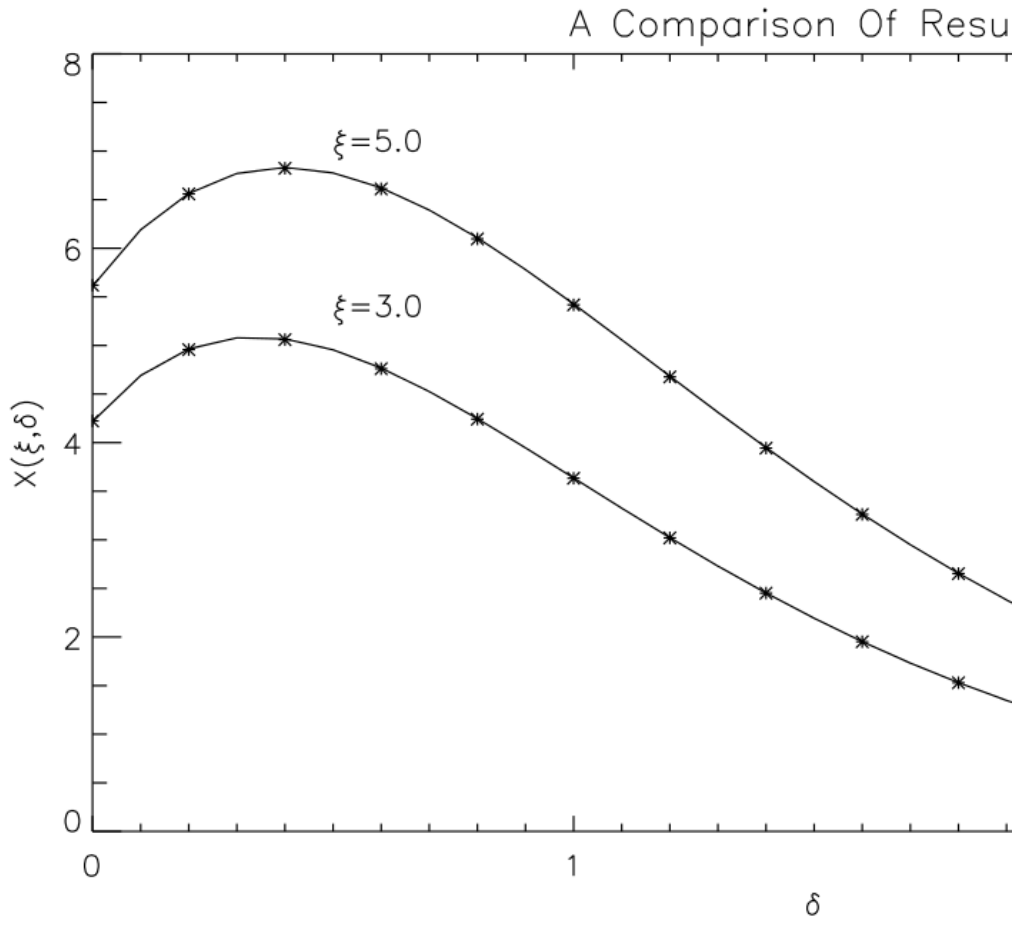

Figure 6.6: A comparison of results using equation 6.33 and from the table of values produced for the same equation in Burgess and Summers [56].

In terms of equation 6.35 we have to make the average in the angle of the impact parameter vector ϕ and the azimuthal orientation of the atom Φ. Both averages are equivalent, so making the one in the orientation of the target leads us again to a cylindrically symmetrical problem and taking advantage of it we can just calculate the transition probability versus just the module of b assuming symmetry for its orientation.

$$\sigma_{if}(E) \;=\; 2\pi \int_0^{\infty} b\,\mathrm{d}b \int_0^{\pi} \sin\Theta\,\mathrm{d}\Theta \int_0^{2\pi} \mathrm{d}\Phi \int_0^{2\pi} \mathrm{d}\Psi\, P_{if}(E, b; \Theta, \Phi, \Psi)\,. \tag{6.36}$$

Unfortunately this is not the case that assists our problem, because in a neutral beam injector of a tokamak the electric and the magnetic field are fixed in space, so we have a not randomly distributed target. In the other hand, neutrals penetrate in the plasma with a determined velocity and collision with electrons and ions which have an approximate Maxwellian velocity distribution, so the relative velocity between projectile and target is not isotropic and we can not use this approximation when we make the integral of the cross sections to obtain the rate coefficients. So we can not treat the problem from an "averaging" point of view and we need to keep all the information about the directional transition probability $P_{if}(E, \vec{b}; \Theta, \Phi, \Psi)$.

A second difference lays in equation 6.17, this time we can not assume a spherically symmetrical wave function, so we have to calculate all the components of the dipole moment $\langle \Psi_i | \vec{r} \Psi_f \rangle$ and we can not assume the collision taking place in the zx plane without loosing generality, so we have to calculate the three components $\langle z \rangle$, $\langle x \rangle$ and $\langle y \rangle$ of the vector.

6.7.1 Transition Probability

Before, in the isotropic case, one was able to calculate the cross sections integrated over a sphere. For the Stark case, it is necessary to integrate over all rectangular planes perpendicular to the z-axis, to begin the analysis, equation 6.17 should be considered, there will now be an additional z term added to provide a full description,

$$P_{if} = \frac{e^4}{\hbar^2}\left|\int_{-\infty}^{+\infty} \mathrm{d}t\, \mathrm{e}^{ipt}\left(\frac{Z(t)}{R^3(t)}\langle\Psi_{i\sigma}\,|\,z\,|\,\Psi_{j\eta}\rangle + \frac{X(t)}{R^3(t)}\langle\Psi_{i\sigma}\,|\,x\,|\,\Psi_{j\eta}\rangle + \frac{Y(t)}{R^3(t)}\langle\Psi_{i\sigma}\,|\,y\,|\,\Psi_{j\eta}\rangle\right)\right|^2 , \tag{6.37}$$

Now, splitting the integral into its I_z, I_x and I_y parts and setting the impact parameter vector as $\vec{b} = (X, Y)$, components which will remain constant as we assume straight-line trajectory, one obtains

$$\begin{aligned} I_z &= \int_{-\infty}^{+\infty} \mathrm{d}t\, \frac{vt\,\mathrm{e}^{ipt}}{(X^2 + Y^2 + v^2t^2)^{3/2}}\langle\Psi_i\,|\,z\,|\,\Psi_f\rangle \\ &= \frac{1}{bv}\int_{-\infty}^{+\infty} \mathrm{d}u\, \frac{u\,\mathrm{e}^{i\beta u}}{(1+u^2)^{3/2}}\langle\Psi_i\,|\,z\,|\,\Psi_f\rangle \\ &= \frac{i\beta}{bv}K_0(\beta)\langle\Psi_i\,|\,z\,|\,\Psi_f\rangle , \end{aligned} \tag{6.38}$$

$$\begin{aligned} I_x &= \int_{-\infty}^{+\infty} \mathrm{d}t\, \frac{X\,\mathrm{e}^{ipt}}{(X^2 + Y^2 + v^2t^2)^{3/2}}\langle\Psi_{i\sigma}\,|\,x\,|\,\Psi_{j\eta}\rangle \\ &= \frac{1}{bv}\int_{-\infty}^{+\infty} \mathrm{d}u\, \frac{\mathrm{e}^{i\beta u}}{(1+u^2)^{3/2}}\langle\Psi_{i\sigma}\,|\,x\,|\,\Psi_{j\eta}\rangle \\ &= \frac{iX\beta}{bv}K_1(\beta)\langle\Psi_{i\sigma}\,|\,x\,|\,\Psi_{j\eta}\rangle , \end{aligned} \tag{6.39}$$

and

$$\begin{aligned} I_y &= \int_{-\infty}^{+\infty} \mathrm{d}t\, \frac{Y\,\mathrm{e}^{ipt}}{(X^2 + Y^2 + v^2t^2)^{3/2}}\langle\Psi_{i\sigma}\,|\,y\,|\,\Psi_{j\eta}\rangle \\ &= \frac{Y}{bv}\int_{-\infty}^{+\infty} \mathrm{d}u\, \frac{\mathrm{e}^{i\beta u}}{(1+u^2)^{3/2}}\langle\Psi_{i\sigma}\,|\,y\,|\,\Psi_{j\eta}\rangle \\ &= \frac{i\beta Y}{bv}K_1(\beta)\langle\Psi_{i\sigma}\,|\,y\,|\,\Psi_{j\eta}\rangle , \end{aligned} \tag{6.40}$$

where

$$\begin{aligned} u &= \frac{vt}{b} \\ \beta &= \frac{pb}{v} \\ b^2 &= X^2 + Y^2 . \end{aligned} \tag{6.41}$$

Therefore, the transition probability is put back together in the form,

$$P_{if} = \frac{\mathrm{e}^4}{\hbar^2}\left|I_x + I_y + I_z\right|^2 . \tag{6.42}$$

The modified Bessel functions may be solved in the same manner as before for the neutral collision case.

6.8 Implementation

There are a lot of details that need to be discussed in the implementation of the asymmetric cross sections theory into code. Again, like with the field ionisation code, it is necessary to construct an isolated code which can be used to calculate the cross sections before they are implemented into ADAS305. This Fortran code was named *dircol*. However, there are many subroutines which make up the core of this code. The next subsections will describe each step.

6.8.1 Transition Probability

The analysis of the code will start with a 'bottom-up' approach. Therefore, the first part which should be considered is the evaluation of the modified Bessel functions, $K_{i\xi}(|\xi|\epsilon)$ and $K'_{i\xi}(|\xi|\epsilon)$. There are two situations which should be addressed: when $\xi = 0$ and $\xi \neq 0$. More specifically, when ξ is equal to zero, the scenario is that of the neutral atom, linear orbit case. When ξ is not zero, the analysis then turns to the parabolic orbit case. Both methods can be treated by a universal formula. However, when computing the functions, the case of $\xi = 0$ must be treated as a special case as $\xi \to 0$, $\epsilon \to \infty$.

Two subroutines were created, named *vk* and *vk*1. These can be viewed in appendix A.7 and A.7. They calculate the modified Bessel functions $K_{i\xi}(|\xi|\epsilon)$ and $K'_{i\xi}(|\xi|\epsilon)$ respectively. Equations 6.22 and 6.24 are used when $\xi \neq 0$. For the case of $\xi = 0$, equations 6.22 and 6.24 are used if the bracket term, x is less than or equal to two. It also incorporates formulae of periodicity from Abramowitz and Stegun [16] which deal with the case of $x > 2$. To operate, the parameters ξ and x must be passed into the function as real numbers.

With a method for calculating the modified Bessel functions in place, the next subroutine to be built calculates the transition probability. This subroutine was named *xs*. The code has the variables of speed, transition energy, impact parameter, Y value, rotation angles and the mean distribution of electrons, $\langle\psi_i|z|\psi_j\rangle$, $\langle\psi_i|x|\psi_j\rangle$ and $\langle\psi_i|y|\psi_j\rangle$ (denoted $\langle z\rangle$, $\langle x\rangle$ and $\langle y\rangle$ from here on) passed into the subroutine. The complex parts of the wave function and $I_{z,x,y}$ parts are split into their real and imaginary parts. The modified Bessel functions are then evaluated through a call to *vk* and *vk1* and then stored in their respective imaginary variables. The full equation is then put back together in the following way,

$$P_{ij} = (a^2 + b^2), \tag{6.43}$$

where a and b signify the summation of the imaginary and real parts respectively.

The wave functions and transition energy in this code had to be given reasonable estimates as actual results from ADAS305 were not yet available. Therefore, for testing, the mean value of $\langle z\rangle$, $\langle x\rangle$ and $\langle y\rangle$ from equations 6.38, 6.39 and 6.40 were initially made up to produce a dipole along the y-axis. This was done by setting the mean values $\langle z\rangle = \langle x\rangle = 0$ and $\langle y\rangle = 2a_0$ where a_0 is the Bohr radius. The case $\langle z\rangle = \langle x\rangle = \langle y\rangle$ represents the isotropic atom case. The energy transition was taken to be the energy between the $n = 3 \to 2$ transition ($\approx 1.9\,\text{eV}$). In addition, the beam speed was arbitrarily set in the initial stages of the code. It is important to make sure all of these constants are set as variables at the beginning of the code as once the code is put together and integrated with ADAS305, these will be variables passed into the code. Now the transition probability can be deduced as a function of speed, impact parameter, y-axis and the transition energy. These results are seen in figure 6.7.

Firstly, in graph 6.7(a), the probability is plotted against beam speed. As the speed tends to infinity, the transition probability tends to zero. This is as expected, the turning point somewhat completes the picture, this follows that as the beam starts from rest the probability is zero. As it speeds up the probability begins to increase until it hits a saturation point, after this the probability then exponentially decreases. In graph 6.7(b), the transition probability is plotted against the impact parameter. Here it is seen that as the impact parameter approaches zero, the probability tends above unity, the region therefore above $P = \frac{1}{2}$ corresponds to the strong coupling region. The next graph in 6.7(c) shows the relation between the transition probability and the change in y-axis, here the graph is similar to that of the 6.7(a). To understand this turning point one has to study the set up of the atom, the electrons are lying in lobe stretching out to twice the Bohr radius and the impact parameter has been set to the Bohr radius, therefore as the trajectory heads towards $Y = 0$, the probability will enter in the lobe of high electron distribution, as it continues to follow the trajectory it will then pass out the other end of the lobe into a region of low electron distribution, this corresponds to the turning point of the graph. However, when considering this problem, one must take account the dimensions of the atom, this graph will not take into account a 'direct hit' of the atom, this must be interpreted separately. Lastly, the graph shown in 6.7(d) shows how the transition probability varies with the transition energy, one can see that as you increase the energy between the transition the probability decreases, this is due to the fact that to produce a higher transition there must be stronger coupling of the collider atom with the target, through this hypothetical test, the code was thought to be running efficiently and giving out sensible results.

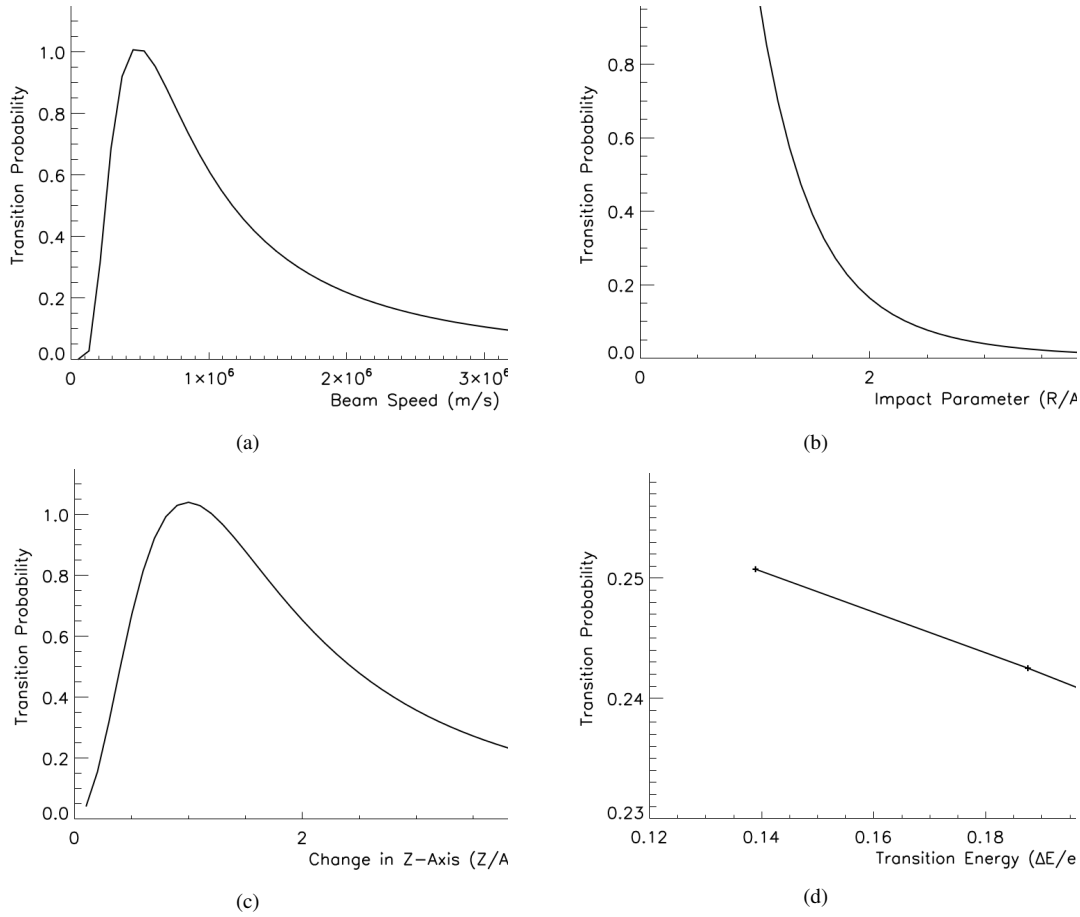

Figure 6.7: A graph of transition probabilities plotted against a) speed with $\Delta E = \mathrm{H}_\alpha$, $Y = X = 3a_0$ and $\theta = \varphi = 0$, b) impact parameter for $\Delta E = \mathrm{H}_\alpha$, $Y = a_0$, $v = 3 \times 10^6$ m/s and $\theta = \varphi = 0$, c) change in z-axis for $\Delta E = \mathrm{H}_\alpha$, $X = a_0$, $v = 3 \times 10^6$ m/s and $\theta = \varphi = 0$ and finally d) the change in transition energy for $Y = X = 2a_0$, $v = 3 \times 10^6$ m/s and $\theta = \varphi = 0$. The crosses marked in d) indicate the energies of the Balmer series starting at H_α. Each graph has an electron distribution of $2a_0$ along the y-axis.

6.8.2 Differential Cross Sections

The next section of the coding is to look at setting up the differential cross sections. This involves two integration processes over the X and Y parameters, when considering this, one must first look to define the regions of weak and strong coupling. The integration should only cover the weak-coupling region. As was shown in figure 6.7, the probability has the ability to form a turning point, this has the ability to cause confusion as to where to take the lower limit from in the integration as the probability may hit the specified cut off point twice, therefore, to carry out the integration over the impact parameter, one should look carefully at how this region is defined.

The integration over the X component of the impact parameter was carried out in the subroutine *intr*. The parameters θ, φ and Y along with the constants defined in the previous section are all passed into the code. The X component of the impact parameter is brought in from $\infty \rightarrow 0$, in coding terms, $50\,a_0$ was used to place the infinity. When the transition probability is equal to 0.001, the upper limit is stored, next, when the transition probability reaches higher than 0.5, the lower limit is stored. There are four scenarios which must considered to ensure the robustness of this code. Firstly, if the position of the projectile falls within the area of the atom then the impact parameter is increased until it is out with the boundaries of the atom, the lower limit is then set to this new value of X. Next, the impact parameter has a stationary point at some point along the curve and then decrease as X tends to zero, therefore, if the stationary point lies underneath the cut off of 0.5, then the code must store the value of X at this maximum for the lower limit, this can be done by checking the sign of the gradient. Thirdly, if there has been no turning point in gradient, the transition probability has stayed below 0.5 and the projectile lies out with the boundary of the atom then the impact

parameter can reach zero, however this scenario would cause an infinite loop, therefore a cut off is introduced whereby if the impact parameter reaches 0.1 a_0, then the lower limit is set to $X = 0$. Lastly, if the transition probability begins at a higher value than the upper limit, the upper limit is set to the first value of X, ensuring these scenarios are embedded within the code, there should be an inherent robustness for all projectile speeds.

With the upper and lower limits discussed, the focus is now turned to the method of integration, Simpson's rule is used to carry out this integration. The iteration process of the rule is set to twenty to save time whilst in the testing stage. On inspection, a higher iteration may be needed to gain a more accurate result, with each iteration the code calls the subroutine *xs* and passes in the respective values of X.

With this integration complete, the focus can be switched to the second integration over Y. The subroutine designed to carry out this step was called *intz*. There are two parameters passed into this code: θ, φ and the constants. Again, care must be taken on the procedure of finding the upper and lower limits, now the integration is from zero to infinity, the upper limit is set when the integral of X is equal to 0.01 and the lower limit is set equal to zero. To add robustness, there are now only two scenarios which must be considered. Firstly, if the initial conditions do not allow the integral to fall below 0.01, then a new upper limit is taken equal to the lowest value allowed. Lastly, if the initial conditions do not allow the integral to go above 0.01 then the code will produce an infinite loop, therefore a condition is added whereby if the gradient of the curve falls below 10^{-6} and the integral has not reached > 0.01, the upper limit is set to the outer most Y value calculated. The first scenario will only be evident at low collision speeds, whereas the second scenario would become evident at high collision speeds. Therefore it is important to allow the code to deal with any collision speed to avoid any unforeseen errors, the integration over X is again carried out by the use of Simpson's rule, the iteration process is set to twenty, again for a more accurate picture this could be increased.

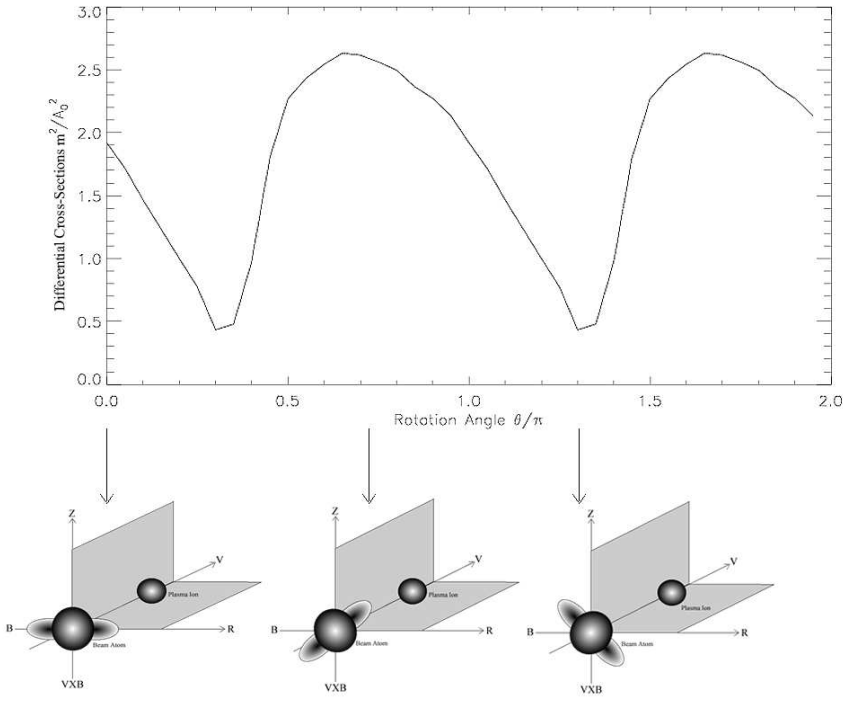

Figure 6.8: The differential cross section is plotted against the rotation angle θ. The φ angle is set to zero. The configuration of the atom can be seen for three points along the curve. A dipole along the z-axis is used as a starting point.

Now these two integrations are complete, the code can now be tested against the two rotation angles. The result of

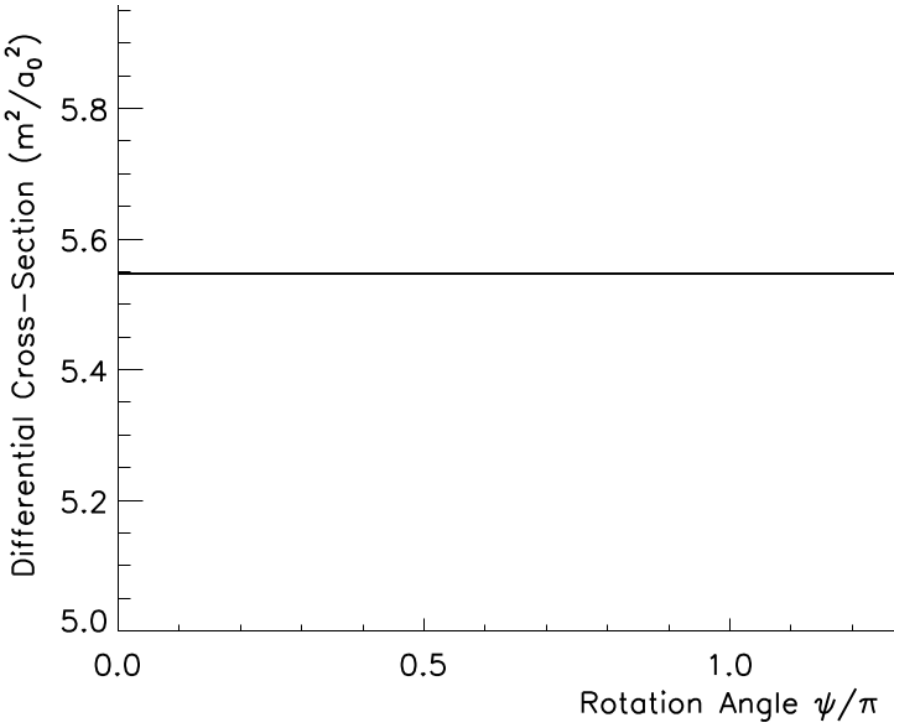

Figure 6.9: The differential cross section is plotted against the rotation angle φ. The θ angle is set to zero. A dipole is set along the y-axis.

the θ rotation for dipole along the z-axis is seen in figure 6.8, the differential cross section is calculated each time in the top left quadrant of the atom, therefore it is clear that when the distribution of the atoms is fully within this quadrant, the differential cross section goes to a maximum. Likewise, when it is totally out of this quadrant, there is a minimum. A rotation around the φ angle is seen in figure 6.9, here the differential cross section is a constant over the angle, that is due to the initial dipole being set along the y-axis. Had this been set along the x-axis, one would see a similar plot to that of figure 6.8.

6.8.3 Strong Coupling

So far, attention has been given to all configurations whereby the probability of a transition is less than 0.5 or within the atomic boundaries, the vector $\vec{R}$ is expected to form a continuous line around the atom depicting the region of strong-coupling, the method of calculating the area of this region requires an integration technique.

To integrate this region, the shape is first segmented into triangles originating from the origin of the atom, this can be seen more easily in figure 6.10a). However, before the area can be considered, detail must be given on how to obtain the vector points in an order which allows the vector array to go smoothly from start to finish. The method will not work if the vector points do not go in the order of the integration. In order to achieve this directionality, three loops are constructed over the quadrants, the impact parameter and the change in y-axis. The outer loop runs from $1 \rightarrow 4$ signifying each quadrant of the atom. When the top right quadrant is considered, the change in y-axis runs from ∞ to 0 and likewise for the impact parameter in the x-axis. In the second quadrant the change in y-axis runs from $-\infty$ to 0 and from ∞ to 0 for the impact x-axis. For the third quadrant, the change in y and x-axis runs from $-\infty$ to 0. Lastly, in the fourth quadrant the change in y-axis runs from ∞ to 0 and from $-\infty$ to 0 for the x-axis. This procedure allows the vector to be built in the order of integration.

The point which is stored in the vector array is theoretically defined as being the point at which the transition probability reaches 0.5, however there are few points where the probability is exactly 0.5 therefore a window of $(0.49, 0.51)$ is created, this means that for each theoretical single point there are a range of points, therefore the code must take an average of these points to output one singular point in the array. However, when doing this one must

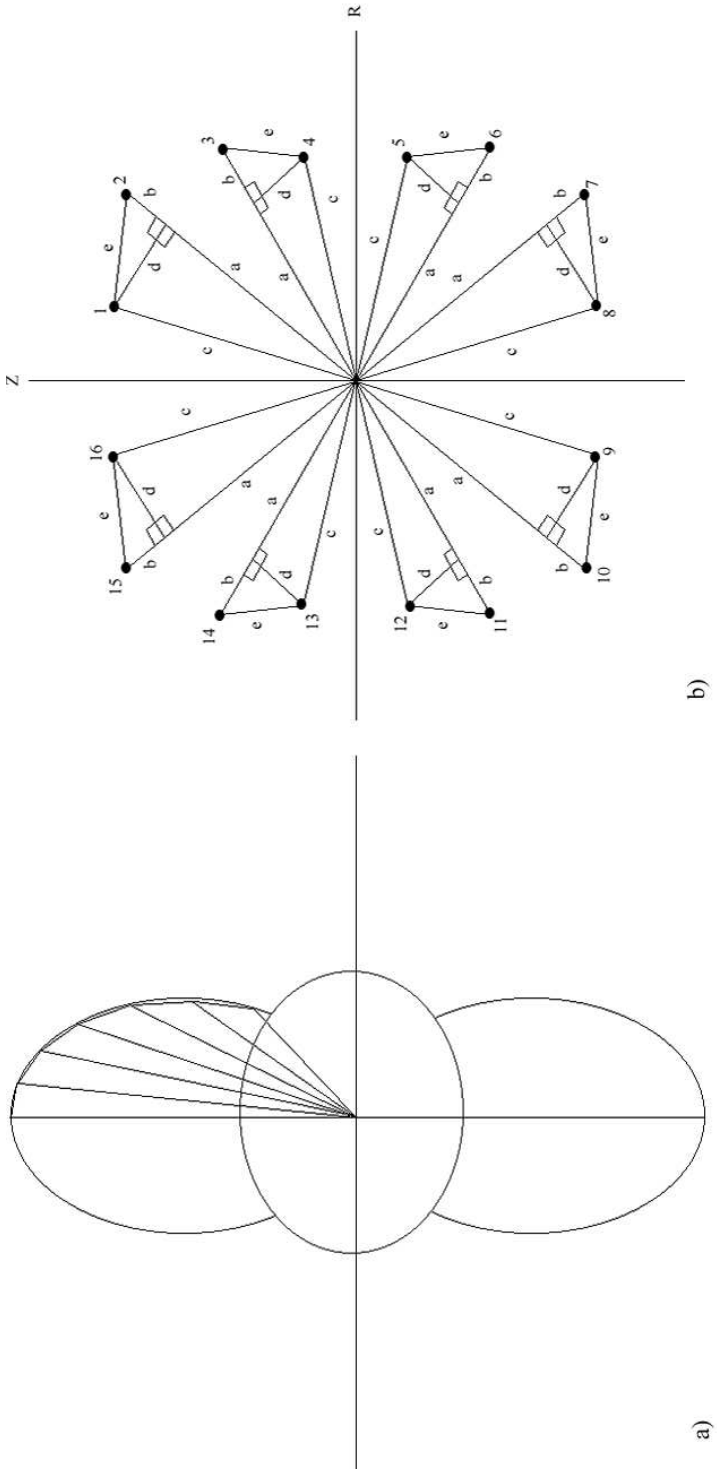

Figure 6.10: a) A diagram revealing the method of integration for the strong-coupling cross section regime and b) the geometry used in calculating the right-angled triangles.

consider the fact that depending on the orientation of the electron distribution, there may be two theoretical points in which the probability is 0.5, for example, if the electrons are distributed along the z-axis (R axis), then due to the shape of the lobe, the probability may go in and out of regions of high probability. Therefore, to avoid this second point being merely averaged out as a single point, the vector array is split into two sub-arrays, one can imagine the first array to run down the side of the lobe which has the second point and the second array to run down the other side of the lobe, these two arrays would therefore join at the point where the lobe has a stationary point with respect to a horizontal line being brought down from $Y = \infty \rightarrow 0$. Therefore, if the electron distribution is along the y-axis, only one sub-array will be populated as there would only be one theoretical point, in addition, if the vector goes within the boundary of the atom, no vector points are stored, this method of creating the array of vector points was created in the subroutine *qstrg1*.

Now, with the vector array complete, the routine used to work out the area, *irreg*, is discussed. For each quadrant of the atom, there are two shapes which can be both be split into two right-angled triangles, this is shown in figure 6.10b). To calculate the area of these triangles, the following method is used, the geometry will follow that used in the diagram, the numbers indicate vector points. For point $1 \rightarrow 2$,

$$\begin{aligned} c &= \sqrt{Y_1^2 + X_1^2} \\ e &= \sqrt{(Y_1 - Y_2)^2 + (X_2 - X_1)^2} \\ a &= c\,[\cos\alpha] \\ b &= \sqrt{Y_2^2 + X_2^2} - a \\ d &= \sqrt{c^2 - a^2}\,, \end{aligned} \tag{6.44}$$

where α is the angle between $\vec{R_1}$ and $\vec{R_2}$ and the area x_1 is worked out as

$$x_1 = \frac{1}{2}\,ad + \frac{1}{2}\,db\,. \tag{6.45}$$

For points $3 \rightarrow 4$,

$$\begin{aligned} c &= \sqrt{Y_4^2 + X_4^2} \\ e &= \sqrt{(Y_3 - Y_4)^2 + (X_3 - X_4)^2} \\ a &= c\,[\cos\alpha] \\ b &= \sqrt{Y_3^2 + X_3^2} - a \\ d &= \sqrt{c^2 - a^2} \end{aligned} \tag{6.46}$$

where α is the angle between $\vec{R_3}$ and $\vec{R_4}$ and the area, x_2, is worked out as

$$x_2 = \frac{1}{2}\,ad + \frac{1}{2}\,db\,. \tag{6.47}$$

Therefore, the total area, y_1, for the first quadrant is

$$y_1(\vec{R}) = \sum_i x_i \tag{6.48}$$

where i runs over all the triangles in the quadrant. The method is repeated now over all the quadrants so that the final area is built through

$$A(\vec{R}) = \sum_{j=1}^{4} y_j \tag{6.49}$$

where j runs through each quadrant.

To test this method, vectors of known areas and shapes were passed into the code and tested against their theoretical area, the results of this can be seen in table 6.1. It is clear that this code is producing results within a suitable range, it is important when testing this code to remember that the code calculates the area by presuming the segments are

Shape	Actual Area	Calculated Area
Square	16.00	16.00
	64.00	64.00
Right Angled Triangle	15.75	15.75
Scalene Triangle	0.752	0.75
Circle	12.566	12.461
	113.097	112.149
	452.389	448.596

Table 6.1: The subroutine *irreg* is used to calculate areas of shapes with known theoretical area. The calculated area is through use of *irreg*.

starting from the origin, $(0, 0)$, therefore the vectors of the shapes must be built around the origin. This does put a restriction on the code, however, for the case of calculating the strong-coupling region this restriction does not hinder the process as the vector is built with respect to the origin.

Therefore now the code can include the strong-coupling region, it is important to further test the code by producing graphs of what areas are actually being calculated. The strong-coupling region can be seen in figure 6.11 as a function of rotation angle, it is difficult to produce the area with an associated error as there is no actual area already calculated, therefore the accuracy or reliability of these results are based upon the codes ability to reproduce areas given in table 6.1 and by viewing the calculated area.

6.8.4 Total Cross Sections

The code is now at a stage where the full cross sections can be calculated, therefore the integration over the solid angle must now be implemented. Due to the method of calculating the strong-coupling regime, the code performs more efficiently re-writing equation 6.35 as

$$\sigma_{if} = \frac{1}{2\pi\Psi} \int_0^{\Psi} \sin\Theta \, \mathrm{d}\Theta \left[A(\vec{R}, \Theta) + \int_0^{2\pi} \mathrm{d}\Phi \int_0^{\infty} \mathrm{d}X \int_{R_1}^{\infty} \mathrm{d}Y \, P_{if}(\Theta, \Phi, X, Y) \right], \tag{6.50}$$

where we suppose the target cylindrically symmetrical. The integral over the azimuthal angle Φ is carried out in the subroutine *intt*, this sets the upper and lower limits as 2π and 0 respectively, then Simpson's rule is initiated, after this integration step is complete, the last integral over the polar angle Θ is started. The subroutine used to calculate this is called *intp*, the upper limit is set through v_p given in equation **??** and the equation for Θ given in equation **??** and the lower limit is set as 0. In the special case of the upper limit equalling zero, the integration over Θ is skipped and the factor of $\frac{1}{\Theta}$ in equation 6.50 is disregarded. On each call to *intt*, the three integral result passed back is added to the strong-coupling region.

The final cross sections as a function of field can be seen in figure 6.12, the jagged part near the turning point can be attributed to the strong-coupling region effects. The method of calculating the vector $\vec{R}$ when calculating the area is often slightly volatile at different conditions, the cross sections are given in terms atomic units (a_0^2), this provides good confidence that the code is passing out sensible results. It is also still evident that the cross sections increase with speed up to a certain point, an then begin exponentially decrease.

This code has not yet been integrated in ADAS305 due to time limitations, however the calling routine *xsec* is set up to accept the variables from ADAS305 which are needed to calculate these cross sections. The parameters needed from ADAS305 are the electron wave-functions, the transition energy of the perturbed Stark states, the speed of the beam atoms and the temperature of the plasma species. With these in place, the cross sections can be calculated for the Stark states.

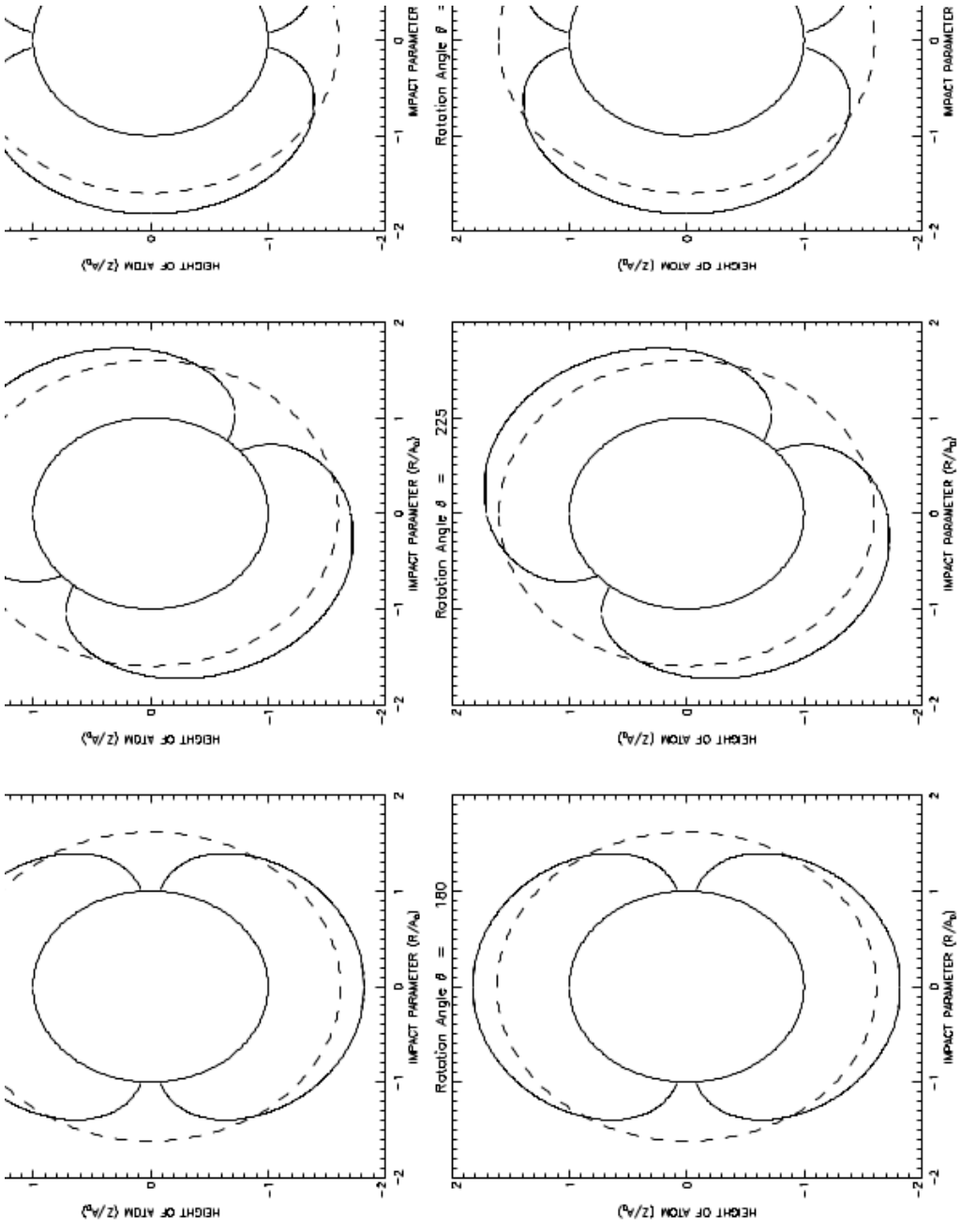

Figure 6.11: The strong-coupling region is plotted as a function of electron distribution at rotation angle 0, the electrons are distributed along the y-axis with $\langle y \rangle = 2a_0$, where a_0 is the Bohr radius. The dotted line represents the strong-coupling area calculated by the subroutine *irreg*, the central circle represents the atom boundaries, the lobes represent the region of strong-coupling, the x-axis shows the impact parameter divided by the Bohr radius and the y-axis shows the change in y-axis divided by the Bohr radius.

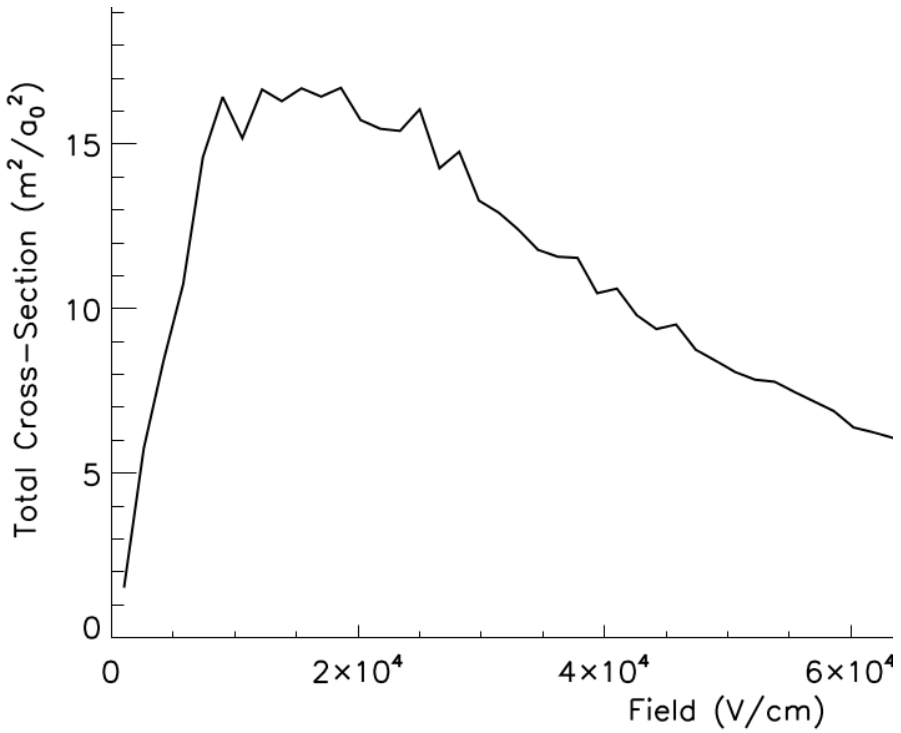

Figure 6.12: The final cross section as a function of field with a magnetic field of 2 T, the plasma temperature is set to 1×10^5 K, the transition energy was set to the H_α line.

Chapter 7

Summary

There are two main sections which should be discussed in this chapter. Firstly, the ways in which the implementation of the theory can be improved will be discussed, this will include any areas which aren't working as expected and detail how to improve areas which are working but could still be improved. Next, the future work of the project will be discussed, any areas which weren't reviewed due to time restrictions will be detailed. Lastly, a final conclusion of where the project got to will be given in the last section of this chapter.

7.1 Improvements

Firstly, the implementation of the field ionisation code will be discussed. When implementing the two regimes of low and medium field regimes, no real cut-off point was given, a graph of the two methods was given in figure 3.2, this gave a rough idea of where the cut-off point lay. A more accurate way of finding the point could be found by studying the theory of Damburg and Kolosov (1978) [44] and Kolosov (1983) [49] in more detail, they provide theory based on certain assumptions, these assumptions should be highlighted and studied more closely.

In addition to this cut-off point, there were unpredicted results calculated when dealing with negative values of the magnetic quantum number, m. In these states, the ionisation rates gave much higher results than expected, the theory states that the electrons should be degenerate with respect to the sign of m, therefore it is important to check that throughout the code, the absolute value of m has been used. If this is not the case, the theory may break down at negative values of m and give these unusually high ionisation rates.

Now, switching focus to the cross section implementation, the first section which needs to be revised is the way in which the vector of the strong-coupling region is stored. It is evident from the graph in figure 6.12 that the strong-coupling area is not a smooth function of beam speed, after further investigation this was found to be caused by deviations in the vector away from the smooth area that should be calculated, in addition when the strong-coupling area becomes comparable with the size of the atom, an area is neglected which at high areas of strong-coupling is negligible but becomes valid at small areas. This is due to the fact that the lobe which is calculated does not take into account the area of the atom, therefore when the lobe hits the sphere of the atom, the vector should then follow the perimeter of the atom round to the beginning of the next lobe. This feature has not yet been included in the code, the vector stops at this point, therefore the pseudo-triangular segment of the atom between the two lobes is not added to the final area. For increased accuracy in results, this method of calculating the vector should therefore be revised.

Lastly, still on the topic of the strong-coupling region, the method for finding the vector also takes a lot of computational time, this is due to the fact that the method involves scanning the entire atom at every integration step of the Θ integral, this could be altered by combining the strong-coupling region into the integral of Φ. This integral basically produces a scan of the whole atom for the weak coupling region by use of rotation, if the strong-coupling region was calculated for each quadrant of the atom simultaneously with the calculation of the weak coupling regime, this may increase the speed at which the code calculates the final cross section.

7.2 Future Work

The first, most immediate area of further research should be given to finding a method of calculating the field ionisation rates for the strong-field regime. There are no papers available to the knowledge of this report that provide simple, analytical formulae for this regime, therefore either a new set of equations may need to be revised or an implementation of one of the current, more drawn out methods should be implemented (Kolosov, 1987 [48]; Tian, 2002 [43]). This should provide an insight into the hypothesised theoretical asymmetry occurring in the beam emission of the atom.

The cross section isolated analysis is by all means complete, therefore detail must now be given to how this code is implemented into the final code ADAS305. In doing this, one must look at how to pull out the wave functions of the electrons in a way which can then be passed into the cross section code giving the distribution of the electrons. In addition, the transition energy must be passed in as a variable, although this step is already somewhat complete through previous work done on ADAS305. Once this has been done, the cross sections should be compared with previous results calculated by ADAS305, furthermore the current calculations largely focused on linear orbits for the impact parameter, this is valid for the case of neutral beams, however a more complete picture would include an analysis of the elliptic orbits for two charged particles colliding.

Lastly, the labelling of states should be revised in more detail, this is will provide a way of telling whether the magnetic or electric field is the dominant perturbation. With this knowledge, experimentalists may accurately tell which polarisations to expect at the respective orientations of the polarisers. A way of finding these labelling was discussed in section 2.7, however there was not enough time to actually implement this theory, therefore, a further topic of investigation could be to implement the transformation of the angular and other matrices and form a grading system to label the quantum numbers.

7.3 Conclusions

The full picture has now been discussed. In chapter 2, a full description of the general theory behind the way in which an atom is effected when passing through a field is discussed, in addition a method was put forward for a way of labelling the states when dealing with two perturbative fields. This produced a normalised 'grade' that indicates the purity of either the nkm or $nlm_l m_s$ basis states. The report then focused on one aspect of the field theory in chapter 3, the ability of the field to remove an electron entirely from the atom. It was seen that the ionisation theory could be split into three regimes: low, medium and strong field, a description of the first two was described with the third regime remaining a topic for further investigation. This theory was then implemented into the population structure of the atom in chapter 5, different aspects of the atom were discussed in this chapter including the way in which the atom cascades down to its relaxed state when lying in an excited state, the electron tended to stick to its relative k quantum number as it relaxed down to lower levels, this meant that indirect effects of the high shells on the H_α multiplet must be taken into consideration, it was seen that the field ionisation did reduce the intensity of the total Stark multiplet for the H_α emission line, the results were then implemented in ADAS305 and the three main processes of radiative decay, collisions and field ionisation were compared. The hypothesised theoretical asymmetry was not evident due to the high field regime producing unrealistic results.

The report then moved on to discuss the collisional cross sections in chapter 6. A review of previous methods detailing the isolated atom case where the electrons are lying in their isotropic states was first provided, this was then extended to deal with electrons lying in their perturbed Stark states, a full description of the theory behind the new calculations was provided and then the implementation of the theory was described. The final results showed the code giving out sensible results, in terms of the area of the atom, however these were not implemented into the final code, ADAS305, due to time restrictions.

It is evident therefore, that these effects should be revised in further detail to provide a better understanding of the processes involved when the beam atoms travel at a certain speed across a magnetic field. Now, there is a starting point which further investigations can be based on. There is good evidence to suggest that these two areas could have a significant effect on the generated emission line from ADAS305. This is important for the future diagnosis of ITER and for the overall understanding of the beam emission.

Bibliography

[1] S. S. Henderson. 'Collisional Radiative Modelling and Population Structure of Resolved Angular Momentum States in Hydrogen and Helium'. 4th yr. dissertation, University of Strathclyde (2009)

[2] G. M. McCracken and P. Stott. *Fusion: The Energy of the Universe*. Elsevier Academic Press (2005). ISBN 978-0124818514

[3] J. Wesson. *Tokamaks, 4th Edition*. Oxford University Press (2011). ISBN 978-0199592234

[4] D. Ciric. 'JET Neutral Beams – Yesterday, Today and Tomorrow' (2010). EFDA–JET Science Meeting: Neutral Beams in JET, ITER and DEMO

[5] R. McAdams. 'Negative ion beams for ITER' (2010). EFDA–JET Science Meeting: Neutral Beams in JET, ITER and DEMO

[6] G. Duesing, H. Altmann, H. Falter, A. Goede, R. Haange, R. S. Hemsworth, P. Kupschus, D. Stork and E. Thompson. 'Additional heating systems for JET: Neutral Beam Injection system'. Fusion Technology, **11** (1987) 163–202

[7] G. F. Matthews. 'Overview of the ITER-like wall project'. Phys. Scr., **T128** (2007) 137–143. doi:doi:10.1088/0031-8949/2007/T128/027

[8] D. H. McNeil. 'H-alpha photon yield in fuelling of tokamaks'. J. Nucl. Mater., **162–164** (1989) 476–481. doi:10.1016/0022-3115(89)90315-2

[9] M. G. von Hellermann, G. Bertschinger, W. Biel, C. Giroud, R. Jaspers, C. Jupen, O. Marchuk, M. O'Mullane, H. P. Summers, A. Whiteford and K.-D. Zastrow. 'Complex Spectra in Fusion Plasmas'. Physica Scripta, **2005**(T120) (2005) 19. Available from: http://stacks.iop.org/1402-4896/2005/i=T120/a=003

[10] E. Källne, J. Källne, E. S. Marmor and J. E. Rice. 'High Resolution X-Ray Spectroscopy Daignotics of High Temperature Plasmas'. Physica Scripta, **31**(6) (1985) 551. doi:10.1088/0031-8949/31/6/016

[11] A. Boileau, M. von Hellermann, L. D. Horton, J. Spence and H. P. Summers. 'The deduction of low-Z ion temperature and densities in the JET tokamak using charge exchange recombination spectroscopy'. Plasma Phys. Control. Fusion, **31**(5) (1989) 779–804. doi:10.1088/0741-3335/31/5/006

[12] W. Mandl, R. C. Wolf, M. G. von Hellermann and H. P. Summers. 'Beam emission spectroscopy as a comprehensive plasma diagnostic tool'. Plasma Phys. Control. Fusion, **35**(10) (1993) 1373–1394. doi:10.1088/0741-3335/35/10/003

[13] F. M. Levinton, R. J. Fonck, G. M. Gammel, R. Kaita, H. W. Kugel, E. T. Powell and D. W. Roberts. 'Magnetic field pitch-angle measurments in the PBX-M tokamak using the motional Stark effect'. Phys. Rev. Lett., **63**(17) (1989) 2060–2063. doi:10.1103/PhysRevLett.63.2060

[14] A. Boileau, M. von Hellerman, W. Mandl, H. P. Summers, H. Weisen and A. Zinoviev. 'Observations of motional Stark features in the Balmer spectrum of deuterium in the JET plasma'. J. Phys. B, **22**(7) (1989) L145–L152. doi:10.1088/0953-4075/22/7/002

[15] B. den Hartog, J. Ko, D. den Hartog and D. Craig. 'MSE Spectral Analysisd on the Madison Symmetric Torus'. In 'ADAS Workshop', (2009). Schloss Ringberg, Germany. 4–7 October. Available from: http://www.adas.ac.uk/2009talks/2009_ADAS_Bdenhartog.ppt

[16] M. Abramowitz and I. A. Stegun. *Handbook of Mathematical Functions*. Dover Publications Inc. (1965). ISBN 978-0486612720 (1965 paperback)

[17] H. A. Bethe and E. E. Salpeter. *Quantum Mechanics of One- and Two-Electron Atoms*. Dover Publications Inc. (2009). ISBN 978-0486466675 (paperback)

[18] A. Messiah. *Quantum Mechanics*. Dover Publications Inc. (2003). ISBN 978-0486409245

[19] B. H. Bransden and C. J. Joachain. *Introduction to Quantum Mechanics*. Prentice Hall (2000). ISBN 978-0582356917

[20] J. Stark. 'Observations of the effect of the electric field on spectral lines I. Transverse effect'. Annalen der Physik, **43** (1914) 965–983

[21] E. U. Condon and G. H. Shortley. *The Theory of Atomic Spectra*. Cambridge University Press (1935). ISBN 0521092094 (1991 paperback)

[22] T. F. Gallagher. *Rydberg Atoms*. Cambridge University Press (2005). ISBN 978-0521021661 (paperback)

[23] E. Schrödinger. 'Quantification of the eigen value problem'. Annalen der Physik, **80**(13) (1926) 437–490. doi:10.1002/andp.19263851302

[24] P. S. Epstein. 'The Stark effect from the point of view of Schroedinger's quantum theory'. Phys. Rev., **28** (1926) 695–710

[25] B. Thaller. *Advanced Visual Quantum Mechanics*. Springer (2005). ISBN 978-0387207773

[26] Y. Ishida and S. Hiyama. Sci. Pap. Inst. Phys. and Chem. Res., Tokyo, **152**

[27] M. Courtney, N. Spellmeyer, H. Jiao and D. Kleppner. 'Classical, semiclassical, and quantum dynamics in the lithium Stark system'. Phys. Rev. A, **51**(5) (1995) 3604–3620. doi:10.1103/PhysRevA.51.3604

[28] D. Park. 'Relation between the parabolic and spherical eigenfunctions of hydrogen'. Zeitschrift für Physik, **159**(2) (1960) 155–157. doi:10.1007/BF01338343

[29] C. Cohen-Tannoudji, B. Diu and F. Laloë. *Quantum Mechanics, Vol. 2*. J. Wiley, New York. (1977). ISBN 978-0471164356

[30] J. H. Poynting. 'On the Transfer of Energy in the Electromagnetic Field'. Phil. Trans, **175** (1884) 277

[31] J. R. Oppenheimer. 'Three Notes on the Quantum Theory of Aperiodic Effects'. Phys. Rev., **31** (1928) 66–81. doi:10.1103/PhysRev.31.66

[32] H. R. von Traubenberg. 'Über den Starkeffekt II. Ordnung bei der Balmerserie des Wasserstoffs. I'. Zeitschrift für Physik, **54** (1929) 307

[33] H. R. von Traubenberg. 'Über den Starkeffekt II. Ordnung bei der Balmerserie des Wasserstoffs. II'. Zeitschrift für Physik, **56** (1929) 254–258

[34] C. Lanczos. Z. Physik, **62** (1930) 518–544

[35] D. S. Bailey, J. R. Hiskes and A. C. Riviere. 'Electron Field Ionization Probabilities for the Hydrogen Atom'. Nucl. Fusion, **5** (1965) 41–46

[36] B. M. Karnakov and V. P. Krainov. *WKB Approximation in Atomic Physics*. Springer (2012). ISBN 978-3642315572

[37] M. H. Rice and R. H. Good. 'Stark effect in hydrogen'. J. Opt. Soc. Amer., **52**(3) (1962) 239–246. doi:10.1364/JOSA.52.000239

[38] M. H. Alexander. 'Exact Treatment of the Stark Effect in Atomic Hydrogen'. Phys. Rev., **178**(1) (1969) 34–40. doi:10.1103/PhysRev.178.34

[39] M. Hehenberger, H. V. McIntosh and E. Brändas. 'Weyl's theory applied to the Stark effect in the hydrogen atom'. Phys. Rev. A, **10**(5) (1974) 1494–1506. doi:10.1103/PhysRevA.10.1494

[40] R. J. Damburg and V. V. Kolosov. 'A hydrogen atom in a uniform electric field'. J. Phys. B, **9**(18) (1976) 3149–3157. doi:10.1088/0022-3700/9/18/006

[41] E. Luc-Koenig and A. Bachelier. 'Systematic theoretical study of the Stark spectrum of atomic hydrogen. I. Density of continuum states'. J. Phys. B, **13**(9) (1980) 1743–1767. doi:10.1088/0022-3700/13/9/009

[42] D. Farrelly and W. P. Reinhardt. 'Uniform semiclassical and accurate quantum calculations of complex energy eigenvalues for the hydrogen atom in a uniform electric field'. J. Phys. B, **16**(12) (1983) 2103–2117. doi:10.1088/0022-3700/16/12/008

[43] R. Tian. Chin. Phys. Lett, **20** (2002) 4

[44] R. J. Damburg and V. V. Kolosov. 'An asymptotic approach to the Stark effect for the hydrogen atom'. J. Phys. B, **11**(11) (1978) 1921–1930. doi:10.1088/0022-3700/11/11/009

[45] G. F. Drukarev. 'Highly excited states of the hydrogen atom in an electric field'. Zh. Eksp. Teor. Fiz., **75** (1978) 473–483

[46] M. B. Kadomtsev and B. M. Smirnov. 'Decay of highly excited atoms in an electric field'. Zh. Eksp. Teor. Fiz., **80** (1981) 1715

[47] G. F. Drukarev. 'Top energy levels of the hydrogen atom in an electric field'. Zh. Eksp. Teor. Fiz., **82** (1982) 1388–1392

[48] V. V. Kolosov. 'A hydrogen atom in a strong electric field'. J. Phys. B, **20**(11) (1987) 2359–2367. doi:10.1088/0022-3700/20/11/008

[49] V. V. Kolosov. 'Stark effect near the peak of the potential barrier'. J. Phys. B, **16**(1) (1983) 25–31. doi:10.1088/0022-3700/16/1/004

[50] W. P. Reinhardt. 'Complex coordinates in the theory of atomic and molecular structure and dynamics'. Ann. Rev. Phys. Chem., **33** (1982) 223–255. doi:10.1146/annurev.pc.33.100182.001255

[51] Y. K. Ho. 'The method of complex coordinate rotation and its application to atomic collision'. Physics Reports, **99**(1) (1983) 1–68. doi:10.1016/0370-1573(83)90112-6

[52] C. Y. Lin and Y. K. Ho. 'Complex scaling in Lagrange-mesh calculations for Stark shifts and widths of the screened Coulomb potential'. J. Phys. B, **44**(17) (2011) 175001. doi:10.1088/0022-3700/13/9/009

[53] D. Baye and P. H. Hennen. 'Generalised meshes for quantum mechanical problems'. J. Phys. A, **19**(11) (1986) 2041–2059. doi:10.1088/0305-4470/19/11/013

[54] M. Vincke, L. Malegat and D. Baye. 'Regularization of singularities in Lagrange-mesh calculations'. J. Phys. B, **26**(5) (1993) 3811–826. doi:10.1088/0953-4075/26/5/006

[55] M. J. Seaton. 'The impact parameter method for electron excitation of optically allowed atomic transitions'. Poc. Phys. Soc, **79**(3) (1962) 1105–1117. Available from: http://iopscience.iop.org/0370-1328/79/6/304

[56] A. Burgess and H. P. Summers. 'The recombination and level populations of ions. I - Hydrogen and hydrogenic ions'. Mon. Not. R. Astr. Soc., **174** (1976) 345–391. ADS: http://adsabs.harvard.edu/abs/1976MNRAS.174..345B

[57] G. B. Arfken, H. J. Weber and F. E. Harris. *Mathematical Methods for Physicists, 6th edition*. Academic Press (2005). ISBN 978-0120598762

[58] L. Fernández-Menchero. *Intercambio de carga, disociación y excitación vibracional en colisiones ión–molécula. Estudio teórico de colisiones ión–*H_2. Ph.D. thesis, Universidad Autónoma de Madrid (2005)

[59] P. Angelo, H. Derfoul, P. Gauthier, P. Sauvan, A. Poquerusse, T. Ceccotti, E. Leboucher-Dalimier, T. Shepard, C. Back, M. Vollbrecht, I. Uschmann and E. Förster. 'Generation of hot and dense plasmas in laser accelerated colliding foil systems'. Laser and Particle Beams, **16** (1998) 21–30

Appendix A

Coding

A.1 Adas305 Expansion

```
C DATE     : 07-08-2009
C MODIFIED : Stuart Henderson
C              - Increased Stark resolved matrix up to n=8
C Dimension Analysis:
C           Variable             Dimension()/Value
C           ---------------------------------------------------------
C           ndmx                 (Sum_{n=1}^{nmax}2*n^2)+(nmaxb-nmax-2)
C           mwave                 Unknown(ndcomp must be equal to mwave)
C           ipar()               (Sum_{1}^{nmax}2*n^2)+(nmaxb-nmax)
C           na()                 (Sum_{1}^{nmax}2*n^2)+(nmaxb-nmax)
C           cmatr(,)             (2*n^2,2*n^2)
C           cmati(,)             (2*n^2,2*n^2)
C           vr(,)                (2*n^2,2*n^2)
C           vi(,)                (2*n^2,2*n^2)
C           vupr(,)              (2*n^2,2*n^2)
C           vupi(,)              (2*n^2,2*n^2)
C           vlowr(,)             (2*n^2,2*n^2)
C           vlowi(,)             (2*n^2,2*n^2)
C           rup()                 2*n^2
C           vstkr()              (2*n^2(2*n^2-1)+2*n^2)+sum_{n=1}^{n-1}(
C                                 2*n^2(2*n^2-1)+(2*n^2-1))
C           vstki()              (2*n^2(2*n^2-1)+2*n^2)+sum_{n=1}^{n-1}(
C                                 2*n^2(2*n^2-1)+(2*n^2-1))
C           estk()               (Sum_{1}^{nmax}2*n^2)+(nmaxb-nmax)
C           bk()                 (Sum_{1}^{nmax}2*n^2)+(nmaxb-nmax)
C           rlow()               (Sum_{1}^{nmax}2*n^2)+(nmaxb-nmax)
C           ak(,)                ((Sum_{1}^{nmax}2*n^2)+(nmaxb-nmax),
C                                (Sum_{1}^{nmax}2*n^2)+(nmaxb-nmax))
C           xborn(,)             ((Sum_{1}^{nmax}2*n^2),(Sum_{1}^{nmax}2*n^2))
C
C Further Notes: Variable dimensions not mentioned above remain the same.
C                nmax is changed to 8
C                These variables should be changed to remain consistent in:
C                hydemi.for
C                lumsis.for
C                sigma.for
C                sigmel
```

```
C               sigmin.for
C               Within these subroutines, there are four new variables:
C          Variable             Dimension()/Value
C          ------------------------------------------------------
C          a(,)                 ((Sum_{1}^{nmax}2*n^2)+(nmaxb-nmax)-1,
C                                (Sum_{1}^{nmax}2*n^2)+(nmaxb-nmax)-1)
C          b()                  (Sum_{1}^{nmax}2*n^2)+(nmaxb-nmax)-1
C          wr()                 (Sum_{1}^{nmax}2*n^2)+(nmaxb-nmax)
C          sig()                (Sum_{1}^{nmax}2*n^2)+(nmaxb-nmax)
C
C               The IDL routine ADAS305_GET_STARK should be altered to
C               allow the code to produce higher transitions than n=4->1
```

A.2 fldizn

```
C-----------------------------------------------------------------------
C  ******************* FORTRAN 77 PROGRAM: FLDIZN *********************
C
C  PURPOSE: Code for modelling the effects of field ionization on
C           neutral beam atoms within a stark field
C
C  STEPS: 1.Assign parabolic quantum numbers n1, n2 and m and electric
C         field
C
C         2.Calculate the Stark energies using 3rd order perturbation
C         formula
C
C         3.Calculate ionization rates using semi-empirical formula
C
C  NOTES: The code has presumed spin to be degenerate. Therefore, the
C         number of resolved states that are assigned are n^2 - not
C         2*n^2.
C
C
C  PARAMETERS:
C           NAME                BRIEF DESCRIPTION
C           ------------------------------------------------------------
C                VXB      ***     Lorentz field set in V/M
C               SADDLE  ***     Classical ionization limit
C                N       ***     Principal n-shell
C               NDIM    ***     Number of resolved states
C               M_1()   ***     Parabolic quantum number m
C               N_1()   ***      Parabolic quantum number n1
C               N_2()   ***      Parabolic quantum number n2
C               E0      ***     Zero order term of Stark energy level
C               E1      ***     First order term of Stark energy level
C               E2      ***     Second order term of Stark energy level
C               E3      ***     Third order term of Stark energy level
C               E_0     ***      Stark energy level
C               N2F     ***     N2 factorial
C               N2MF    ***     N2+M factorial
C               G()     ***     Ionization probability
C
C
C  ROUTINES:
```

```
C           ROUTINE              BRIEF DESCRIPTION
C          -------------------------------------------------------------
C               GAMAF1  ***     Scales factorial
C               GAMAF2  ***     Scales base^exponent
C
C  AUTHOR: S.S.HENDERSON, JET
C          24 JULY 2009
C
C
C-----------------------------------------------------------------------
```

A.3 getpn

```
C********************************** f77 getpn.for ********************
C
C Purpose: Assigns quantum parabolic numbers to
C          to the energy vector created in
C          stark.for up to n=8. To achieve higher
C          n-shells set n1(2*n**2), n2(2*n**2)
C          and m(2*n**2)
C Notes: Energy is calculated from -k --> +k
C
C Variables: n         ***  principal quantum n-shell
C            n1(ndim)  ***  parabolic quantum number, n1
C            n2(ndim)  ***  parabolic quantum number, n2
C            m(ndim)   ***  magnetic quantum number, m
C
C Author: S S Henderson, University of Strathclyde
C         stuart.s.henderson@strath.ac.uk
C Date: 28/10/2009
C
C-----------------------------------------------------------------------
```

A.4 gamaf1

```
C-----------------------------------------------------------------------
C ******************** GAMAF1.FOR ***************************************
C
C PURPOSE : CONVERT FACTORIAL, NMAX, TO BASE X1*64^J1
C           BASED ON GAMAF.FOR FROM ADAS LIBRARY
C

C PARAMETERS :   NMAX *** N!
C                G1   *** X1
C               JG1  *** J1
C
C AUTHOR :  S.S.HENDERSON, JET
C           10 JULY 2009
```

```
C
C-----------------------------------------------------------------------
```

A.5 gamaf2

```
C-----------------------------------------------------------------------
C ******************** GAMAF2.FOR ***********************************
C
C PURPOSE : CONVERT FROM BASE K TO BASE 64 AND PASS OUT J1 AND X1
C           FROM EQUATION X1*64^J1. BASED ON GAMAF.FOR FROM ADAS LIBRARY
C
C PARAMETERS :   NMAX *** INTEGER PART OF EXPONENT
C                EF   *** FRACTIONAL PART OF EXPONENT
C               K    *** BASE
C               E    *** EXPONENT
C               FAC  *** B**EF
C                G1   *** X1
C               JG1  *** J1
C
C AUTHOR :  S.S.HENDERSON, JET
C           10 JULY 2009
C
C-----------------------------------------------------------------------
```

A.6 casmat

```
C-------------------------f77 casmat.for-----------------------------------
C Purpose: Calculates the cascade matrix for Stark substates
C
C Parameters: ISMAX ---- TOTAL NUMBER OF STATES
C             BMENER---- BEAM ENERGY
C             N1,N2,M,S- PARABOLIC, SPIN AND MAGNETIC QUANTUM NUMBERS
C             AK    ---- RADIATIVE MATRIX
C             AKSUM ---- SUMMED SUBSTATES
C             E0    ---- ENERGY LEVELS
C
C
C
C CONTACT: Stuart S Henderson, University of Strathclyde
C   EMAIL: stuart.s.henderson@strath.ac.uk
C-----------------------------------------------------------------------
```

A.7 Vk

```
C-----------------------------------------------------------
C ****************** Fortran77 Function VK ******************
C
C Purpose: Calculates the modified Bessel function of
C          imaginery order and real argument - Kia(x)
C
```

```
C
C Input  : (r*8) a  = real order
C Input  : (r*8) x  = real argument
C Output : (r*8) kv = Kia(x)
C
C Author:  S. S. Henderson, University of Strathclyde
C
C     Email: stuart.s.henderson@strath.ac.uk
C
C Date:    25/08/09
C-----------------------------------------------------------
```

A.8 Vk1

```
C-----------------------------------------------------------
C ***************** Fortran77 Function VK1 ******************
C
C Purpose: Calculates the modified Bessel function of
C          imaginery order and real argument - Kia'(x)
C
C
C Input  : (r*8) a   = real order
C Input  : (r*8) x   = real argument
C Output : (r*8) kv1 = Kia'(x)
C
C Author:  S. S. Henderson, University of Strathclyde
C
C     Email: stuart.s.henderson@strath.ac.uk
C
C Date:    25/08/09
C-----------------------------------------------------------
```

A.9 irreg

```
C------------------------irreg.for----------------------------------
C PURPOSE: Calculates the area of an irregular shape.
C
C METHOD: Splits the shape into triangular sections originating
C         from the origin and sums the area of each triangle
C         together.
C
C AUTHOR: Stuart S Henderson, Dec '09
C CONTACT: stuart.s.henderson@strath.ac.uk
C
C PARAMETERS:    (A-F)DIM *** Correspond to a-f dimensions in geometry
C                M(A-C)   *** Gradients of lines A-C
C                ANG(1-4) *** Angles 1-4
C                A1,A2    *** Intermediate areas
C                A        *** Total area
```

```
C               XARR()   *** X coordinates of shape
C               YARR()   *** Y coordinates of shape
C               DIM      *** Number of array points in shape
C-------------------------------------------------------------
```

Appendix B

Calculated roots of Laguerre polynomials

We show the calculated roots of the Laguerre polynomials $L_N(x)$ for $N \leq 40$. The roots were obtained through a bisection method with an accuracy of 10^{-12}, taking in advantage that all the roots of the Laguerre polynomials are real, greater than zero and of multiplicity one. The Laguerre polynomials were calculated using the recurrence relation

$$\begin{aligned} L_0(x) &= 1 \\ L_1(x) &= 1 - x \\ N L_N(x) &= (2N - 1 - x) L_{N-1}(x) - (N - 1) L_{N-2}(x) . \end{aligned} \tag{B.1}$$

N				
1	$1.000000000 \cdot 10^{0}$			
2	$5.857864376 \cdot 10^{-1}$	$3.414213562 \cdot 10^{0}$		
3	$4.157745568 \cdot 10^{-1}$	$2.294280360 \cdot 10^{0}$	$6.289945083 \cdot 10^{0}$	
4	$3.225476896 \cdot 10^{-1}$	$1.745761101 \cdot 10^{0}$	$4.536620297 \cdot 10^{0}$	$9.395070912 \cdot 10^{0}$
5	$2.635603197 \cdot 10^{-1}$	$1.413403059 \cdot 10^{0}$	$3.596425771 \cdot 10^{0}$	$7.085810006 \cdot 10^{0}$
	$1.264080084 \cdot 10^{1}$			
6	$2.228466042 \cdot 10^{-1}$	$1.188932102 \cdot 10^{0}$	$2.992736326 \cdot 10^{0}$	$5.775143569 \cdot 10^{0}$
	$9.837467418 \cdot 10^{0}$	$1.598287398 \cdot 10^{1}$		
7	$1.930436766 \cdot 10^{-1}$	$1.026664895 \cdot 10^{0}$	$2.567876745 \cdot 10^{0}$	$4.900353085 \cdot 10^{0}$
	$8.182153445 \cdot 10^{0}$	$1.273418029 \cdot 10^{1}$	$1.939572786 \cdot 10^{1}$	
8	$1.702796323 \cdot 10^{-1}$	$9.037017768 \cdot 10^{-1}$	$2.251086630 \cdot 10^{0}$	$4.266700170 \cdot 10^{0}$
	$7.045905402 \cdot 10^{0}$	$1.075851601 \cdot 10^{1}$	$1.574067864 \cdot 10^{1}$	$2.286313174 \cdot 10^{1}$
9	$1.523222277 \cdot 10^{-1}$	$8.072200227 \cdot 10^{-1}$	$2.005135156 \cdot 10^{0}$	$3.783473973 \cdot 10^{0}$
	$6.204956778 \cdot 10^{0}$	$9.372985252 \cdot 10^{0}$	$1.346623691 \cdot 10^{1}$	$1.883359779 \cdot 10^{1}$
	$2.637407189 \cdot 10^{1}$			
10	$1.377934705 \cdot 10^{-1}$	$7.294545495 \cdot 10^{-1}$	$1.808342902 \cdot 10^{0}$	$3.401433698 \cdot 10^{0}$
	$5.552496140 \cdot 10^{0}$	$8.330152747 \cdot 10^{0}$	$1.184378584 \cdot 10^{1}$	$1.627925783 \cdot 10^{1}$
	$2.199658581 \cdot 10^{1}$	$2.992069701 \cdot 10^{1}$		
11	$1.257964422 \cdot 10^{-1}$	$6.654182558 \cdot 10^{-1}$	$1.647150546 \cdot 10^{0}$	$3.091138143 \cdot 10^{0}$
	$5.029284402 \cdot 10^{0}$	$7.509887864 \cdot 10^{0}$	$1.060595100 \cdot 10^{1}$	$1.443161376 \cdot 10^{1}$
	$1.917885740 \cdot 10^{1}$	$2.521770934 \cdot 10^{1}$	$3.349719285 \cdot 10^{1}$	
12	$1.157221174 \cdot 10^{-1}$	$6.117574845 \cdot 10^{-1}$	$1.512610270 \cdot 10^{0}$	$2.833751338 \cdot 10^{0}$
	$4.599227639 \cdot 10^{0}$	$6.844525453 \cdot 10^{0}$	$9.621316842 \cdot 10^{0}$	$1.300605499 \cdot 10^{1}$
	$1.711685519 \cdot 10^{1}$	$2.215109038 \cdot 10^{1}$	$2.848796725 \cdot 10^{1}$	$3.709912104 \cdot 10^{1}$
13	$1.071423885 \cdot 10^{-1}$	$5.661318990 \cdot 10^{-1}$	$1.398564336 \cdot 10^{0}$	$2.616597108 \cdot 10^{0}$
	$4.238845929 \cdot 10^{0}$	$6.292256271 \cdot 10^{0}$	$8.815001941 \cdot 10^{0}$	$1.186140359 \cdot 10^{1}$
	$1.551076204 \cdot 10^{1}$	$1.988463566 \cdot 10^{1}$	$2.518526386 \cdot 10^{1}$	$3.180038630 \cdot 10^{1}$

N				
	$4.072300867 \cdot 10^{1}$			
14	$9.974750703 \cdot 10^{-2}$	$5.268576489 \cdot 10^{-1}$	$1.300629121 \cdot 10^{0}$	$2.430801079 \cdot 10^{0}$
	$3.932102822 \cdot 10^{0}$	$5.825536218 \cdot 10^{0}$	$8.140240142 \cdot 10^{0}$	$1.091649951 \cdot 10^{1}$
	$1.421080501 \cdot 10^{1}$	$1.810489222 \cdot 10^{1}$	$2.272338163 \cdot 10^{1}$	$2.827298172 \cdot 10^{1}$
	$3.514944366 \cdot 10^{1}$	$4.436608171 \cdot 10^{1}$		
15	$9.330781202 \cdot 10^{-2}$	$4.926917403 \cdot 10^{-1}$	$1.215595412 \cdot 10^{0}$	$2.269949526 \cdot 10^{0}$
	$3.667622722 \cdot 10^{0}$	$5.425336627 \cdot 10^{0}$	$7.565916227 \cdot 10^{0}$	$1.012022857 \cdot 10^{1}$
	$1.313028248 \cdot 10^{1}$	$1.665440771 \cdot 10^{1}$	$2.077647890 \cdot 10^{1}$	$2.562389423 \cdot 10^{1}$
	$3.140751917 \cdot 10^{1}$	$3.853068331 \cdot 10^{1}$	$4.802608557 \cdot 10^{1}$	
16	$8.764941048 \cdot 10^{-2}$	$4.626963289 \cdot 10^{-1}$	$1.141057775 \cdot 10^{0}$	$2.129283645 \cdot 10^{0}$
	$3.437086634 \cdot 10^{0}$	$5.078018615 \cdot 10^{0}$	$7.070338535 \cdot 10^{0}$	$9.438314336 \cdot 10^{0}$
	$1.221422337 \cdot 10^{1}$	$1.544152737 \cdot 10^{1}$	$1.918015686 \cdot 10^{1}$	$2.351590569 \cdot 10^{1}$
	$2.857872974 \cdot 10^{1}$	$3.458339870 \cdot 10^{1}$	$4.194045265 \cdot 10^{1}$	$5.170116034 \cdot 10^{1}$
17	$8.263821471 \cdot 10^{-2}$	$4.361503236 \cdot 10^{-1}$	$1.075176578 \cdot 10^{0}$	$2.005193532 \cdot 10^{0}$
	$3.234256124 \cdot 10^{0}$	$4.773513514 \cdot 10^{0}$	$6.637829205 \cdot 10^{0}$	$8.846685511 \cdot 10^{0}$
	$1.142552932 \cdot 10^{1}$	$1.440782304 \cdot 10^{1}$	$1.783828473 \cdot 10^{1}$	$2.177826826 \cdot 10^{1}$
	$2.631531781 \cdot 10^{1}$	$3.158177168 \cdot 10^{1}$	$3.779609384 \cdot 10^{1}$	$4.537571653 \cdot 10^{1}$
	$5.538975179 \cdot 10^{1}$			
18	$7.816916667 \cdot 10^{-2}$	$4.124900853 \cdot 10^{-1}$	$1.016520180 \cdot 10^{0}$	$1.894888510 \cdot 10^{0}$
	$3.054353113 \cdot 10^{0}$	$4.504205539 \cdot 10^{0}$	$6.256725074 \cdot 10^{0}$	$8.327825157 \cdot 10^{0}$
	$1.073799005 \cdot 10^{1}$	$1.351365621 \cdot 10^{1}$	$1.668930628 \cdot 10^{1}$	$2.031076763 \cdot 10^{1}$
	$2.444068136 \cdot 10^{1}$	$2.916820866 \cdot 10^{1}$	$3.462792707 \cdot 10^{1}$	$4.104181677 \cdot 10^{1}$
	$4.883392272 \cdot 10^{1}$	$5.909054644 \cdot 10^{1}$		
19	$7.415878376 \cdot 10^{-2}$	$3.912686133 \cdot 10^{-1}$	$9.639573440 \cdot 10^{-1}$	$1.796175582 \cdot 10^{0}$
	$2.893651382 \cdot 10^{0}$	$4.264215540 \cdot 10^{0}$	$5.918141562 \cdot 10^{0}$	$7.868618915 \cdot 10^{0}$
	$1.013242372 \cdot 10^{1}$	$1.273088146 \cdot 10^{1}$	$1.569127834 \cdot 10^{1}$	$1.904899321 \cdot 10^{1}$
	$2.285084976 \cdot 10^{1}$	$2.716066933 \cdot 10^{1}$	$3.206912225 \cdot 10^{1}$	$3.771290580 \cdot 10^{1}$
	$4.431736280 \cdot 10^{1}$	$5.231290246 \cdot 10^{1}$	$6.280242315 \cdot 10^{1}$	
20	$7.053988969 \cdot 10^{-2}$	$3.721268180 \cdot 10^{-1}$	$9.165821025 \cdot 10^{-1}$	$1.707306531 \cdot 10^{0}$
	$2.749199255 \cdot 10^{0}$	$4.048925314 \cdot 10^{0}$	$5.615174971 \cdot 10^{0}$	$7.459017454 \cdot 10^{0}$
	$9.594392870 \cdot 10^{0}$	$1.203880255 \cdot 10^{1}$	$1.481429344 \cdot 10^{1}$	$1.794889552 \cdot 10^{1}$
	$2.147878824 \cdot 10^{1}$	$2.545170279 \cdot 10^{1}$	$2.993255463 \cdot 10^{1}$	$3.501343424 \cdot 10^{1}$
	$4.083305706 \cdot 10^{1}$	$4.761999405 \cdot 10^{1}$	$5.581079575 \cdot 10^{1}$	$6.652441653 \cdot 10^{1}$
21	$6.725781792 \cdot 10^{-2}$	$3.547728953 \cdot 10^{-1}$	$8.736601668 \cdot 10^{-1}$	$1.626869942 \cdot 10^{0}$
	$2.618626411 \cdot 10^{0}$	$3.854652138 \cdot 10^{0}$	$5.342369281 \cdot 10^{0}$	$7.091168813 \cdot 10^{0}$
	$9.112778854 \cdot 10^{0}$	$1.142177176 \cdot 10^{1}$	$1.403627070 \cdot 10^{1}$	$1.697895269 \cdot 10^{1}$
	$2.027850941 \cdot 10^{1}$	$2.397184559 \cdot 10^{1}$	$2.810752860 \cdot 10^{1}$	$3.275149741 \cdot 10^{1}$
	$3.799718782 \cdot 10^{1}$	$4.398524576 \cdot 10^{1}$	$5.094735119 \cdot 10^{1}$	$5.932599412 \cdot 10^{1}$
	$7.025568863 \cdot 10^{1}$			
22	$6.426762874 \cdot 10^{-2}$	$3.389672548 \cdot 10^{-1}$	$8.345899854 \cdot 10^{-1}$	$1.553713387 \cdot 10^{0}$
	$2.500006237 \cdot 10^{0}$	$3.678420344 \cdot 10^{0}$	$5.095349069 \cdot 10^{0}$	$6.758835516 \cdot 10^{0}$
	$8.678853314 \cdot 10^{0}$	$1.086768689 \cdot 10^{1}$	$1.334045105 \cdot 10^{1}$	$1.611581134 \cdot 10^{1}$
	$1.921700368 \cdot 10^{1}$	$2.267331660 \cdot 10^{1}$	$2.652231959 \cdot 10^{1}$	$3.081335794 \cdot 10^{1}$
	$3.561333520 \cdot 10^{1}$	$4.101696860 \cdot 10^{1}$	$4.716675785 \cdot 10^{1}$	$5.429738526 \cdot 10^{1}$
	$6.285709625 \cdot 10^{1}$	$7.399550701 \cdot 10^{1}$		
23	$6.153203776 \cdot 10^{-2}$	$3.245113292 \cdot 10^{-1}$	$7.988739687 \cdot 10^{-1}$	$1.486886334 \cdot 10^{0}$
	$2.391755830 \cdot 10^{0}$	$3.517797443 \cdot 10^{0}$	$4.870560369 \cdot 10^{0}$	$6.456991307 \cdot 10^{0}$
	$8.285651893 \cdot 10^{0}$	$1.036700904 \cdot 10^{1}$	$1.271382503 \cdot 10^{1}$	$1.534168757 \cdot 10^{1}$
	$1.826974239 \cdot 10^{1}$	$2.152172785 \cdot 10^{1}$	$2.512747713 \cdot 10^{1}$	$2.912517511 \cdot 10^{1}$
	$3.356489656 \cdot 10^{1}$	$3.851445968 \cdot 10^{1}$	$4.406980781 \cdot 10^{1}$	$5.037522660 \cdot 10^{1}$
	$5.766830435 \cdot 10^{1}$	$6.640287307 \cdot 10^{1}$	$7.774322728 \cdot 10^{1}$	

N				
24	$5.901985218 \cdot 10^{-2}$	$3.112391462 \cdot 10^{-1}$	$7.660969055 \cdot 10^{-1}$	$1.425597591 \cdot 10^{0}$
	$2.292562059 \cdot 10^{0}$	$3.370774264 \cdot 10^{0}$	$4.665083703 \cdot 10^{0}$	$6.181535119 \cdot 10^{0}$
	$7.927539247 \cdot 10^{0}$	$9.912098015 \cdot 10^{0}$	$1.214610271 \cdot 10^{1}$	$1.464273229 \cdot 10^{1}$
	$1.741799265 \cdot 10^{1}$	$2.049146008 \cdot 10^{1}$	$2.388732985 \cdot 10^{1}$	$2.763593717 \cdot 10^{1}$
	$3.177604135 \cdot 10^{1}$	$3.635840580 \cdot 10^{1}$	$4.145172048 \cdot 10^{1}$	$4.715310645 \cdot 10^{1}$
	$5.360857454 \cdot 10^{1}$	$6.105853145 \cdot 10^{1}$	$6.996224004 \cdot 10^{1}$	$8.149827923 \cdot 10^{1}$
25	$5.670477545 \cdot 10^{-2}$	$2.990108986 \cdot 10^{-1}$	$7.359095554 \cdot 10^{-1}$	$1.369183116 \cdot 10^{0}$
	$2.201326054 \cdot 10^{0}$	$3.235675804 \cdot 10^{0}$	$4.476496615 \cdot 10^{0}$	$5.929083763 \cdot 10^{0}$
	$7.599899310 \cdot 10^{0}$	$9.496749221 \cdot 10^{0}$	$1.162901491 \cdot 10^{1}$	$1.400795798 \cdot 10^{1}$
	$1.664712560 \cdot 10^{1}$	$1.956289801 \cdot 10^{1}$	$2.277524199 \cdot 10^{1}$	$2.630877239 \cdot 10^{1}$
	$3.019429116 \cdot 10^{1}$	$3.447109757 \cdot 10^{1}$	$3.919060880 \cdot 10^{1}$	$4.442234934 \cdot 10^{1}$
	$5.026457499 \cdot 10^{1}$	$5.686496717 \cdot 10^{1}$	$6.446667062 \cdot 10^{1}$	$7.353423479 \cdot 10^{1}$
	$8.526015556 \cdot 10^{1}$			
26	$5.456448272 \cdot 10^{-2}$	$2.877079791 \cdot 10^{-1}$	$7.080160195 \cdot 10^{-1}$	$1.317081366 \cdot 10^{0}$
	$2.117120945 \cdot 10^{0}$	$3.111093879 \cdot 10^{0}$	$4.302770876 \cdot 10^{0}$	$5.696818826 \cdot 10^{0}$
	$7.298909963 \cdot 10^{0}$	$9.115862897 \cdot 10^{0}$	$1.115582495 \cdot 10^{1}$	$1.342850903 \cdot 10^{1}$
	$1.594550395 \cdot 10^{1}$	$1.872068615 \cdot 10^{1}$	$2.177077461 \cdot 10^{1}$	$2.511609366 \cdot 10^{1}$
	$2.878164687 \cdot 10^{1}$	$3.279867322 \cdot 10^{1}$	$3.720698263 \cdot 10^{1}$	$4.205861592 \cdot 10^{1}$
	$4.742389936 \cdot 10^{1}$	$5.340218520 \cdot 10^{1}$	$6.014277569 \cdot 10^{1}$	$6.789147971 \cdot 10^{1}$
	$7.711799907 \cdot 10^{1}$	$8.902840275 \cdot 10^{1}$		
27	$5.257989821 \cdot 10^{-2}$	$2.772291060 \cdot 10^{-1}$	$6.821639114 \cdot 10^{-1}$	$1.268814181 \cdot 10^{0}$
	$2.039159278 \cdot 10^{0}$	$2.995835582 \cdot 10^{0}$	$4.142194483 \cdot 10^{0}$	$5.482371716 \cdot 10^{0}$
	$7.021376025 \cdot 10^{0}$	$8.765202717 \cdot 10^{0}$	$1.072097905 \cdot 10^{1}$	$1.289715090 \cdot 10^{1}$
	$1.530372420 \cdot 10^{1}$	$1.795258016 \cdot 10^{1}$	$2.085789274 \cdot 10^{1}$	$2.403669039 \cdot 10^{1}$
	$2.750962763 \cdot 10^{1}$	$3.130207079 \cdot 10^{1}$	$3.544567067 \cdot 10^{1}$	$3.998072262 \cdot 10^{1}$
	$4.495986479 \cdot 10^{1}$	$5.045419615 \cdot 10^{1}$	$5.656413090 \cdot 10^{1}$	$6.344054668 \cdot 10^{1}$
	$7.133184806 \cdot 10^{1}$	$8.071276385 \cdot 10^{1}$	$9.280261353 \cdot 10^{1}$	
28	$5.073462485 \cdot 10^{-2}$	$2.674872686 \cdot 10^{-1}$	$6.581366284 \cdot 10^{-1}$	$1.223971808 \cdot 10^{0}$
	$1.966767612 \cdot 10^{0}$	$2.888883326 \cdot 10^{0}$	$3.993311659 \cdot 10^{0}$	$5.283736063 \cdot 10^{0}$
	$6.764603404 \cdot 10^{0}$	$8.441216328 \cdot 10^{0}$	$1.031985046 \cdot 10^{1}$	$1.240790341 \cdot 10^{1}$
	$1.471408516 \cdot 10^{1}$	$1.724866342 \cdot 10^{1}$	$2.002378333 \cdot 10^{1}$	$2.305389014 \cdot 10^{1}$
	$2.635629737 \cdot 10^{1}$	$2.995196683 \cdot 10^{1}$	$3.386660552 \cdot 10^{1}$	$3.813225441 \cdot 10^{1}$
	$4.278967237 \cdot 10^{1}$	$4.789207163 \cdot 10^{1}$	$5.351129796 \cdot 10^{1}$	$5.974879608 \cdot 10^{1}$
	$6.675697728 \cdot 10^{1}$	$7.478677815 \cdot 10^{1}$	$8.431783711 \cdot 10^{1}$	$9.658242063 \cdot 10^{1}$
29	$4.901448999 \cdot 10^{-2}$	$2.584072979 \cdot 10^{-1}$	$6.357472158 \cdot 10^{-1}$	$1.182201056 \cdot 10^{0}$
	$1.899366498 \cdot 10^{0}$	$2.789363538 \cdot 10^{0}$	$3.854876158 \cdot 10^{0}$	$5.099200089 \cdot 10^{0}$
	$6.526302885 \cdot 10^{0}$	$8.140899733 \cdot 10^{0}$	$9.948548894 \cdot 10^{0}$	$1.195577194 \cdot 10^{1}$
	$1.417020584 \cdot 10^{1}$	$1.660079655 \cdot 10^{1}$	$1.925804791 \cdot 10^{1}$	$2.215434543 \cdot 10^{1}$
	$2.530438376 \cdot 10^{1}$	$2.872574103 \cdot 10^{1}$	$3.243966674 \cdot 10^{1}$	$3.647218971 \cdot 10^{1}$
	$4.085572234 \cdot 10^{1}$	$4.563146770 \cdot 10^{1}$	$5.085319152 \cdot 10^{1}$	$5.659346290 \cdot 10^{1}$
	$6.295472850 \cdot 10^{1}$	$7.009089460 \cdot 10^{1}$	$7.825537042 \cdot 10^{1}$	$8.793259364 \cdot 10^{1}$
	$1.003674916 \cdot 10^{2}$			
30	$4.740718054 \cdot 10^{-2}$	$2.499239168 \cdot 10^{-1}$	$6.148334544 \cdot 10^{-1}$	$1.143195826 \cdot 10^{0}$
	$1.836454555 \cdot 10^{0}$	$2.696521875 \cdot 10^{0}$	$3.725814508 \cdot 10^{0}$	$4.927293766 \cdot 10^{0}$
	$6.304515591 \cdot 10^{0}$	$7.861693293 \cdot 10^{0}$	$9.603775985 \cdot 10^{0}$	$1.153654660 \cdot 10^{1}$
	$1.366674469 \cdot 10^{1}$	$1.600222119 \cdot 10^{1}$	$1.855213484 \cdot 10^{1}$	$2.132720432 \cdot 10^{1}$
	$2.434003576 \cdot 10^{1}$	$2.760555480 \cdot 10^{1}$	$3.114158670 \cdot 10^{1}$	$3.496965201 \cdot 10^{1}$
	$3.911608495 \cdot 10^{1}$	$4.361365291 \cdot 10^{1}$	$4.850398616 \cdot 10^{1}$	$5.384138541 \cdot 10^{1}$
	$5.969912186 \cdot 10^{1}$	$6.618061779 \cdot 10^{1}$	$7.344123860 \cdot 10^{1}$	$8.173681051 \cdot 10^{1}$
	$9.155646652 \cdot 10^{1}$	$1.041575244 \cdot 10^{2}$		
31	$4.590194762 \cdot 10^{-2}$	$2.419801638 \cdot 10^{-1}$	$5.952538942 \cdot 10^{-1}$	$1.106689500 \cdot 10^{0}$

N				
	$1.777595693 \cdot 10^{0}$	$2.609703415 \cdot 10^{0}$	$3.605196802 \cdot 10^{0}$	$4.766747084 \cdot 10^{0}$
	$6.097554567 \cdot 10^{0}$	$7.601400949 \cdot 10^{0}$	$9.282714313 \cdot 10^{0}$	$1.114664976 \cdot 10^{1}$
	$1.319918958 \cdot 10^{1}$	$1.544726832 \cdot 10^{1}$	$1.789892983 \cdot 10^{1}$	$2.056352634 \cdot 10^{1}$
	$2.345197348 \cdot 10^{1}$	$2.657708135 \cdot 10^{1}$	$2.995399087 \cdot 10^{1}$	$3.360075953 \cdot 10^{1}$
	$3.753916441 \cdot 10^{1}$	$4.179583087 \cdot 10^{1}$	$4.640386681 \cdot 10^{1}$	$5.140531448 \cdot 10^{1}$
	$5.685499287 \cdot 10^{1}$	$6.282685591 \cdot 10^{1}$	$6.942527719 \cdot 10^{1}$	$7.680704776 \cdot 10^{1}$
	$8.523035861 \cdot 10^{1}$	$9.518893989 \cdot 10^{1}$	$1.079522438 \cdot 10^{2}$	
32	$4.448936583 \cdot 10^{-2}$	$2.345261095 \cdot 10^{-1}$	$5.768846293 \cdot 10^{-1}$	$1.072448754 \cdot 10^{0}$
	$1.722408776 \cdot 10^{0}$	$2.528336706 \cdot 10^{0}$	$3.492213273 \cdot 10^{0}$	$4.616456770 \cdot 10^{0}$
	$5.903958504 \cdot 10^{0}$	$7.358126733 \cdot 10^{0}$	$8.982940924 \cdot 10^{0}$	$1.078301863 \cdot 10^{1}$
	$1.276369799 \cdot 10^{1}$	$1.493113976 \cdot 10^{1}$	$1.729245434 \cdot 10^{1}$	$1.985586094 \cdot 10^{1}$
	$2.263088901 \cdot 10^{1}$	$2.562863602 \cdot 10^{1}$	$2.886210182 \cdot 10^{1}$	$3.234662915 \cdot 10^{1}$
	$3.610049481 \cdot 10^{1}$	$4.014571977 \cdot 10^{1}$	$4.450920800 \cdot 10^{1}$	$4.922439499 \cdot 10^{1}$
	$5.433372133 \cdot 10^{1}$	$5.989250916 \cdot 10^{1}$	$6.597537729 \cdot 10^{1}$	$7.268762809 \cdot 10^{1}$
	$8.018744698 \cdot 10^{1}$	$8.873534042 \cdot 10^{1}$	$9.882954287 \cdot 10^{1}$	$1.117513981 \cdot 10^{2}$
33	$4.316113562 \cdot 10^{-2}$	$2.275178028 \cdot 10^{-1}$	$5.596166559 \cdot 10^{-1}$	$1.040268508 \cdot 10^{0}$
	$1.670559196 \cdot 10^{0}$	$2.451920796 \cdot 10^{0}$	$3.386155338 \cdot 10^{0}$	$4.475459498 \cdot 10^{0}$
	$5.722454720 \cdot 10^{0}$	$7.130224344 \cdot 10^{0}$	$8.702359231 \cdot 10^{0}$	$1.044301365 \cdot 10^{1}$
	$1.235697376 \cdot 10^{1}$	$1.444974168 \cdot 10^{1}$	$1.672763922 \cdot 10^{1}$	$1.919793659 \cdot 10^{1}$
	$2.186901352 \cdot 10^{1}$	$2.475056291 \cdot 10^{1}$	$2.785385111 \cdot 10^{1}$	$3.119205555 \cdot 10^{1}$
	$3.478070915 \cdot 10^{1}$	$3.863829672 \cdot 10^{1}$	$4.278707208 \cdot 10^{1}$	$4.725420660 \cdot 10^{1}$
	$5.207345190 \cdot 10^{1}$	$5.728763454 \cdot 10^{1}$	$6.295256595 \cdot 10^{1}$	$6.914351338 \cdot 10^{1}$
	$7.596668701 \cdot 10^{1}$	$8.358163722 \cdot 10^{1}$	$9.225113944 \cdot 10^{1}$	$1.024778443 \cdot 10^{2}$
	$1.155547564 \cdot 10^{2}$			
34	$4.190992002 \cdot 10^{-2}$	$2.209164020 \cdot 10^{-1}$	$5.433536946 \cdot 10^{-1}$	$1.009967765 \cdot 10^{0}$
	$1.621751953 \cdot 10^{0}$	$2.380014626 \cdot 10^{0}$	$3.286400154 \cdot 10^{0}$	$4.342910167 \cdot 10^{0}$
	$5.551929289 \cdot 10^{0}$	$6.916256712 \cdot 10^{0}$	$8.439144796 \cdot 10^{0}$	$1.012434611 \cdot 10^{1}$
	$1.197617070 \cdot 10^{1}$	$1.399955595 \cdot 10^{1}$	$1.620015203 \cdot 10^{1}$	$1.858442711 \cdot 10^{1}$
	$2.115979765 \cdot 10^{1}$	$2.393479131 \cdot 10^{1}$	$2.691925258 \cdot 10^{1}$	$3.012460565 \cdot 10^{1}$
	$3.356419492 \cdot 10^{1}$	$3.725373335 \cdot 10^{1}$	$4.121190386 \cdot 10^{1}$	$4.546118331 \cdot 10^{1}$
	$5.002900054 \cdot 10^{1}$	$5.494941289 \cdot 10^{1}$	$6.026562168 \cdot 10^{1}$	$6.603391492 \cdot 10^{1}$
	$7.233019308 \cdot 10^{1}$	$7.926155449 \cdot 10^{1}$	$8.698888681 \cdot 10^{1}$	$9.577719042 \cdot 10^{1}$
	$1.061334485 \cdot 10^{2}$	$1.193621067 \cdot 10^{2}$		
35	$4.072920906 \cdot 10^{-2}$	$2.146874527 \cdot 10^{-1}$	$5.280103843 \cdot 10^{-1}$	$9.813861735 \cdot 10^{-1}$
	$1.575725948 \cdot 10^{0}$	$2.312228297 \cdot 10^{0}$	$3.192397939 \cdot 10^{0}$	$4.218064125 \cdot 10^{0}$
	$5.391402735 \cdot 10^{0}$	$6.714963280 \cdot 10^{0}$	$8.191701759 \cdot 10^{0}$	$9.825020497 \cdot 10^{0}$
	$1.161881639 \cdot 10^{1}$	$1.357753936 \cdot 10^{1}$	$1.570626340 \cdot 10^{1}$	$1.801077329 \cdot 10^{1}$
	$2.049767111 \cdot 10^{1}$	$2.317450800 \cdot 10^{1}$	$2.604994871 \cdot 10^{1}$	$2.913397921 \cdot 10^{1}$
	$3.243817184 \cdot 10^{1}$	$3.597602877 \cdot 10^{1}$	$3.976343410 \cdot 10^{1}$	$4.381926012 \cdot 10^{1}$
	$4.816619797 \cdot 10^{1}$	$5.283192506 \cdot 10^{1}$	$5.785079502 \cdot 10^{1}$	$6.326637368 \cdot 10^{1}$
	$6.913541388 \cdot 10^{1}$	$7.553443513 \cdot 10^{1}$	$8.257140552 \cdot 10^{1}$	$9.040852386 \cdot 10^{1}$
	$9.931297366 \cdot 10^{1}$	$1.097959909 \cdot 10^{2}$	$1.231732532 \cdot 10^{2}$	
36	$3.961320641 \cdot 10^{-2}$	$2.088002857 \cdot 10^{-1}$	$5.135107755 \cdot 10^{-1}$	$9.543811531 \cdot 10^{-1}$
	$1.532249225 \cdot 10^{0}$	$2.248215818 \cdot 10^{0}$	$3.103661490 \cdot 10^{0}$	$4.100262546 \cdot 10^{0}$
	$5.240010109 \cdot 10^{0}$	$6.525233330 \cdot 10^{0}$	$7.958627509 \cdot 10^{0}$	$9.543288035 \cdot 10^{0}$
	$1.128275129 \cdot 10^{1}$	$1.318104390 \cdot 10^{1}$	$1.524274227 \cdot 10^{1}$	$1.747304463 \cdot 10^{1}$
	$1.987785893 \cdot 10^{1}$	$2.246391051 \cdot 10^{1}$	$2.523887526 \cdot 10^{1}$	$2.821154568 \cdot 10^{1}$
	$3.139204037 \cdot 10^{1}$	$3.479207145 \cdot 10^{1}$	$3.842529076 \cdot 10^{1}$	$4.230774567 \cdot 10^{1}$
	$4.645849004 \cdot 10^{1}$	$5.090042150 \cdot 10^{1}$	$5.566145791 \cdot 10^{1}$	$6.077624068 \cdot 10^{1}$
	$6.628869068 \cdot 10^{1}$	$7.225601475 \cdot 10^{1}$	$7.875533816 \cdot 10^{1}$	$8.589548143 \cdot 10^{1}$
	$9.383992978 \cdot 10^{1}$	$1.028580101 \cdot 10^{2}$	$1.134651355 \cdot 10^{2}$	$1.269880152 \cdot 10^{2}$

N				
37	$3.855673419 \cdot 10^{-2}$	$2.032275099 \cdot 10^{-1}$	$4.997870664 \cdot 10^{-1}$	$9.288254993 \cdot 10^{-1}$
	$1.491115012 \cdot 10^{0}$	$2.187669072 \cdot 10^{0}$	$3.019757468 \cdot 10^{0}$	$3.988920303 \cdot 10^{0}$
	$5.096984545 \cdot 10^{0}$	$6.346084061 \cdot 10^{0}$	$7.738683814 \cdot 10^{0}$	$9.277608942 \cdot 10^{0}$
	$1.096607963 \cdot 10^{1}$	$1.280775291 \cdot 10^{1}$	$1.480677283 \cdot 10^{1}$	$1.696783086 \cdot 10^{1}$
	$1.929623895 \cdot 10^{1}$	$2.179801837 \cdot 10^{1}$	$2.448000859 \cdot 10^{1}$	$2.735000162 \cdot 10^{1}$
	$3.041690963 \cdot 10^{1}$	$3.369097614 \cdot 10^{1}$	$3.718404564 \cdot 10^{1}$	$4.090991253 \cdot 10^{1}$
	$4.488478042 \cdot 10^{1}$	$4.912787781 \cdot 10^{1}$	$5.366230174 \cdot 10^{1}$	$5.851620322 \cdot 10^{1}$
	$6.372450358 \cdot 10^{1}$	$6.933147003 \cdot 10^{1}$	$7.539475330 \cdot 10^{1}$	$8.199207200 \cdot 10^{1}$
	$8.923308273 \cdot 10^{1}$	$9.728253367 \cdot 10^{1}$	$1.064118573 \cdot 10^{2}$	$1.171405711 \cdot 10^{2}$
	$1.308062254 \cdot 10^{2}$			
38	$3.755515263 \cdot 10^{-2}$	$1.979445866 \cdot 10^{-1}$	$4.867785379 \cdot 10^{-1}$	$9.046053593 \cdot 10^{-1}$
	$1.452138374 \cdot 10^{0}$	$2.130312744 \cdot 10^{0}$	$2.940299106 \cdot 10^{0}$	$3.883515862 \cdot 10^{0}$
	$4.961643595 \cdot 10^{0}$	$6.176642449 \cdot 10^{0}$	$7.530773049 \cdot 10^{0}$	$9.026621537 \cdot 10^{0}$
	$1.066712948 \cdot 10^{1}$	$1.245562951 \cdot 10^{1}$	$1.439588797 \cdot 10^{1}$	$1.649215579 \cdot 10^{1}$
	$1.874922978 \cdot 10^{1}$	$2.117252653 \cdot 10^{1}$	$2.376817221 \cdot 10^{1}$	$2.654311242 \cdot 10^{1}$
	$2.950524786 \cdot 10^{1}$	$3.266360325 \cdot 10^{1}$	$3.602854026 \cdot 10^{1}$	$3.961202923 \cdot 10^{1}$
	$4.342800076 \cdot 10^{1}$	$4.749280846 \cdot 10^{1}$	$5.182584921 \cdot 10^{1}$	$5.645041308 \cdot 10^{1}$
	$6.139487752 \cdot 10^{1}$	$6.669443658 \cdot 10^{1}$	$7.239369576 \cdot 10^{1}$	$7.855074022 \cdot 10^{1}$
	$8.524387023 \cdot 10^{1}$	$9.258356301 \cdot 10^{1}$	$1.007358074 \cdot 10^{2}$	$1.099741054 \cdot 10^{2}$
	$1.208220095 \cdot 10^{2}$	$1.346277283 \cdot 10^{2}$		
39	$3.660429196 \cdot 10^{-2}$	$1.929294668 \cdot 10^{-1}$	$4.744306515 \cdot 10^{-1}$	$8.816185218 \cdot 10^{-1}$
	$1.415153403 \cdot 10^{0}$	$2.075900054 \cdot 10^{0}$	$2.864940087 \cdot 10^{0}$	$3.783582804 \cdot 10^{0}$
	$4.833377810 \cdot 10^{0}$	$6.016130156 \cdot 10^{0}$	$7.333918496 \cdot 10^{0}$	$8.789116762 \cdot 10^{0}$
	$1.038441992 \cdot 10^{1}$	$1.212287459 \cdot 10^{1}$	$1.400791538 \cdot 10^{1}$	$1.604340819 \cdot 10^{1}$
	$1.823370185 \cdot 10^{1}$	$2.058369013 \cdot 10^{1}$	$2.309888640 \cdot 10^{1}$	$2.578551437 \cdot 10^{1}$
	$2.865061891 \cdot 10^{1}$	$3.170220279 \cdot 10^{1}$	$3.494939706 \cdot 10^{1}$	$3.840267556 \cdot 10^{1}$
	$4.207412867 \cdot 10^{1}$	$4.597781756 \cdot 10^{1}$	$5.013024019 \cdot 10^{1}$	$5.455095618 \cdot 10^{1}$
	$5.926344277 \cdot 10^{1}$	$6.429629778 \cdot 10^{1}$	$6.968498128 \cdot 10^{1}$	$7.547442957 \cdot 10^{1}$
	$8.172315339 \cdot 10^{1}$	$8.851002367 \cdot 10^{1}$	$9.594632357 \cdot 10^{1}$	$1.041992613 \cdot 10^{2}$
	$1.135443740 \cdot 10^{2}$	$1.245091829 \cdot 10^{2}$	$1.384523795 \cdot 10^{2}$	
40	$3.570039431 \cdot 10^{-2}$	$1.881622832 \cdot 10^{-1}$	$4.626942813 \cdot 10^{-1}$	$8.597729640 \cdot 10^{-1}$
	$1.380010821 \cdot 10^{0}$	$2.024209136 \cdot 10^{0}$	$2.793369354 \cdot 10^{0}$	$3.688702678 \cdot 10^{0}$
	$4.711641147 \cdot 10^{0}$	$5.863850878 \cdot 10^{0}$	$7.147247908 \cdot 10^{0}$	$8.564017018 \cdot 10^{0}$
	$1.011663405 \cdot 10^{1}$	$1.180789229 \cdot 10^{1}$	$1.364093371 \cdot 10^{1}$	$1.561928589 \cdot 10^{1}$
	$1.774690595 \cdot 10^{1}$	$2.002823283 \cdot 10^{1}$	$2.246824998 \cdot 10^{1}$	$2.507256077 \cdot 10^{1}$
	$2.784748001 \cdot 10^{1}$	$3.080014574 \cdot 10^{1}$	$3.393865708 \cdot 10^{1}$	$3.727224588 \cdot 10^{1}$
	$4.081149282 \cdot 10^{1}$	$4.456860318 \cdot 10^{1}$	$4.855776353 \cdot 10^{1}$	$5.279561119 \cdot 10^{1}$
	$5.730186332 \cdot 10^{1}$	$6.210017907 \cdot 10^{1}$	$6.721937093 \cdot 10^{1}$	$7.269515885 \cdot 10^{1}$
	$7.857280291 \cdot 10^{1}$	$8.491123114 \cdot 10^{1}$	$9.178987467 \cdot 10^{1}$	$9.932080872 \cdot 10^{1}$
	$1.076724406 \cdot 10^{2}$	$1.171223095 \cdot 10^{2}$	$1.282018420 \cdot 10^{2}$	$1.422800445 \cdot 10^{2}$

Calculated roots for Laguerre polynomials of grad N. The accuracy is the last cipher.

Index